NTNU – Trondheim
Norwegian University of
Science and Technology

GROWTH AND PROPERTIES OF CARBON NANOTUBES

Karl Erik Nordheim

Mechanical Engineering
Submission date: June 2012
Supervisor: Christian Thaulow, IPM

Norwegian University of Science and Technology
Department of Engineering Design and Materials

THE NORWEGIAN UNIVERSITY
OF SCIENCE AND TECHNOLOGY
DEPARTMENT OF ENGINEERING DESIGN
AND MATERIALS

MASTER THESIS SPRING 2012
FOR
STUD.TECHN. KARL ERIK NORDHEIM

GROWTH AND PROPERTIES OF CARBON NANOTUBES
Groing og egenskaper til carbon nanotubes

CNTs are new materials that possess unique mechanical, electrical and thermal properties compared to traditional materials. The ballistic transport of electrons, which means that no heat is generated, is the reason for the extreme electrical conductivity. The latest measured values of the mechanical properties have shown improvements compared to older experiments, which is most likely because of more advanced and accurate measuring methods, but have not reached values of the same level as the theoretical predictions. The huge gap is because the theoretical simulations do not consider the defects that are present. A single missing carbon atom in the shell is able to reduce the strength by 25%. Although the measured values have been unable to reach the level as the predicted ones yet, CNTs are still the material with the highest power to weight ratio.
The PECVD is a promising method for producing CNTs since it requires a lower synthesis temperature compared to the other methods and is able to give untangled and vertically CNTs. Unfortunately the post-treatments that are needed involves several steps, which makes the synthesis quite cumbersome.

In the future it will be important to improve the PECVD method by considering how to scale up the production, synthesis of a batch of CNTs with equal properties and with minimal defects. Detailed knowledge of the fundamental growth mechanism of CNTs is necessary for the development of large-scale and structure controlled synthesis. New catalyst materials have been discovered, which could show to solve some of the issues with the many pre-treatment steps involved in the synthesis. In addition, they could be able to minimize the defects in the CNTs which could results in enhancement of the mechanical, electrical and thermal properties.

The first task should be to grow CNTs on a stainless steel surface at the NTNU NanoLab which is complicated because of the protective passive layer on the surface. This is why growing CNTs on less complex materials could be a way to start, to obtain successfully parameters, such as type of gas, gas flow, temperature, pressure etc. Additionally sub tasks that should be investigated:

- Find the most suited technique for removal of the oxide layer on stainless steel prior to CNT growth
- To see how different gas flow rates and gas types, affects the structure and morphology of the CNTs
- Check different types of catalyst materials
- The effects of pre-treatment

The next task is to characterize the grown CNTs (diameter, length, alignment, MWCNT/SWCNT etc).

Finally perform testing to quantify mechanical and other properties

The thesis should include the signed problem text, and be written as a research report with summary both in English and Norwegian, conclusion, literature references, table of contents, etc. During preparation of the text, the candidate should make efforts to create a well arranged and well written report. To ease the evaluation of the thesis, it is important to cross-reference text, tables and figures. For evaluation of the work a thorough discussion of results is appreciated.

Three weeks after start of the thesis work, an A3 sheet illustrating the work is to be handed in. A template for this presentation is available on the IPM's web site under the menu "Undervisning". This sheet should be updated when the Master's thesis is submitted.

The thesis shall be submitted electronically via DAIM, NTNU's system for Digital Archiving and Submission of Master's thesis.

Contact person

Espen Rogstad, NTNU NanoLab

Torgeir Welo
Head of Division

Christian Thaulow
Professor/Supervisor

NTNU
Norges teknisk-
naturvitenskapelige universitet

Institutt for produktutvikling
og materialer

Abstract

An experimental study of Carbon Nanotube (CNT) growth has been performed by using radio frequency plasma enhanced chemical vapour deposition with methane (CH_4) as the hydrocarbon source. The experimental results have been compared towards earlier experiments and theories that exist. A study of the effect by changing parameters during thermal- and plasma- pretreatment has been conducted which have led to successful yield of vertically aligned CNTs forests. Different growth conditions have been conducted in order to see the influence of the following: Methane (CH_4) flow, plasma power, growth time, temperature, methane (CH_4)/ammonia (NH_3) mixtures during growth, no barrier layer, thermal- versus plasma-pretreatment and oxidizing pretreatment. The conclusion from this experiment is that oxidizing pretreatment seems yields the tallest vertically aligned CNTs with the narrowest diameter.

Sammendrag

Et eksperimentelt studie av Karbon Nanorør (CNT) vekst har blitt utført ved bruk av radiofrekvensiell plasma forbedrende kjemisk damp deponering ved bruk av metan (CH_4) som hydrokarbon kilde. De eksperimentelle resultater har blitt sammenligned mot tidligere experiment og teorier som eksisterer. Et studie av effekten ved å endre parametere under termisk- og plasma-forbehandling har blitt utført, som har ført til at groing av velykkede skoger med vertikal justerte CNTs. Forskjellige gro miljøer har blitt analysert, for å se effekten av: Metan (CH_4) strømning, plasma styrke, grotid, temperatur, metan (CH_4)/amoniakk (NH_3) blandinger, intet barrierlag, termisk- og plasma-forbehandling og oksiderende forbehandling. Konklusjonen fra experimentet er at den oksiderende forbehandling ser ut til å gi groing av de høyeste vertikale justerte CNTs med den smallest diameter.

Declaration

I declare that this work has been performed independently and in accordance with the rules and regulations for examinations at the Norwegian University of Science and Technology (NTNU).

_____

Karl Erik Nordheim

Trondheim, 22th of June 2012

Preface

This Master Thesis is submitted for a Master's degree at the Department of Engineering Design and Materials at the Norwegian University of Science and Technology (NTNU).The work has been done at the NTNU NanoLab and is a continuation of the specialization project performed during the autumn of 2011.

I would like to thank my supervisor, Professor Christian Thaulow, for being the one that introduced me to this new and exciting material and for being helpful and supportive during the project. I would also like to thank Espen Rogstad who has spent a lot of his time on technical support and who have been an inspiration during long working hours. I would also like to thank everyone that has helped solving issues during this project:

- Fredrik Martinsen (Department of Physics) for his help during TEM sample preparation.
- Gurvinder Singh (Department of Chemical Engineering) for his help during TEM sample preparation.
- Yingda Yu (Department of Material Science and Engineering) for his help with TEM analysis.
- Håkon A. Holm Gundersen (Department of Engineering Design and Materials) for always being helpful.
- Søren Heinze, Ida Noddeland and other lab technicians.

_____

Karl Erik Nordheim

Trondheim, 22th of June 2012

Table of content

Definitions and acronyms 1
1 Introduction 3
1.1 The discovery of the CNTs 4
1.2 What is a CNT? 5
1.3 Structure of a SWCNT 5
1.4 CNT versus CNF 7
2 Fabrication of CNTs 8
2.1 Arc discharge 8
2.2 Laser ablation 9
2.3 CVD 9
2.4 Plasma Enhanced Chemical Vapor Deposition (PECVD) 11
2.4.1 What is plasma? 12
2.4.2 How does the PECVD work? 12
2.4.3 Ion bombardment 14
2.4.4 Catalyst particles: 15
3 Growth mechanism of carbon nanotubes 18
3.1 General mechanisms 19
3.1.1 The bulk diffusion 19
3.1.2 Diffusion over surface 20
3.1.3 Vapor-Liquid-Solid (VLS) 20
3.2 Base- versus tip-growth 21
3.3 Vertically aligned CNTs 22
4 Theory 24
4.1 The purpose with the barrier layer 24
4.1.1 What type of material should be chosen 24
4.1.2 Ostwald ripening effect 25
4.2 The role of the NH_3 and/or H_2 27
4.3 Effect of variation in the different parameters 28
4.3.1 Temperature 28
4.3.2 Time 29
4.3.3 Power 30
4.3.4 Gas flow 31
4.3.5 Pressure 32

4.3.6 Catalyst thickness layer 33
4.4 Plasma pretreatment versus thermal pretreatment 34
4.4.1 Reducing- (RP) and oxidizing pretreatment (OP) 36
5 Instruments 38
5.1 Creating samples 38
5.1.1 Technical information 38
5.2 Applying the thermal barrier- and catalyst layer 38
5.2.1 Increasing the thickness and the quality of the aluminum oxide layer 39
5.2.2 Technical information 40
5.3 Pretreatment and growth 40
5.3.1 Technical information 41
5.4 Removing a:C from the Si CNT carrier 41
5.4.1 Technical information 42
5.5 Characterization 42
5.5.1 Hitachi S-5500 S(T)EM and FEI Helios NanoLab DualBeam FIB 42
5.5.2 JEOL JEM-2010 TEM 42
5.5.3 Vecco Dektak 150 profilometer 43
5.5.4 Technical information 43
6 Experiment 45
6.1 Cleaning procedures of the Si samples 45
6.2 Preparation of samples 45
6.3 Deposition of barrier/catalyst layers 46
6.3.1 Pfeiffer vacuum classic 500 e-beam evaporator 46
6.3.2 Cressington 308R sputter and evaporator 46
6.3.3 Increasing the thickness and the quality of the aluminum oxide layer 49
6.4 Characterization 49
6.4.1 The FIB and the S(T)EM 49
6.4.2 JEOL JEM-2010 TEM 50
6.4.3 Making the Holy Cu-C grids for TEM analysis 51
6.4.4 Plasma cleaner 52
6.5 Pretreated samples 53
6.5.1 Parameters for the pretreated samples 54
6.5.2 The effect of variation in time 54
6.5.3 The effect of variation in power 56
6.5.4 The effect of variation in gas flow 58

6.5.5 The effect of variation in pressure 60
6.5.6 The effect of variation in thickness of catalyst layer 62
6.5.7 The effect of variation in temperature 64
6.5.8 Thermal treatment 66
6.5.9 Summary of the successful parameter from the pretreatment study 68
6.6 Growth of CNTs 68
6.6.1 Variation in CH_4 flow 69
6.6.2 Adding NH_3 in the CNT growth step 70
6.6.3 Variation of power 72
6.6.4 Variation of growth time 74
6.6.5 Variation in temperature 76
6.6.6 No barrier layer 78
6.6.7 PP versus TP 80
6.6.8 Replacing NH_3 with N_2O 82
6.6.9 Starting directly at 650^0C 84
6.6.10 TEM analysis 85
7 Discussion 90
7.1 Decomposition of hydrocarbons 90
7.2 Temperature during growth 92
7.3 Long initiation time before growth 92
7.4 PP versus TP 93
7.5 Reproducibility among the samples 93
7.5.1 In the Cressington 308R sputter and evaporator 93
7.5.2 In the PECVD 94
8 Conclusion 95
9 Index of figures 96
10 Index of tables 106
11 References 107
Appendix A 116
Appendix B 117
Appendix C 118
Appendix D 125
Growth of SWCNT 125
Mechanical testing 125
Testing of other catalyst materials 125

Various other tasks..... 125

Definitions and acronyms

SWCNT	Single walled carbon canotube
MWCNT	Multi walled carbon nanotube
VACNT	Vertically aligned carbon nanotube
CNT	Carbon nanotubes
CNF	Carbon nanofiber
PECVD	Plasma enhanced chemical vapor deposition
CVD	Chemical vapor deposition
um	Micrometer (10^{-6} meter)
nm	Nanometer (10^{-9} meter)
Å	Ångstrom (10^{-10} meter)
K	Kelvin (^{0}C + 273.15)
^{0}C	Degree Celsius (K - 273.15)
sscm	Standard cubic centimeters per minute (cm^3/min)
WD	Working distance
PP	Plasma Pretreatment
TP	Thermal Pretreatment
RMS	Root Mean Square
RTP	Rapid Thermal Process
V	Volt
mA	milliampere = 10^{-3} ampere
TF	Tooling factor
RF	Radio frequency
DC	Direct current
N/A	Not available (means that there exists no value)
2”	2 inch = 50.8 mm
SEM	Scanning Electron Microscope
TEM	Transmission Electron Microscope
a:C	Amorphous carbon
C_2H_2	Acetylene
C_2H_4	Ethylene
C_2H_6	Ethane
CH_4	Methane
NH_3	Ammonia
H	Hydrogen
N	Nitrogen
O	Oxygen
CO_2	Carbon dioxide
Ar	Argon
He	Helium
Fe	Iron
Cu	Cupper
Ni	Nickel
Co	Cobolt
Si	Silicon

Al	Aluminum/aluminium
Al_2O_3	Aluminum oxide/alumina
TiN	Titanium nitride
TiO_2	Titanium dioxide
SiO_2	Silicon dioxide
DAIM	The electronic delivery system for the Master Thesis at NTNU

1 mbar ≈ 750 mTorr ≈ 0.1 kPa

1 Introduction

As the development in the society is going on full speed and where requirements to the material are becoming more demanding, there is need of new ones that holds better properties and is cheaper than the traditional ones. An issue with the traditional materials is that there is usually a "trade-off" between the properties, which mean that it is uncommon that a material holds multiple of the desired properties, e.g. silicon (Si) and cupper (Cu) are good electrical conductors, but lacks flexibility and strength. This is why it has been a huge interest for nanotechnology, since understanding at the atomic level grants the possibility of re-engineering materials and devices.

Carbon nanotubes (CNTs) have been of huge interest since their discovery. They are known to be one of the most versatile materials yet discovered because of the unique mechanical, electrical and thermal properties they possess, compared to other materials. The CNTs have been of huge interest for the chip and manufactures, such as Intel and AMD, since they gives the possibility of transporting huge currents without any generation of heat which can give a reduction of the chip's size. In addition to offering very high strength, conductivity and no heat generation, they also possess a quite unique flexibility which makes them capable of being used as supercapacitors, sensors and probes, biosensors, field-effect transistors, lithium batteries and futuristic displays [1, 2, 3]. CNTs have also been reported to have the potential to give surfaces a superhydrophobic character. Such surfaces can possess new functions such as antifouling, self-cleaning and water-repellent properties which are useful in wetting environments and could lead to the development of anti-icing films or materials/coatings with higher corrosion resistance [4, 5, 6, 7, 8, 9]. They have been reported to improve the mechanical strength when combined with other materials [10, 11, 12, 13], they can be used to make adhesive tapes with a huge potential [14, 15], they are capable to be used for absorption of gases or to be used as new superior filters [16]. A more science fiction feature of the CNTs is to be used as cables/anchors for the widely mentioned space elevator [17, 18]. One thing is certain, CNTs have a wide area of applications.

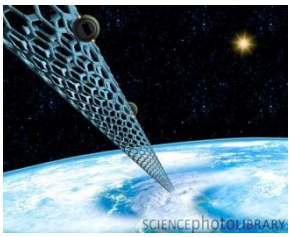

Figure 1.1: Picture of the CNT space elevator, where the cable is believed to be made of CNTs [19]

Figure 1.2: CNTs have a wide area of applications. In the future they could lead to development of anti-icing films for airplanes [20]

In agreement with my supervisor, the tasks for my Master Thesis have been changed. Growing of CNTs was much more time demanding than expected. This especially the case since no other experiments was found that used the combination of gases and the same type of PECVD that was used for this project. The new tasks for this Thesis have been to focus on growing CNTs on Si substrates by PECVD and to continually improve the results so that CNTs becomes perpendicular to the surface (VACNTs). In addition, the growth conditions were going to be changed, too see the effect of variation in the parameters. The final task was to characterize the CNTs, as it was necessary to verify:

- Whether it is carbon nanotubes or carbon nanofibers that have been grown.
- The diameter of the grown filaments.

This Thesis will start by giving an introduction to CNTs and manufacture methods. Some theory will be presented, and the final chapters will cover the experimental work that has been done at the NTNU NanoLab. Information regarding the applications and properties of CNTs can be found from the work that was submitted for my pre-project.

1.1 The discovery of the CNTs

Carbon is an atom that contains six electrons, where two being in the core and the four remaining being available to bond with other atoms. The two most known allotropes of carbon are diamond and graphite. In diamond, the four available electrons in each carbon bonds with the nearest neighbors, which forms a tetrahedral structure (sp^3). This arrangement is called a covalent bonding and is known to be of high strength which is the reason of the high strength in diamond. Since all the electrons are involved in the bonding, they do not interact with light, which causes the low electrical- and high thermal conductivity properties. In graphite, the in-plane bonds of the electrons form a hexagonal structure (sp^2), which is even stronger than the sp^3 in diamond. However, the different layers of graphite (planes) interact weakly by van der Waals bonding which makes them capable to slip easily with respect to each other. This is in general what gives the graphite its softness, high electrical conductivity and lubricating properties. A single plane of grahite is known as a graphene, and consists of a flat hexagonal arrangement of carbon atoms with very strong in-plane bondings. Fullerene is a newly discovered allotrope of carbon. The first characterization of a fullerene was the C_{60}, or Buckministerfullerene ("Buckyball"), which was discovered by Richard Smalley and his crew in 1985. The "buckyball" is made from curled sheets of graphene, by introducing 12 pentagonal rings in the cage [21, 22].

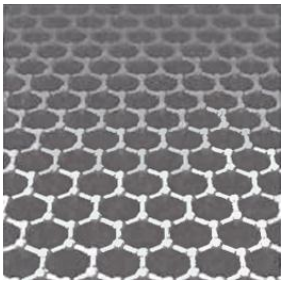

Figure 1.3: Shows a graphene which is the basis for the formation of fullerenes. Defect-free hexagonal arrangement will remain flat, while defects (such as the pentagonal or heptagonal rings will curl the sheet [21]

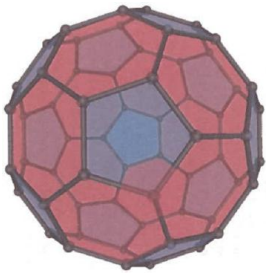

Figure 1.4: Buckministerfullerene, C60 [21]

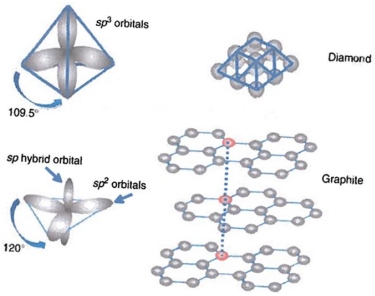

Figure 1.5: Carbon bonding in diamond and graphite [21]

The effort made in finding the fullerene inspired a man called Sumio Iijima. He had a passion for electron microscopes, and one day in 1991 he did analysis of carbon soot samples in order to recognize the C_{60}. During his electron microscope session he discovered some fibers that were long, and thin. After some further analysis he found them to be hollow and mainly consist of carbon atoms as well. He was about to realize that he had discovered CNTs [23].

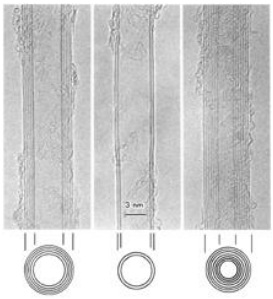

Figure 1.6: First reported electron microscope image of CNTs by Sumio Iijima [23]

1.2 What is a CNT?

A CNT can be considered to be a seamlessly rolled sheet of graphene which yields a cylindrical shape (they are also referred to as cylindrical fullerenes). The primary cause for their name is because of the very thin diameter. The CNTs have no specified length requirements, they can be as short as a couple of nanometer (nm) or thousands of micrometer (um) in length. In general, there are to variants, one is the single walled carbon nanotube (SWCNT) which can be considered as a single rolled layer of graphene. The other one is the multi walled carbon nanotubes (MWCNT) which can be considered to be multiple and concentrically rolled SWCNTs of different diameters [22, 23].

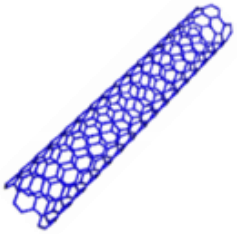

Figure 1.7: Structure of a SWCNT

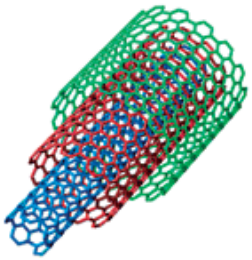

Figure 1.8: Structure of a MWCNT

1.3 Structure of a SWCNT

There are three types of SWCNTs:

- Zigzag
- Armchair
- Chiral

Their names are descended from how the 2D graphene sheets curls, which is the basis of the tubular structure of the CNTs (Figure 1.10 - Figure 1.12). The diameter and the helicity, also known as the chirality, are determined from the chiral vector $\mathbf{C_h}$. This vector is defined as: $\mathbf{C_h} = n\mathbf{a_1}+m\mathbf{a_2}$, where n and m are integers and is often donated as (n, m) [23]. The diameter of an ideal SWCNT can be determined by the rolling graphene sheer model:

$$d = \frac{\sqrt{3} * b}{\pi}\sqrt{(n^2 + nm + m^2)}$$

Where b is the carbon-carbon bond length and is usually set to the value of 0.142 nm [24]. A CNT with a chirality of (5, 5) has a smaller diameter than a (10, 10). One way of determine the chirality is given below:

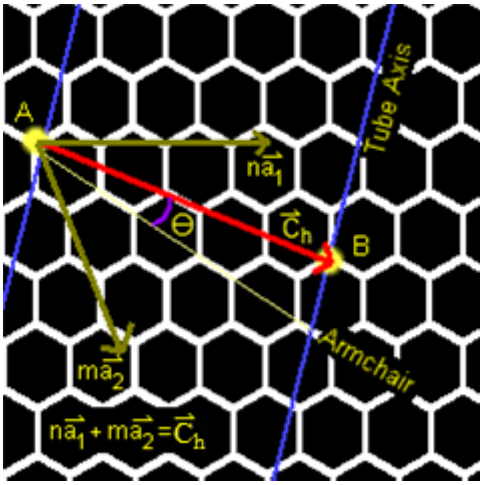

Figure 1.9: Illustration for finding the chirality [25]

1. Draw two lines (in blue) along the tube axis where the separation takes place (the edge of the nanotube). In other words, if you cut along the blue lines and then match their ends together in a cylinder, you will get the nanotube.
2. Find any point on the blue line that interacts with one of the carbon atoms (point A).
3. Draw the armchair line (thin yellow line) by finding any point along the tube axis that travels across each hexagon, separating them into two equal halves.
4. Find any point at the other tube axis that intersects a carbon atom nearest to the armchair line (point B).
5. Connect A and B with the chiral vector $\mathbf{C_h}$ (red arrow).
6. The wrapping angle θ is formed between the $\mathbf{C_h}$ and the armchair line.
    - If $\theta = 0^0$ => Armchair nanotube (n=m, the $\mathbf{C_h}$ is collinear with the armchair line).
    - If $\theta = 30^0$ => Zigzag nanotube (m=0).
    - If $0^0 < \theta < 30^0$ => Chiral nanotube [25].

Figure 1.10: Armchair nanotube [26]

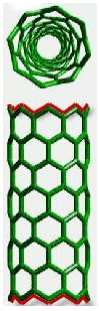
Figure 1.11: Zigzag nanotube [26]

Figure 1.12: Chiral nanotube [26]

1.4 CNT versus CNF

CNTs exist when the tubular graphene walls are parallel to the filament axis. Carbon nanofibers (CNFs) are the case when the graphene is non-parallel to the filament axis, and are classified into two types:

- Herringbone CNFs
- Stacked CNFs

The graphene platelets are canted to the filament axis in the herringbone form and are often recognized as a fishbone pattern, while the platelets are perpendicular to the filament axis in the stacked form [27].

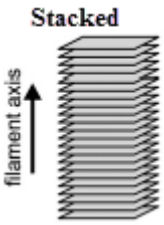

Figure 1.13: Structural form of a stacked CNF [27]

Figure 1.14: Image of a stacked CNF [27]

Figure 1.15: Structural form of an herringbone CNF [27]

Figure 1.16: Image of a herringbone CNF [27]

Figure 1.17: Structural form of a CNT [27]

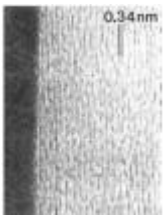

Figure 1.18: Image of a CNT [27]

2 Fabrication of CNTs

There are several methods used for fabrication of CNTs. The focus is to find a technique that is easy, can produce cheap CNTs of high quality, with high production rate (which yields a lot of CNTs per unit of time) and that produces CNTs with minimal defects. Additionally, it is very important to be able to control the diameter, chirality, the number of shells (for a MWCNT) and the purity, since all these parameters will influence the properties [28]. There are several methods for synthesis of CNTs, but three of them are considered as the general and widely known synthesis methods [29]:

- Arc discharge.
- Laser ablation.
- Chemical Vapor Deposition (CVD) methods.

Figure 2.1: Overview of the synthesis methods for CNTs [30]. A figure of higher quality can be seen in Appendix A

2.1 Arc discharge

This method is known to be the first synthesis method for the production of CNTs, since the discovered tubes were synthesized by this technique. It was originally used in the production of the C_{60} ("buckyballs"), but because of its simplicity it is still one of the most common fabrication methods. The most frequently used arc discharge technique is the electric charge method, commonly known as the electric arc discharge. An electric arc discharge is generated between two graphite electrodes in this method, which causes the graphite to vaporize and condense at the cathode. The process is done under an inert atmosphere that consists of helium (He) or argon (Ar). A very high temperature is obtained that allows transition of carbon from solid- to gas-phase without passing through an intermediate liquid phase (sublimitation). Two kind of synthesis can be performed:

- Evaporation of pure graphite
- Co-evaporation of graphite and metal

The end product is soot that contains a complex mixture of fullerenes and other carbon structures, such as CNTs. To obtain them, purification by gasification with oxygen (O) or carbon dioxide (CO_2) is necessary since other carbonaceous material needs to be removed. The effect of gasification depends on the type of reactant that is used. To produce SWCNT there is need of a metal catalyst. The typical yield for this method is about 30% and it is capable of producing SWCNTs and MWCNTs [31, 32, 33].

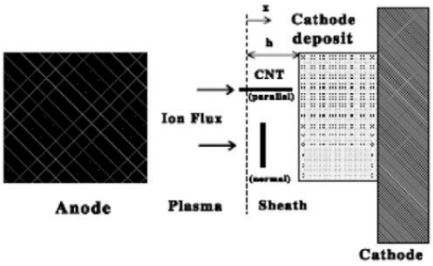

Figure 2.2: CNT formation and transport in the sheath of the arc discharge [31]

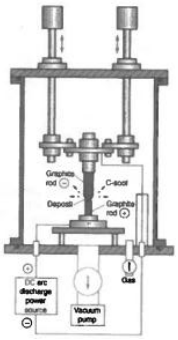

Figure 2.3: The arc discharge technique [31]

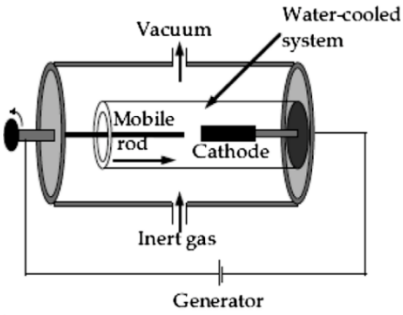

Figure 2.4: The electric arc discharge method [31]

2.2 Laser ablation

This method vaporizes a piece of graphite by irradiation with a Nd YAG laser in a chamber with temperature of 1200^{0}C in a flow of inert gas, such as He or Ar. The vapor is carried with the gas flow to a cooled wall of quartz tube where it condenses into a mixture of fullerenes and CNTs. As in the arc discharge method, a purification step is needed to obtain the CNTs. The laser ablation method is capable of yield up to 70% and is able to produce SWCNTs and MWCNTs. It is especially known to give SWCNTs of high quality and purity.

Nevertheless, the equipment requirements and the large amount of energy consumed in the synthesis by the arc discharge and the laser ablation method makes them less favorable in production of CNTs. Controlled synthesis on substrates with ordered CNT structures has not been possible for none of these two methods. The main technological drawback with these two methods is that neither one of them are able to produce CNTs directly on a surface, which means that they first need to be produced separately and then being manipulated onto substrates before use [27, 31, 32, 33, 34].

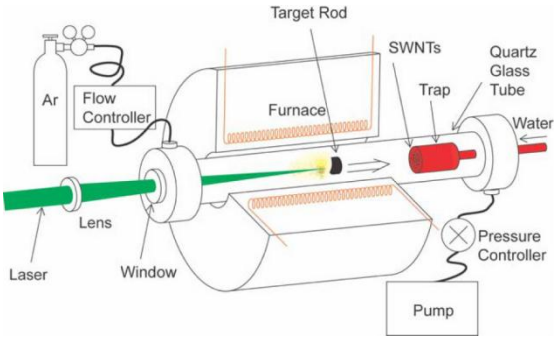

Figure 2.5: The laser ablation technique [35]

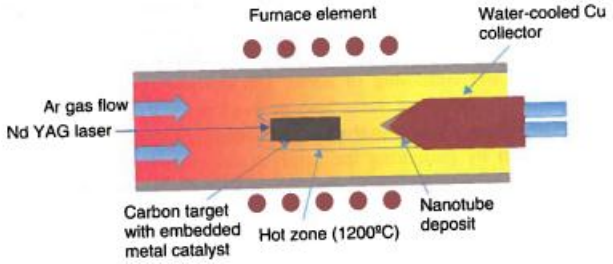

Figure 2.6: Close up of the chamber in the laser ablation technique [32]

2.3 CVD

CVD is a parent to a family of processes where deposition of a solid material on a surface is caused by reactions with the precursor gases in the chamber and the heated surface of the substrate. The growth process of the CNTs involves decomposition of carbon containing gases where carbon is diffused towards a heated substrate which is coated with catalyst particles. The carbon binds to

these particles and acts as a nucleation site for the initiation of CNT growth. As long as the catalyst particles are supplied with carbon, the growth process continues. The particle is either on top or at the bottom during CNT growth (Figure 2.7 - Figure 2.8). Regardless of the type, the catalyst particle is always the starting point for CNT growth [1, 28, 31]. The growth process is illustrated in Figure 2.9.

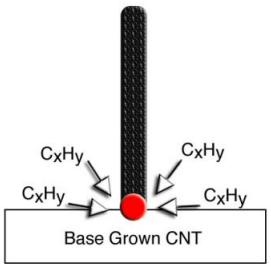

Figure 2.7: Catalyst particle at the root during CNT growth (base growth) [35]

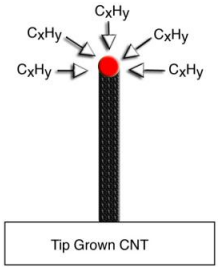

Figure 2.8: Catalyst particle at the top during CNT growth (tip growth) [35]

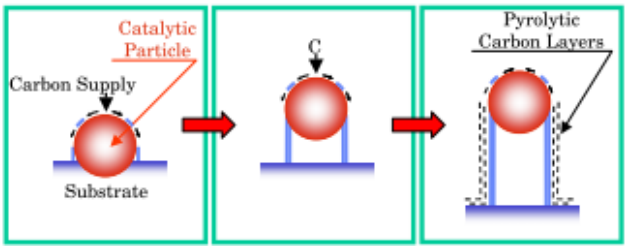

Figure 2.9: Illustration of the tip-growth model. Carbon diffuses around the catalyst particle to form the tubular structure [28]

The CVD process offer good control of the growth rate and the diameter. What type of CNT that is synthesized, depends on the temperature in the process and the size of the catalyst particle being used, where [35]:

- Low temperature, 600-900^{0}C, favors the growth of MWCNTs
- High temperature, 900-1200^{0}C, favors the growth of SWCNTs

Since it is impossible to remove the catalyst particle during growth, post treatments are necessary. Such a treatment can be high temperature heat treatment or acid washing. During growth of CNT, it is common to find impurities, such as graphite compounds, amorphous carbon (a:C), fullerenes, coal and un-reacted metal particles. Since the target is CNTs of high purity, a purification step is required, which can be done by acid treatment, oxidative treatments in the gaseous phase/liquid phase and ultrasound methods [28, 31].

The two most important parameters in the synthesis of CNTs by CVD is the size of the catalyst particle and the carbon source. If the chosen carbon source is unfavorable for growth conditions one can end up with a mixture of SWCNTs and MWCNTs, along with deposited a:C. The produced a:C during the CVD process coats the catalyst particle which reduces its activity and lifetime, and will influence the growth significantly.

The major advantage with CVD is that it allows more control over the morphology and structure of the produced CNTs and can give controlled alignment, such as producing small freestanding SWCNTs if the process parameters are controlled, instead of the “mixtures” which is obtained by the arc discharge and laser ablation method. In addition, CNTs can be produced directly on substrates without any further purification unless the catalyst particle is required to be removed. The CVD is known to produce CNTs of high purity and offers a yield between 20 - 100%. Even though it possesses promising characteristics, the main problem with this method is the scalability and reproducibility in the production of CNTs [1, 27].

2.4 Plasma Enhanced Chemical Vapor Deposition (PECVD)

PECVD is similar to CVD as it uses gaseous sources. The most important difference is that the CVD uses thermal energy to decompose the hydrocarbons, but in the PECVD the molecules are activated by electron impact (molecule collisions) in the plasma. The decomposition takes place in non-equilibrium plasma, which is often referred to as the glow discharge. The glow discharge is often generated by a high frequency power supply. As in the CVD, a catalytic particle is required to yield CNTs. The main purpose of using plasma is to reduce the activation energy which is needed for the deposition process. The growth temperature for producing CNTs in the PECVD could be lowered significantly, relative low substrate temperatures down to 300^0C can be used [32, 36, 37, 38].

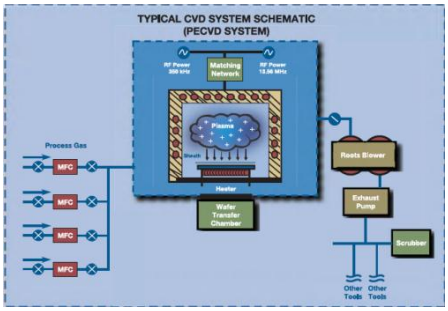

Figure 2.10: Typical schematic of PECVD set-up [39]

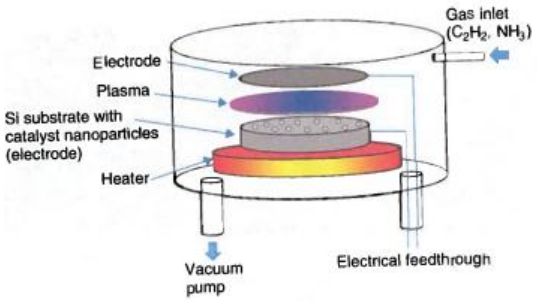

Figure 2.11: Illustration of the PECVD [32]

Due to the electric field which is generated by the high-frequency supply that is used to setup a time varying electric field between the plasma and the electrode (Figure 2.12), the CNTs are able to grow perpendicular and aligned on a surface, much like grass or pillars. This grants the possibility of creating pattern of catalysts, which means that it is possible to grow CNTs in selected regions on the sample's surface. An example of catalyst patterning can be seen in Figure 2.13. The "Nanobamas" were synthesized by patterning of catalysts onto a Si surface by a process called photolithography.

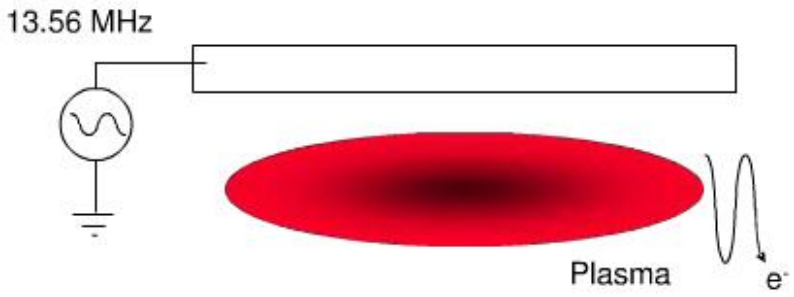

Figure 2.12: Illustration of the Radio frequency (RF) plasma. The RF signal is used to setup a time varying electric field between the plasma and the electrode. The electric field accelerates electrons in and out of the plasma. The electrons gain energy and ionize the local gas [40]

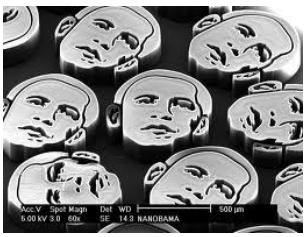

Figure 2.13: Face of President Obama synthesized by growing vertically aligned CNTs on a patterned catalyst. Each face consists of about 150 million parallel CNTs. By patterning the catalyst, CNT can be grown out of selected regions on the substrate [32]

Boscovic et al [38] proposed a radio frequency (RF) field that could selectively heat the catalyst particles while keeping the substrate temperature low. If this is true, his experiment can be one of the most important discoveries done on the work for lowering the substrate temperature. However, no further evidence of this has been published yet.

PECVD has become the method for the commercial growth of CNTs because of its simplicity, controllability and the relative low synthesis temperature. Some of the drawbacks with the PECVD method today are that the preparation is quite cumbersome. For instance, the process of growing CNTs on stainless steel involves polishing, etching in hydrofluoric acid and hydrogen (H)/ammonia (NH_3) plasma pre-treatment to create the catalyst particles. In addition, the evidence from most of

the CNT growth by PECVD up to now operates at almost equal temperatures as CVD which indicate the absence of the benefits by using plasma, and it is not really clear how the carbon diffusion step through the catalyst particle could be promoted by the plasma assistance yet [32, 38, 41, 42, 43].

2.4.1 What is plasma?

Solid phase form when the thermal energy in a material is too low such that rigid bonds between the atoms can form. Liquid phase form when the thermal energy is too high to allow rigid bonds, but still low enough so that atoms stick to each other, just like slimy marbles. Gas phase form when the thermal energy is high enough, such that no atoms stick at all, then individual atoms is set free to fill the enclosure. A further increase in temperature makes the molecules come apart into free ions and free electrons forming a fourth gaseous state of matter which is known as plasma. The new feature of this state which distinguishes it from an ordinary gas is that it conducts electricity.

If there is enough energy to free weakly bound electrons, there is also enough to promote more deeply bound electrons to excited states which is why almost all plasmas glows in the dark, such as stars, fluorescent lights, flames, the northern and southern lights, meteor trails, etc. [44].

2.4.2 How does the PECVD work?

To be able to understand the mechanism that is involved in the growth of CNTs, the basic processes that occur in the plasma must be understood. The direct current (DC) reactor is the simplest case, where a DC voltage is applied across a space filled with low pressure gas (a few Torrs). The glow discharge that is initiated can be divided into three regions that are visible, and is arranged from cathode to anode:

1. Cathode dark space
2. Negative glow
3. Faraday dark space

The DC discharge is maintained by the processes at the cathode and in the dark space which creates an electrical field. Due to this field, growth of vertically aligned carbon nanotubes (VACNTs) is possible as it forces the CNTs to align in the direction of the field as they grow. The ions are accelerated by the applied voltage and some of them bombard the cathode which causes generation of secondary electrons that are accelerated away from the cathode. The collisions excite molecules, and energetic electrons ionize some of them, which is the reason for the negative glow. The thickness of the dark space is related to the electron mean free path. The current in it is primarily carried by ions, while the current in the negative glow is primarily carried by electrons. Thus, the negative glow has a low impedance region and most of the applied voltage drops over the dark space. Since it varies from a few hundred um to a few mm, several hundred volts can be created in the electric field, such as in the order of 10^3 V/mm [38].

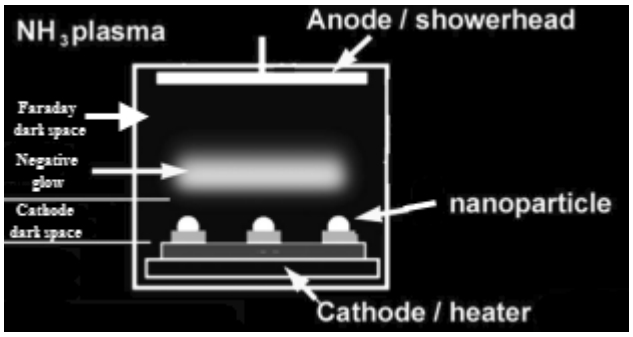

Figure 2.14: Schematic representation of the PECVD process during catalyst pretreatment which leads to the formation of catalyst nanoparticles [38]

The radicals that are produced in the plasma and the supplied feed gas drifts to the substrate surface. The radicals does not chemically react with the substrate, instead they combine to form stable chemicals (solids). Ions are accelerated across the sheath which delivers energy that is driving the chemical reaction(s) between the radicals and the surface material [40] [45]. Since hydrocarbon decomposition is better activated by molecule collisions (plasma) and is done at a much faster rate than by thermal pyrolysis, lower processing temperature should be allowed which makes the PECVD more beneficial than pure CVD methods. The activation energy for the breakdown of reactive species and their subsequent interaction with other species to form a deposit in the PECVD is provided by the high kinetic energy of electrons in the plasma [27].

The electron density in the radio frequency PECVD (RF-PECVD) is much higher than in the direct current PECVD (DC-PECVD) since DC waste a lot of its input power on accelerating the ions whereas the desire is to use the power efficiently for generation of reactive species. Higher electron densities result in higher ionization rates since the electrons are responsible for the ionization rate and for the formation of reactive free radicals. One major advantage with the RF is therefore its efficient decomposition of gas molecules and a clear difference is the higher number of H ions present in RF, that can enhance the activity of the metal catalysts by reduction and increase in the wetting ability. In addition, RF can also facilitate etching of a:C. It is the best suited plasma source for deposition on large areas as the plasma is very stable and homogenous. Because of the higher density of reactive radicals and the stability, the RF-PECVD seems to be preferred for growing CNTs at low temperatures. The trend in the industry is to move away from DC reactors and towards higher frequency plasma reactors. The effect of 180^0C in the PECVD appears to be comparable to that of 750^0C in the CVD [27, 36, 38, 46, 47, 48, 49, 50, 51, 52].

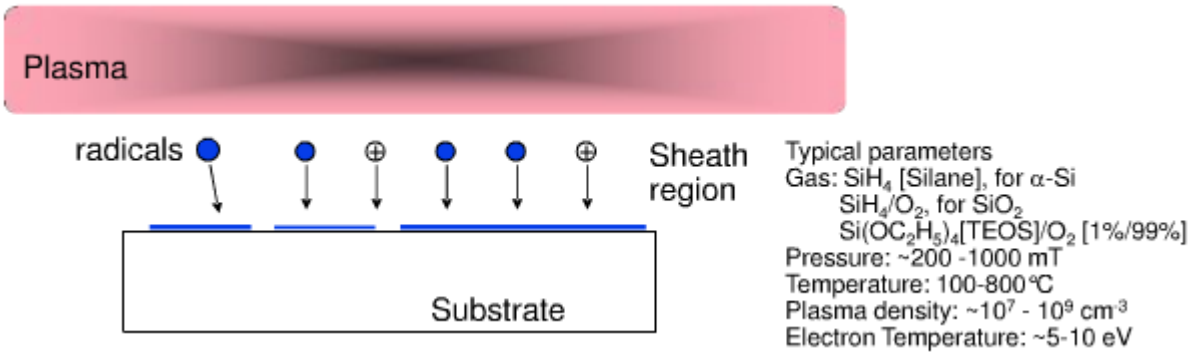

Figure 2.15: Illustration and details regarding the PECVD [40]

The main tasks of the plasma in CNT growth is of course to ionize the gas, as well as to cause a dissociation and diffusion of hydrocarbons into the catalyst particles (which also depends on the temperature) and etch any a:C that may deposited on top of the catalyst particle thereby providing a

steady support of carbon atoms. The plasma is also likely to provide a heating effect to the sample, since it is subsequently exposed to conduction from hot gases as well as ion bombardment. The additional heating effect leads to that less heat needs to be generated by the external heater.

Figure 2.16 and Figure 2.18 shows the effect of heating due to the plasma power. High pressure results in fairly collisional plasma which contributes to significant heating of the gas, making the hot gas to the main contributor of the heating. In contrast, at lower pressures, the plasma is less collisonal which means that less power is transferred to the gas and ion bombardment surpasses gas conduction as the main source of substrate heating. Figure 2.17 shows that the heating of the substrate is a function of the axial distance between the cathode (substrate) and the anode (plasma).

Figure 2.19 shows the number densities of the six most abundant species and atomic hydrogen as a function of plasma power without the aid for an external heater. It can be seen that acetylene (C_2H_2) dissociates more easily than methane (CH_4) at all power levels. The density profile indicates that there is more dissociated C_2H_2 at 200 W, compared to those values that are obtained at 66 W. As C_2H_2 dissociates more easily on the metal nanoparticle than CH_4, it will promote a higher growth rate [47, 53].

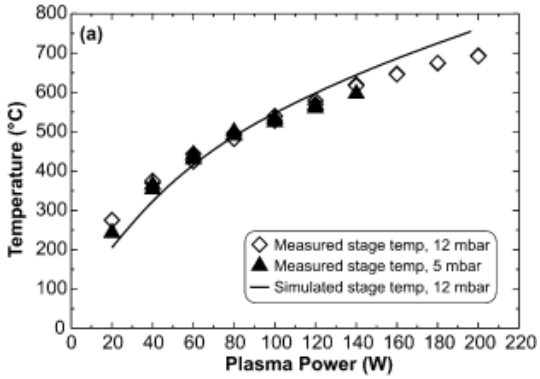

Figure 2.16: Measured and simulated cathode temperatures as a function of plasma power. The gas mixture simulated was 54:200 sccm C2H2/NH3 at 12 mbar [53]

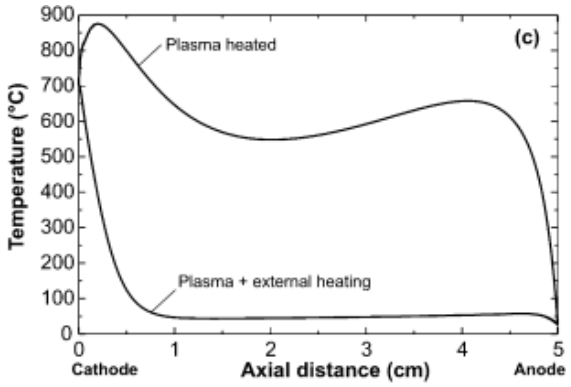

Figure 2.17: Cathode-to-anode temperatures profiles for the cases of pure plasma heating versus plasma plus external heating [53]

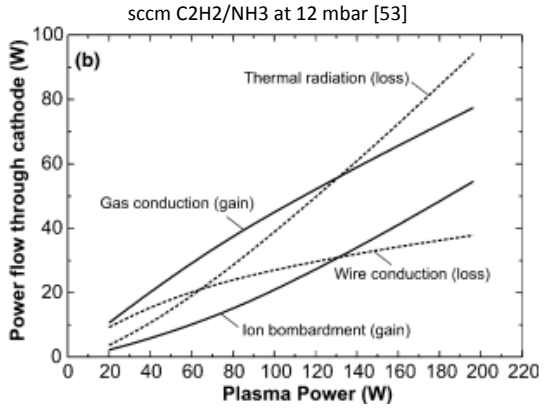

Figure 2.18: Simulated power flows through the cathode under the same conditions (as figure above). The dashed line denotes mechanisms in which energy is gained in the cathode (i.e. heating), while the solid line denotes energy loss mechanisms (i.e. cooling) [53]

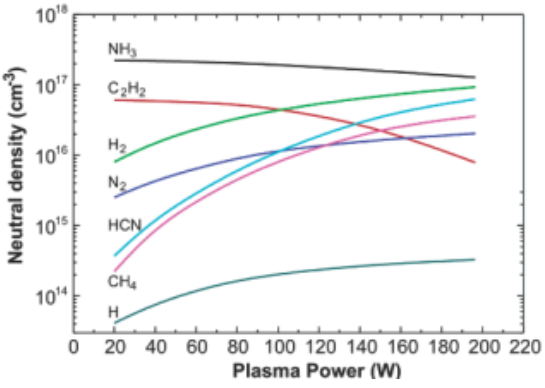

Figure 2.19: Simulated neutral species in the gas phase as a function of plasma power. The six most dominant species with atomic hydrogen are shown here [53]

2.4.3 Ion bombardment

There is uncertainty whether bombardment is favorable or not for growth of CNTs. Some believes that bombardment during CNT growth can introduce lattice defects which cause bending and alternations of its diameter. How serious these defects are depends on the synthesis temperature. When temperatures above 600^{0}C have been used, no damage by ion bombardment to the CNTs has

been recorded, but when lowered below 500^0C the growth rate is significantly decreased, which is most likely because that the ion etching rate exceeds the growth rate [54].

Other suggests that the ion bombardment enhances the CNT growth. An experiment by Poche et al [49] found no growth directly in the area that was shielded by a dust particle, whereas growth occurred in the zone outside of the dust particle. They believed that this was due to the formation of a polycrystalline area on the top surface of the catalyst particle that was created by the high energy of the positive ions impinging on its surface. This area can function as a layer that provides a preferential diffusion path into the catalysts via the grain boundaries, which avoids few absorbed carbon species to be directly etched at the top of the particle's surface and allows these species to be efficient in formation of CNTs [49] .

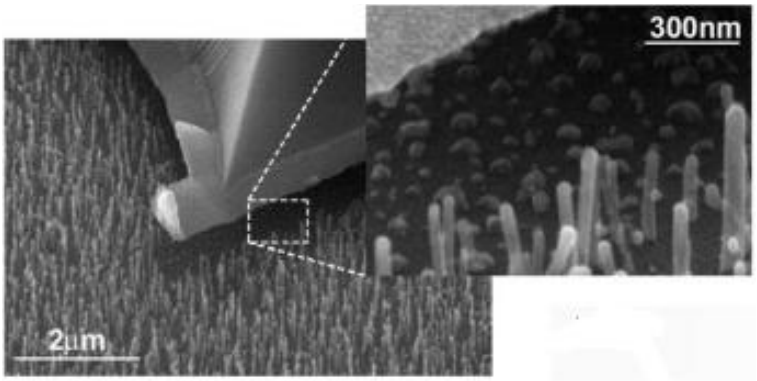

Figure 2.20: SEM images close to a dust particle and where the inset shows the area under it. No growth occurred directly under the dust particle [49]

2.4.4 Catalyst particles:

Since the quality and the structure of CNTs depends greatly on the properties and the type of catalyst material being used, it is essential to study the catalysts. A key factor for controlling the diameter and the number of shells in a CNT is to gain control of the catalyst particle's diameter, since they are the basis of the grown CNTs. This means that growing SWCNTs requires a strict diameter control, and what usually makes it easier to produce MWCNTs. The generally considered proper sized of nanoparticles to initiate SWCNT growth is approximately 1 nm.

One of the challenging tasks with catalyst particles is that it is difficult to define a specific relation between the size of them and the resulting diameter of the CNT. Such factors have to do with the reduced size and subsequent exhaustion of catalyst material during growth. This is believed to be because of to ion-beam sputtering, loss of catalyst material due to evaporation of metal atoms at high temperatures and dissolution of carbon species which tends to change the size of the particles during synthesizing. One of the major functions of the catalyst particle during growth is to function as an etch mask, by protecting the core of the growing nanostructure from physical and chemical etching. Only moderate size particles ensures a suitable carbon supply for nucleation and growth of SWCNTs at a given carbon feet rate [29, 38, 55], which is illustrated in Figure 2.21.

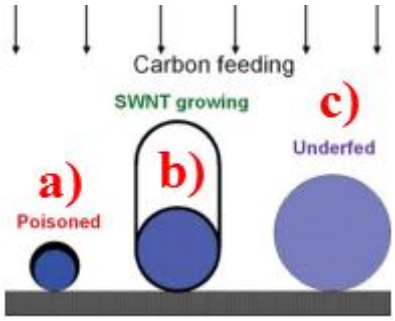

Figure 2.21: a) Smaller particles are too active and dissolve too much carbon at the beginning. The excess carbon will form a thin layer of graphite that cover the surface of the catalyst particle and will cut the carbon supply to the particle, hence no SWCNT can grow.
b) Shows a moderate sized particle where SWCNT growth occurs.
c) The larger particles cannot efficiently catalyze the decomposition of carbon stocks which makes them unable to supply enough carbon to nucleate the SWCNT [29]

For no more than a decade ago, scientists believed that transition metals only, such as iron (Fe), nickel (Ni) and cobolt (Co), were the only materials that yielded CNTs. Recent experiments with new materials, such as aluminum (Al), silver (Ag), copper (Cu), gold (Au), manganese (Mn), tin (Sn), magnesium (Mg) and chromium (Cr), have proven to be useful for CNT growth. Some of them have shown to possess better properties as catalyst compared to the transition metals, such as narrower diameter distribution (because of the weaker bond energies on their surface), lower temperatures in CNT growth and enhanced carbon diffusion and reaction rates. Some of them have also shown to give less a:C. One should note that different metal catalysts are active at different temperatures [55, 56, 57].

Optimal growth requires a metal catalyst that exhibit sufficient carbon solubility, rapid carbon diffusion and limited carbide formation. Ni is a frequently used catalyst since it is active over a wide temperature range. Fe on the other hand, is favored because it has shown to give rise to the highest density forest which gives the highest yield. However, Fe is less active at lower temperatures than Ni since it is still an oxide. That is why it is necessary to use atomic H to reduce it back to its metallic state. Large-scale and structure controlled synthesis of CNTs is still a huge challenge since the fundamental growth mechanism of CNTs is not yet fully understood, as well as the difficulty of controlling the atomic-scale physical and chemical reactions during the growth. In addition, for large-scale production of CNTs, it is a desirable to anchor the metal catalyst firmly to the support (base-growth) to hinder formation of larger nanoparticles. Catalyst sintering/coalescence are present because of the high CNT growth temperature, typically 500-900^{0}C which gives the catalysts sufficient mobility to coalescence into larger particles. This is especially unwanted if the desire is SWCNT growth. It is important to mention that decomposition with common hydrocarbons, except CH_4, is highly exothermic and can therefore dramatically increase the catalyst local temperature even if synthesis temperatures are low. Experiments has shown that significant catalyst activity occurs when the catalyst is in its liquid state and that phase transition from liquid to solid (solidification) reduces the diffusion of carbon and the efficiency of hydrocarbon decomposition in the catalyst which could initiate deactivation of its activity [3, 27, 29, 38, 52, 58, 59, 60].

Experiment on the effect of C_2H_2 content during CNT growth has been reported. Low C_2H_2 concentration leads to well-aligned CNTs and high concentrations leads to significant amount of a:C which gradually build up on the nanotube as it grow. Since there is more a:C at the base, the CNTs appears tip-shaped. A delicate balance must be achieved in the feedstock gas composition between the hydrocarbon source and the etching gas, in order to avoid the formation of any graphitic layer which could terminate the growth [49, 61].

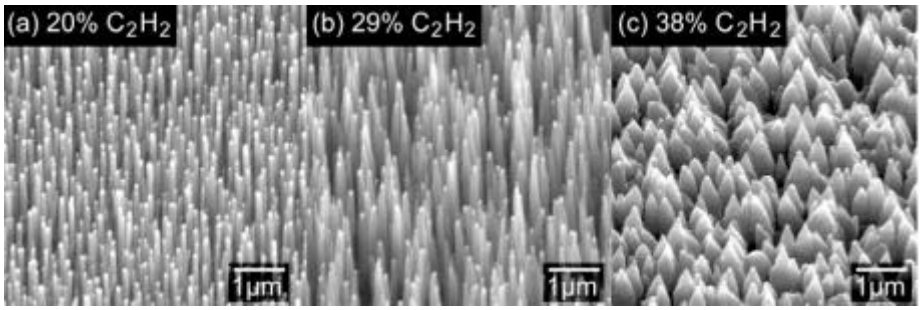

Figure 2.22: Carbon nanotubes grown at different gas ratios, while keeping the other parameters unchanged, a) shows well aligned CNTs, b) shows obelisk-like CNTs, c) shows significant amount of a:C [61]

3 Growth mechanism of carbon nanotubes

One common question is whether the catalyst is a liquid or solid during growth. In the laser or arc methods, a high temperature gas of carbon and metal is created which is condensed, followed by CNT growth. Growth on solid surfaces, involves much lower temperatures. If one considers Fe as the metal catalyst, most experiments have typically been performed below the melting temperature of Fe (1534^0C) and the Fe-Carbon eutectic temperature (1147^0C). Even though the growth is done below both these temperature limits, one should note that the catalyst metal nanoparticles will behave completely differently than their bulk metal form as these small particles will have exceptionally high surface energy, area and mobility [27, 62]. For example, Hou et al [63] reported that annealing Fe encapsulated carbon particles in Ar between 1000-1100^0C completely removed them, which indicates that the particles were highly mobile at this temperature.

The small particles melting temperature is lowered due to the three following effects. Firstly, the melting temperature is depressed by the Gibbs Thomson effect:

$$\Delta T = \frac{2T_m\gamma}{L\rho r}$$

Where T_m is the melting temperature in K, γ is the surface tension, ρ is the density and r is the particle's radius. Secondly, the melting point is depressed by forming a eutectic with carbon. In the laser and arc methods, more than one CNT grows from each particle, which tends to make the nanoparticles larger. In the CVD methods, a single CNT tends to grow from each nanoparticle, which causes the final diameter of the CNT to greatly depend on the nanoparticle's diameter. Figure 3.1 shows estimated relation of the local melting point versus the nanoparticle's radius and indicate that the local melting point of a particle is related to its size. Thirdly, the surface energy of the metal-carbon particles is known to be strongly dependent on the carbon content, where increased surface energy is known to reduce the melting temperature of them [27, 64].

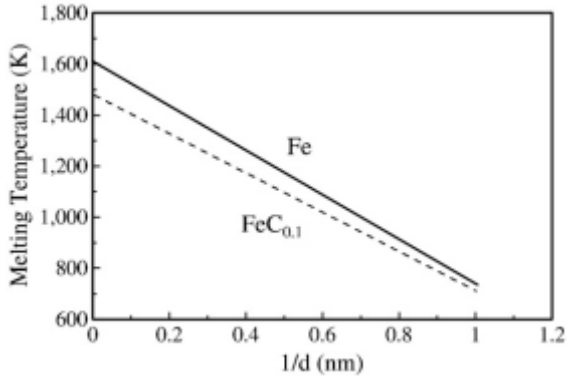

Figure 3.1: Calculated melting points of Fe as a function of particle size (larger particle size to the left) [29]

In general, the growth mechanism by Baker et al is believed to apply for catalyst that remains in the solid phase, which means that the temperature is below the metal-carbon eutectic point. When growth at temperature above this point occurs, where diffusion through a liquid/quasi-liquid state particle is responsible for the synthesis of filaments, the growth is believed to be similar to the general VLS mechanism which was proposed by Wagner. Some suggest that the nanoparticles could be in the solid phase during growth, but that CNT growth needs to be is initiated by liquid nanoparticles [27, 65, 66]. A brief introduction to these growth mechanisms are given below.

3.1 General mechanisms

3.1.1 The bulk diffusion

The most commonly accepted mechanism was postulated by Baker et al in the early 1970s, who explained the growth of carbon filaments by catalytic decomposition of hydrocarbons and the bulk diffusion of carbon.

According to this mechanism, the hydrocarbon gas decomposes on the front-exposed surface of the metal particle to release hydrogen and carbon, which dissolves in the solid particle (Figure 3.2 b)). The dissolved carbon diffuses through the particle (Figure 3.2 c)) and upon saturation gets precipitated at the trailing end to form the body of the carbon filament (Figure 3.2 d) and e))).

Due to the exothermic decomposition of the hydrocarbons, it is believed that a temperature gradient exists across the catalyst particle. Since the solubility of carbon in a metal is temperature dependent, precipitation of excess carbon will occur at the colder zone behind the particle, thus allowing the solid filament to grow with the same diameter as the width of the catalyst particle. Such a process will continue until the leading tip of catalyst particle is "poisoned" or deactivated. A common cause of catalyst poisoning is the formation of a graphitic layer around it, thus preventing the hydrocarbon gas from reaching the catalyst particle and growth terminates. The rate limiting step in the growth is believed to be diffusion of carbon through the catalyst [27, 41, 47, 49, 66, 67, 68, 69, 70, 71].

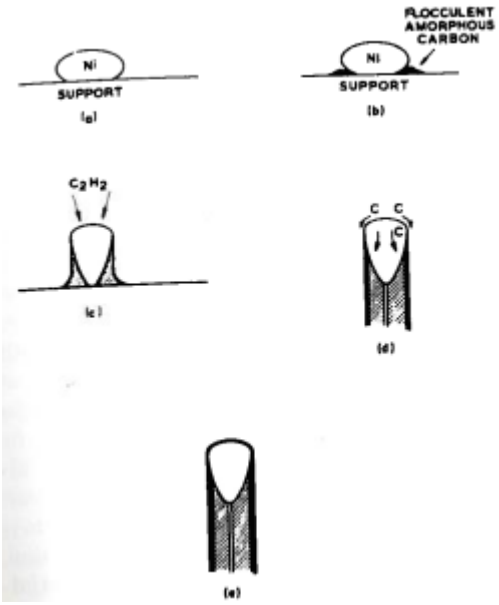

Figure 3.2: Stages in the growth of filaments by the bulk diffusion mechanism [67]

There are two irregularities regarding this growth mechanism. Firstly, not all hydrocarbon decomposing reactions are exothermic (e.g. CH_4) and yet growth has been observed by these hydrocarbons. Secondly, since the metal particles are so small, there is unlikely that there exists any temperature gradient at all. This is because the metal particle has a high thermal conductivity and thus a small temperature gradient implies that a massive heat flow occurs through the particle, which is physically intangible. The exothermic decomposition of hydrocarbon will most likely raise the temperature of the entire filament, and the growth of carbon filament is probably driven by the concentration gradient of carbon across the particle. The bulk diffusion mechanism considers diffusion of carbon through the metal or carbide only, but lacks consideration of any diffusion of

metal into carbon [27]. That is why the “diffusion over the surface” mechanism has been proposed by Barid et al [72].

3.1.2 Diffusion over surface

An explanation that seems to be more satisfactory has been proposed by Barid et al [72] which involves the diffusion of “metal-metal hydrocarbon species” across the edge of the carbon layer planes.

In the beginning small “liquid-like” droplets of Fe are fixed on the wall of the furnace because of the reduction by H. The beginning of the carbon shell is initiated by nucleation of an association of metal and hydrocarbons, which diffuses on the surface and dissociates at a contact angle between the droplet and the wall of the furnace that acts like a substrate. New metal hydrocarbons species dissociates on its edges and carbon layers develops by lateral growth that follow the external surface of the catalyst (Figure 3.3 a and b). Such growth exerts a force strong enough to lift up the catalyst particle from the surface of the substrate (Figure 3.3 c). The layer always progress laterally in the same way which results in a filament. The hollow channel in the center is due to that no carbon supply can reach the back of the droplet. The growth of carbon layers continues as long as there is sufficient supply of metal from the top of the catalyst particle. When the droplet is covered by graphitic layers at the tip, diffusion stops which terminates the growth. It is still unclear whether carbon diffuses by the bulk or the surface mechanism, or if both of them compete in a way [27, 45, 41, 49, 68, 70, 71, 73].

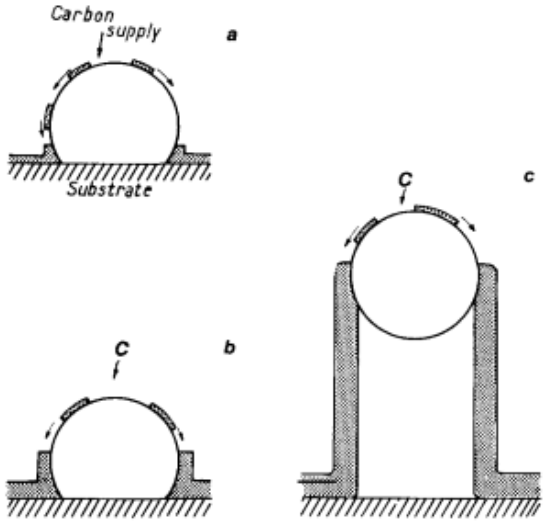

Figure 3.3: Stages in the growth of filaments by the diffusion over surface mechanism [68]

3.1.3 Vapor-Liquid-Solid (VLS)

The VLS mechanism can be used to explain the formation of CNTs. The catalytic particle surface adsorbs hydrocarbons and releases the carbon upon decomposition at high temperature, which dissolves and diffuses into the catalytic metal droplet or particle. When a supersaturated state is reached, carbon precipitates in a crystalline tubular at high temperatures. The particle solidifies when the temperature drops below the eutectic temperature of the system. Because much more carbon can be dissolved in a liquid than in a solid particle, process temperature must be high enough (400-850^{0}C) so that hydrocarbons is thermally decomposed in the thermal CVD processes. Without thermal decomposition, such as in the PECVD, the decomposition takes place in the plasma which gives the possibility of reducing the growth temperature. Since the temperature is reduced, the

catalysts are believed to be in its solid-phase during growth, which makes it reasonable to think that carbon diffusion occurs over the catalyst surface, rather than into the bulk [16, 74].

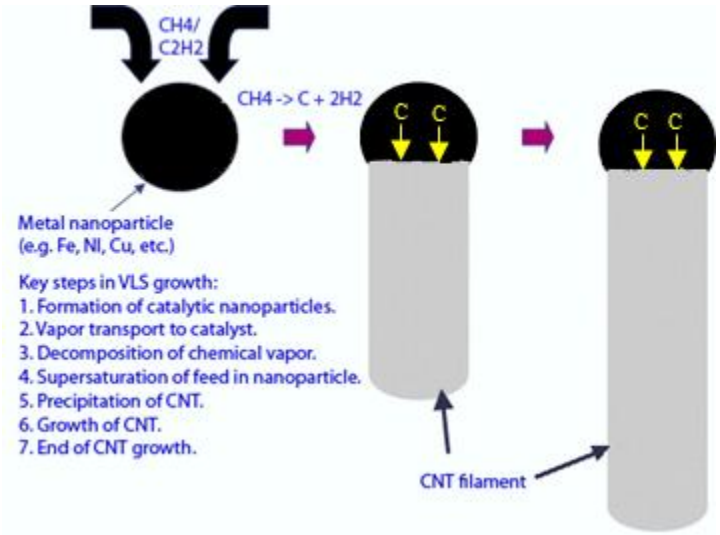

Figure 3.4: Schematic illustration of the VLS growth mechanism where metallic particle is marked in black and the resulting CNT filament during growth is marked in grey

3.2 Base- versus tip-growth

When the catalyst remains anchored to the substrate during growth of a CNT the synthesis mode is called “base-growth”. On the contrary, the growth follows a “tip-growth” mechanism when the particle lifts off the substrate and is observed in the top of the CNT during growth. The difference in growth mode is often explained in terms of the adhesion force between the catalyst particle and the substrate. A weak bonding favors the tip-growth mechanism while a strong interaction promotes base-growth [46, 75]. In principle, one might expect that smaller particles should more easily break off the surface, which is however not the case. Song et al demonstrated [76] that interconnected catalyst particles promotes base-growth, while tip-growth occurs for isolated ones under the assumption that the adhesive force is proportional to the contact area.

Small particles (< 5 nm) which promote SWCNTs have been observed to hold base-growth while larger particles that promoted MWCNTs experienced tip-growth [70]. This is explained by the stronger interaction between the support and the catalyst which is observed when using Si substrates, since metallic silicide enhance the interaction with the catalyst. When a barrier layer, such as silicon dioxide (SiO_2) or titanium nitride (TiN), has been used the interaction has shown to be weakened which resulted in tip-growth. That is why the chosen growth mode depends on more, than just the size of the catalyst particles.

In terms of kinetics for large particles, one may consider that carbon paths have sufficient time for diffusion on the surface of large catalyst particles before the formation of a complete hemispherical cap. Thus, in the early stage of the CNT nucleation the first graphitic sections or reticulated carbon chains that is formed on the surface of the large catalyst can quickly diffuse to the catalyst/substrate interface and stabilize it, which is illustrated in Figure 3.5 (step 2). This step leaves the top surface of the nanoparticle exposed for further carbon adsorption. The nucleation step leads to particle elongation (step 3) and finally causes the particle to lift-off from the substrate (step 4). Once the connection with the substrate is broken, tip growth is the only available growth mechanism mode [70].

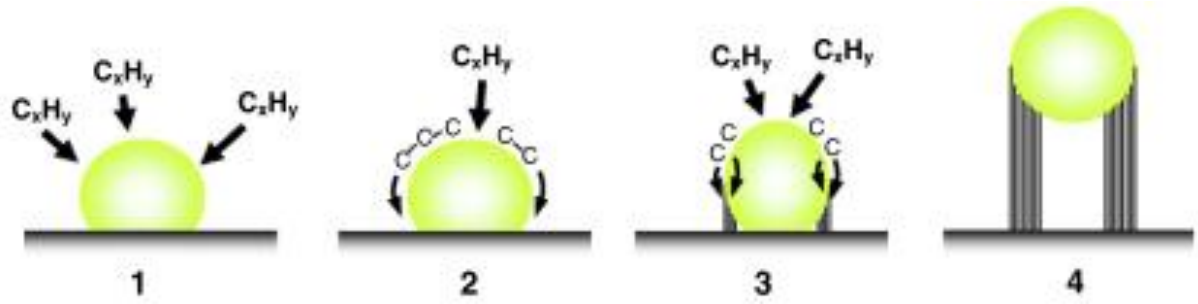

Figure 3.5: MWCNT growth scenario from large particles (typically >> 5 nm) [70]

In the case of small particles, one can assume a much more reactive metal particle. This implies a stronger interaction with the carbon path. Hence, after decomposition of the first molecules of C_xH_y, a graphene cap is formed and cuts off the carbon source over the particles, which is illustrated in Figure 3.6 (step 2 and 3). Therefore, the carbon flux can be provided at the nearby interface between the catalyst and the substrate only. In the case of SWCNT growth, carbon is incorporated at the edges of the graphene cap which lift-off the catalyst surface (step 4). Then the SWCNT growth occurs (step 5).

If the base-growth catalyst particle is still to play a catalytic role in the decomposition and adsorption of the feed gas, it must remain exposed to the gas, i. e. there must remain a band of exposed catalyst metal between the growing nanotube and the substrate which implies that there is no directional interaction between them. The only alternative, which is unlikely, is that the substrate plays a much stronger role than previously imagined, breaking down and transporting the carbon species to the catalyst particle [70].

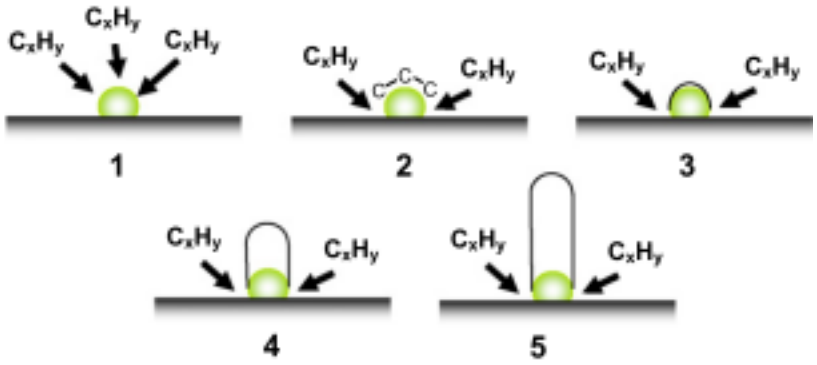

Figure 3.6: SWCNT growth scenario from small particles (typically < 5 nm) [70]

3.3 Vertically aligned CNTs

There are two ways to obtain VACNTs. One is to exploit the electric field in the plasma of the PECVD to align the CNTs normal to the surface. The other one is to grow densely packed arrays by CVD which forces the CNTs to grow normal to the surface in addition to the van der Walls interaction between them, which is often referred to as the "crowding effect" or "self-orientated growth". The vertical growth depends highly on the support-catalyst interaction. If it is strong, as in aluminum oxide (Al_2O_3)-Fe, the catalyst nanoparticles have restricted mobility and yield surface bound VACNTs by the base-growth mode. Conversely, if the interactions are weak, as in SiO_2-metal, the nanoparticles diffuse during the pretreatment/growth stage which yield entangled CNTs by the tip-growth mode. In addition, the conductivity of the chosen substrates is important in PECVD since the electric field lines of the plasma sheath needs to be perpendicular to the substrate [27, 50, 52, 77, 78, 79].

Growth of VACNTs on Al_2O_3 has strict fundamental requirements to the Fe-catalyst and requires:

1) Catalyst nanoparticles smaller than ≈3 nm.
2) Average spacing between neighboring nanoparticles must not exceed ≈20 nm.
3) Catalyst nanoparticles stability at chosen growth temperature, typically above 700^0C.

These fundamental requirements are not easy to maintain for some catalyst metals, e.g. Fe migrate on the surface at high temperatures which leads to morphological changes since larger particles grow at the expense of smaller ones (Ostwald ripening) which could terminate growth [58].

4 Theory

4.1 The purpose with the barrier layer

The barrier layer is an intermediate layer between the metal catalyst layer and the substrate. It has several purposes, but where the primary reason is to prevent any chemical reactions (e.g. diffusion) between the substrate and the metal catalyst at the temperatures that are used in the formation of nanoparticles and during CNT growth. It is also important that it does not react or alloy with the catalyst as this would decrease activity during CNT growth or/and can result in that the catalyst particles are depleted from the surface. The secondary is that it promotes adhesion by increasing the surface roughness. It needs to have sufficient adhesion to the catalyst as well as to the substrate, while maintaining sufficient wettability with the liquid phase of the catalyst, so that the catalyst film is able to be transformed into uniform and discrete nanoparticles without any particle agglomeration during the pretreatment step [27, 36, 38, 52, 77, 78, 80, 81, 82].

Earlier experiments have shown that Ni catalyst film directly on Si substrates at growth temperatures above 300^0C has resulted in diffusion of Ni into Si, which forms silicides that are unwanted as they are known to decrease the yield and the uniformity of the grown CNTs. Co and Fe are known to have higher diffusion temperatures with Si, which means that they can be used directly on Si substrates at ≈700^0C. However, a barrier layer is still recommended as it can significantly improve the yield [27, 41, 73, 83].

4.1.1 What type of material should be chosen

Oxide thin films, such as Al_2O_3, titanium dioxide (TiO_2) or SiO_2, are widely used as barrier layers because of their stability and chemical inertness at the growth temperatures that are necessary for CNT growth. Al_2O_3 has shown to be best for stabilizing Fe based catalysts, compared to SiO_2. This can clearly be observed in Figure 4.1 and Figure 4.2, where the resulting Fe nanoparticles on SiO_2 and Al_2O_3 supports are compared after being annealed in H flows at 750^0C. It is observed that the nanoparticles are much smaller in size and are better dispersed on the Al_2O_3 support [82].

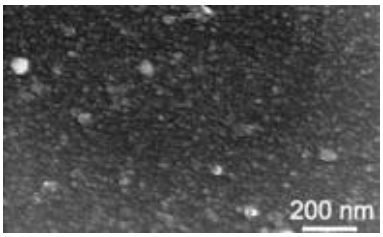

Figure 4.1: SEM images after annealing treatment for Al_2O_3/Si wafer [82]

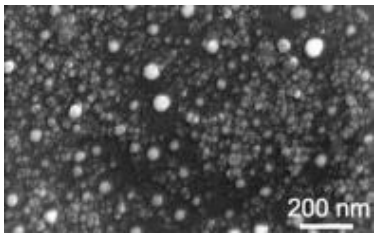

Figure 4.2: SEM images after annealing treatment for SiO_2/Si wafer [82]

In Figure 4.3 - Figure 4.4, the nanoparticles with Al_2O_3 support resulted in CNTs that was almost an order of magnitude higher (419 um) compared to SiO_2 (53 um), and shows CNTs with higher density and alignment [29, 82].

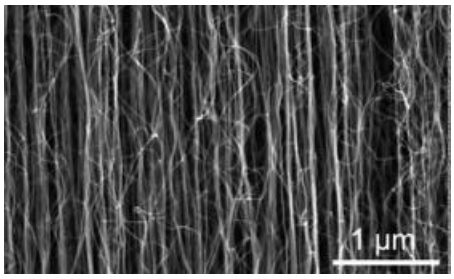

Figure 4.3: SEM images of CNTs grown on Al_2O_3/Si [82]

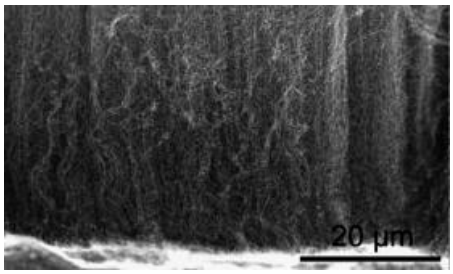

Figure 4.4: SEM images of CNTs grown on SiO_2/Si [82]

So why are Al_2O_3 more preferred as a barrier layer compared to SiO_2? This has to do with that it is thermodynamically more favorable than SiO_2 and analysis have shown that there exists a much stronger interaction between Fe- Al_2O_3 than Fe-SiO_2. This is believed to be because of formation by Fe-O bonds at the metal- Al_2O_3 interface or because of the possible charge transfer from Fe to the surface oxygen atom. Fe could in some cases dewets SiO_2 so that some areas get completely depleted of Fe which is because of increasing surface roughness. The resulting Fe nanoparticles coarsen by cluster migration or Ostwald ripening. The coalescence is driven by a minimization of the surface free energies and the free energy at the support-metal interface. In comparison, the surface roughness remains roughly constant on Al_2O_3 which leads to that Fe coarsen significantly less and confirm the lower mobility of Fe on such a support. In Figure 4.5, the nanoparticle size distribution on the Al_2O_3 shows a single narrow peak compared to the much broader distribution on the SiO_2, which confirm the restricted coalescence of Fe particles [58, 81, 84, 85, 86, 87].

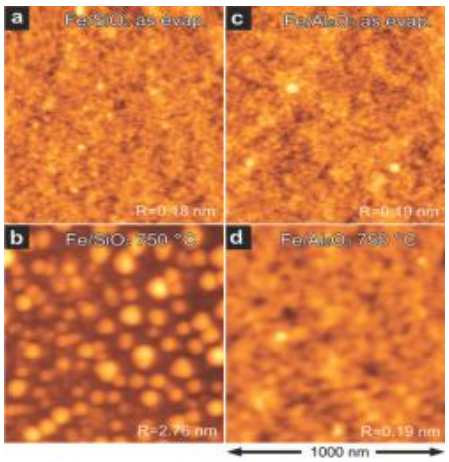

Figure 4.5: AFM tophology images of as-evaporated and subsequently annealed Fe (≈1.1 nm) films on (a, b) SiO_2/Si and (c, d) Al_2O_3/Si. The catalyst films are annealed at 750^0C at atmospheric pressure in 200:500 sscm of Ar/H_2 for 3 min [85]

4.1.2 Ostwald ripening effect

When catalyst films are subjected to annealing, mobility of the metal atoms increases which results in Ostwald ripening – a phenomenon that is driven by reduction of the surface free energy for the catalyst nanoparticles relative to the bulk, which means that larger particles grow at the expense of smaller ones to relieve the excess surface energy. A general rule is that samples with high inward diffusion rate and porosity will have low Ostwald ripening rates. Catalytic activity and the quality of the CNTs are high for samples with low Ostwald ripening rate and vice versa.

The best deposition of Fe on Al_2O_3 is by sputtering. Sputtered-Fe has shown to have a mild inward diffusion- and a high subsurface diffusion rate, which results in a low Ostwald ripening rate. This is important to achieve a high catalytict lifetime and activity [87].

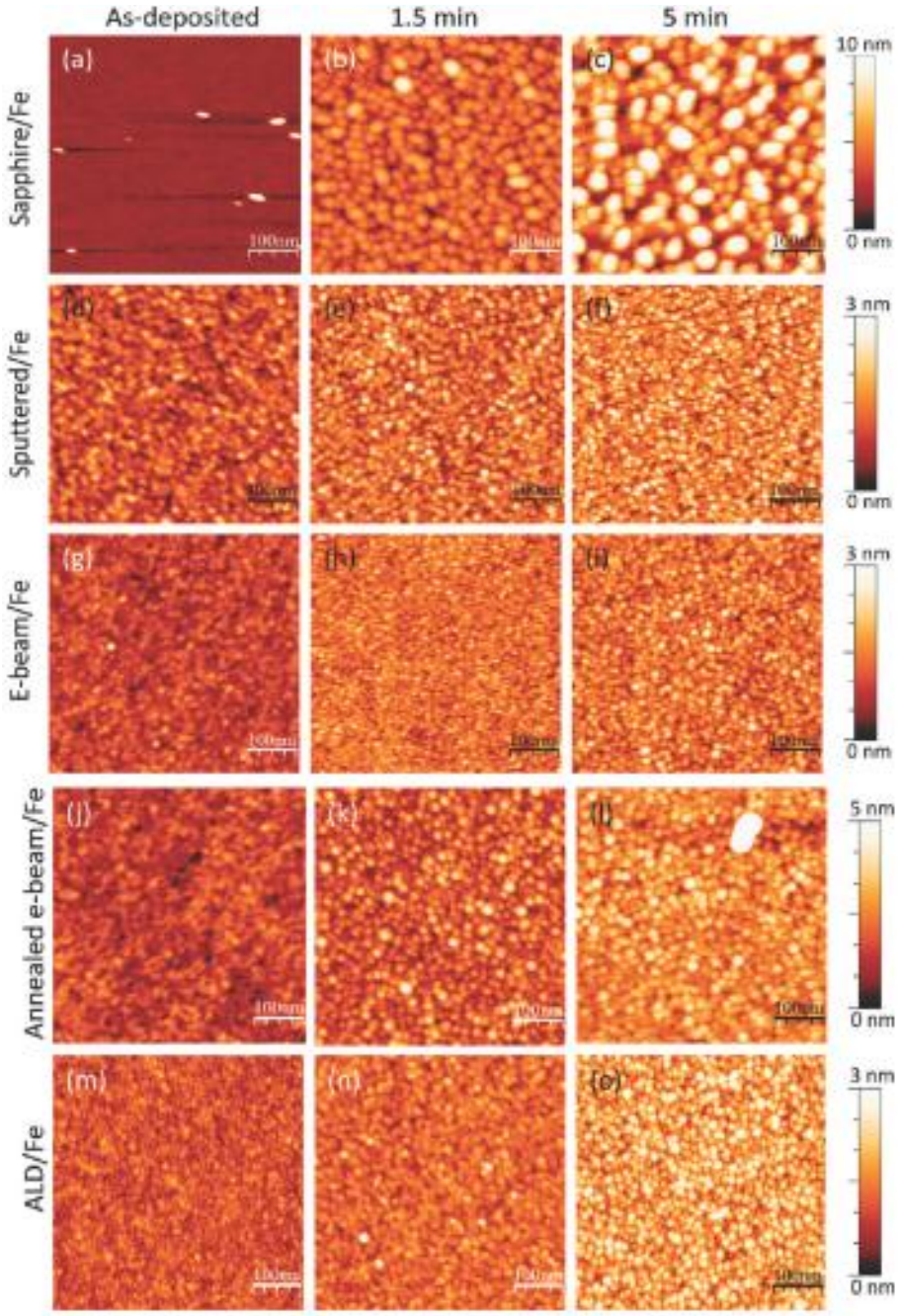

Figure 4.6: Catalyst evolution: AFM topography images of as-deposited catalyst and catalyst nanoparticles formed on different Al_2O_3 supports after exposure to growth conditions in the absence of C_2H_2 for 1.5 and 5 min. All scale bars are 100 nm [87]

4.2 The role of the NH_3 and/or H_2

Treating in NH_3 or H_2 is a crucial step during pretreatment and during the CNT growth stage. Both of them have reported to act as good sources of atomic H, which is important during the whole CNT growth process since it:

- Removes excess carbon species which would otherwise lead to a:C.
- Contributes to the formation of catalytic nano-sized particles as it functions as an etchant.
- Keeps a reducing atmosphere during growth that hinders oxidation of the catalytic particles.
- Help the catalyst in producing CNTs at low substrate temperatures.
- (H ions can chemisorb on the catalyst surface and modify its properties, e.g. surface energy, which alters the interaction with the carbon source. This could accelerate the adsorption of hydrocarbon to the catalyst surface which provides higher diffusion during growth.)

The tasks of the atomic H which is listed above is important to ensure that the catalysts have high enough growth rates and will cause enhanced lifetime of them which would lead to growth of long CNTs [36, 41, 51, 61, 80, 88, 89, 90] [91, 92, 93, 94, 95, 96].

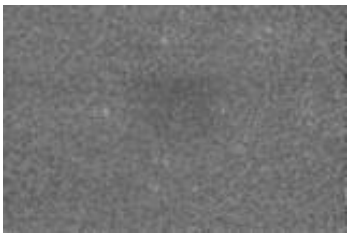

Figure 4.7: SEM image showing the effect of Ar [92]

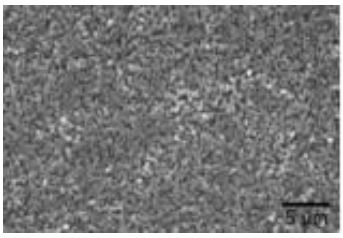

Figure 4.8: SEM image showing the effect of NH3 on pure catalyst surfaces. NH3 treatment enhances the formation of catalyzed nanoparticles [92]

NH_3 is believed to be more efficient than H_2, as it has been reported to be a more effective generator of atomic H that could enhance the formation of smaller particles. The N and H species in the NH_3 plasma react with a:C to form volatile C-N and C-H species which keeps the production and etching of a:C balanced, thus yielding substrate that are free from a:C. In addition, it is able to suppress decomposition of C_2H_2, because of the weaker chemical bonds that are present in the NH_3 molecule compared to the C_2H_2. This allows the latter to decompose slowly to provide the necessary amount of carbon that are required for growth which could yield clean and well aligned CNTs. On the left side of Figure 4.9, where the plasma is predominantly NH_3, it can be noticed that the amount of generated H_2 increases as the NH_3 increases [27, 61, 92, 96].

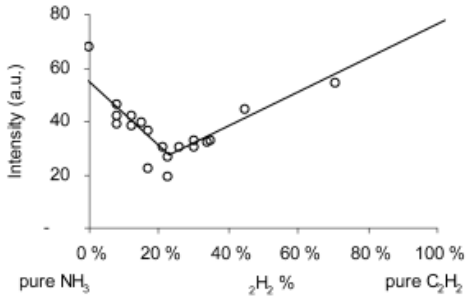

Figure 4.9: H_2 signal for varying gas ratio [61]

The incorporation of N into the nanoparticles has reported to change the composition and structure of the catalyst's surface. NH_3 contributes by incorporate N or NH_X radicals into the catalyst layer which causes an additional strain energy between the metal-metal bonding that will aid the

formation of nanoparticles due to strain relaxation in the metal layer, or by physical etching of atomic N or NH_X radicals since they are recognized of keeping the catalyst's front clean which enhances bulk diffusion of carbon [80, 90].

At low growth temperatures it is believed that some defects could be present because of N doping. However, this is not the case at higher temperatures since the N and H species can form stable gaseous cyanide acids (HCN) which are transported away by the flowing gases in the chamber, e.g. a carrier gas. This will cause a lower amount of N that is available for doping and leads to that the temperature defects replaces the N induced [92].

Figure 4.10 shows the effect of treating Fe films with TP for various atmospheres at a constant pressure of 0.7 mbar and temperature of 500^0C. It is observed that it contains samples with considerable varied morphology. Annealing in vacuum yields the highest average particle's size, this explains why no CNT growth is obtained. All other atmospheres can be noticed of dramatically reducing the average particle's height, with NH_3 being the most effective at restructuring the films [97].

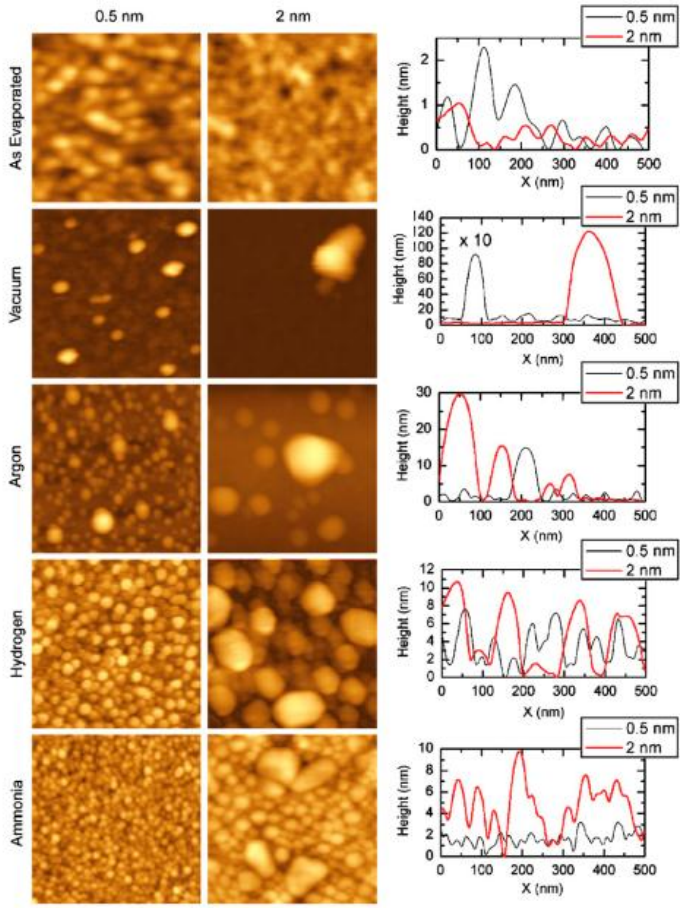

Figure 4.10: AFM topography and line profiles of Fe thin films, 0.5 and 2 nm thick, as deposit and annealed at 500^0C in different atmospheres [97]

4.3 Effect of variation in the different parameters

4.3.1 Temperature

At low temperatures there is an excess of carbon deposition which is responsible for graphitization of CNTs and the formation of an a:C network. This is why a high temperature is important since it

enhance diffusion of carbon through the particle which will increase growth rates. In addition, it is believe to aid the formation of nanoparticles as it increases the surface energy and mobility of metal atoms. Unfortunately, the average diameter of the CNTs increases with temperature [45, 41, 49].

The intensity ratio (I_D/I_G) indicates the degree of crystallinity of CNTs, where a low ratio corresponds to a superior degree of graphitization with small amount of defects and a:C. Figure 4.11 states that the defects and impurities in the CNTs are reduced with increasing temperature [82, 98]. In Figure 4.12, it can be observed that higher temperatures yield longer CNTs (the time is kept constant) [99].

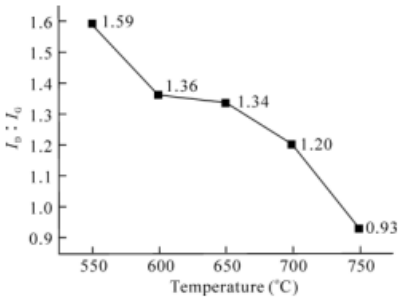

Figure 4.11: I_D/I_G in Raman spectra at different substrate temperatures [98]

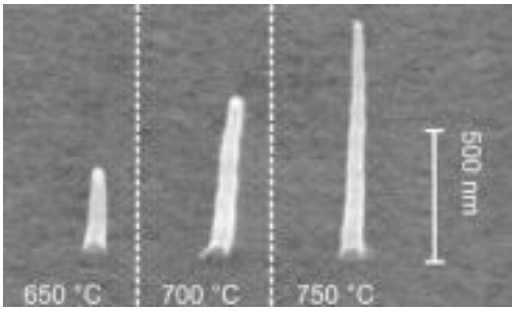

Figure 4.12: Influence of the variation in temperature on individual CNTs. Increasing growth temperature increases the growth rate [99]

Figure 4.13 to Figure 4.17 shows morphologies of CNTs grown at different substrate temperatures. The CNTs in Figure 4.13 and Figure 4.14 are short and distributed disorderly and with a handful of a:C. The CNTs improves in Figure 4.15 as they hold better alignment, but disordered CNTs are still present. In Figure 4.16 the alignment, density and length of the CNTs improves, as they are less disordered and that the number of impurities is relative small when comparing it with the CNTs in Figure 4.15. However, the best CNTs is achieved at the highest temperature (Figure 4.17), because of their superior alignment, highest density and very small amount of a:C [98].

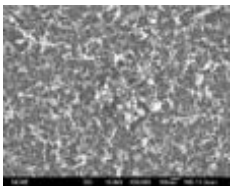

Figure 4.13: CNT growth at 550^{0}C [98]

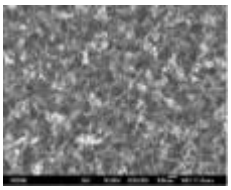

Figure 4.14: CNT growth at 600^{0}C [98]

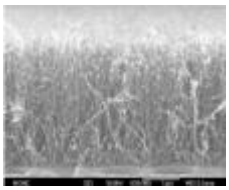

Figure 4.15: CNT growth at 650^{0}C [98]

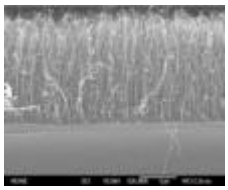

Figure 4.16: CNT growth at 700^{0}C [98]

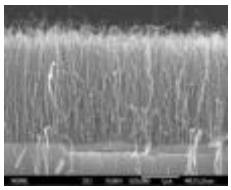

Figure 4.17: CNT growth at 750^{0}C [98]

4.3.2 Time

The CNT length is expected to depend linearly on growth time, but too long growth time has been observed to shorten them. This is because that no more catalyst material remains left after a certain time (due to permanent sputtering during growth). This involves that the plasma etching becomes dominant as it exceeds the growth rate which causes shortening of the CNTs [51, 99].

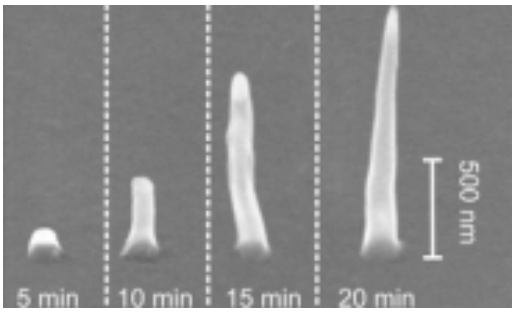

Figure 4.18: Influence of the variation in time on individual CNTs. CNT height increases approximately linearly with growth time as long as catalyst material is available at the CNT tip [99]

Brown et al [54] observed the effect of increased pretreatment time. They found the following changes to apply when time was increased (Figure 4.19):

1. The nanoparticles became flatter and possessed a smaller contact angle with the substrate.
2. The nanoparticles appeared to partially diffuse into the barrier layer and increase with pretreatment time (which on average increased the size of the nanoparticles).
3. The size and the spatial distributions of nanoparticles became less uniform.

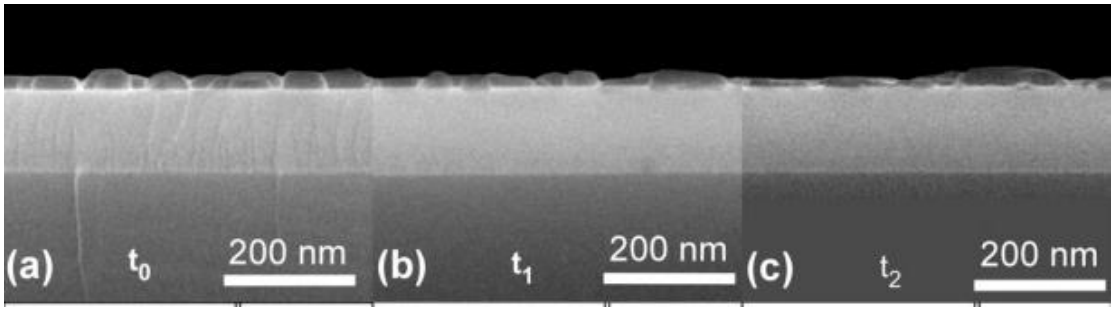

Figure 4.19: Cross section SEM images of pretreated samples for 0 min (t_0), 1 min (t_1) and 3 min (t_3) [54]

Figure 4.20 reveals that the average CNT length increases with decreasing pretreatment time, despite the fact that they all have the same growth time. This is explained on the basis of that as the pretreatment time decreases, the reaction with the barrier layer decreases which result in smaller particles. Smaller particles are more catalytic active than larger ones since they possess a more rapid diffusion of carbon, which result in higher growth rates [54, 89, 96, 100].

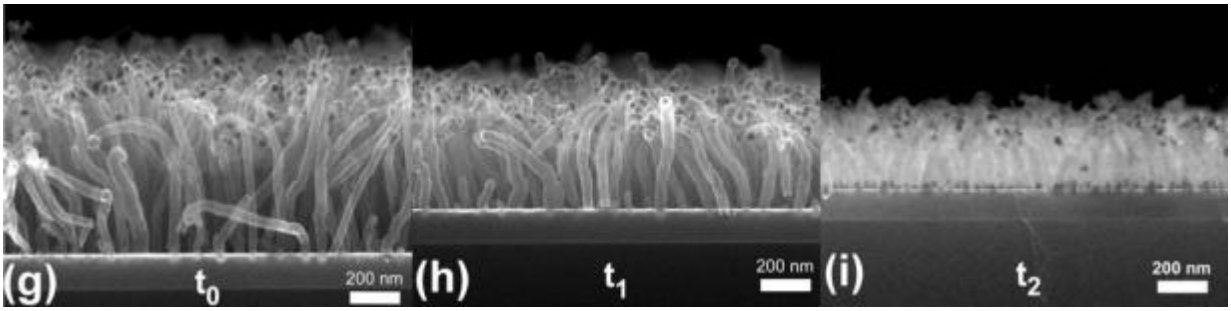

Figure 4.20: Cross section SEM images of Pt-CNT growth on SiO_2 support using CH_4/NH_3 ratios of 3. T_0, t_1 and t_2 are equal to those in Figure 4.19 [54]

4.3.3 Power

Higher power will in general cause better alignment of the tubes as the electrical field becomes more intense, but would at the same time speed up the etching rate as well. The increased etch rates with increasing power is demonstrated in Figure 4.23. With increased power, more carbon species

becomes available to react with the particles since the decomposition of hydrocarbons becomes intensified. This could involve CNT growth with higher growth rates, densities and alignment [42, 95]. Some believe that the increased decomposition of hydrocarbons, shown for C_2H_2 in Figure 4.21, could lower the growth rate since fewer hydrocarbons are available to react with the catalyst particles (see Figure 4.22) [61, 99].

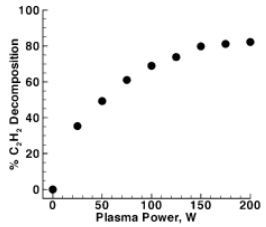

Figure 4.21: Variation of gas decomposition with plasma power [61]

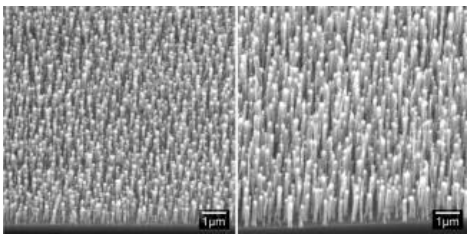

Figure 4.22: Effect of varying the plasma power while keeping the other parameters constant. Power is 200W on the left and 66W on the right [61]

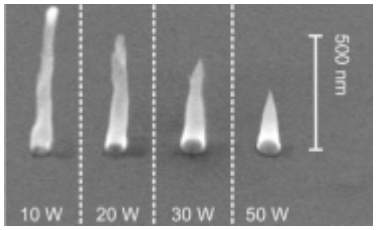

Figure 4.23: Influence of the variation in plasma power on individual CNTs. Increasing power increases etching of the CNT in the NH3 plasma [99]

An experiment that studied the variation of power for pretreated samples suggests that the average size of the nanoparticles decreases with increasing power, but only up to a certain point. Higher power will in general assist on breaking the catalyst layer into smaller nanoparticles, but creates defects when exceeding a certain power level. This can be observed in Figure 4.24 - Figure 4.29, where the nanoparticle's size decreases up to a power level of 350 W, but start to increase again at higher powers [101].

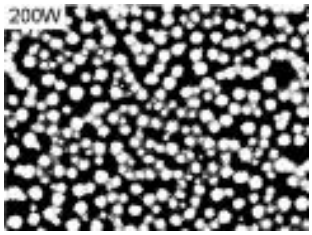

Figure 4.24: Effect of microwave power on nanostructuration under hydrogen plasma at 200W (when pressure is 25 mbar and time is set to 2 min) [101]

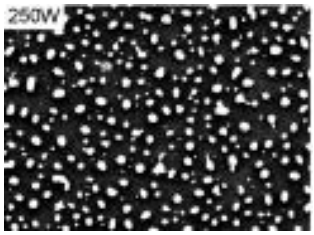

Figure 4.25: Effect of microwave power on nanostructuration under hydrogen plasma at 250W (when pressure is 25 mbar and time is set to 2 min) [101]

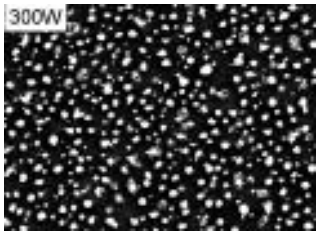

Figure 4.26: Effect of microwave power on nanostructuration under hydrogen plasma at 300W (when pressure is 25 mbar and time is set to 2 min) [101]

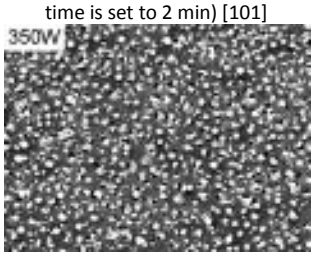

Figure 4.27: Effect of microwave power on nanostructuration under hydrogen plasma at 350W (when pressure is 25 mbar and time is set to 2 min) [101]

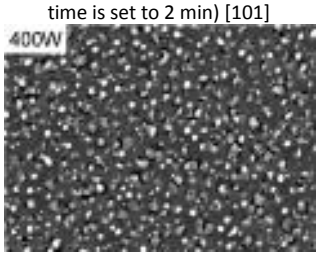

Figure 4.28: Effect of microwave power on nanostructuration under hydrogen plasma at 400W (when pressure is 25 mbar and time is set to 2 min) [101]

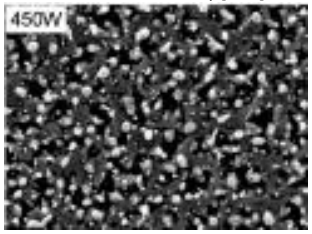

Figure 4.29: Effect of microwave power on nanostructuration under hydrogen plasma at 450W (when pressure is 25 mbar and time is set to 2 min) [101]

4.3.4 Gas flow

A consequence of higher H_2 flows is that the etching increases as well. Increased etching is positive as it promotes formation of smaller, uniform and more spherical-shaped nanoparticles. Figure 4.30 - Figure 4.32 shows the effect of various H_2 flows during PP on Ni particles and how it affects the apparent crystallinity and geometric shape of them. In Figure 4.30 and Figure 4.31 the Ni particle seems rather disordered with a broad based shape, while the particles in Figure 4.32 appear to be

more crystallized and hold a semispherical shape. The morphological differences occur since higher flows will [52, 102]:

- Increase the mobility of atoms in the catalyst particles.
- Hinder formation of a:C.

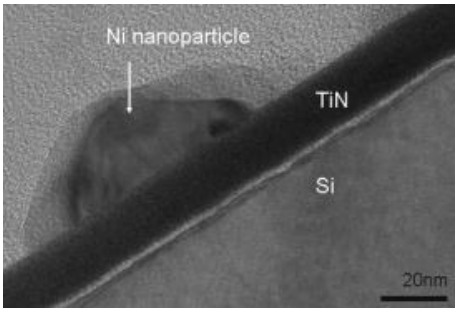

Figure 4.30: TEM image of Ni catalyst nanoparticle at H2 plasma treatment flow of 200 sccm [102]

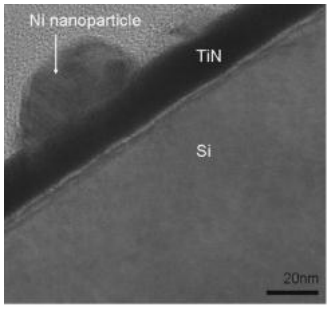

Figure 4.31: TEM image of Ni catalyst nanoparticle at H2 plasma treatment flow of 300 sccm [102]

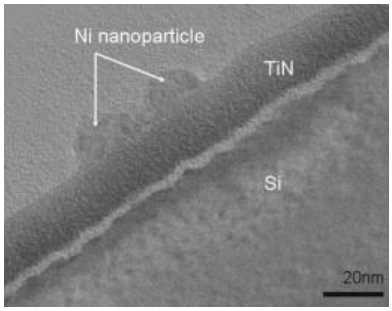

Figure 4.32: TEM image of Ni catalyst nanoparticle at H2 plasma treatment flow of 400 sccm [102]

4.3.5 Pressure

Higher pressure will cause increased growth rate due to the increased density of the hydrocarbons near the catalytic particle. In addition, higher pressures are beneficial as they will inherently avoid ion damage to the sample as it cause higher collision frequency among the molecules in the plasma sheath that suppress transportation of reactive species. This could lower the bombardment energy towards the surface of the sample significantly and could hinder that any as grown CNTs are being damaged. Higher pressure also offer the possibility of reducing the amount of a:C networks, since the excess amount of species are believed to be the ones that are responsible for the overgrowth of these networks. A drawback of higher pressure is that it will cause faster back etching of CNTs in the growth process after the catalyst particle have been consumed, which can be seen in Figure 4.33 [43, 52, 80, 95, 99].

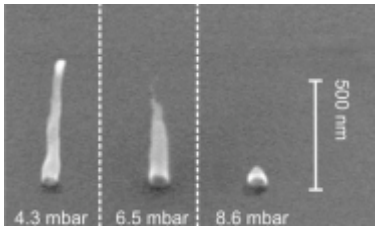

Figure 4.33: Influence of the variation in pressure on individual CNTs. With increasing pressure, etching of the CNT increases, leading to smaller CNTs [99]

In general, the ionization fraction increases exponentially with decreasing total pressure, which subsequently leads to larger supplies of reactive species. As already mentioned, an excess supply of them are believed to promote a:C deposition, but they are also believed to promote catalyst coagulation that preferentially yield MWCNTs with large diameters. The undesired catalyst coagulation induced by the overdose of reactive species takes place independently of high temperature catalyst coagulation [43, 95].

Figure 4.34 to Figure 4.36 shows results of increasing the pressure during PP with H. It can be seen that the size and the heterogeneity increases with increasing pressure. In other words, the nanoparticle formation decreases with increasing pressures. The principal reason for the slowdown in the nanoparticle formation is the reduction in the H atoms energy and density as the pressure increases. Earlier models on plasma behavior suggest that the majority of the electron-neutral

reactions become vibrational with increasing gas pressure. As pressure increases even further, neutral particles that are present collide with the electrons, hence the mean free path for the electrons is shorter. More frequent collisions give a reduction in the electron temperature which shifts electron-neutral reactions towards processes with low threshold energy, hence vibrational transfer. Since input power is primarily lost to vibrational excitation, the fraction of input power that leads to dissociation is significantly reduced [101].

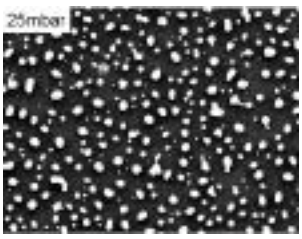

Figure 4.34: Effect of pressure on nanostructuration at 25 mbar with 2 min by hydrogen plasma [101]

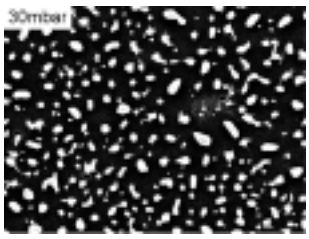

Figure 4.35: Effect of pressure on nanostructuration at 30 mbar with 2 min by hydrogen plasma [101]

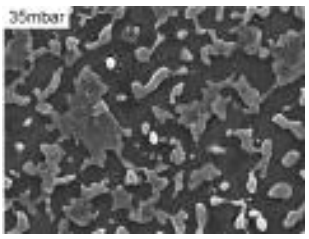

Figure 4.36: Effect of pressure on nanostructuration at 35 mbar with 2 min by hydrogen plasma [101]

Figure 4.37 demonstrates how varying the gas pressure during TP of Fe films can affect the resulting average particle's height. In general, higher pressure lowers the islands heights and gives narrower distributions. This can be due to the increased interaction between gas and metal which enhances the effect of the gas [97].

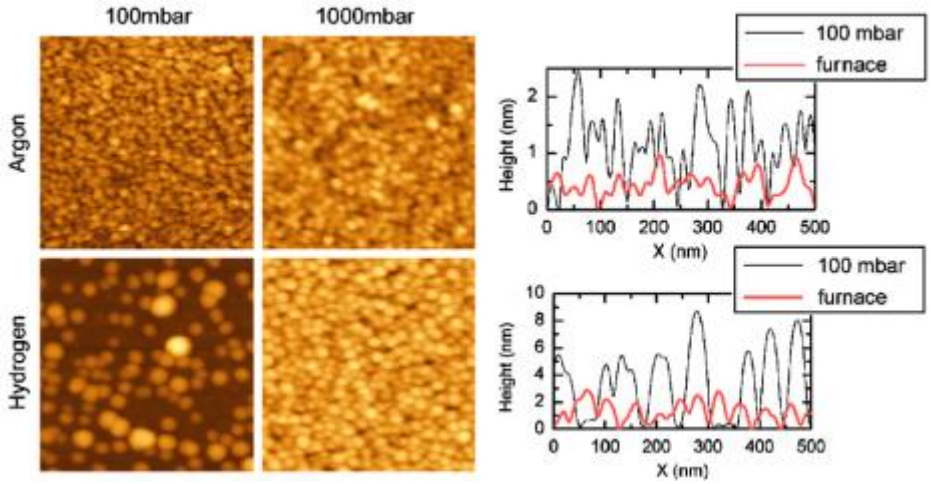

Figure 4.37: AFM topography and line profiles of Fe thin films 0.5 nm annealed in 500^0C [97]

4.3.6 Catalyst thickness layer

Since the catalyst layer is transformed into islands/nanoparticles during the pretreatment, the thickness of the catalyst is crucible for determining the density, length and diameter of the grown CNTs. As the thickness of the layer increases the resulting diameter of the formed nanoparticles will normally increase and vice versa [27, 54, 88, 89, 101]. Study of Figure 4.38 - Figure 4.40 shows that a Fe film of 10 nm thickness resulted in nanoparticles with an average diameter of 100 nm, a thickness of 5 nm resulted in particles of 20 nm and a thickness of 2 nm formed 10 nm particles

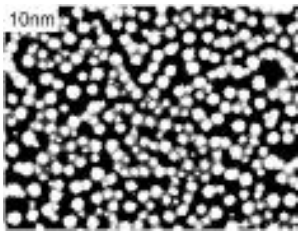

Figure 4.38: The result of Fe nanoparticles size as a function of a 10 nm catalyst film [101]

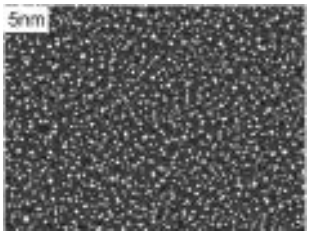

Figure 4.39: The result of Fe nanoparticles size as a function of a 5 nm catalyst film [101]

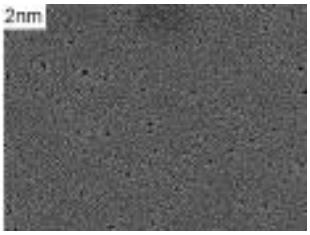

Figure 4.40: The result of Fe nanoparticles size as a function of a 2 nm catalyst film [101]

An experiment with Co/Fe catalysts indicate that a reduction of the initial catalyst layer below 3 nm generally gave growth to small diameter (≈ 5 nm) MWCNTs, while thicker films led to CNFs of larger diameter (> 40 nm) [89].

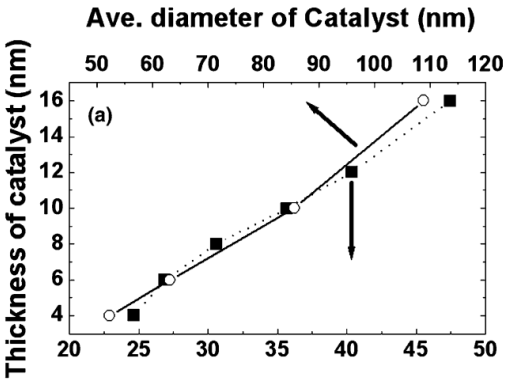

Figure 4.41: Dependency of the average diameter of catalyst nanoparticles on the thickness of Co particles [89]

Thin films tend to promote a morer uniform distribution of small sized catalyst nanoparticles. If the thickness is too thin, a sparse distribution of particles will be formed during the pretreatment which will give CNTs of low density. In contrast, a thick film will result in sintering of the metal catalyst that will prevent the film from being transformed into isolated nanoparticles that are required for growing CNTs. As the thickness increases the particles tend to coalesce and form elongated shapes. By decreasing the thickness, e.g. from 7 to 1 nm, the CNTs becomes longer, more aligned and uniform in height and diameter. This can be seen from Figure 4.42 - Figure 4.46 [42, 52].

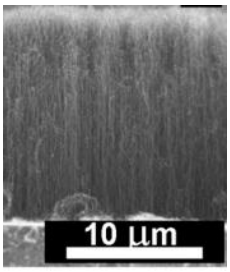

Figure 4.42: SEM image of CNT grown using Fe catalyst with thickness 7 nm (low magnification) [42]

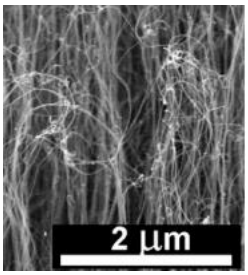

Figure 4.43: SEM image of CNT grown using Fe catalyst with thickness 7 nm (high magnification) [42]

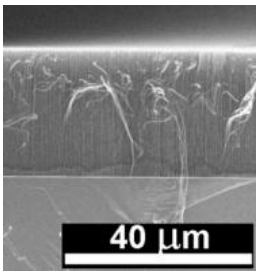

Figure 4.44: SEM image of CNT grown using Fe catalyst with thickness 3 nm (low magnification) [42]

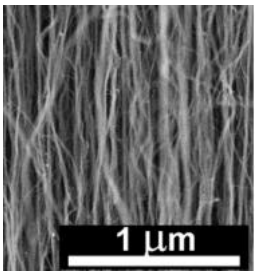

Figure 4.45: SEM image of CNT grown using Fe catalyst with thickness 3 nm (high magnification) [42]

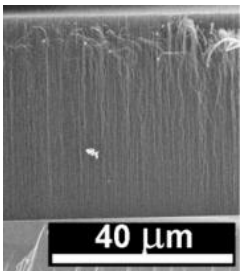

Figure 4.46: SEM image of CNT grown using Fe catalyst with thickness 1 nm (low magnification) [42]

4.4 Plasma pretreatment versus thermal pretreatment

There are two different methods to form nanoparticles from the continuous catalyst film prior to CNT growth. One is thermal annealing (TP) which is done in the presence of thermal energy and the

other is to use plasma (PP). Both these methods are usually done in an H rich atmosphere. The metal film is broken into nanoparticles during this treatment because of their increased surface mobility and the strong cohesive forces between the metal atoms. The pretreatment is a very important step since the nanoparticle's diameter and density reflects the resulting CNTs [27, 69].

Figure 4.47 compare different pretreatments that are done to Ni, Co and Fe films on a TiN support, when pretreated for 5 minutes at 500^{0}C by 100 mbar in an H atmosphere. It can be seen that the resulting nanoparticles after PP are smaller and more uniform separated than for the TP. In addition, PP is preferred since the plasma could give the possibility of lower process temperatures which result in that sintering/coalescence of nanoparticles are inhibited, which promotes more active catalyst as their size and size distribution are reduced. This would enhance the growth as smaller nanoparticles cause higher densities and longer CNTs [77, 94, 100, 101, 103]. PP has also shown to give VACNT that are higher than those treated with TP [30]. The TP treated nanoparticles have a root mean square (RMS) roughness of ≈ 50 nm while the PP nanoparticles have a smoother and more homogenous surface topology with a RMS roughness of ≈ 3 nm [77].

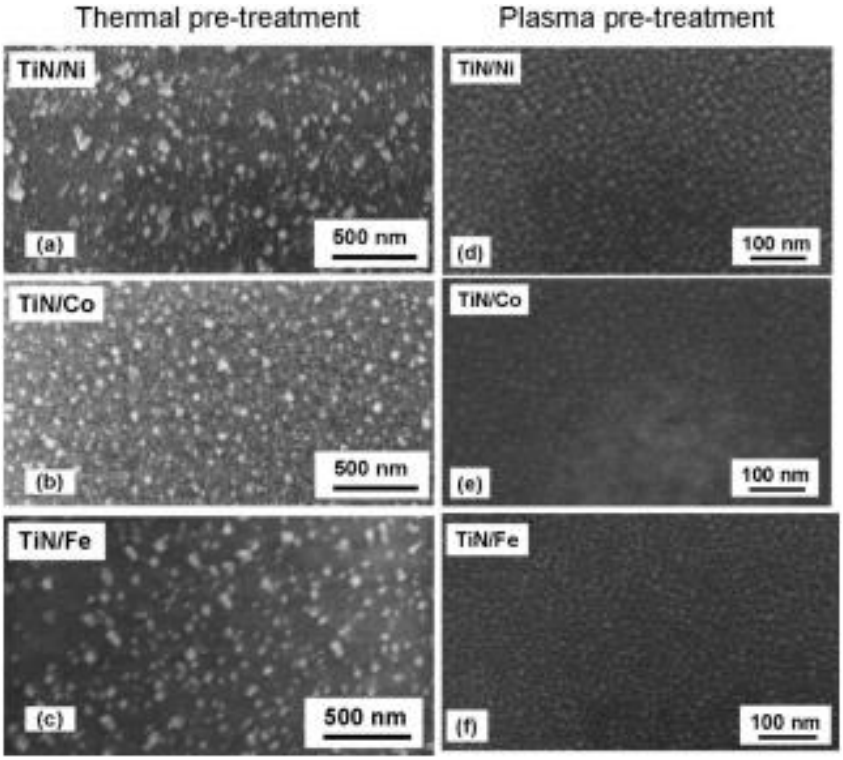

Figure 4.47: SEM images of 1 nm Ni, Co, Fe deposited onto TiN auppoer and pretreated for 5 min at 500^{0}C in 100 mbar of H_2 under TP (a-c) and PP (d-f) under 50W plasma power [77]

The PP treated nanoparticles have shown to be more stable and catalytically active (even after air exposure). Stable nanoparticles are preferred since they are able to withstand dimensional/compositional changes as annealing time elapses, while non-immobilized particles diffuse on the surface or bulk of the support which changes their topology and chemical pattern. That is why PP is believed to be able to resist bulk diffusion for longer times than those obtained with TP. Thus, stabilization of nanoparticles in the PP degrades with pretreatment time if no further changes are introduced to the system, which mean that they will diffuse into the support and lose their catalytic active for long PP time which is similar to long TP time [94]. To achieve the benefits with PP, treatment time must be below a critical time, which is illustrated in Figure 4.48.

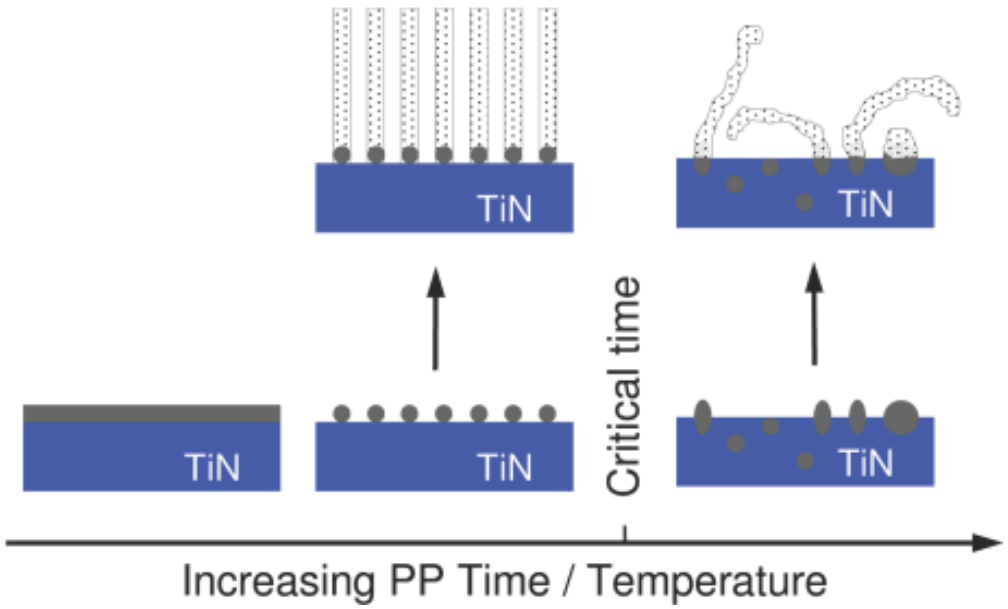

Figure 4.48: Growth model for PP nanoparticles. Schematic diagram of PP sequence (of Fe coated TiN) as function of time or temperature. At PP critical time nanoparticles start diffusing into the underlying support, which is similar to TP growth [94]

A thicker film will require longer pretreatment time to transform the film into smaller particles and vice versa. In some cases with TP, the heat alone is not enough to break the catalyst film into nanoparticles and additional assistance of PP is required. Note that when the catalyst film exceeds a few tens of nm, nanoparticles are no longer formed and the film form islands of a few um in sizes. These usually behave like a continuous film, which mean that they do not nucleate CNTs [27, 38, 52].

4.4.1 Reducing- (RP) and oxidizing pretreatment (OP)

Experiments with RP and OP have been done for the TP. The OP was done in a furnace with open air while the RP was done with a mixture of H and Ar. None of these atmospheres caused significant loss of catalytic activity, but dramatically changed the CNT morphology and growth mode. Figure 4.49 shows images of a 1 nm Ni film that have been exposed for RP and OP.

The samples that were subjected to RP yielded very disordered and entangled CNTs with no preferential alignment (Figure 4.50 a) and b)). These images shows that the CNTs forms a three-dimensional networks which tends to corrugate as the tubes increases in length. This is most likely because of a mismatch of the increased CNT network and the supported area. This mismatch causes loss of contact between the SiO_2-Ni catalyst which causes network lift-off and leads to the tip-growth mode. The samples subjected to OP lead to nucleation of CNTs that had a vertically aligned arrangement (Figure 4.50 d) and e)).

These results show that VACNT/CNT growth is able to be obtained in RP and OP. It is widely believed that the catalyst is active in its metallic state only, and if oxidized it requires activation/partly activation by a reducing atmosphere prior to growth. OP can make nanoparticles catalytic active for CNT growth, by reducing treatment with H_2 (dilution gas) or hydrocarbons, or both, before carbon precipitation. The hydrocarbons can be used to reduce the oxidized catalyst nanoparticles, but in a much lower degree than H_2. This is why it is suggested to use a strong reducing agent, such as H_2/NH_3, for activation of these oxidized nanoparticles. Figure 4.51 is a schematic representation of the resulting growth in both of these atmospheres [79, 104].

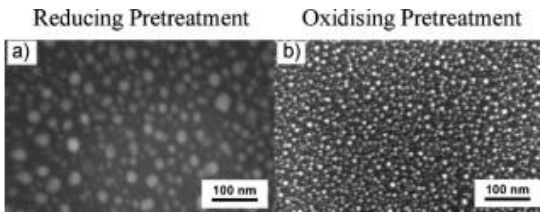

Figure 4.49: SEM images of 1 nm Ni film deposited onto SiO_2 and pretreated for 5 min at 650^0C in atmospheric pressure, under a) reducing b) oxidizing environments [79]

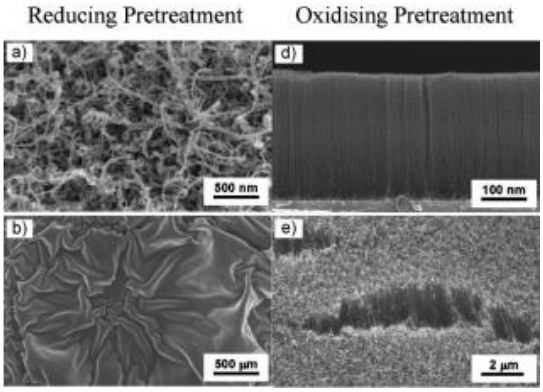

Figure 4.50: High and low magnification top-view SEM images of CNTs grown for 10 min at 650^0C in atmospheric pressure on a 1 nm thin Ni film subjected to a) and b) in RP and d) and e) in OP [79]

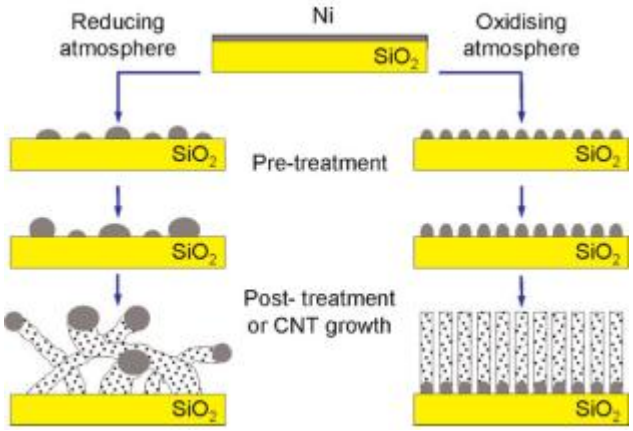

Figure 4.51: Schematic representation of SiO_2 supported Ni restructuring into nanoparticles under RP or OP, and their influence on post-treatment/CNT growth [79]

5 Instruments

5.1 Creating samples

The samples are pieces of a 2" Si (100) 250um thick wafer that are made with the Dynatex DXIII scriber. The Dynatex DXIII is combined scriber and breaker with a diamond tip scriber and an impulse bar breaker [105].

Figure 5.1: The Dynatex DXIII scriber unit [105]

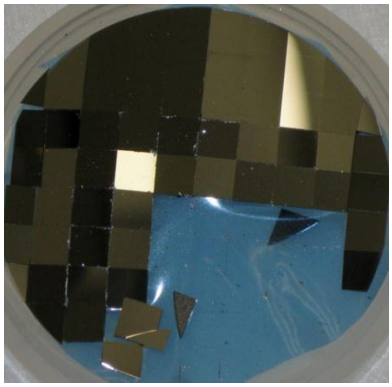

Figure 5.2: Shows a Si wafer after being scribed into several smaller samples by the Dynatex machine

5.1.1 Technical information

Dynatex DXIII scriber unit
Scribe method: Diamond tip **Scribe channel width:** < 5 um **Scribe speed:** Max 75 mm/s **Break method:** Impulse bar **Break rate:** 2 breaks per second

Table 5.1: Technical information of the The Dynatex DXIII scriber unit [105]

5.2 Applying the thermal barrier- and catalyst layer

The thermal barrier layer was deposited with the Pfeiffer Vacuum Classic 500 e-beam evaporator. An e-beam evaporator is used for depositing single or multilayer thinfilms of metal, oxides, magnetic materials and dielectrics. The metal target is placed in a crucible. A high voltage electron beam transforms the target metal into gaseous phase which precipitates into a solid form at the substrate. This process is usually done under high vacuum (≈ $4*10^{-4}$ mbar) and the deposited thickness is measured by a quartz crystal monitor [106].

The Cressington 308R is a combined DC magnetron sputter and thermal evaporator system and is used for deposition of thin films. Thermal evaporation is done by resistive heating of a target material until it evaporates. Sputtering is executed with ionized Ar atoms that bombard the target which leads to ejection of atoms from the surface. These atoms will in turn hit the substrate and coat its surface with a thin film of the target material. The substrate stage is able to rotate during the deposition process which leads to a more uniform deposition [107].

Originally, the idea was to deposit Fe by sputtering instead of evaporation since it is:

- Less time consuming.
- Suggested to give the lowest Ostwald ripening rate (see chapter 4.1.2).
- Deposition at 90^0 is not necessary (which is one of the main benefit of evaporation) since the sample does not contain any features on the surface.

Until receiving the delayed Fe sputter targets it seemed reasonable to start with evaporation of Fe since Fe pellets was in storage and available in the NanoLab. The e-beam was the primary choice for Fe deposition, but since it required careful heating and cooling cycles, the crucibles had a tendency of cracking all the time. This is why the evaporation function of the Cressington 308R became the chosen evaporation technique and was used for all the pretreated samples (chapter 0). The Fe target was received after the pretreatment session was finish. That was why subsequent samples were done by sputtering.

Figure 5.3: The Pfeiffer Vacuum Classic 500 e-beam evaporator [106]

Figure 5.4: Cressington 308R Sputter and Evaporator [107]

5.2.1 Increasing the thickness and the quality of the aluminum oxide layer

The JetFirst 200 RTP furnace has a stainless steel chamber suitable for rapid heating of thin films under controlled atmosphere or vacuum. It is suitable for processing up to 200 mm wafers, as well as powders and non-conductive materials in a temperature range up to 1200°C [108]

Figure 5.5: The JetFirst 200 RTP unit [108]

5.2.2 Technical information

Pfeiffer Vacuum Classic 500 e-beam evaporator
Currently available standard targets: Au, Ti, Pt, SiO_2, MgO, Pd, Ni, Ge, Co, C, Sb, Sn, NiFe, Cr, Cu, Al, Fe, Ag, Ta
Acceleration voltage: 8 kV
Substrate heating: up to 900°C
6 evaporation pockets

Table 5.2: Technical information of the Pfeiffer Vacuum Classic 500 e-beam evaporator [106]

Cressington 308R Sputter and Evaporator
Available targets: Al, Au, Cr, Cu, Fe, Ni, Pt, Pt/Pd, Si, Ti and W
2 Sputter heads (one with water cooling)
2 Thermal evaporation boats (both with water cooling)
Quartz crystal thickness monitor
Ar process gas

Table 5.3: Technical information of the Cressington 308R Sputter and Evaporator [107]

JetFirst 200 RTP unit
Max temperature: 1200°C
Maximum heating range of 100°C/s (50°C/s with SiC susceptor)
1 N_2 purge gas line
2 process gas lines (O_2 1000 sccm and N_2 1000 sccm)
Equipped with 16 6000 W halogen lamps

Table 5.4: Technical information of the JetFirst 200 RTP unit [108]

5.3 Pretreatment and growth

The TP/PP and growth sessions was done in the PlasmaLab System 100 PECVD unit. The PECVD unit offer deposition of thin films at lower temperatures compared to CVD at a pressure around 0.5 - 2 Torr. The PECVD process chamber consists of two electrodes, a gas inlet and an exhaust. It is equipped with two powers supplies, a RF source (13.56 Mhz) and a low frequency source (50 – 460 Khz), which can be applied to the top electrode one at a time or simultaneously. Sequential use of the two sources allows for stress control of deposited films. The sample stage (bottom electrode) is grounded and is able to be heated up to a maximum temperature of 700°C. Gas molecules are introduced in the chamber from a shower head inlet which is ionized by the oscillating electric field and plasma is struck. Electrons are absorbed at the bottom electrode creating a DC voltage of ≈ 10-20V. Ionized gas and radicals react with the substrate and creates a deposition process. Because the reactive and energetic species are a product of collisions in the gas phase the temperature at the substrate is kept at a relatively low value. Thin films deposited with PECVD generally have good uniformity, adhesion, step coverage and low pinhole density [109].

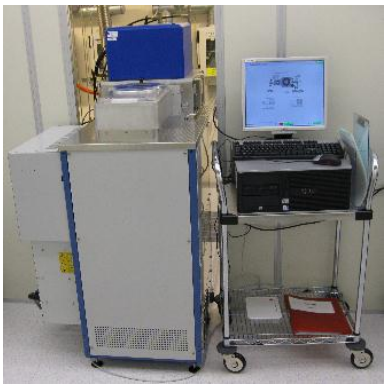

Figure 5.6: The PlasmaLab System 100 PECVD (Oxford Instruments) [109]

5.3.1 Technical information

Plasmalab System 100 PECVD
Process gases: SiH_4 50 sccm, NH_3 50 sccm, N_2O 1000 sccm, N_2 2000 sccm, Ar 2000 sccm, CF_4 500 sccm and CH4 100 sccm, 10% PH3/Ar 50 sccm, 0. 1% B2H6/0.23 % H2/Ar 50 sccm
Plasma source: 13.56 MHz RF source/50-460 KHz LF source
Operating temperature: 20°C to 700°C
Typical applications: SiOx, SiNx, SiOxNy, SiC and amorphous Si deposition

Table 5.5: Technical information of the PlasmaLab System 100 PECVD [109]

5.4 Removing a:C from the Si CNT carrier

The Femto plasma cleaner was used to remove any a:C on the Si carriers that have been deposited during the growth step. Plasma systems offer cleaning and can activate surfaces. Etching and coating is also feasible. Gas in a low pressure chamber is excited by a supply of energy. Oxygen and ambient air are the gases which were used in this unit. It is designed to fit 4" wafers (≈102 mm) in the chamber. As good as all material can be cleaned with plasma. The surface is cleaned because of physically ion bombardment and chemical cleaning by ionized gas. UV radiation helps breaking down long-chain complex carbon compounds. Oxygen plasma creates radical sites on the surface, leaving it hydrophilic [110].

Figure 5.7: The Femto plasma cleaner (Diener Electronics) [110]

5.4.1 Technical information

Femto plasma cleaner
Process gases: O_2 or air (With flow from 0 – 100%) **Chamber size (Width x Height x Depth):** 103x103x285 mm (up to 4" wafers) **Plasma power:** 100 W

Table 5.6: Technical information of the PlasmaLab System 100 PECVD [110]

5.5 Characterization

5.5.1 Hitachi S-5500 S(T)EM and FEI Helios NanoLab DualBeam FIB

For characterization of the samples, the Hitachi S-5500 S(T)EM and the FEI FIB was used. Only the SEM feature of these instruments was used. SEM is an electron microscope that exposes a sample of a high-energy beam. The electrons in the beam interact with the sample and gives useful information about its topography, composition and other properties, such as electrical conductivity. The SEM is equipped with different detectors that can collect secondary electrons (SE), back-scattered electrons (BSE) or x-rays. The SEs contains information about the topography (low energy-electrons) and will usually give images of high quality. The BSE usually have a lower quality images but provides information about the distribution of different elements in the sample (high-energy electrons). The characteristic x-rays are used to identify the composition and measure the abundance of elements in the sample. The SEM is often used in surface analysis [111].

The S(T)EM unit is an in-lens cold field emission electron microscope and is able to achieve a resolution down to 0.4 nm. It also offers the possibility of viewing cross section of samples [112]. The FIB is equipped with an Everhart Thornley Detector (ETD) and a Through-Lens Detector (TLD). In addition it offers different operating modes:

- Field free (for navigating/reviewing at lower magnifications
- Immersion (for ultra-high resolution images)

Both instruments are placed in an electromagnetic field-free rom on vibrational isolated ground [113].

Figure 5.8: The Hitachi S-5500 Scanning Transmission Electron Microscopy – S(T)EM [112]

Figure 5.9: The FEI Helios DualBeam Focused Ion Beam microscopy – FIB [113]

5.5.2 JEOL JEM-2010 TEM

TEM is also an electron microscope, but where a high-voltage beam is transmitted through a very thin sample where it interacts with the sample as it passes through. The beam is moving through a projector lens (objective lens) and is transmitted onto a fluorescent screen where the final image is

observed. A view of the interior of the object can be observed since the beam passes through the sample. TEM is often used in sections analysis [114]. The JEOL JEM-2010 is an analytical TEM with a LaB6 electronic gun that can be operated between 80 – 200 kV and is able to achieve a resolution as low as 0.19 nm, point to point, if equipped with a field emission gun [115]. The TEM used for this experiment had a thermal emission gun and was therefore restricted to a resolution of 0.23 nm

Figure 5.10: The JEOL JEM-2010 TEM [115]

5.5.3 Vecco Dektak 150 profilometer

A profilometer measures the surface profiles in order to determine the roughness of the surface. The Dektak 150 is a contact stylus profilometer. The measurements are done by a tip stylus that runs over the sample's surface and record the height difference [116].

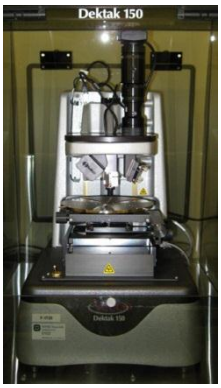

Figure 5.11: The Vecco Dektak 150 profilometer [116]

5.5.4 Technical information

Hitachi S-5500 S(T)EM
Detectors for: Secondary and low- and high-angle back scattered electrons, bright-field and dark-field transmission measurements and Bruker XFlash EDX Detector **Attainable resolution:** 0.4 nm **Acceleration Voltage:** 0.5 – 30 kV (in 0.1 kV steps) **Maximum beam current:** 20 uA **Maximum sample tilting:** 40^0

Table 5.7: Technical information of the Hitachi S-5500 S(T)EM [112]

FEI Helios NanoLab DualBeam FIB
Detectors for: Secondary and back scattered electrons, EDAX EDX Detector **Attainable resolution (SEM):** 1.2 nm **Acceleration Voltage (SEM and FIB):** 0.5 – 30 kV **Maximum sample tilting:** 52^0

Table 5.8: Technical information of the FEI Helios NanoLab DualBeam FIB [113]

JEOL JEM-2010 TEM
Acceleration voltage: 80 – 200 kV **Attainable resolution:** 0.23 nm (thermal emission gun) **Electron probe size:** Down to 0.5 nm **Maximum sample tilting:** 10^0

Table 5.9: Technical information of the JEOL JEM-2010 TEM [115]

Vecco Dektak 150 profilometer
Scan length range: 55 mm **Vertical range:** 524 um **Vertical resolution:** 1 Å maximum (at 6.55 um range) 12.5 um diamond tip stylus

Table 5.10: Technical information of the Vecco Dektak 150 profilometer [116]

6 Experiment

6.1 Cleaning procedures of the Si samples

All the samples used during this experiment were cleaned by the following procedure (Table 6.1):

Cleaning procedure for the samples
1. Immersed in acetone for 15 minutes
2. Immersed in ethanol for 15 minutes
3. Rinsing in de-ionized water (DI water)
4. Dried with N_2 gun
5. Baking at hotplate (180^0C) for 1-2 minutes (dehydration)

Table 6.1: The cleaning procedure that was used for all the samples in this experiment

6.2 Preparation of samples

The samples were made from 2" Si wafers, as earlier mentioned, with the Dynatex DXlll unit. The parameter settings presented in Table 6.2 was found to be correct for the automatic scribing and breaking process. The chosen samples size was 5x5 mm since it was equal to the substrate holder that was used for the S(T)EM. However, the chosen size became an issue during the project during the imaging session as it became obvious that the best images of the CNTs was achieved by capturing the sample's edge, rather than in the center as first predicted. In addition, the height of these samples made restriction to the maximum allowed acceleration voltage (8 kV) which resulted in poor images. An ideal height of 3.5 mm was found to be optimal as no restriction occurred for this height.

Another valuable experience was achieved as well. It was noticed that the small amounts of Al and Fe that was deposited on the sample's edges during sputtering, made it difficult to get good images during imaging of the samples with non-VACNTs or VACNTs with limited growth, as the CNTs on the edge blocked the line of sight.

Unfortunately, both of these experiences occurred after sample E166 was finished, which mean that many samples had already been processed in the PECVD. As there was no time left for re-processing all the samples, the best solution was found to load all of them into the Dynatex lll and manually (interactive mode) scribe and break them. This would hopefully give the possibility of lowering the sample's height and create a fractured line along the sample without CNT growth that would be the new edge. This is most probably the reason why some of the VACNTs in the cross section images are bent. The decision of doing it manually was because the CNTs could be experience intensive damage for the automatic breaker mode as a bar is lowered to the sample's surface during the breaking sequence. The manual session was done by scribing 5 times along the same track and breaking along this line with two tweezers.

The subsequent samples after E166 was therefore done with a new preparation procedure that solved both of these issues and is described below:

1. The size of the samples was kept at 5x5 mm.
2. Just prior to processing samples in the PECVD (after Fe sputtering) one of the edges was sliced off with the Dynatex lll unit. Automatic scribing and breaking mode was used, as the breaker bar was suspected to do minimal damage to the deposited layers on the surface. The process is illustrated in Figure 6.1 - Figure 6.2. Scribing and breaking settings equal to Table 6.2 was used.

General parameters:	Scribe parameters:	Break parameters:
Mode: Scribe and Break **Wafer diameter:** 60 mm **Thickness:** 250 um **Step size Y:** 5 mm **Step Size X:** 5 mm **Indexing accuracy:** 1 um	**Method:** Continuous **Scribe extension:** 76 um **Scribe force:** 1600 cnts **Scribe angle:** 36^0 **Scribe speed:** 20 mm/s **Approach speed:** 12 mm/s **Set Y=X**	**Method:** Anvil **Pressure:** 60 kPa **Anvil height:** 0.41 mm **Anvil gap:** 0.35 mm **Dwell time:** 0.1 seconds **Cycle time:** 0.2 seconds

Table 6.2: The scribe and break parameters for the Dynatex DXIII

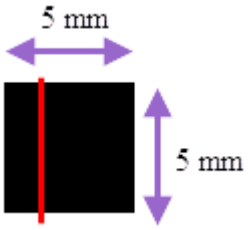

Figure 6.1: A 5x5 mm sample (in black). The red line is the scribing line

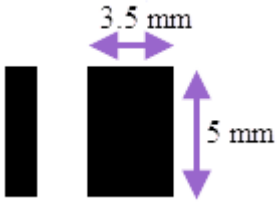

Figure 6.2: After scribing away 1.5 mm on one of the edges, the final size becomes 3.5x5 mm.

6.3 Deposition of barrier/catalyst layers

6.3.1 Pfeiffer vacuum classic 500 e-beam evaporator

Al was deposited on the pretreated samples by the e-beam evaporator as the crucible stayed intact, and that it was possible to deposit aluminum oxide since it had the opportunity of having oxygen flow in the chamber. During the deposition process the oxygen flow was adjusted until reaching a chamber vacuum pressure of ≈ 10^{-4} mbar. As mentioned earlier, deposition of Fe with the e-beam was unsuccessful since the crucible had a tendency to crack all the time. Since the Cressington 308R was able to deposit both Al and Fe, the e-beam evaporator was used for the pretreated samples only.

6.3.2 Cressington 308R sputter and evaporator

Deposition and post measurement of the deposited thicknesses in the layers by the Cressington 308R revealed that the tooling factor (TF) that was given by the manufacturer was wrong. Several deposition and measurement trials were done to get a more precious TF. This session was done by:

1. Mounting one line of tape across the Si sample prior to deposition (Figure 6.3).
2. Sputtering of Al and Fe.
3. Remove the tape after deposition (Figure 6.4).
4. Measuring the depth of the valley that was created by the tape with the profilometer.

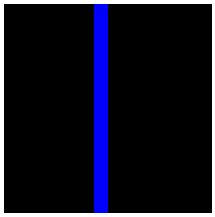

Figure 6.3: The sample (in black) with a line of tape (in blue) across the sample

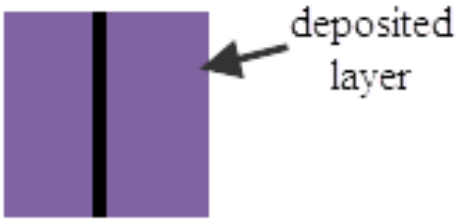

Figure 6.4: The next step is to remove the tape. The tape creates a valley into the deposited layer on the sample

The chosen deposited thickness during calibration of the TF factor was 30 nm. The TF from the manufacture of 1.66 for evaporation was found to be correct, while TF of 2 for sputtering was way of the correct value. A new TF of 6.0 was found to be more accurate. The measurements with the profilometer on the 30nm thick Al and Fe samples can be found in Figure 6.5 - Figure 6.8 where a TF of 6 have been used. The red and green bars are measurement bars which take the average height over the marked distance. Measurements have been done to both sides of the valley. The measured values can be found in Table 6.4. The scan parameters that were used for these measurements are provided in Table 6.3.

Scan parameters for the Vecco Dektak 150 profilometer
Scan type: Standard scan
Stylus: Radius of 12.5 um
Scan length: 1000-1500 um
Scan duration: 90 seconds
Resolution: 0.056 um/sample
Measurement range: 6.5 um
Profile: Hills and Valleys

Table 6.3: The scan parameters for the Deltak 150 profilometer

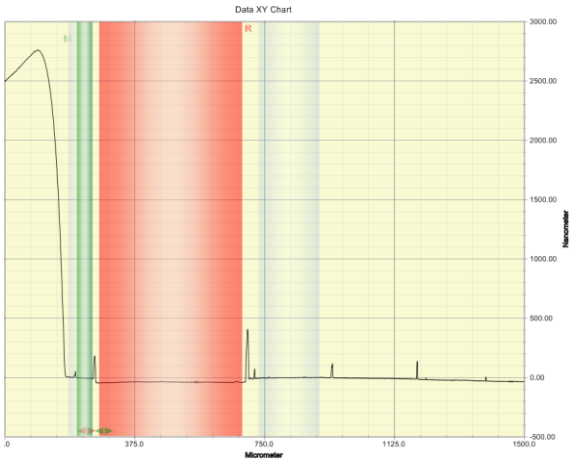

Figure 6.5: Measurements with the profilometer on a 30 nm thick Al film, where the green bar is placed on the left side of the valley

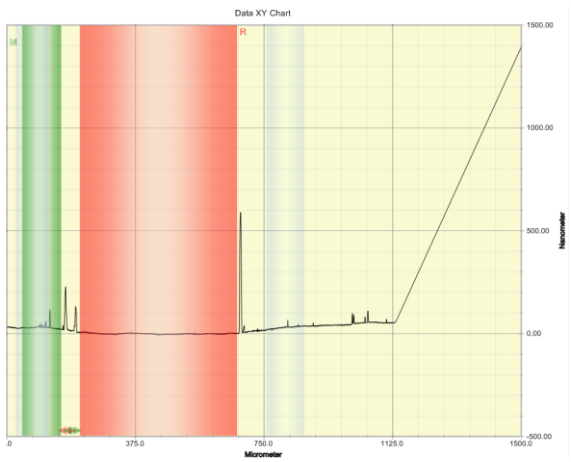

Figure 6.6: Measurements with the profilometer on a 30 nm thick Fe film, where the green bar is placed on the left side of the valley

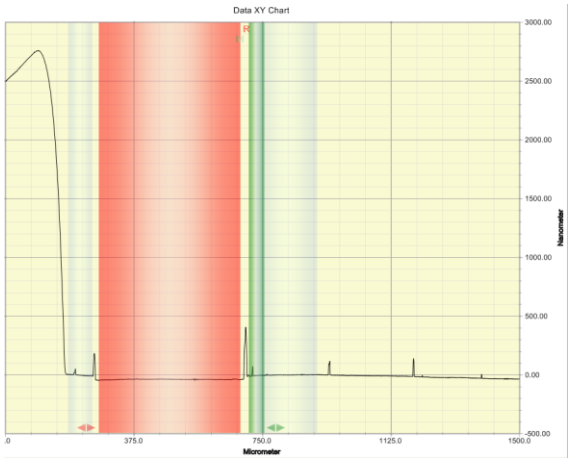

Figure 6.7: Measurements with the profilometer on a 30 nm thick Al film, where the green bar is placed on the right side of the valley

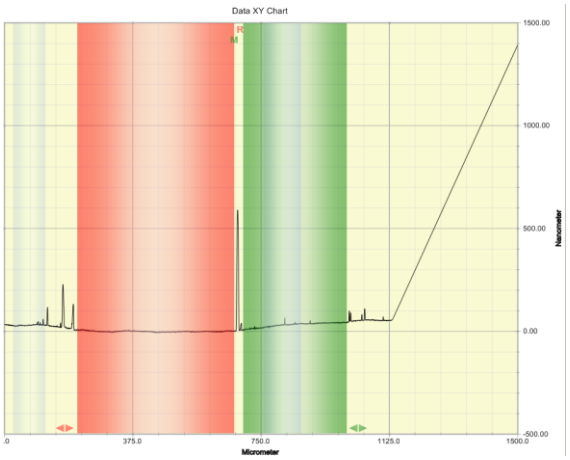

Figure 6.8: Measurements with the profilometer on a 30 nm thick Fe film, where the green bar is placed on the right side of the valley

	Al		**Fe**	
	Left side of valley	**Right side of valley**	**Left side of valley**	**Right side of valley**
Average measured height	33.25 nm	35.81 nm	30.88 nm	31.63 nm
Average height of both sides	34.53 nm		31.26 nm	
Deviance from target thickness	15%		4%	

Table 6.4: Measured thicknesses for calibration of the TF

During the evaporation session with the Cressington 308R, the chamber was firstly pumped to a vacuum pressure 10^{-5} mbar, as high vacuum pressure is favorable since it lowers the melting point of the metal [117] and since higher vacuum minimizes the amount of any remaining oxygen/other gases. Then the current was increased stepwise to evaporate Fe.

For the sputtering session, the chamber was pumped to a little lower vacuum, simply because it was too time demanding. When the desired vacuum was reached, flow of Ar into the chamber was activated as it helped igniting the plasma. The Ar flow was adjusted by turning the knob on the back of the Cressington 308R unit. After reaching the desired leak pressure the plasma was ignited with a current of 80 milliampere (mA) while keeping the shutter above the targeted for 1 - 2 minutes to remove any oxidized layer that could be present. Then the current was adjusted to 70 mA and the shutter was removed to allow deposition to begin.

Not all samples were deposited with an Al barrier layer since comparison of the CNT growth condition were going to be investigated. The parameters that were used for the sputtering process can be found in Table 6.5.

Parameter	**Al**	**Fe**
Vacuum pressure [mbar]	≈ $5*10^{-5}$	≈ $5*10^{-5}$
Leak pressure [mbar]	≈ 0.01	≈ 0.01
Thickness [nm]	30	1, 3, 6 and 10
Current [mA]	70	70
Deposition rate [Å/s]	≈ 0.2	≈ 0.9

Table 6.5: Parameters used for deposition of Al and Fe during sputtering

6.3.3 Increasing the thickness and the quality of the aluminum oxide layer

An oxide layer was already formed on the Al sputtered samples when they were taken out of the sputter chamber and came in contact with air. The RTP recipe can be found in Table 6.6. The reason for running a rapid thermal processing (RTP) unit was to:

- Enhance the thickness of the oxide layer.
- Since the stoichiometry of the aluminum oxide after sputtering was unknown, running of the RTP process would promote formation of the targeted oxide, which was Al_2O_3.

Process gas: O_2 500sccm **Chamber temperature:** 500^{0}C [118, 119] **Duration:** 30 minutes

Table 6.6: Settings used for the RTP process

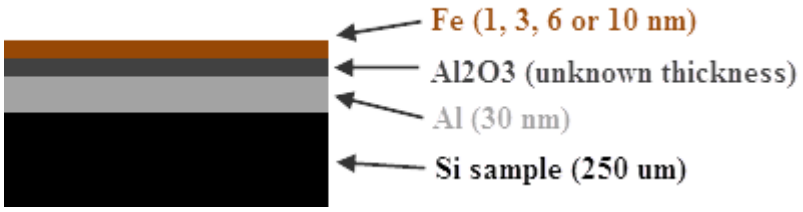

Figure 6.9: Illustration of deposited layers for most samples. Some have been grown without the Al and Al_2O_3 layer

6.4 Characterization

6.4.1 The FIB and the S(T)EM

Even though the S(T)EM was supposed to be used for characterization of all samples, the FIB was used for the pretreated ones since it was difficult to get good images of the nanoparticles on the samples with the S(T)EM. This may have to do that the pretreated samples was done in the early phase of the project before a lot of SEM experience was gained. During this session the through-Lens Detector (TLD) and immersion operating mode (high magnification mode) was used. The settings used during the imaging session of the two microscopes are presented in Table 6.7.

FEI Helios NanoLab DualBeam FIB	Hitachi S-5500 S(T)EM
Acceleration voltage: 5 kV **Current:** 7 uA **WD:** ≈ 3 mm	**Acceleration voltage:** 10 kV (30^0 tilting) and 20 kV (Cross section) **Current:** 7 uA (30^0 tilting) and 15 uA (Cross section) **WD:** 0.1 – 1.5 mm

Table 6.7: Settings used for imaging of the samples with the FIB and the S(T)EM

Some images are blurry during imaging by the S(T)EM. This is due to drifting that occurred from time to time and is especially noticed for images at high resolution. The drifting is most likely because the sample stage moves or because of instabilities in the beam.

6.4.2 JEOL JEM-2010 TEM

The TEM analysis was chosen to be done for 7 samples: E47, E87, E115 (with and without barrier layer), E119, E143 and E159. They were examined to determine the following:

- CNTs or CNFs.
- SWCNTs or MWCNTs.
- Crystalline or amorphous structure
- Comparison of the diameter with the one from the SEM analysis.

The CNTs of the grown samples needed to be deposited on “holy grids” before conducting any TEM analysis. “Commercial holy grids” can be purchased, but as they are very expensive the decision of making them ourselves was done. It should however be noted, that commercial holy grids contains voids that offers much higher quality images compared to the self-made ones that is described below. The difference in quality of the TEM images can be seen in chapter 0, since one “commercial holy grid” was obtained. Holy grids are made from Cu substrates with a 300 mesh grid pattern that are bought from a manufacturer. Deposition of a polymer film was done to decrease the inner-distance of the grid, as well as to promote a sticky surface. When the polymer layer had dried, carbon coating needed to be deposited, so that any charge up effects by the polymer film was avoided. Then CNTs was ready to be transferred onto the grids. The process of making these grids and how the CNTs was deposited onto them is described below.

6.4.3 Making the Holy Cu-C grids for TEM analysis

It is important to know that it is the darkest side of the circular Cu substrate that hits the TEM beam first and should be the one with the deposited polymer film. The polymer was nitrocellulose. The steps needed to make "holy grids" are provided in Table 6.8.

1. Clean the Cu substrates in acetone for a couple of minutes in an ultrasonic bath and let them dry.
2. Fill up a container with water (all the way up to the top) and wait for the water to stabilize (there should be no movement in the water).
3. Gently deposit a few drops of the polymer with a pipette onto the water surface. Be careful not to deposit to much as this will cause a thick film. The container that was used had a height of 100 mm and a diameter of 120 mm. 5 droplets of polymer was deposited.
4. Wait for 5 minutes so that the polymer droplets are allowed to create a film on the water's surface.
5. The Cu substrates should in this step be placed onto the polymer film. Remember to keep the dark side onto the film. Place them on areas which show a continuous film only (keep away from wrinkled areas).
6. Wait for 5 more minutes. Then let the dry paper immerse in the polymer film. If the container that was used was large, decrease the area of the polymer film to an area that is a little larger than the dry paper (2 tweezers was used), as this will cause easier handling.
7. Lift the dry paper with a tweezers (grip the paper and the polymer film) and move it in a box for storage (to protect the film from dust particles). Let it dry for 2 - 3 days.
8. Coat the Cu substrates with carbon to minimize the charging effect during analysis (polymer films is a bad conductor). This session was done with a carbon sputter coater at 4.2 V where deposition was done in two rounds. Each round lasted for 6 seconds and the resulting thickness (from the thickness measuring unit) was ≈ 15 nm.
9. The Cu substrate is now a "holy grid" and is ready to be used.

Table 6.8: Recipe that was used for making the holy grids for TEM analysis

Then CNT had to be deposited onto the "holy grids". First, the CNT growth samples were immersed in a bottle with ethanol. Secondly, it was placed in an ultrasonic bath to disperse the CNTs (10-30 minutes was used). An indication of the required time was when the sample's surface became glossy, or when particles were seen in the bottle. For some of the samples, ultrasonic bath alone did not successfully achieved in separating the CNTs from the sample, which was why scraping them off with a scalpel became necessary. The final step was to use a pipette for deposition of droplets onto the "holy grid" from the solution of the bottle. A couple of minutes after deposition were necessary to wait, as to make sure that all the ethanol had evaporated.

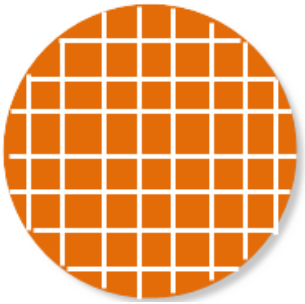

Figure 6.10: Illustration of the Cu substrate with the grid pattern. The polymer film is deposited to decrease the grid inner-distance. It is also sticky so that is it easy for particles to adhere to the grid

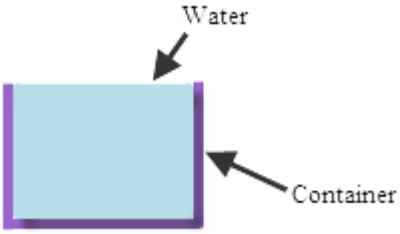

Figure 6.11: It is important to fill up water to the top of the container so that water are able to escape when depositing droplets of polymer

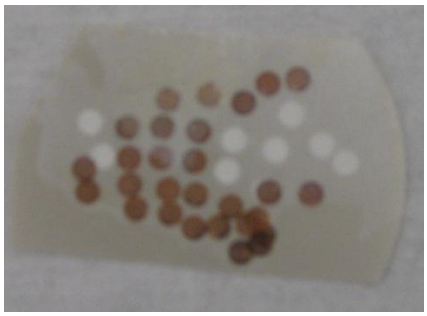

Figure 6.12: Image of self-made holy grids which consist of Cu substrates that are coated with a polymer and carbon film

6.4.4 Plasma cleaner

A 2" Si wafers (thickness of 950 um) was used as carrier for loading the samples into the PECVD chamber. It needed cleaning between every second batch, because too much deposited a:C would make it slippery which could cause the samples to slip of the wafer during processing. The cleaning was done with the plasma cleaner and the settings that were used are provided in Table 6.9.

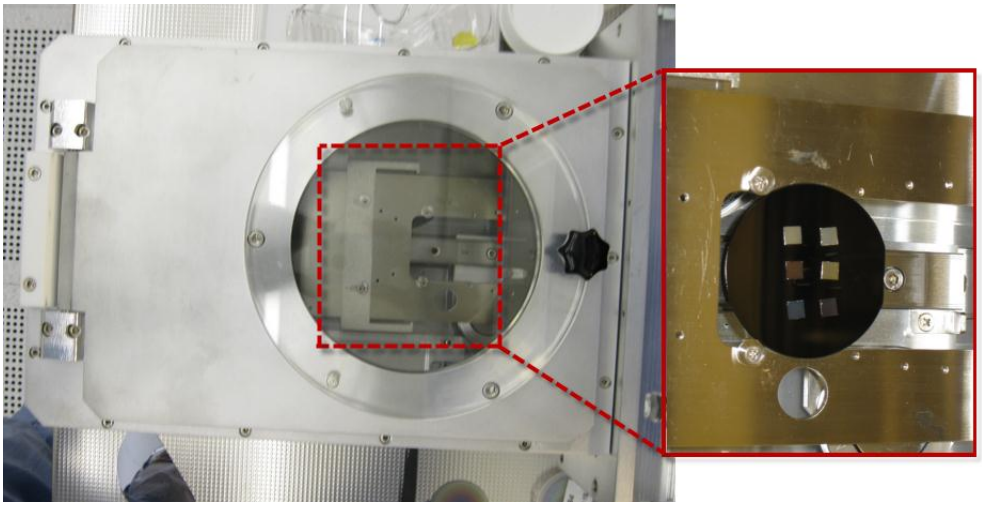

Figure 6.13: Image of the load-dock of the PECVD and 6 samples which are supported on a Si wafer during processing. The black layer on the Si wafer is a:C and/or other carbonaceous particles which needs to be removed since they make the wafer slippery

Process gas: O_2 100sccm
Plasma power: 100W
Duration: 30 minutes

Table 6.9: Settings used for cleaning Si wafers in the plasma cleaner

6.5 Pretreated samples

For the start of this project several CNT growth recipes was executed, which was based on earlier successfully growth experiments [56, 120, 121, 122, 123, 124, 125, 126, 127, 128] [129, 130, 131, 132, 133, 134]. Since the PECVD that was used in the NanoLab distinguished from what were used in these experiments it led to the following challenges:

- Our unit supplied CH_4/NH_3, while earlier successfully CNT growth experiments used combinations of CH_4/H_2 or C_2H_2/NH_3.
- The unit had a temperature limit of 700^0C while earlier experiments used higher temperatures.
- The maximum flow rate that was offered by this unit was much lower than those that were used in the other experiments.

Based on the challenges above, trials by mixing parameters from these experiments were conducted. Unfortunately, none of these trials successfully yielded CNT growth. That was why a study of the nanoparticles prior to the growth step was executed, since it became necessary to find the favorable parameters that would promote CNT growth. One and one sample was processed in the PECVD at a time to see how different parameters affected the nanoparticles during pretreatment. The parameters that could be varied in this session were the following ones:

- Thickness of barrier layer
- Thickness of catalyst layer
- TP or PP treatment
- Temperature (table temperature)
- Time
- Power
- Pressure
- Gas flow

As stated earlier, the pretreatment is an important step since the resulting CNTs is based on the formed nanoparticles that are made during this process. The processing parameters that were used for the samples are listed in Table 6.10.

The reason why some of the particles are bright and that someone is dark is since the particles are ferromagnetic (Fe) which would influence the electromagnetic field in a way so that the contrasts sometimes get reversed.

6.5.1 Parameters for the pretreated samples

Pre-treatment of samples

t	=	Thickness	Max limit NH3	50	sccm
PP	=	Plasma pre-treatment	Max limit CH4	100	sccm
TP	=	Thermal pre-treatment	Max limit Ar	2000	sccm

ID	tOxide[nm]	tCatalyst[nm]	Treatment	Table temp[°C]	Chill temp[°C]	Time[s]	Power[W]	Pressure[mTorr]	CH4[sccm]	NH3[sccm]	Ar[sccm]	N2[sccm]	Comments
SiAlFe-PP1	50	5	PP	700	20	60	50	500		50			Variation of time
SiAlFe-PP2	50	5	PP	700	20	180	50	500		50			
SiAlFe-PP3	50	5	PP	700	20	300	50	500		50			
SiAlFe-PP4	50	5	PP	700	20	600	50	500		50			
SiAlFe-PP5	50	5	PP	700	20	180	20	500		50			Variation of power
SiAlFe-PP6	50	5	PP	700	20	180	100	500		50			
SiAlFe-PP7	50	5	PP	700	20	180	200	500		50			
SiAlFe-PP8	50	5	PP	700	20	180	300	500		50			
SiAlFe-PP9	50	5	PP	700	20	180	50	500		40			Variation of gas flow
SiAlFe-PP10	50	5	PP	700	20	180	50	500		30			
SiAlFe-PP11	50	5	PP	700	20	180	50	500		20			
SiAlFe-PP12	50	5	PP	700	20	180	50	500		10			
SiAlFe-PP13	50	5	PP	700	20	180	50	50		50			Variation of pressure
SiAlFe-PP14	50	5	PP	700	20	180	50	200		50			PP13&PP14; Strike pressure: 0.4Torr, Ramp rate: 10
SiAlFe-PP15	50	5	PP	700	20	180	50	1000		50			
SiAlFe-PP16	50	5	PP	700	20	180	50	1500		50			
SiAlFe-PP17	50	2	PP	700	20	180	50	500		50			Variation of tCatalyst
SiAlFe-PP18	50	8	PP	700	20	180	50	500		50			
SiAlFe-PP19	50	15	PP	700	20	180	50	500		50			
SiAlFe-PP20	50	30	PP	700	20	180	50	500		50			
SiAlFe-PP21	50	5	PP	100	20	180	50	500		50			Variation of temperature
SiAlFe-PP22	50	5	PP	300	20	180	50	500		50			
SiAlFe-PP23	50	5	PP	450	20	180	50	500		50			
SiAlFe-PP24	50	5	PP	600	20	180	50	500		50			
SiAlFe-TP1	50	5	TP	500	20	600	0	500		50			TP, not PP
SiAlFe-TP2	50	5	TP	700	20	600	0	500		50			
SiAlFe-TP3	50	5	TP	500	20	900	0	500		50			
SiAlFe-TP4	50	5	TP	700	20	900	0	500		50			

Table 6.10: Parameters of the pretreated samples. Higher quality can be found in Appendix B

6.5.2 The effect of variation in time

SiAlFe-PP1

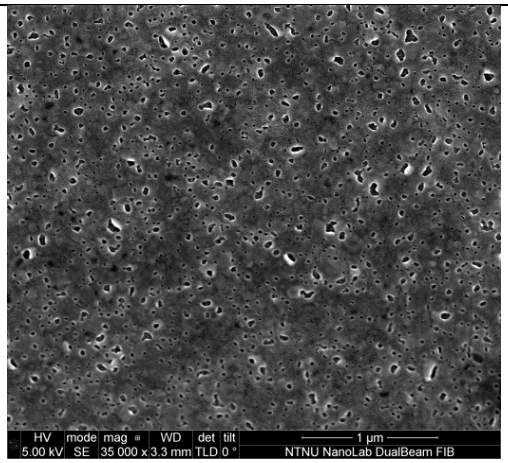

Figure 6.14: SiAlFe-PP1 at 35k magnification

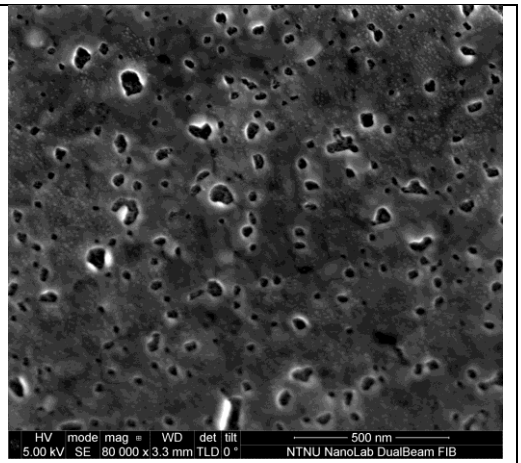

Figure 6.15: SiAlFe-PP1 at 80k magnification

SiAlFe-PP2	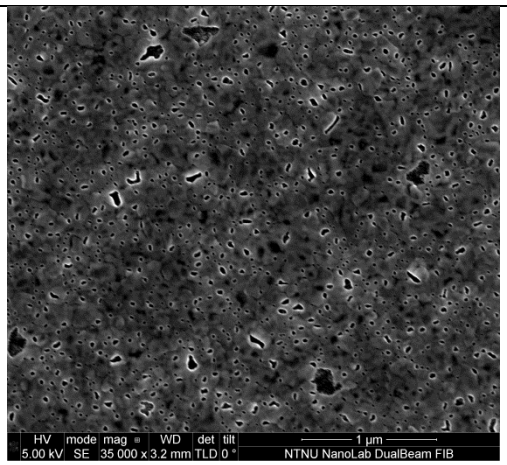 Figure 6.16: SiAlFe-PP2 at 35k magnification	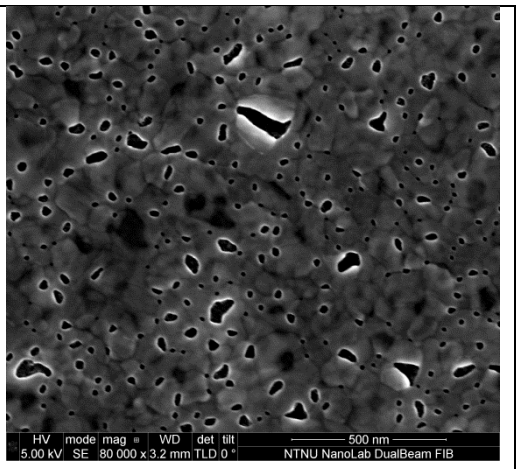 Figure 6.17: SiAlFe-PP2 at 80k magnification
SiAlFe-PP3	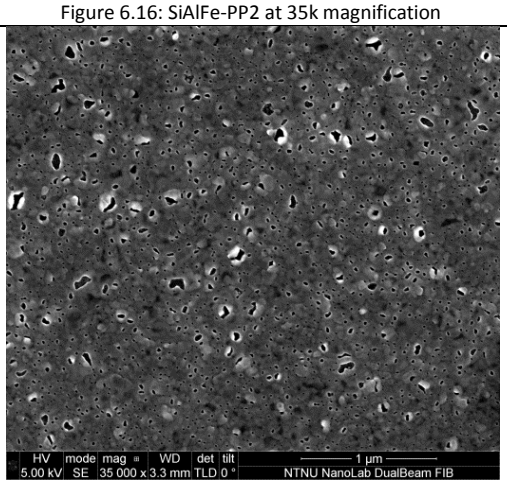 Figure 6.18: SiAlFe-PP3 at 35k magnification	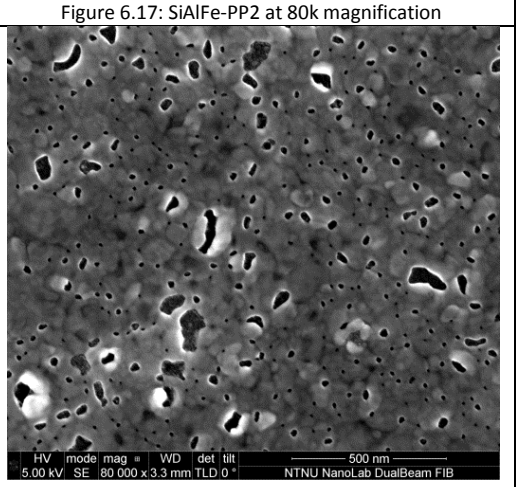 Figure 6.19: SiAlFe-PP3 at 80k magnification
SiAlFe-PP4	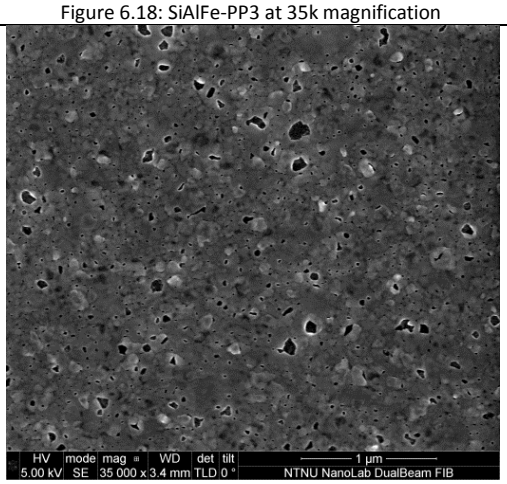 Figure 6.20: SiAlFe-PP4 at 35k magnification	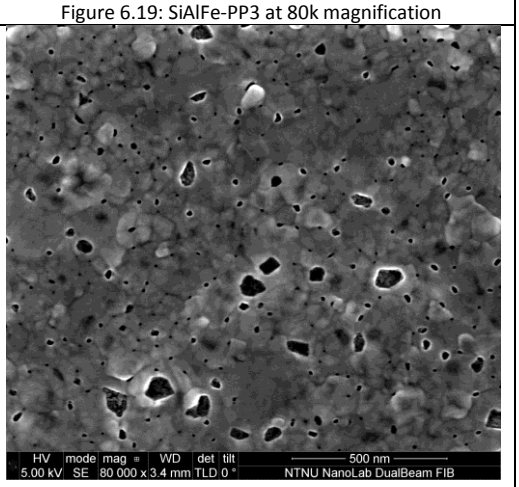 Figure 6.21: SiAlFe-PP4 at 80k magnification

Observation of the images concludes that the size of the nanoparticles decreases with increasing pretreatment time, but the highest density of small particles seems to be found for sample PP2 or PP3. When the pretreatment time is further increased, as in PP4, the Fe nanoparticles slowly get depleted off the surface because of diffusion into the barrier layer. However, it is not clearly observed that this diffusion leads to larger nanoparticles or that uniformity decrease, when comparing with PP1 – PP3.

Sample name	Size of nanoparticles [nm]	Treatment time [s]
PP1	≈ 23 – 70	60 (1 minute)
PP2	≈ 12 – 80	180 (3 minutes)
PP3	≈ 12 – 80	300 (5 minutes)
PP4	≈ 12 – 80	600 (10 minutes)

6.5.3 The effect of variation in power

SiAlFe-PP5

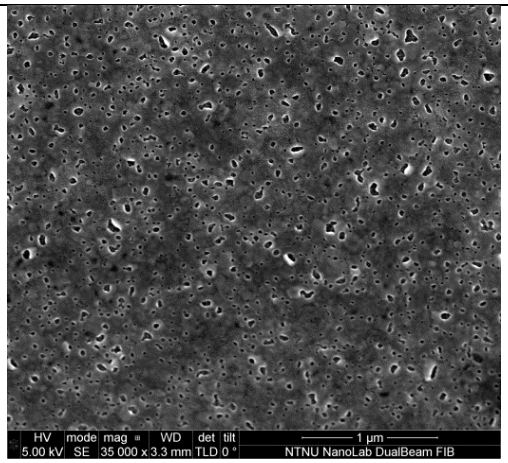

Figure 6.22: SiAlFe-PP5 at 35k magnification

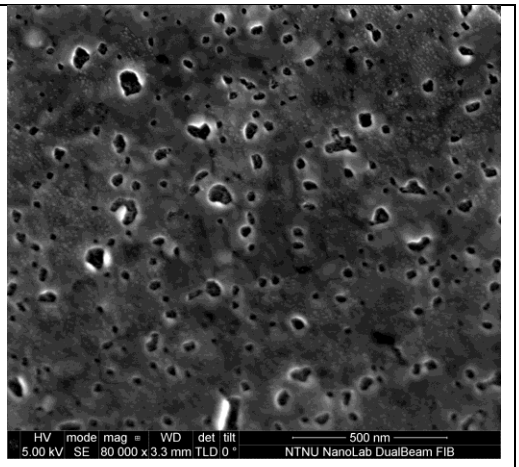

Figure 6.23: SiAlFe-PP5 at 80k magnification

SiAlFe-PP2

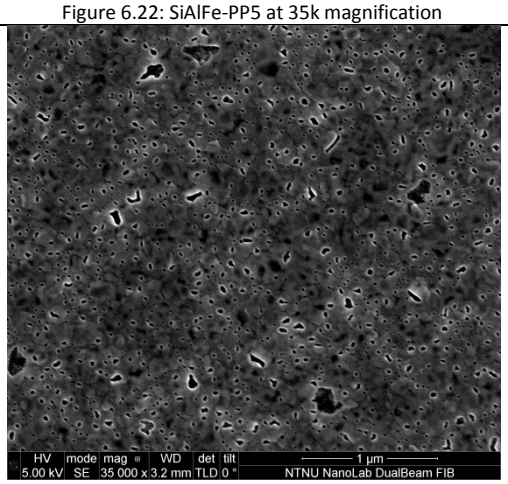

Figure 6.24: SiAlFe-PP2 at 35k magnification

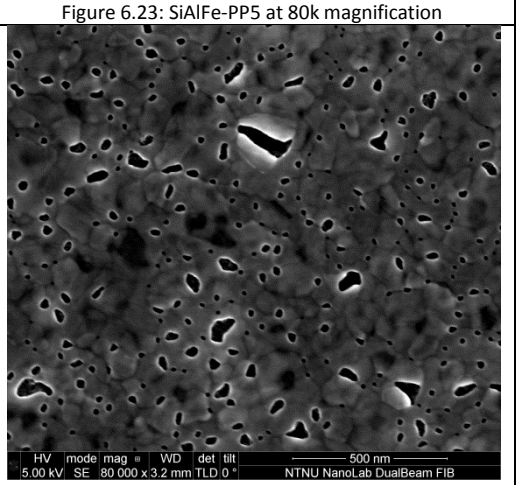

Figure 6.25: SiAlFe-PP2 at 80k magnification

SiAlFe-PP6	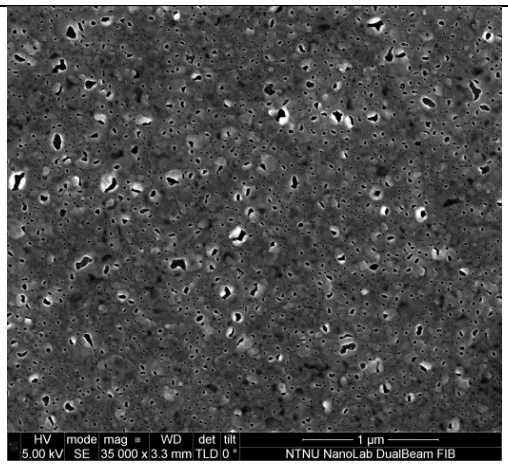 Figure 6.26: SiAlFe-PP6 at 35k magnification	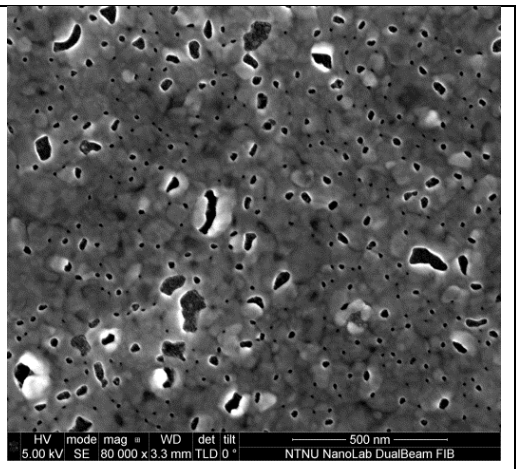 Figure 6.27: SiAlFe-PP6 at 80k magnification
SiAlFe-PP7	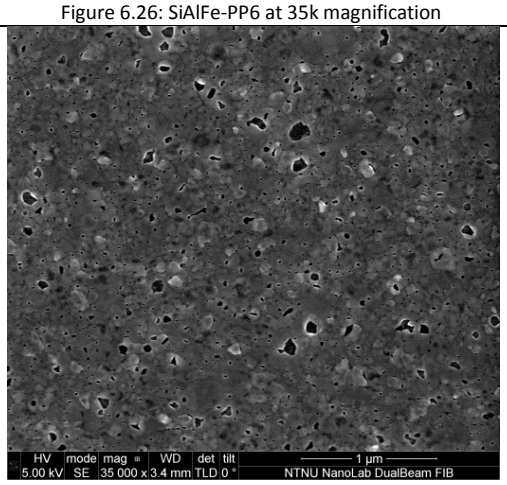 Figure 6.28: SiAlFe-PP7 at 35k magnification	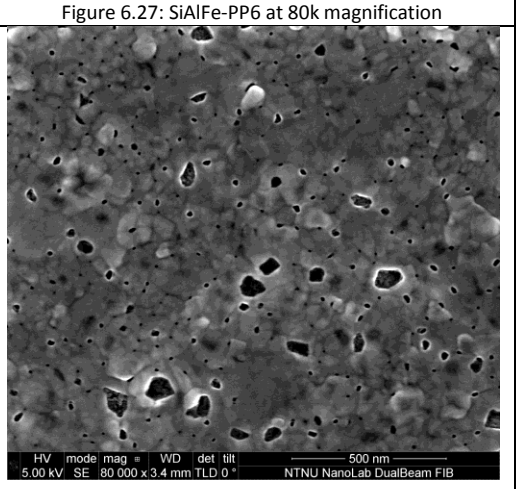 Figure 6.29: SiAlFe-PP7 at 80k magnification
SiAlFe-PP8	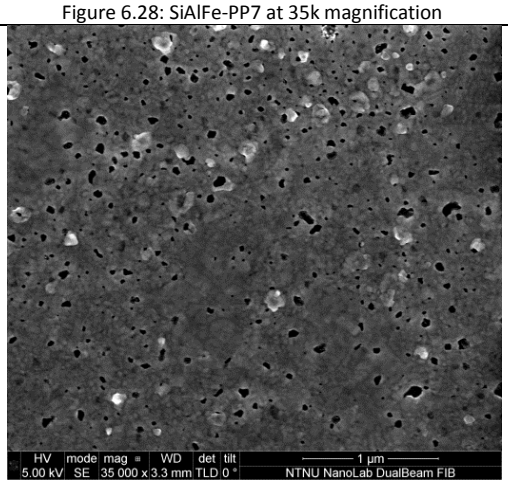 Figure 6.30: SiAlFe-PP8 at 35k magnification	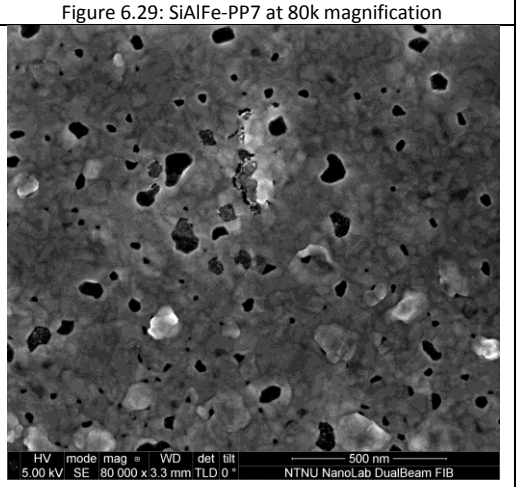 Figure 6.31: SiAlFe-PP8 at 80k magnification

The smallest nanoparticles can be spotted in PP2, PP6 and PP7, but that they increase in PP8. This confirm some of the theory which suggests that increasing plasma powers leads to smaller sized nanoparticles, but only up to a certain power since additional power increases the size, as defects are introduced. The best samples seem to be PP6 since it holds the highest density of small particles compared to sample PP2 and PP7.

Sample name	Size of nanoparticles [nm]	Plasma power [W]
PP5	≈ 23 – 80	20
PP2	≈ 12 – 80	50
PP6	≈ 12 – 100	100
PP7	≈ 12 – 80	200
PP8	≈ 23 – 80	300

6.5.4 The effect of variation in gas flow

SiAlFe-PP2

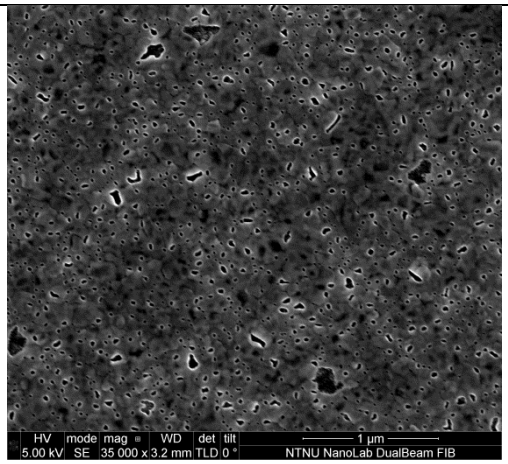

Figure 6.32: SiAlFe-PP2 at 35k magnification

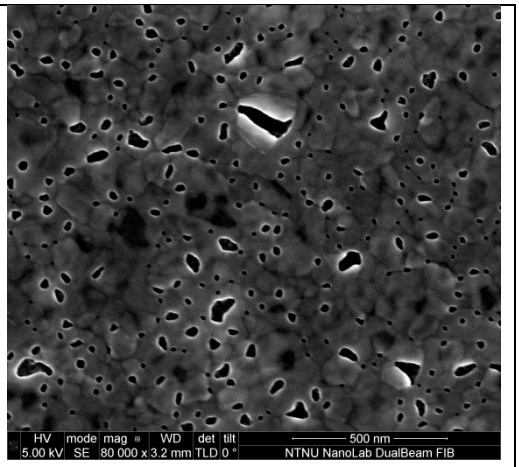

Figure 6.33: SiAlFe-PP2 at 80k magnification

SiAlFe-PP9

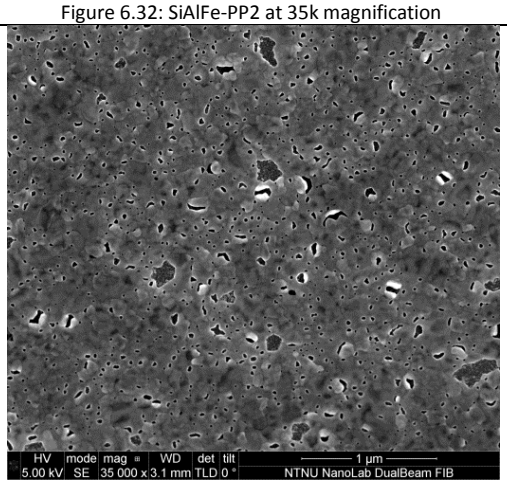

Figure 6.34: SiAlFe-PP9 at 35k magnification

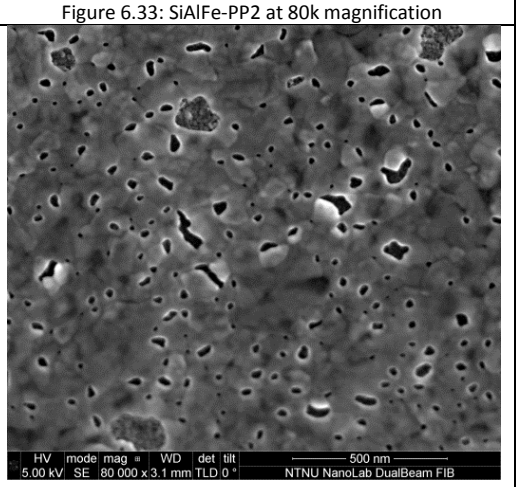

Figure 6.35: SiAlFe-PP9 at 80k magnification

SiAlFe-PP10	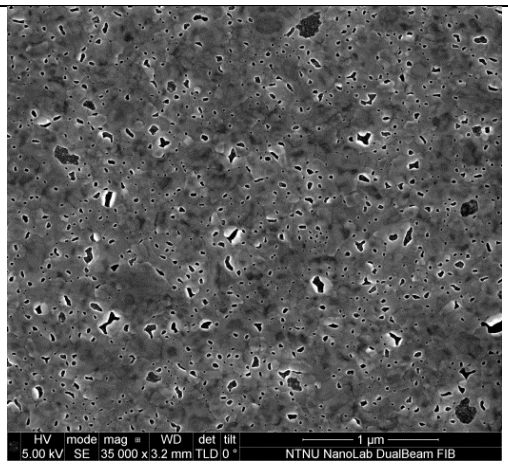 Figure 6.36: SiAlFe-PP10 at 35k magnification	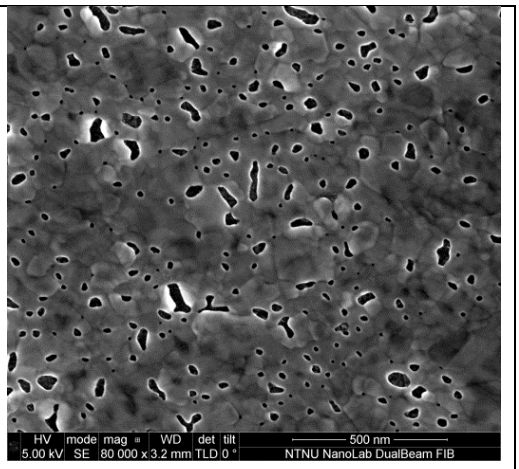 Figure 6.37: SiAlFe-PP10 at 80k magnification
SiAlFe-PP11	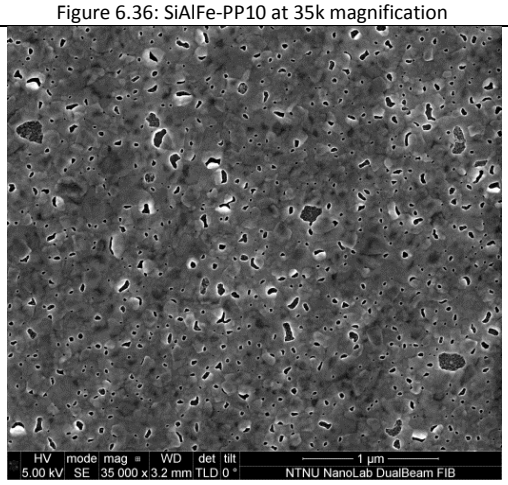 Figure 6.38: SiAlFe-PP11 at 35k magnification	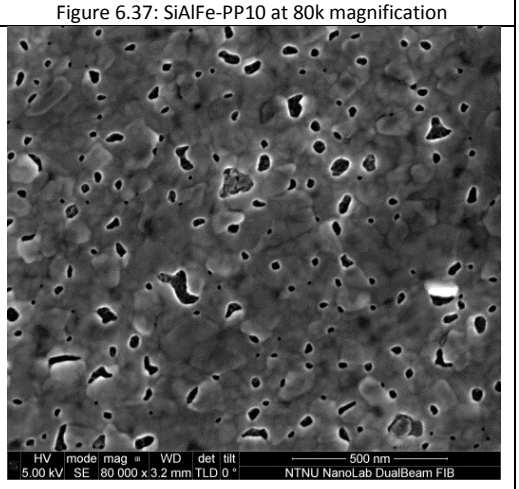 Figure 6.39: SiAlFe-PP11 at 80k magnification
SiAlFe-PP12	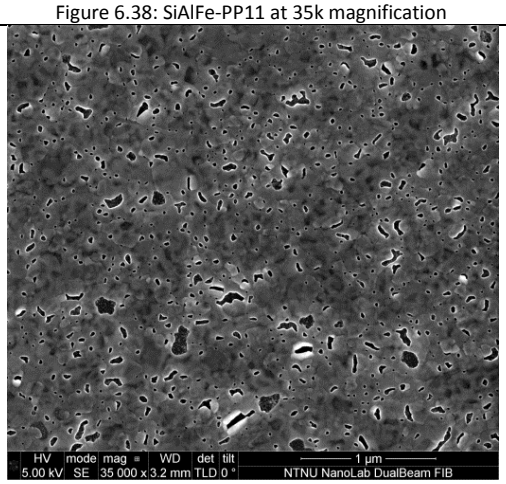 Figure 6.40: SiAlFe-PP12 at 35k magnification	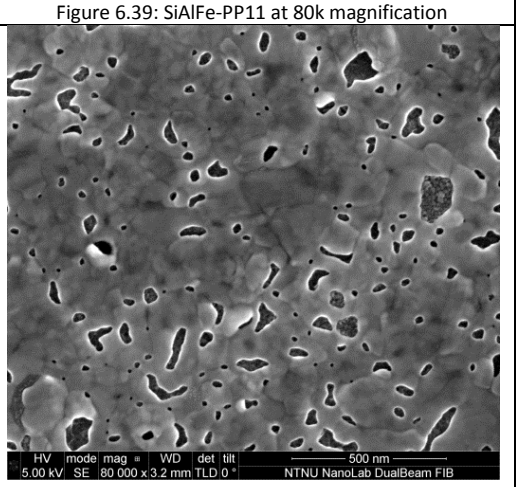 Figure 6.41: SiAlFe-PP12 at 80k magnification

Observation of the SEM images reveals that the density of small particles increases towards higher gas flows. As it increases the particles seem to be transformed from elongated shapes to spherical shapes. In addition, the uniformity among the nanoparticles increases with increasing gas flows. That is why the PP2 sample seems to be the best.

Sample name	Size of nanoparticles [nm]	NH_3 gas flow [sccm]
PP2	≈ 23 – 80	50
PP9	≈ 12 – 120	40
PP10	≈ 12 – 80	30
PP11	≈ 12 – 80	20
PP12	≈ 12 – 100	10

6.5.5 The effect of variation in pressure

SiAlFe-PP13

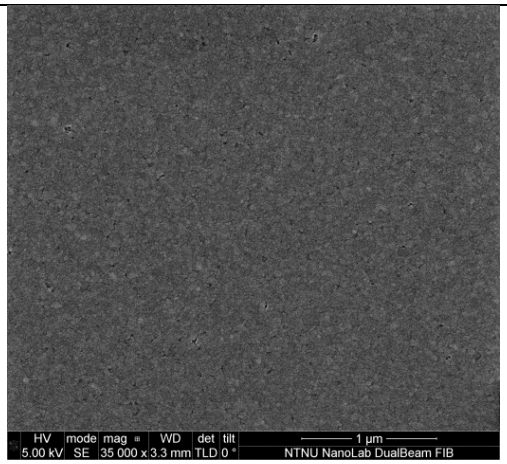

Figure 6.42: SiAlFe-PP13 at 35k magnification

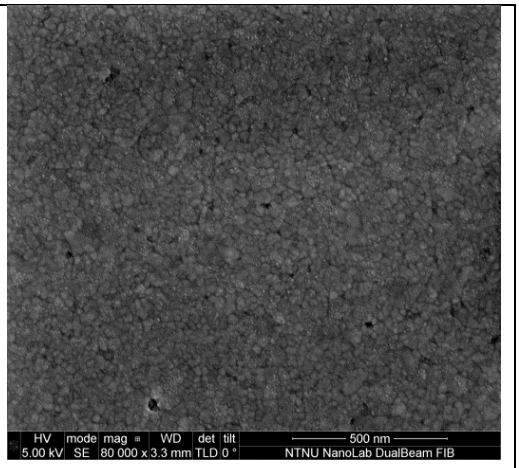

Figure 6.43: SiAlFe-PP13 at 80k magnification

SiAlFe-PP14

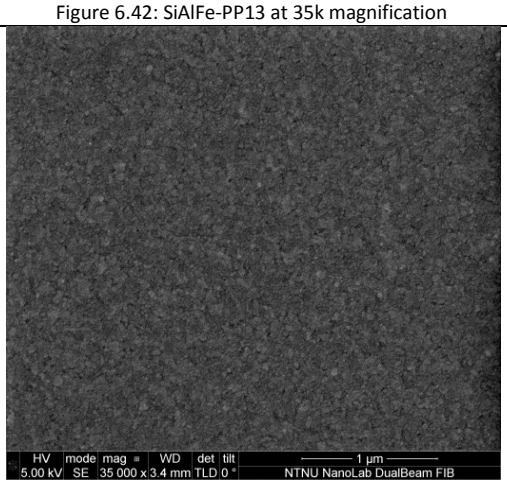

Figure 6.44: SiAlFe-PP14 at 35k magnification

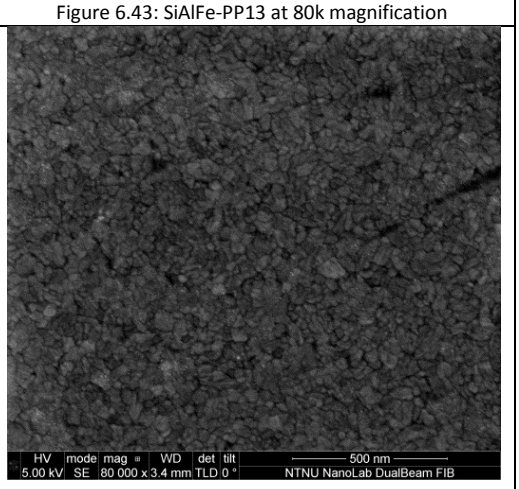

Figure 6.45: SiAlFe-PP14 at 80k magnification

SiAlFe-PP2	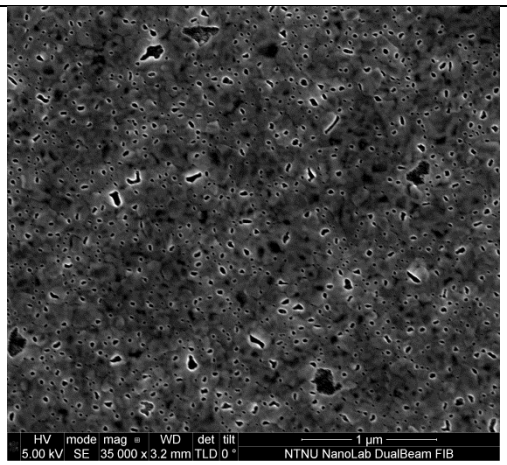 Figure 6.46: SiAlFe-PP2 at 35k magnification	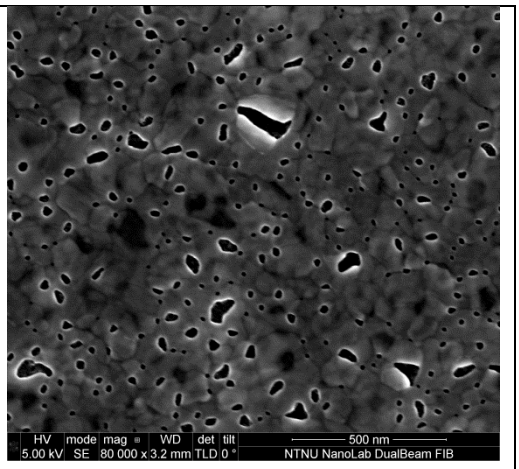 Figure 6.47: SiAlFe-PP2 at 80k magnification
SiAlFe-PP15	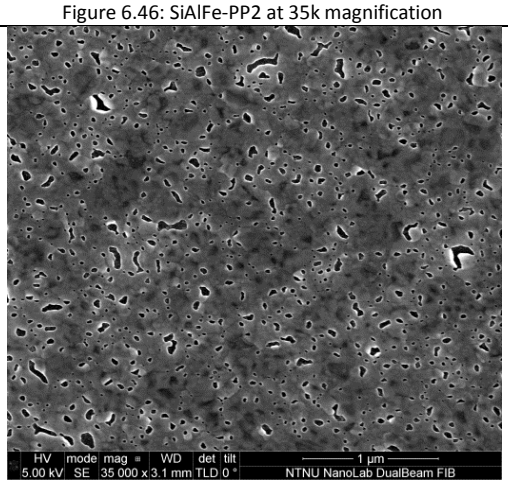 Figure 6.48: SiAlFe-PP15 at 35k magnification	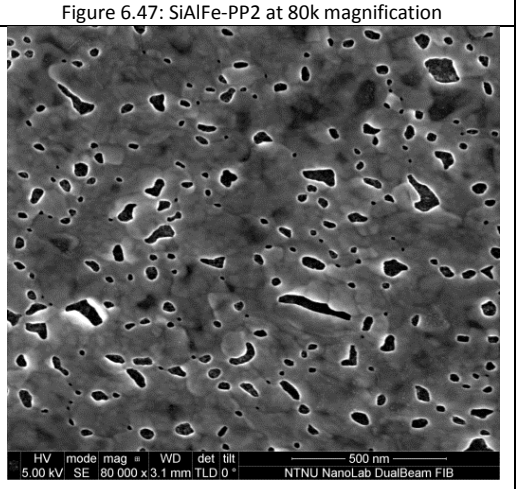 Figure 6.49: SiAlFe-PP15 at 80k magnification
SiAlFe-PP16	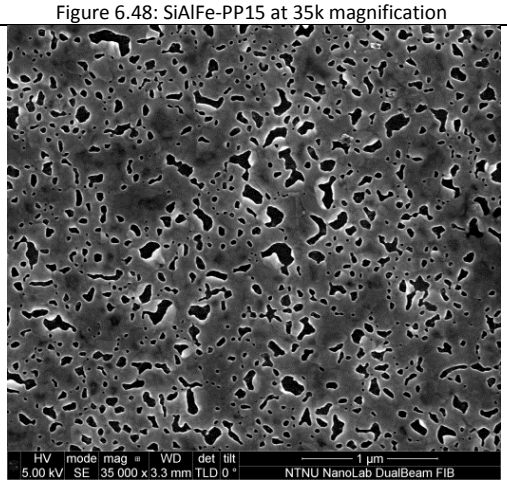 Figure 6.50: SiAlFe-PP16 at 35k magnification	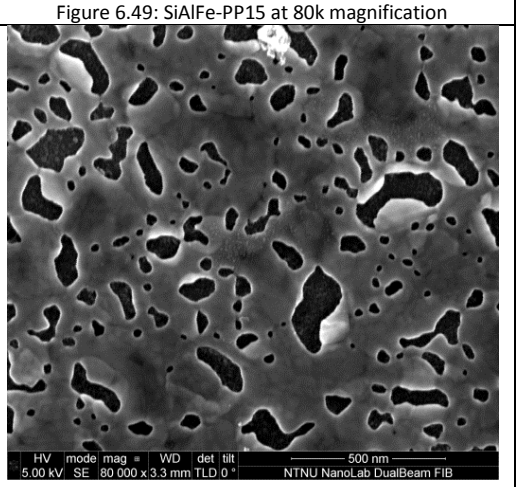 Figure 6.51: SiAlFe-PP16 at 80k magnification

No particles are observed for the samples that were processed at the lowest pressures, such as PP13 and PP14. In general, as the pressure increases the density and uniformity of the small particles improves, but only to a certain point, because the size and heterogeneity in PP17 which seems to verify the parts of the theory. Based on the uniformity and greatest density of small particles, the best samples are PP2 or PP15.

Sample name	Size of nanoparticles [nm]	Pressure [mTorr]
PP13	N/A	50
PP14	N/A	200
PP2	≈ 12 – 80	500
PP15	≈ 12 – 100	1000
PP16	≈ 23 – 150	1500

6.5.6 The effect of variation in thickness of catalyst layer

SiAlFe-PP17

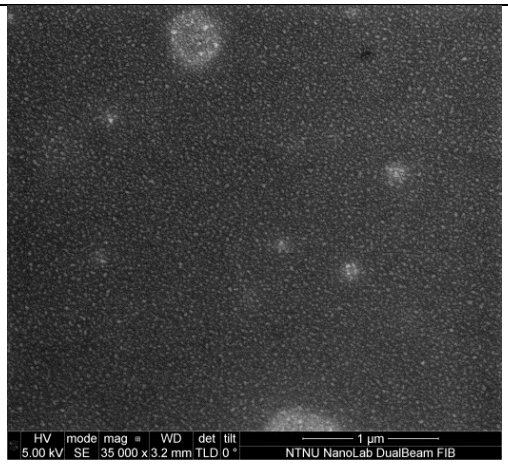

Figure 6.52: SiAlFe-PP17 at 35k magnification

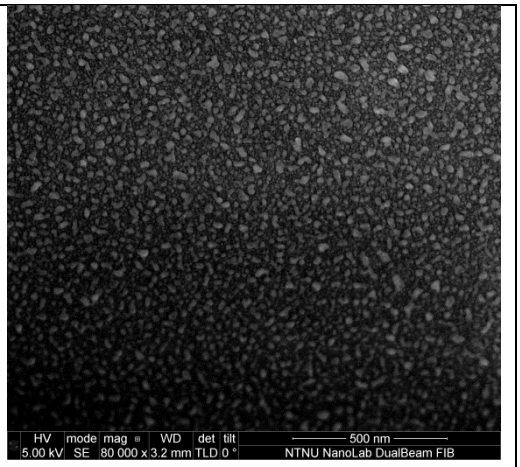

Figure 6.53: SiAlFe-PP17 at 80k magnification

SiAlFe-PP2

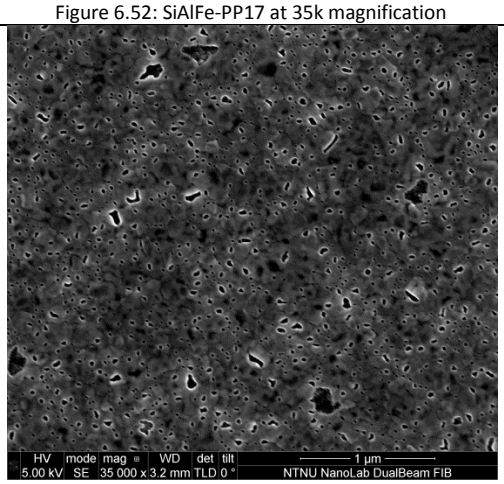

Figure 6.54: SiAlFe-PP2 at 35k magnification

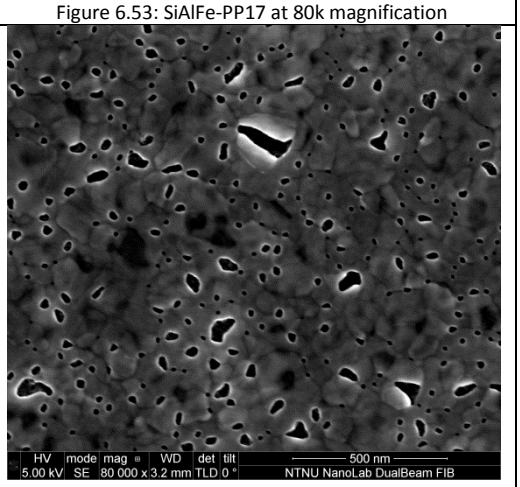

Figure 6.55: SiAlFe-PP2 at 80k magnification

SiAlFe-PP18	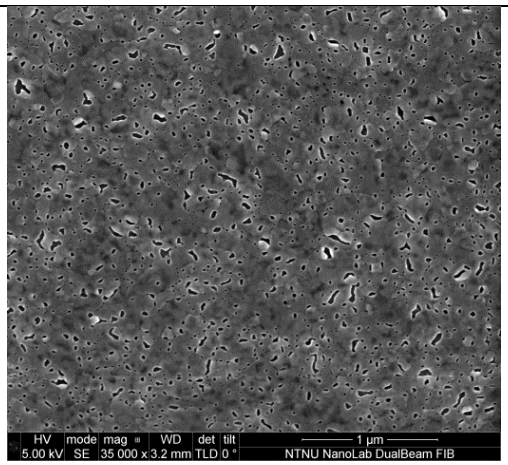	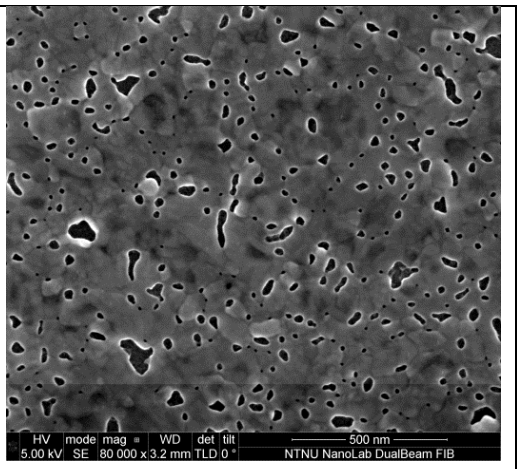
	Figure 6.56: SiAlFe-PP18 at 35k magnification	Figure 6.57: SiAlFe-PP18 at 80k magnification
SiAlFe-PP19	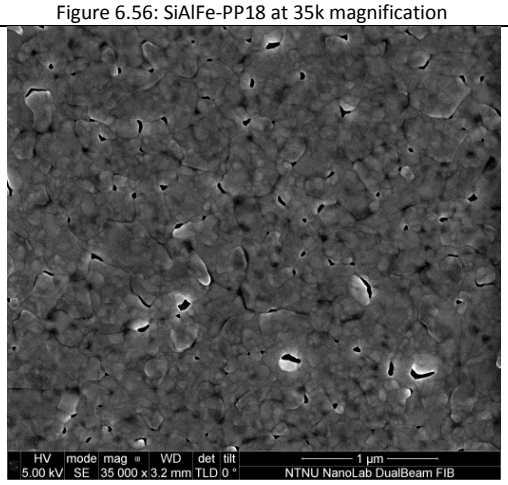	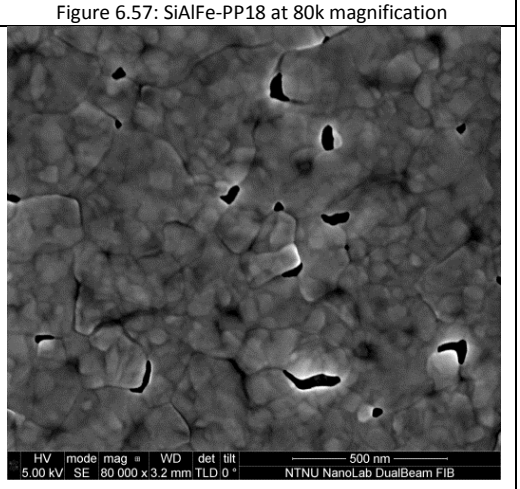
	Figure 6.58: SiAlFe-PP19 at 35k magnification	Figure 6.59: SiAlFe-PP19 at 80k magnification
SiAlFe-PP20	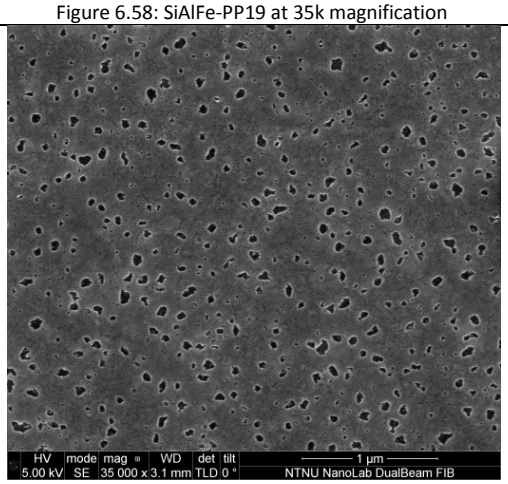	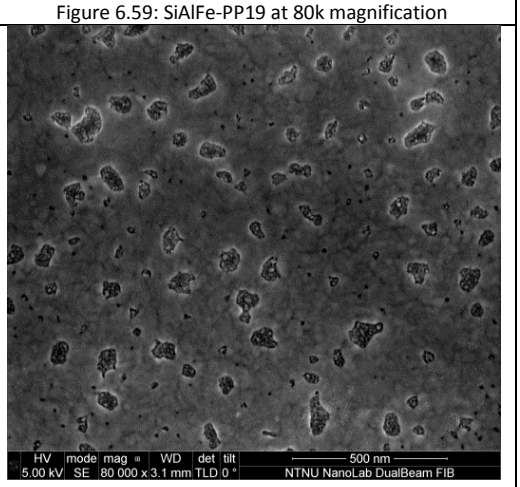
	Figure 6.60: SiAlFe-PP20 at 35k magnification	Figure 6.61: SiAlFe-PP20 at 80k magnification

Sample PP19 distinguishes from the other samples since it has particles that have elongated shapes only, in addition it seems like most of them have vanished from the surface. This result is strange when comparing with PP18 and PP20. One explanation could be that there has been something strange that have occurred during deposition of the Fe layer. In general, it can be observed that the size of the particles increases with increased thickness, which is exactly why a thicker catalyst layer requires longer pretreatment time, since the plasma needs more time to form small catalyst particles. The sample with the highest density, smallest size and uniformity is the PP17, which also seems to possess most spherical nanoparticles among the samples.

Sample name	Size of nanoparticles [nm]	Layer thickness [nm]
PP17	≈ 12 – 50	2
PP2	≈ 12 – 80	5
PP18	≈ 12 – 100	8
PP19	≈ 12 – 100	15
PP20	≈ 12 – 100	30

6.5.7 The effect of variation in temperature

SiAlFe-PP21

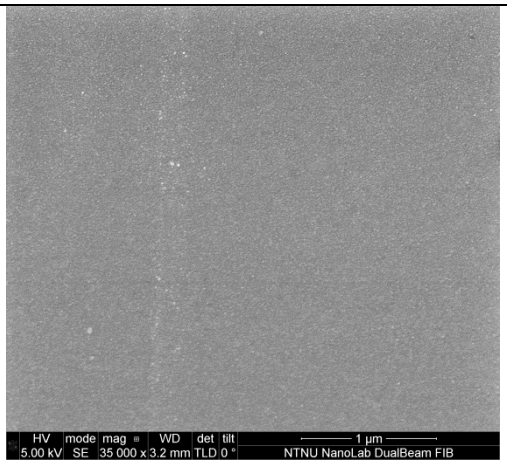

Figure 6.62: SiAlFe-PP21 at 35k magnification

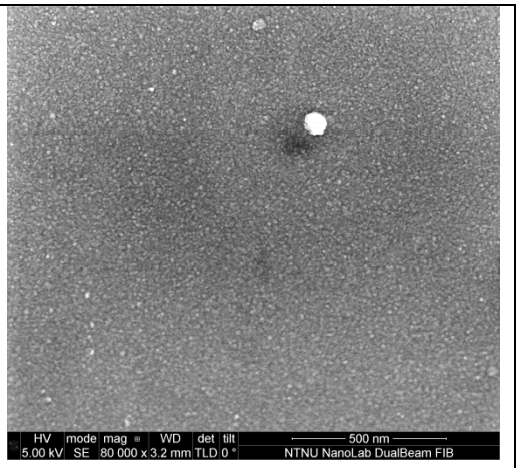

Figure 6.63: SiAlFe-PP21 at 80k magnification

SiAlFe-PP22

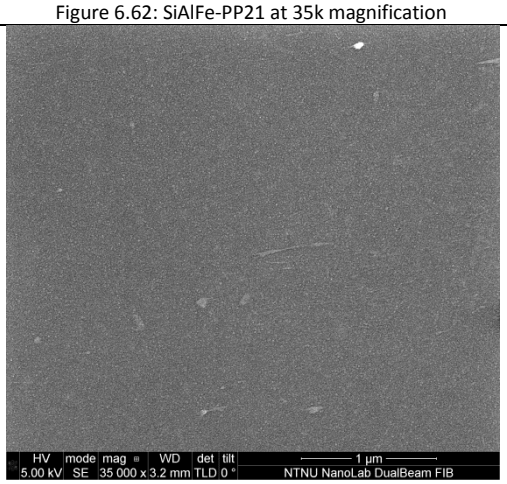

Figure 6.64: SiAlFe-PP22 at 35k magnification

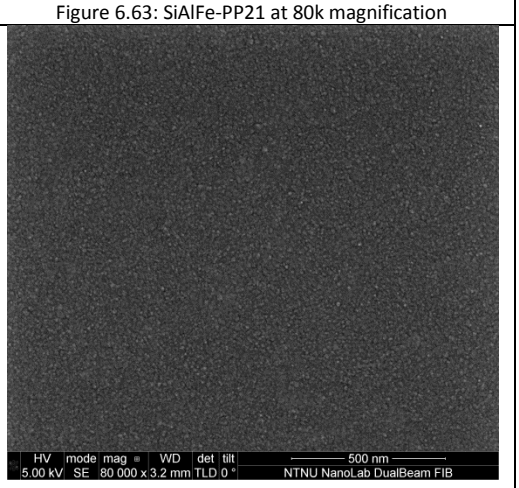

Figure 6.65: SiAlFe-PP22 at 80k magnification

SiAlFe-PP23	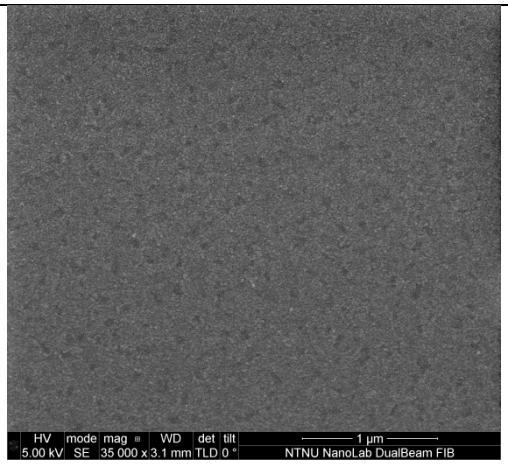 Figure 6.66: SiAlFe-PP23 at 35k magnification	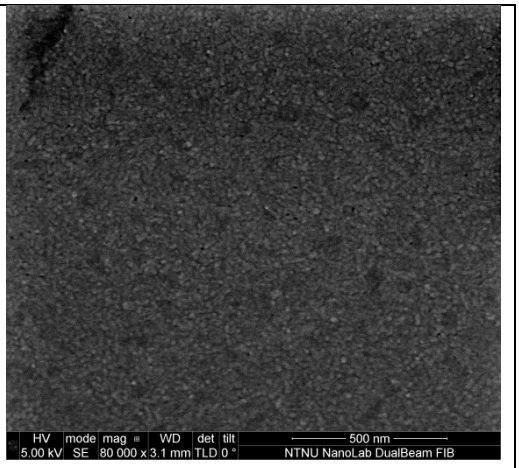 Figure 6.67: SiAlFe-PP23 at 80k magnification
SiAlFe-PP24	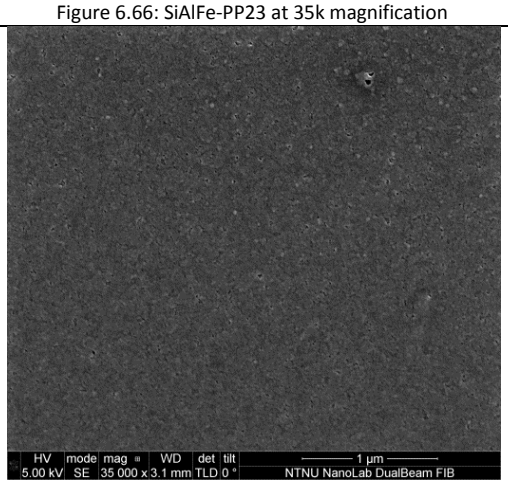 Figure 6.68: SiAlFe-PP24 at 35k magnification	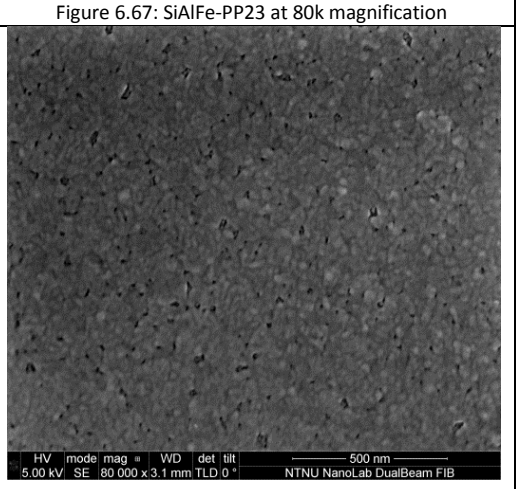 Figure 6.69: SiAlFe-PP24 at 80k magnification
SiAlFe-PP2	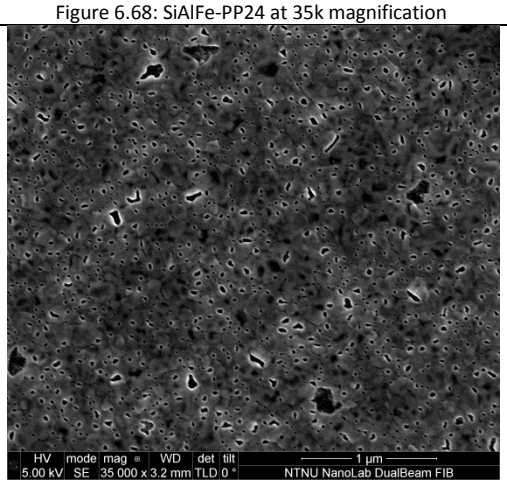 Figure 6.70: SiAlFe-PP2 at 35k magnification	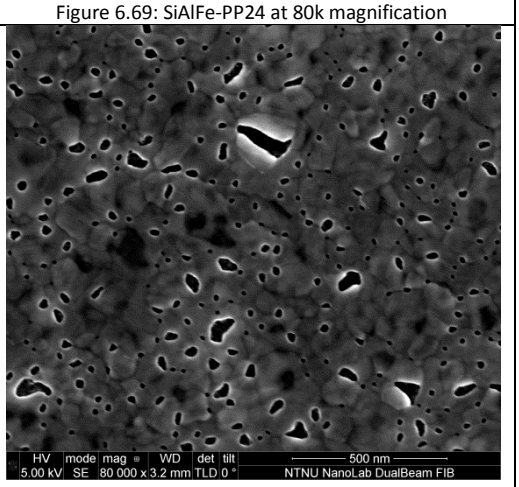 Figure 6.71: SiAlFe-PP2 at 80k magnification

The number and densities of particles seems to be very high for all the samples except PP3. The particles must be very low in the PP21 and PP2, as they are nearly visible. In the PP3 it can be observed that some particles are being formed, but at very low densities. All samples, except PP3 seem to be giving the optimal temperatures and achieved the best results regarding greatest number, uniformity and size. This concludes that a temperature between 600-700^{0}C could be favorable for the formation of the smallest nanoparticles.

Sample name	Size of nanoparticles [nm]	Temperature [^{0}C]
PP21	≈ 20 – 80	100
PP22	≈ 20 – 20	300
PP23	≈ 20 – 20	450
PP24	≈ 12 – 25	600
PP2	≈ 12 – 100	700

6.5.8 Thermal treatment

SiAlFe-TP1

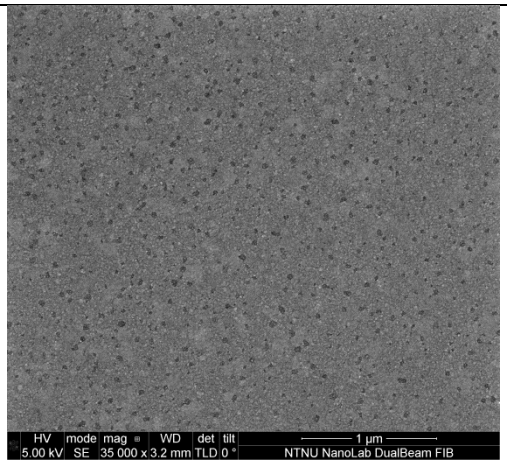

Figure 6.72: SiAlFe-TP1 at 35k magnification

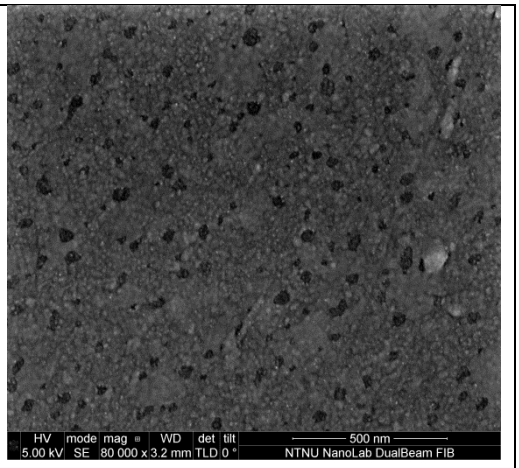

Figure 6.73: SiAlFe-TP1 at 80k magnification

SiAlFe-TP2

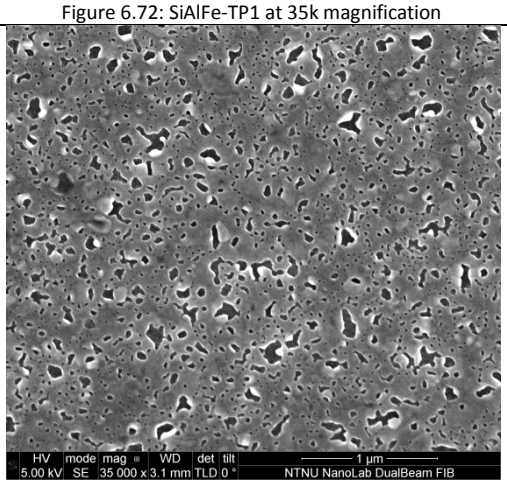

Figure 6.74: SiAlFe-TP2 at 35k magnification

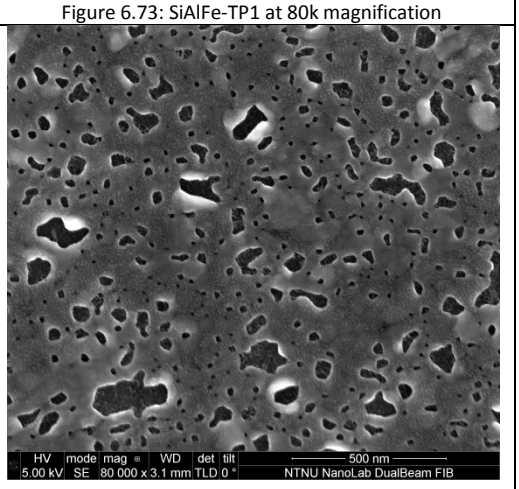

Figure 6.75: SiAlFe-TP2 at 80k magnification

SiAlFe-TP3	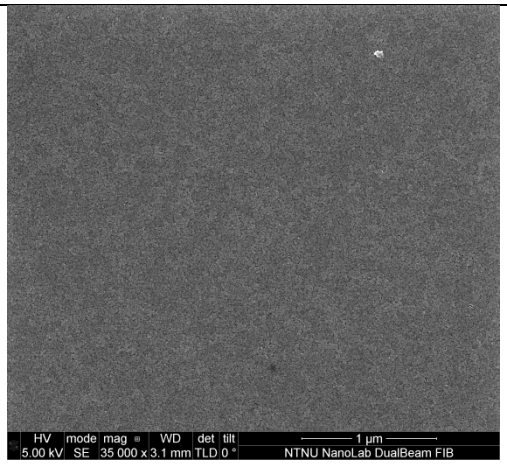 Figure 6.76: SiAlFe-TP3 at 35k magnification	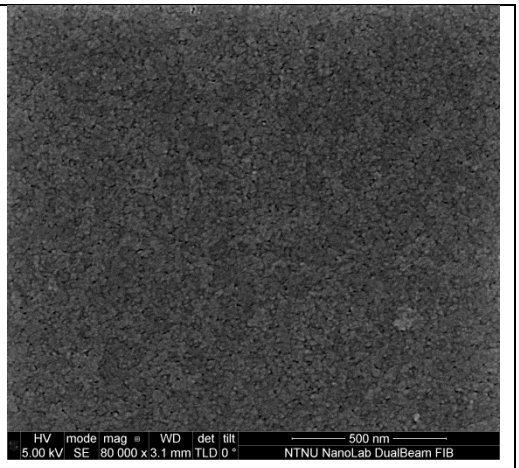 Figure 6.77: SiAlFe-TP3 at 80k magnification
SiAlFe-TP4	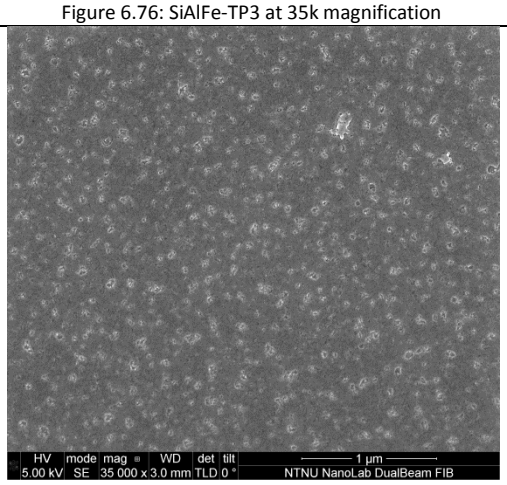 Figure 6.78: SiAlFe-TP4 at 35k magnification	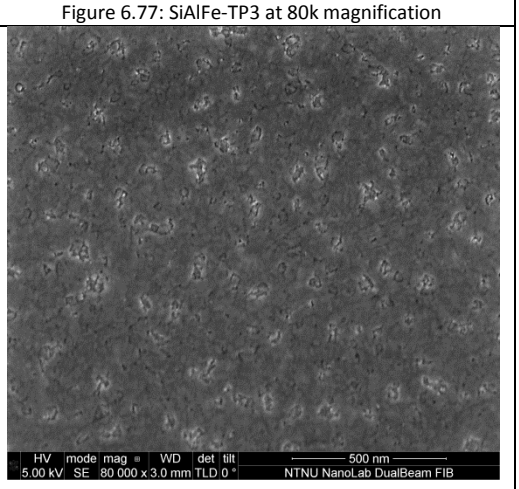 Figure 6.79: SiAlFe-TP4 at 80k magnification

The shortest TP time is done for TP1 and TP2, which result in larger particles than those that are treated with longer treatment time. In addition, TP3 and TP4 seem to have greater density and uniformity of small particles. Since the last mentioned samples do not have particles that vanish from the surface, it should be possible to increase the TP time as this should decrease the size to even smaller particles. The uniformity, density and the spherical shaped nanoparticles in TP3 seems to be better than in most of the PP samples.

Sample name	Size of nanoparticles [nm]	Temperature [^{0}C]
TP1	≈ 23 – 50	500 (10 minutes)
TP2	≈ 12 – 100	700 (10 minutes)
TP3	≈ 12 – 20	500 (15 minutes)
TP4	≈ 12 – 50	700 (15 minutes)

6.5.9 Summary of the successful parameter from the pretreatment study

The parameters from the pretreatment study which were most likely to yield CNTs are summarized in Table 6.11.

Parameter	Value
PP treatment time [minutes]	3 - 5
Power [W]	100
Gas flows [sccm]	50
Pressure [mTorr]	500 – 1000
Catalyst layer [nm]	< 2
Temperature [^{0}]	600 – 700
TP treatment time [minutes]	15 (500^0)

Table 6.11: The parameters that showed the highest potential for CNT growth during the study of the pretreatment

6.6 Growth of CNTs

A recipe was made with basis of the results from the pretreatment study. TP was chosen as the pretreatment method since it formed the smallest nanoparticles for CNT growth. The recipe that was made became the base for all the samples in this experiment since it was the first recipe that successfully yielded CNTs. It was therefore named "CNTRecipe" and can be found in Table 6.12. Even though the results from the pretreatment recommended 500^{0}C, 650^{0}C was chosen as it was more convenient to keep equal temperature during the pretreatment and growth step. When a value from Table 6.11 was provided for a range, e.g. pressure, a trial and error method for this value was performed. The only thing that distinguishes the samples is that one and one parameter has been changed at a time to see how it effects the CNT growth. Different batches have been processed in the PECVD, where one batch consists of samples with catalyst layer thicknesses of 1, 3, 6 and 10 nm. All the samples were processed with a slow heating and cooling cycle to achieve a uniform temperature change on the Si wafer that was used for loading the samples into the PECVD chamber. The heating step occurred prior to pretreatment, while the cooling step occurred after the growth step.

CNTRecipe for CNT growth
1x Pump (3 minutes) & Purge (2 minutes in flow of Ar 1500 sccm).
1x Pump to Base (pump to a base pressure of 5*10^{-6}).
1x Slow heating from 300^{0}C up to 650^{0}C: NH_3 (50 sccm), 0 mTorr, 30 minutes.
1x TP step: NH_3 (50 sccm), 1000 mTorr, 30 minutes, 650^{0}C.
1x CNT growth step: CH_4 (50 sccm), 1000 mTorr, 100 W, 60 minutes, 650^{0}C.
1x Slow cooling from 650^{0}C to 300^{0}C: Ar (1200 sccm), 0 mTorr, 120 minutes.
3x Pump & Purge.
1x Pump to Base

Table 6.12: The "CNTRecipe" was the base recipe for all the processed samples in this experiment and required 4- 5 hours to finish

The "Pump" function is necessary since it removes most of the gases that were present in the chamber and lasted for 3 minutes. The "Purge" flushed the chamber with Ar to remove any remaining gas particles that could be present and lasted for 2 minutes. The "Pump to Base" removed Ar gas from the chamber by pumping to a base pressure of 5*10^{-6} mTorr.

In the following subchapters, images and comments for the final results will be present. Keep in mind that all samples are based on the "CNTRecipe" and that only one parameter in each batch

deviates from this recipe. The E47 sample was processed with the exact same parameters that are provided in the "CNTRecipe", which make it function as a reference towards the other samples. This is why it can be found in each section that will be presented below. An overview of the parameters that was used for each sample can be found in Appendix C.

As many samples have been grown in this experiment, only images of the 1 nm sample from each batch will be provided here, otherwise this document would be overwhelmed with images. The remaining images can be found in zip file(s) which will be available in DAIM. When cross section image is not provided for the sample it means that no VACNTs are present, but there could still be CNTs. The average diameter has been found by taking the average of 5 tubes from the ultra-high resolution image for each sample. It should be noted that the diameter measurements in the SEM images is note accurate as it is difficult to distinguish between individual or bundled CNTs, which is why the diameter value must not be interpret as the real value but could be used when comparing the thickness among the samples since the ultra-high magnifications images are captured at nearly equal conditions. This is why diameter measurements of some selected samples have been done in TEM, so that they can be compared to those provided from the SEM images.

6.6.1 Variation in CH_4 flow

SiAlFe-TP-E55 (CH_4 100 sccm)	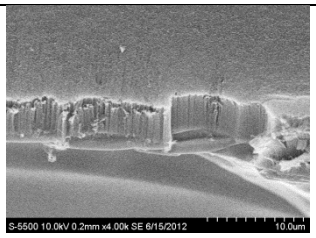 Figure 6.80: Low resolution SEM image of SiAlFe-TP-E55 with 30^0 tilting	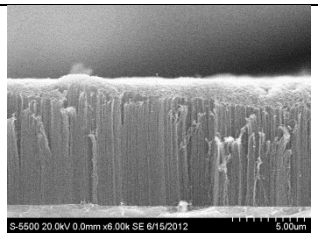 Figure 6.81: Low resolution cross section SEM image of SiAlFe-TP-E55	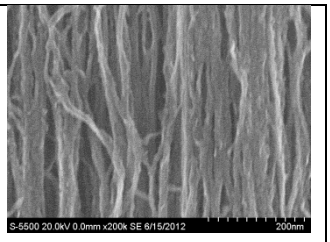 Figure 6.82: Ultra-High resolution cross section SEM image of SiAlFe-TP-E55
SiAlFe-TP-E47 (CH_4 50 sccm)	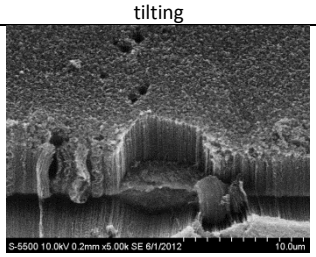 Figure 6.83: Low resolution SEM image of SiAlFe-TP-E47 with 30^0 tilting	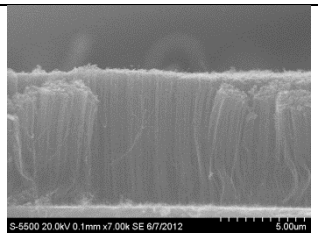 Figure 6.84: Low resolution cross section SEM image of SiAlFe-TP-E47	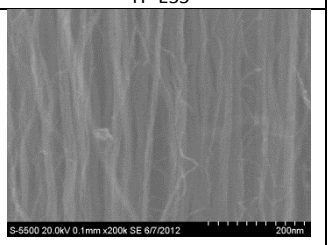 Figure 6.85: Ultra-High resolution cross section SEM image of SiAlFe-TP-E47
SiAlFe-TP-E51 (CH_4 35 sccm)	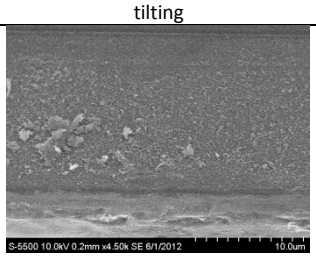 Figure 6.86: Low resolution SEM image of SiAlFe-TP-E51 with 30^0 tilting	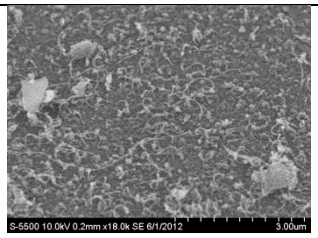 Figure 6.87: High resolution SEM image of SiAlFe-TP-E51 with 30^0 tilting	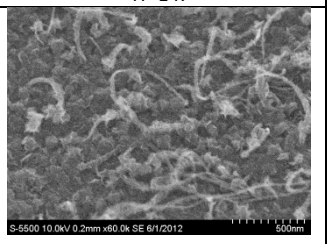 Figure 6.88: Ultra-High resolution SEM image of SiAlFe-TP-E51 with 30^0 tilting

No growth occurred for any of the samples with a catalyst layer of 3, 6 and 10 nm in this section. The only samples that yielded VACNTs was those with CH_4 flow of 50 (E47) and 100 sccm (E55). For the sample that was exposed in CH_4 flow of 35 sccm, only sparse CNT growth could be observed.

Even though the E55 received 100% more flow of CH_4 compared to E47, the VACNTs were shorter. The overall density and uniformity seems to be excellent for sample E47 and E55. It is difficult from the SEM images to see whom of them that have the highest density. The growth rates is not very impressive, as 0.13 um/minute is very slow.

The E55 had to be re-grown since it got broken into thousands of pieces during the manual scribing and breaking process. This means that it followed the new sample preparation procedure. From its SEM images it can be observed that there are no CNT growth on the edge that hinders the sight during cross section imaging. In addition, the Fe layers do not seems to be damaged by the automatic breaking process. Based on these observations, the new sample preparation procedure seems to work excellent. Figure 6.89 - Figure 6.91 gives the average height, average diameter and growth rate of the samples in this section. The growth times for all the samples were 60 minutes.

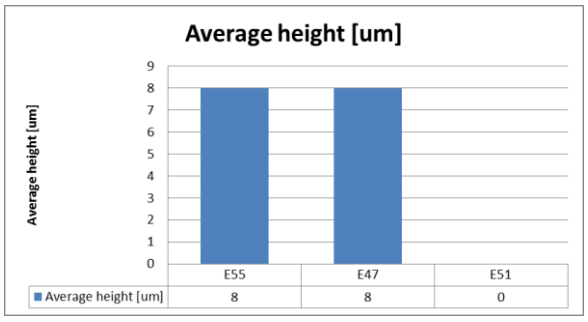

Figure 6.89: The average height of sample E55, E47 and E51

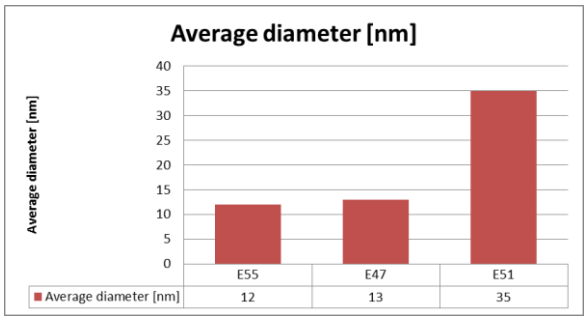

Figure 6.90: The average diameter of sample E55, E47 and E51

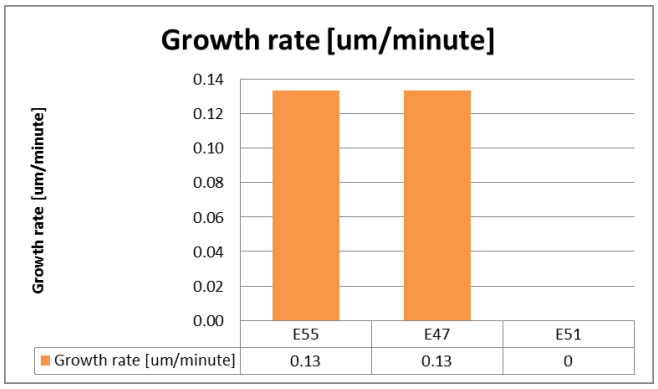

Figure 6.91: The growth rate of sample E55, E47 and E51

6.6.2 Adding NH_3 in the CNT growth step

SiAlFe-TP-E47 (CH_4 50 sccm and NH_3 0 sccm)	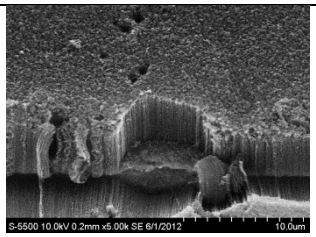	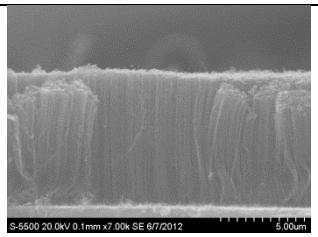	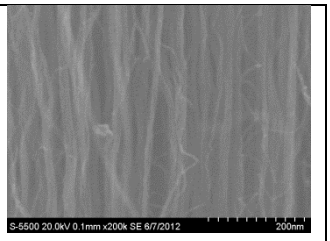
	Figure 6.92: Low resolution SEM image of SiAlFe-TP-E47 with 30^0 tilting	Figure 6.93: Low resolution cross section SEM image of SiAlFe-TP-E47	Figure 6.94: Ultra-High resolution cross section SEM image of SiAlFe-TP-E47

SiAlFe-TP-E79 (CH_4 100 sccm and NH_3 25 sccm)	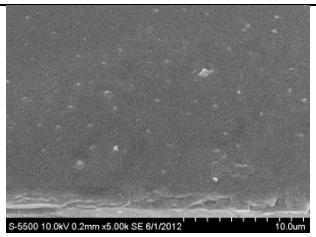 Figure 6.95: Low resolution SEM image of SiAlFe-TP-E79 with 30^0 tilting	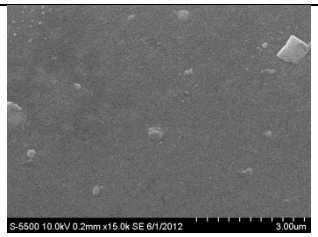 Figure 6.96: High resolution SEM image of SiAlFe-TP-E79 with 30^0 tilting	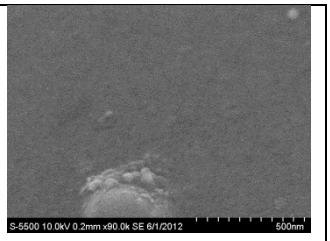 Figure 6.97: Ultra-High resolution SEM image of SiAlFe-TP-E79 with 30^0 tilting
SiAlFe-TP-E75 (CH_4 100 sccm and NH_3 15 sccm)	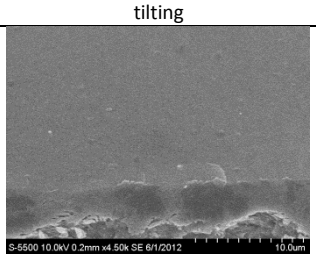 Figure 6.98: Low resolution SEM image of SiAlFe-TP-E75 with 30^0 tilting	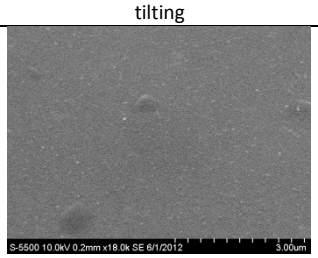 Figure 6.99: High resolution SEM image of SiAlFe-TP-E75 with 30^0 tilting	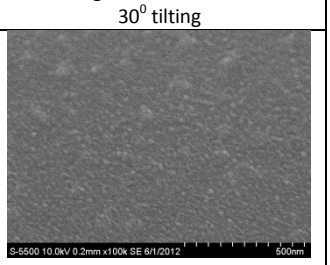 Figure 6.100: Ultra-High resolution SEM image of SiAlFe-TP-E75 with 30^0 tilting
SiAlFe-TP-E71 (CH_4 100 sccm and NH_3 5 sccm)	Figure 6.101: Low resolution SEM image of SiAlFe-TP-E71 with 30^0 tilting	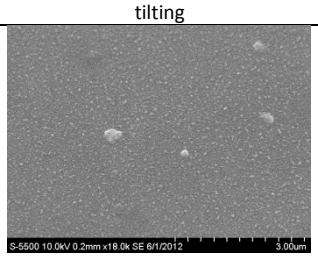 Figure 6.102: High resolution SEM image of SiAlFe-TP-E71 with 30^0 tilting	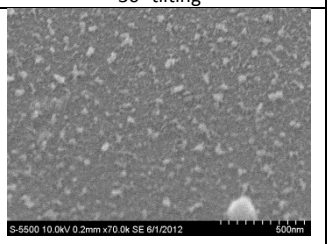 Figure 6.103: Ultra-High resolution SEM image of SiAlFe-TP-E71 with 30^0 tilting
SiAlFe-TP-E103 (CH_4 100 sccm and NH_3 1 sccm)	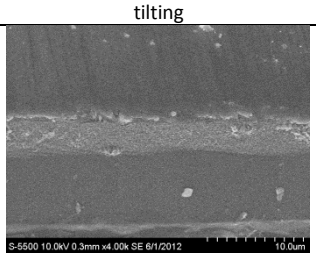 Figure 6.104: Low resolution SEM image of SiAlFe-TP-E103 with 30^0 tilting	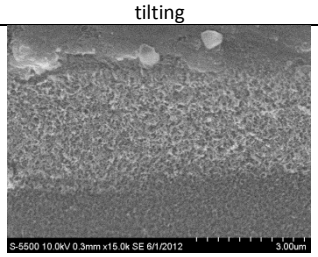 Figure 6.105: High resolution SEM image of SiAlFe-TP-E103 with 30^0 tilting	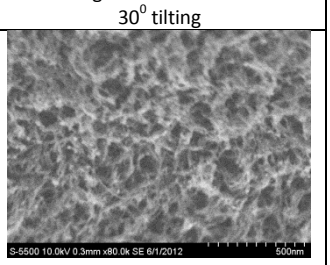 Figure 6.106: Ultra-High resolution SEM image of SiAlFe-TP-E67 with 30^0 tilting
SiAlFe-TP-E59 (CH_4 50 sccm and NH_3 25 sccm)	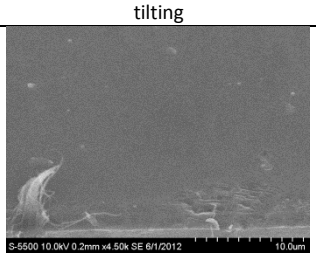 Figure 6.107: Low resolution SEM image of SiAlFe-TP-E59 with 30^0 tilting	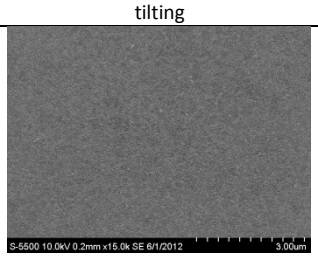 Figure 6.108: High resolution SEM image of SiAlFe-TP-E59 with 30^0 tilting	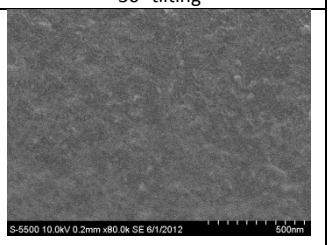 Figure 6.109: Ultra-High resolution SEM image of SiAlFe-TP-E59 with 30^0 tilting

SiAlFe-TP-E63 (CH_4 50 sccm and NH_3 15 sccm)	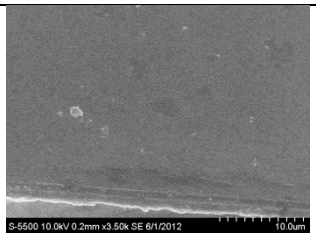 Figure 6.110: Low resolution SEM image of SiAlFe-TP-E63 with 30^0 tilting	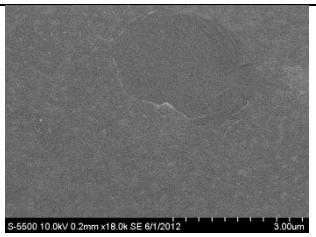 Figure 6.111: High resolution SEM image of SiAlFe-TP-E63 with 30^0 tilting	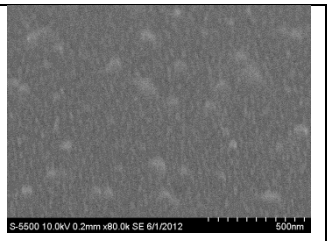 Figure 6.112: Ultra-High resolution SEM image of SiAlFe-TP-E63 with 30^0 tilting
SiAlFe-TP-E67 (CH_4 50 sccm and NH_3 5 sccm)	Figure 6.113: Low resolution SEM image of SiAlFe-TP-E67 with 30^0 tilting	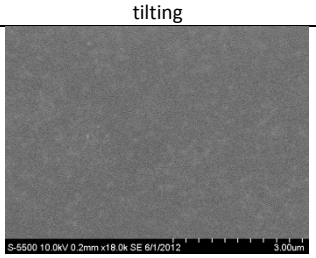 Figure 6.114: High resolution SEM image of SiAlFe-TP-E67 with 30^0 tilting	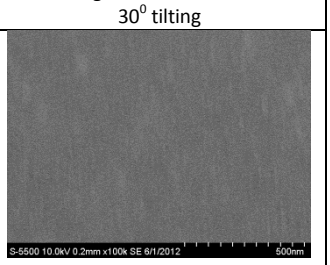 Figure 6.115: Ultra-High resolution SEM image of SiAlFe-TP-E67 with 30^0 tilting
SiAlFe-TP-E99 (CH_4 50 sccm and NH_3 1 sccm)	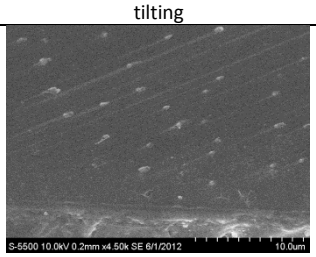 Figure 6.116: Low resolution SEM image of SiAlFe-TP-E99 with 30^0 tilting	Figure 6.117: High resolution SEM image of SiAlFe-TP-E99 with 30^0 tilting	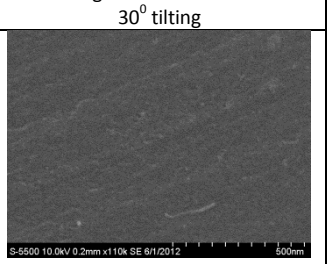 Figure 6.118: Ultra-High resolution SEM image of SiAlFe-TP-E99 with 30^0 tilting

It was quite surprising that no growth occurred for the samples where the flow of CH_4 was mixed with various NH_3 flows. The only sample that contains some features which could be CNTs is E103, where NH_3 flow as little as 1 sccm was used. However, the CNTs are only grown in specific areas on the sample's surface.

6.6.3 Variation of power

SiAlFe-TP-E91 (300 W)	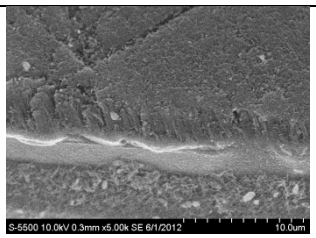 Figure 6.119: Low resolution SEM image of SiAlFe-TP-E91 with 30^0 tilting	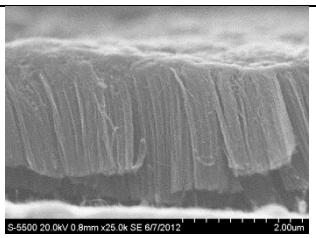 Figure 6.120: Low resolution cross section SEM image of SiAlFe-TP-E91	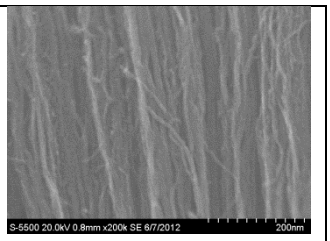 Figure 6.121: Ultra-High resolution cross section SEM image of SiAlFe-TP-E91

SiAlFe-TP-E87 (200 W)	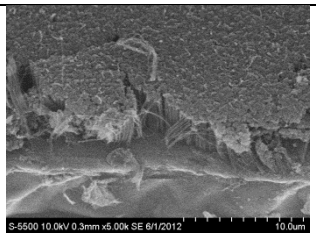 Figure 6.122: Low resolution SEM image of SiAlFe-TP-E87 with 30^0 tilting	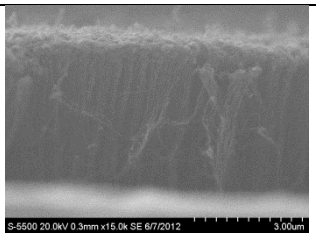 Figure 6.123: Low resolution cross section SEM image of SiAlFe-TP-E87	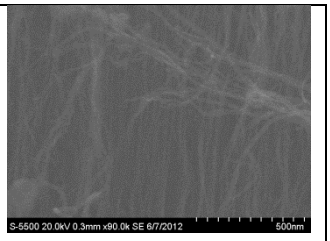 Figure 6.124: Ultra-High resolution cross section SEM image of SiAlFe-TP-E87
SiAlFe-TP-E47 (100 W)	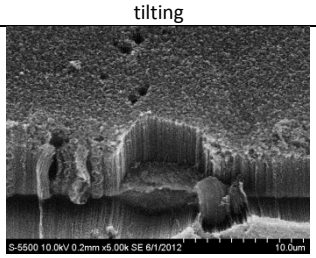 Figure 6.125: Low resolution SEM image of SiAlFe-TP-E47 with 30^0 tilting	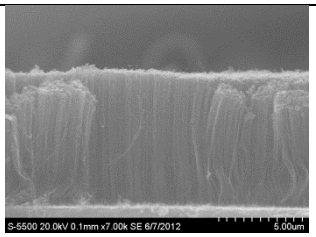 Figure 6.126: Low resolution cross section SEM image of SiAlFe-TP-E47	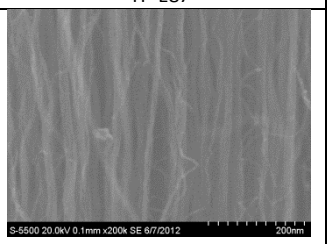 Figure 6.127: Ultra-High resolution cross section SEM image of SiAlFe-TP-E47
SiAlFe-TP-E95 (20 W)	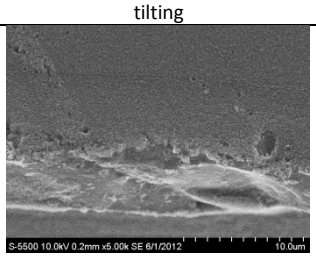 Figure 6.128: Low resolution SEM image of SiAlFe-TP-E95 with 30^0 tilting	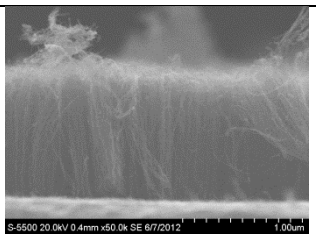 Figure 6.129: Low resolution cross section SEM image of SiAlFe-TP-E95	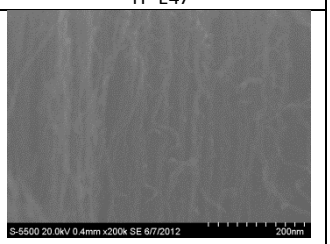 Figure 6.130: Ultra-High resolution cross section SEM image of SiAlFe-TP-E95
SiAlFe-TP-E195 (0 W)	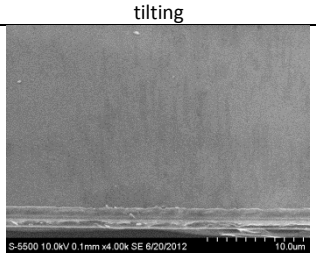 Figure 6.131: Low resolution SEM image of SiAlFe-TP-E195 with 30^0 tilting	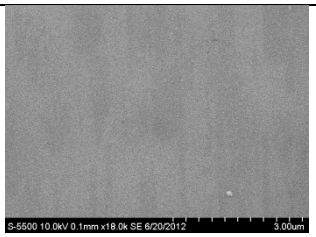 Figure 6.132: High resolution SEM image of SiAlFe-TP-E195 with 30^0 tilting	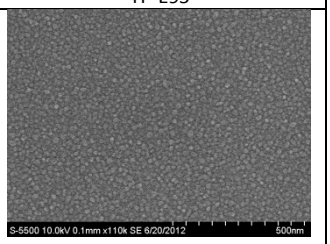 Figure 6.133: Ultra-High resolution SEM image of SiAlFe-TP-E195 with 30^0 tilting

No growth occurred for any of the samples with a catalyst layer of 3, 6 and 10 nm, except for the batch that were processed with plasma power of 300 W, where growth succeeded for the 3 nm sample (E92). The sample that received a power of 0 W did not contain any growth at all, which is not surprising as the processing method changed to CVD that uses thermal decomposition. Since the temperature is not high enough, no hydrocarbons gets decomposed.

It is not possible to verify that the samples with higher power have better alignment than those processed with lower. But one tendency can be seen, the density of the VACNTs seems to increase with higher plasma powers.

It could not be observed that the size of any nanoparticle decreased with increasing plasma power, as they seem to hold the same size. The average height, average diameter and the growth rates for this section can be found in Figure 6.134 - Figure 6.136. All the samples have been grown for 60 minutes.

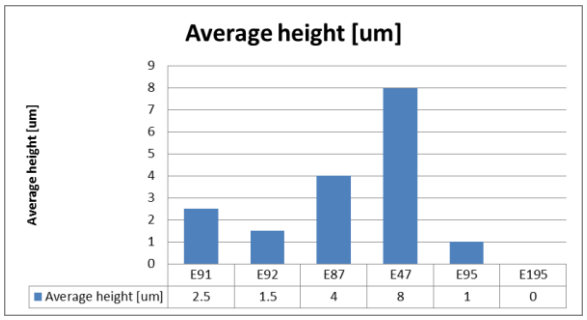

Figure 6.134: The average height of sample E47, E87, E91, E95 and E195

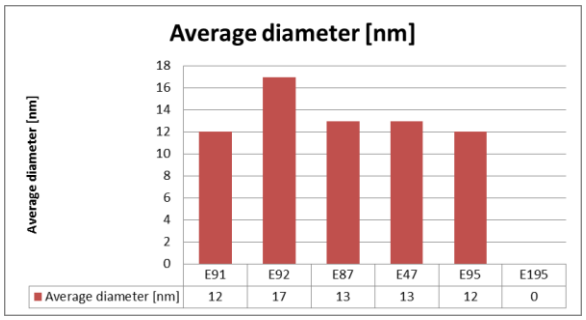

Figure 6.135: The average diameter of sample E47, E87, E91, E95 and E195

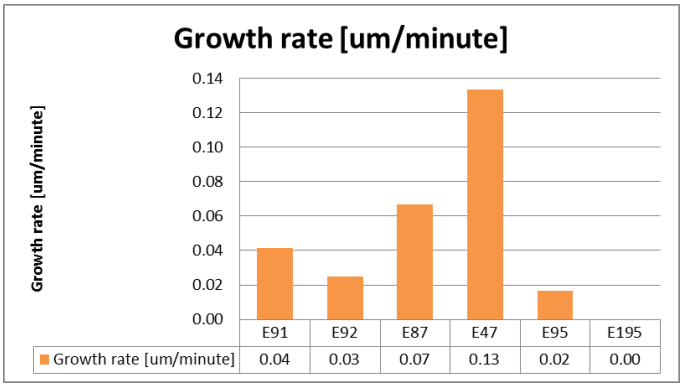

Figure 6.136: The growth rate of sample E47, E87, E91, E95 and E195

6.6.4 Variation of growth time

SiAlFe-TP-E139 (120 minutes)	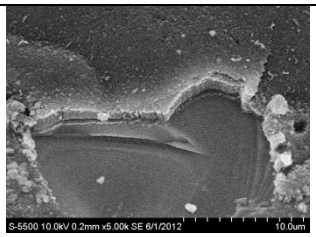 Figure 6.137: Low resolution SEM image of SiAlFe-TP-E95 with 30^0 tilting	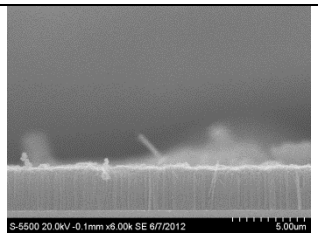 Figure 6.138: Low resolution cross section SEM image of SiAlFe-TP-E139	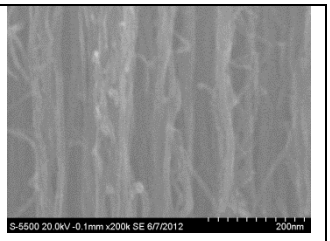 Figure 6.139: Ultra-High resolution cross section SEM image of SiAlFe-TP-E139
SiAlFe-TP-E47 (60 minutes)	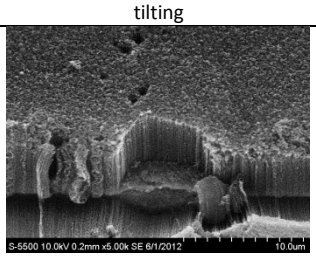 Figure 6.140: Low resolution SEM image of SiAlFe-TP-E47 with 30^0 tilting	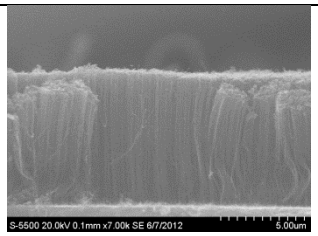 Figure 6.141: Low resolution cross section SEM image of SiAlFe-TP-E47	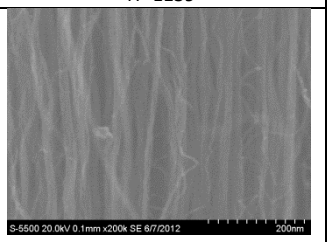 Figure 6.142: Ultra-High resolution cross section SEM image of SiAlFe-TP-E47

SiAlFe-TP-E107 (30 minutes)	Figure 6.143: Low resolution SEM image of SiAlFe-TP-E107 with 30^0 tilting	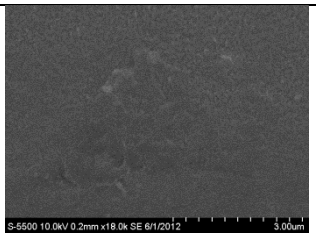 Figure 6.144: High resolution SEM image of SiAlFe-TP-E107 with 30^0 tilting	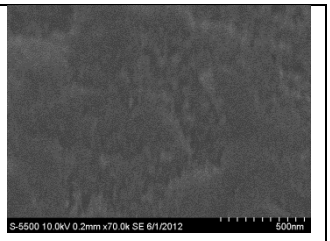 Figure 6.145: Ultra-High resolution SEM image of SiAlFe-TP-E107 with 30^0 tilting
SiAlFe-TP-E111 (10 minutes)	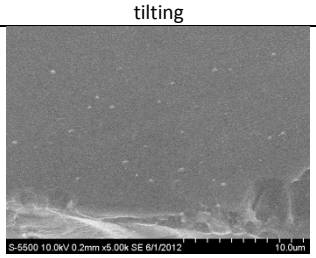 Figure 6.146: Low resolution SEM image of SiAlFe-TP-E111 with 30^0 tilting	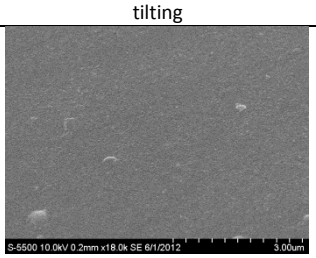 Figure 6.147: High resolution SEM image of SiAlFe-TP-E111 with 30^0 tilting	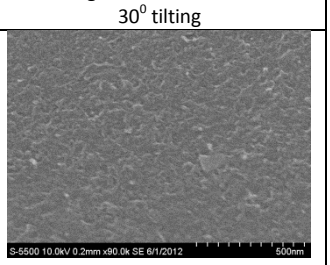 Figure 6.148: Ultra-High resolution SEM image of SiAlFe-TP-E111 with 30^0 tilting

No growth were recorded for any of the batches that hold catalyst layers of 3, 6 and 10 nm, except for the batch that was ran for 120 minutes which successfully yielded VACNTs onto the 3 nm sample (E140).

The tallest VACNTs were in E47, which seem to hold the optimal time for VACNT growth. No CNT or VACNT growth occurred for those samples with growth time less than the E47. For the sample that had twice as long growth time as the E47, the VACNTs were much shorter. It is important to remember that growth rate is not necessary constant through the whole growth process, which means that it could e.g. have its peak value for a limit time after growth initiation, then slowly decrease throughout in the process and end up being deactivated. An explanation for the termination of the catalytic particle for long growth time could be because of the following reasons:

- The catalyst particle vanishes due to continuously sputtering during growth.
- The a:C layer that gets deposited onto the catalytic particle deactivates the catalytic activity since it blocks any further transport of hydrocarbons to the particle.

Even though the growth stops, etching continuous for the remaining time of the growth step, this causes shortening of the VACNTs.

The long time that are needed to initiate growth is seen when considering that growth occurred for the 3 nm (E139) sample, while no growth was detected for the equal thickness (E48) sample within the same batch of E47. The increased growth time did not seem to affect the size of the nanoparticles, as they look to be similar. The average height, diameter and growth rates for this section are provided in Figure 6.149 - Figure 6.151.

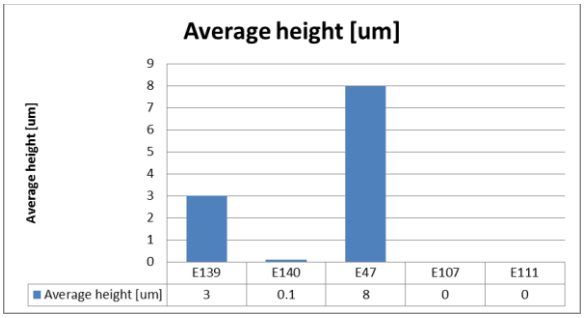

Figure 6.149: The average height of sample E47, E107, E111, E139 and E179

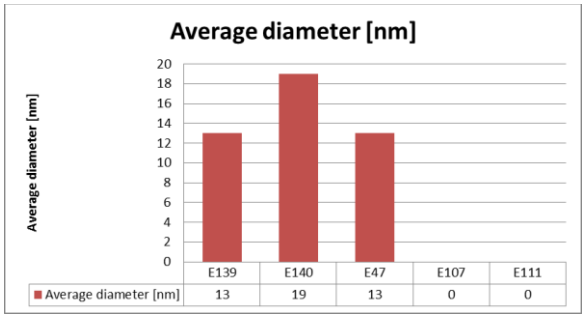

Figure 6.150: The average diameter of sample E47, E107, E111, E139 and E179

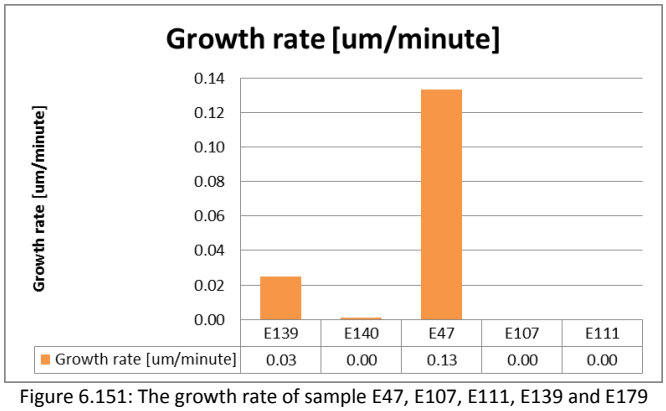

Figure 6.151: The growth rate of sample E47, E107, E111, E139 and E179

6.6.5 Variation in temperature

SiAlFe-TP-E119 (700^0C)	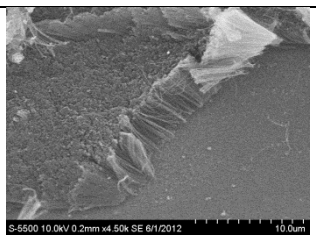 Figure 6.152: Low resolution SEM image of SiAlFe-TP-E119 with 30^0 tilting	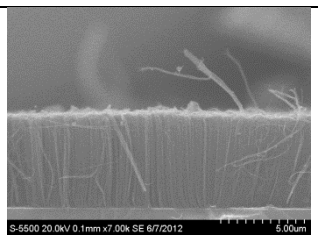 Figure 6.153: Low resolution cross section SEM image of SiAlFe-TP-E119	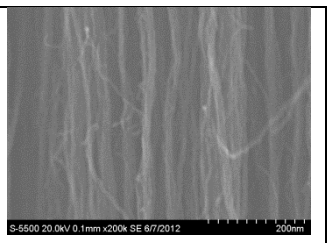 Figure 6.154: Ultra-High resolution cross section SEM image of SiAlFe-TP-E119
SiAlFe-TP-E47 (650^0C)	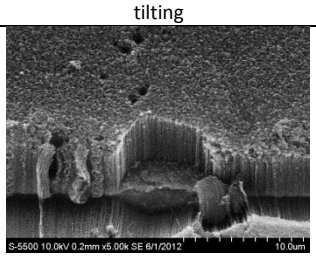 Figure 6.155: Low resolution SEM image of SiAlFe-TP-E47 with 30^0 tilting	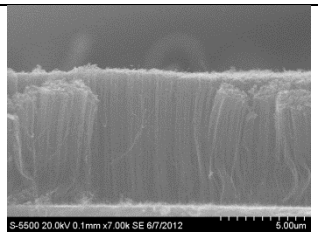 Figure 6.156: Low resolution cross section SEM image of SiAlFe-TP-E47	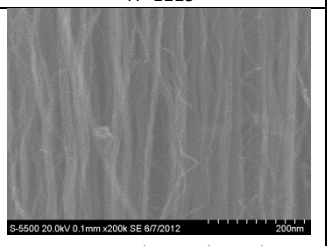 Figure 6.157: Ultra-High resolution cross section SEM image of SiAlFe-TP-E47

SiAlFe-TP-E123 (600^{0}C)	Figure 6.158: Low resolution SEM image of SiAlFe-TP-E123 with 30^0 tilting	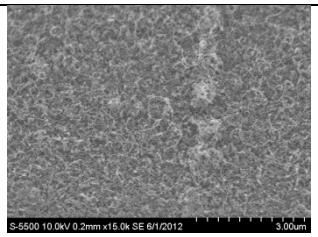 Figure 6.159: High resolution SEM image of SiAlFe-TP-E123 with 30^0 tilting	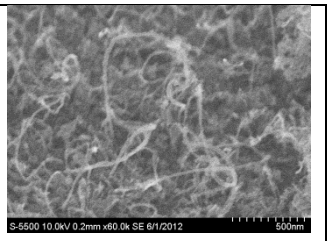 Figure 6.160: Ultra-High resolution SEM image of SiAlFe-TP-E123 with 30^0 tilting
SiAlFe-TP-E127 (500^{0}C)	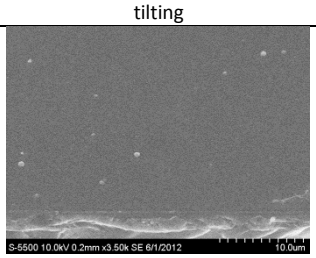 Figure 6.161: Low resolution SEM image of SiAlFe-TP-E127 with 30^0 tilting	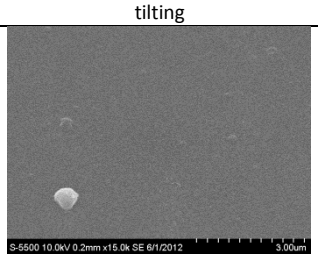 Figure 6.162: High resolution SEM image of SiAlFe-TP-E127 with 30^0 tilting	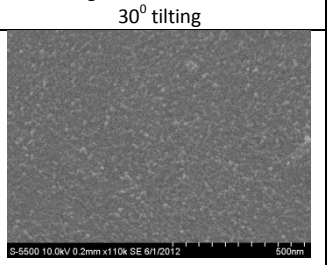 Figure 6.163: Ultra-High resolution SEM image of SiAlFe-TP-E127 with 30^0 tilting
SiAlFe-TP-E131 (400^{0}C)	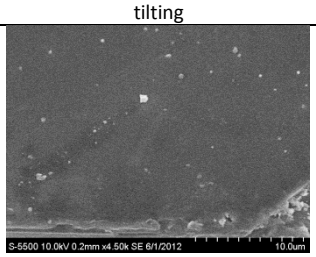 Figure 6.164: Low resolution SEM image of SiAlFe-TP-E131 with 30^0 tilting	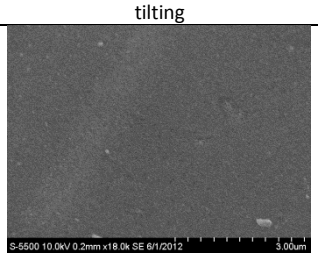 Figure 6.165: High resolution SEM image of SiAlFe-TP-E131 with 30^0 tilting	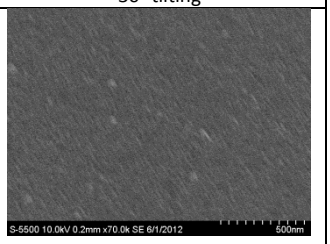 Figure 6.166: Ultra-High resolution SEM image of SiAlFe-TP-E131 with 30^0 tilting
SiAlFe-TP-E135 (300^{0}C)	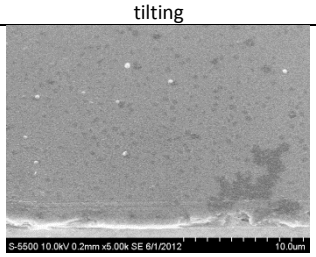 Figure 6.167: Low resolution SEM image of SiAlFe-TP-E135 with 30^0 tilting	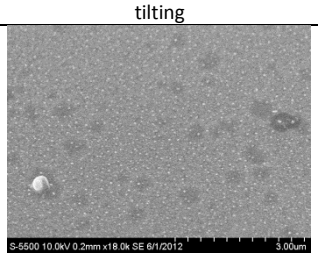 Figure 6.168: High resolution SEM image of SiAlFe-TP-E135 with 30^0 tilting	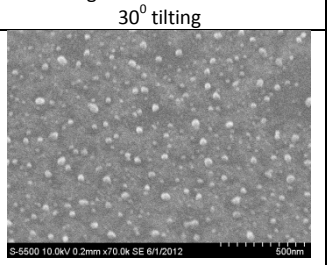 Figure 6.169: Ultra-High resolution SEM image of SiAlFe-TP-E135 with 30^0 tilting

No growth were recorded for any of the batches with catalyst layers of 3, 6 and 10 nm, except for the batch that was ran at 700^{0}C minutes which successfully yielded VACNTs onto the 3 nm sample (E120).

The E47 seems to hold the tallest VACNTs which led to the highest growth rate among the samples. When comparing E47 to E119 it can be observed that the 50^{0}C increase in temperature for the latter did not cause any diameter changes. To investigate if any temperature increase will result in larger diameters, sample E119 can be compared with E123, which does not seem to verify that this is the case. Our results suggest that it is quite the opposite. The average height, diameter and growth rate is provided in Figure 6.170 - Figure 6.172. All samples have been grown for 60 minutes.

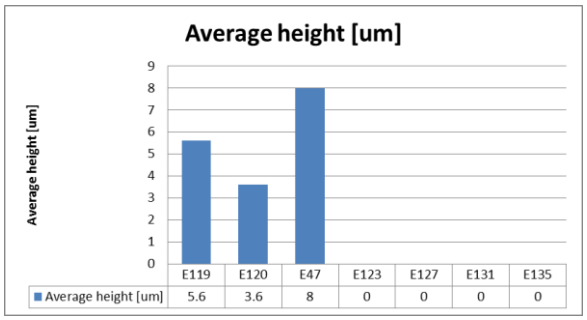

Figure 6.170: The average height of sample E47, E119, E123, E127, E131 and E135

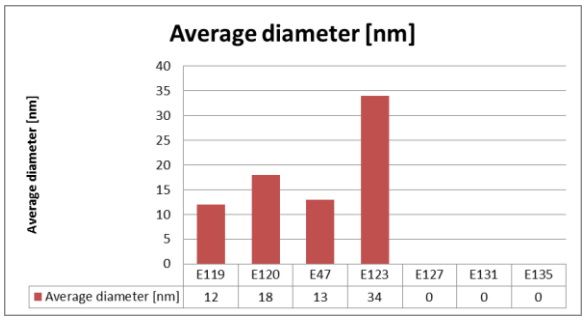

Figure 6.171: The average diameter of sample E47, E119, E123, E127, E131 and E135

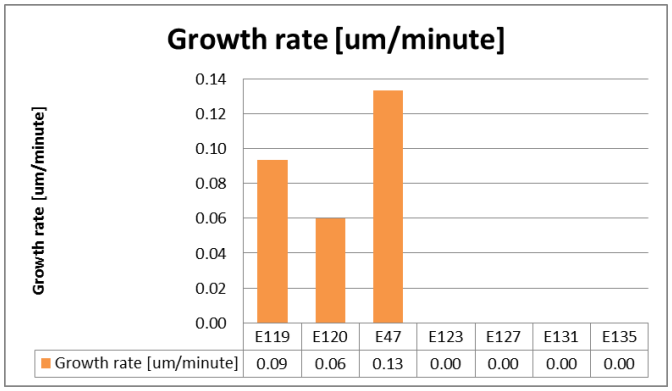

Figure 6.172: The growth rate of sample E47, E119, E123, E127, E131 and E135

6.6.6 No barrier layer

SiAlFe-TP-E47 (With barrier layer)	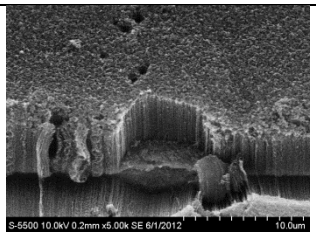 Figure 6.173: Low resolution SEM image of SiAlFe-TP-E47 with 30^0 tilting	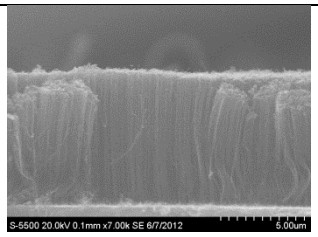 Figure 6.174: Low resolution cross section SEM image of SiAlFe-TP-E47	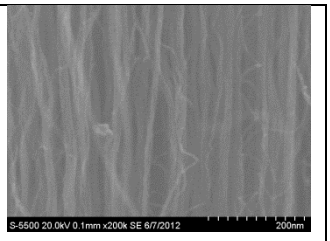 Figure 6.175: Ultra-High resolution cross section SEM image of SiAlFe-TP-E47
SiAlFe-TP-E159 (TP: No barrier layer)	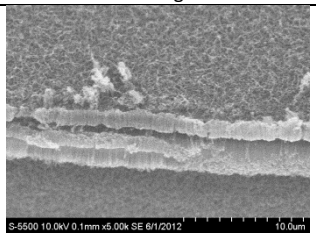 Figure 6.176: Low resolution SEM image of SiAlFe-TP-E159 with 30^0 tilting	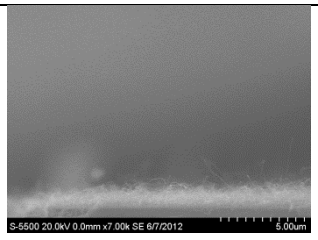 Figure 6.177: Low resolution cross section SEM image of SiAlFe-TP-E159	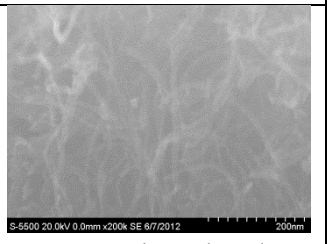 Figure 6.178: Ultra-High resolution cross section SEM image of SiAlFe-TP-E159

SiAlFe-TP-E163 (PP: No barrier layer)	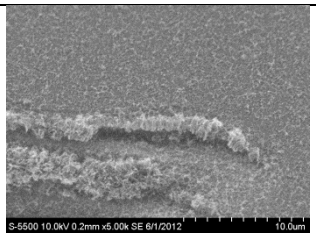 Figure 6.179: Low resolution SEM image of SiAlFe-TP-E163 with 30^0 tilting	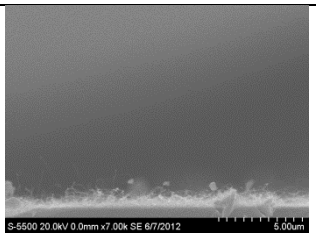 Figure 6.180: Low resolution cross section SEM image of SiAlFe-TP-E163	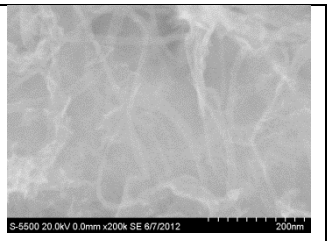 Figure 6.181: Ultra-High resolution cross section SEM image of SiAlFe-TP-E163

No growths were recorded for any of the batches that lacked a barrier layer with catalyst layers of 3, 6 and 10 nm.

The barrier layer seems to be highly necessary when studying the SEM images above, as they promote growth of VACNTs. The density of these samples is very impressive, compared to those samples without such as layer, which yielded CNTs only. The sample that was processed with PP shows a particular increase in diameter when compared to the sample with TP. The average height, diameter and growth rate is presented in Figure 6.182 - Figure 6.184.

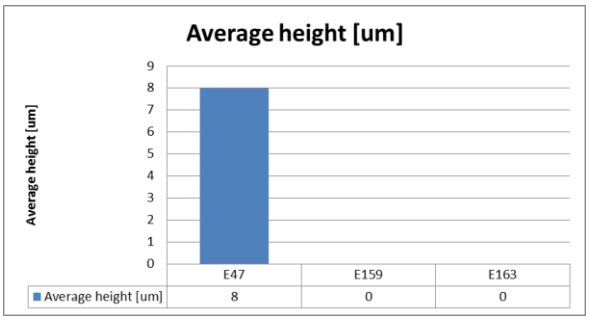

Figure 6.182: The average height of sample E47, E159 and E163

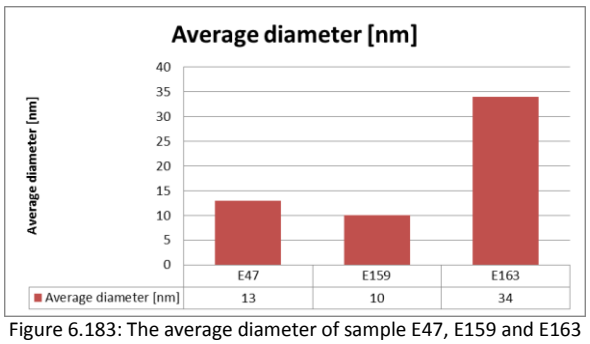

Figure 6.183: The average diameter of sample E47, E159 and E163

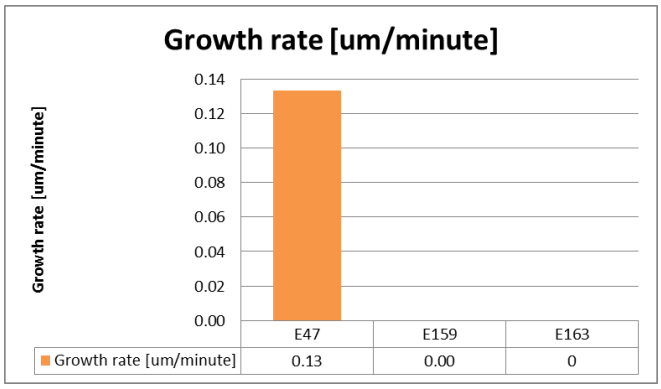

Figure 6.184: The growth rate of sample E47, E159 and E163

6.6.7 PP versus TP

SiAlFe-TP-E47 (TP: 30 minutes)	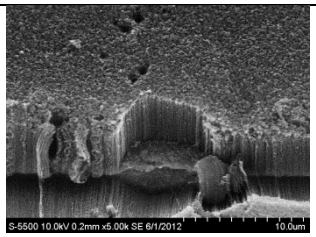 Figure 6.185: Low resolution SEM image of SiAlFe-TP-E47 with 30^0 tilting	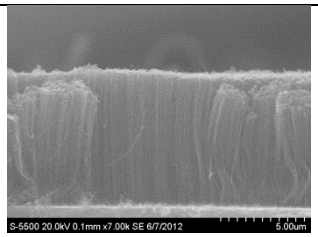 Figure 6.186: Low resolution cross section SEM image of SiAlFe-TP-E47	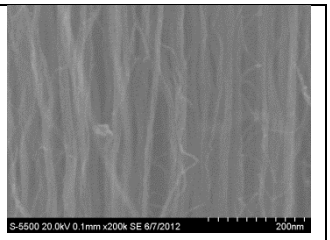 Figure 6.187: Ultra-High resolution cross section SEM image of SiAlFe-TP-E47
SiAlFe-TP-E183 (TP: 15 minutes)	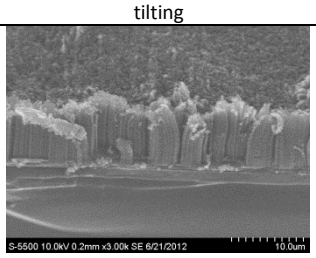 Figure 6.188: Low resolution SEM image of SiAlFe-TP-E183 with 30^0 tilting	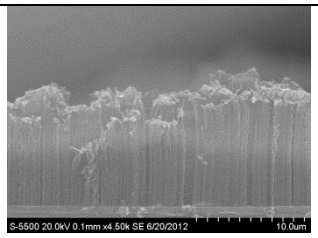 Figure 6.189: Low resolution cross section SEM image of SiAlFe-TP-E183	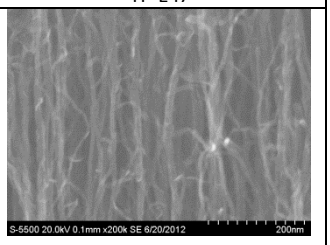 Figure 6.190: Ultra-High resolution cross section SEM image of SiAlFe-TP-E183
SiAlFe-TP-E155 (TP: 5 minutes)	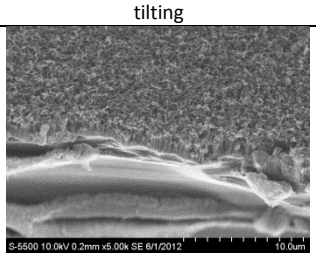 Figure 6.191: Low resolution SEM image of SiAlFe-TP-E155 with 30^0 tilting	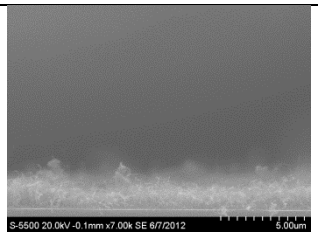 Figure 6.192: Low resolution cross section SEM image of SiAlFe-TP-E155	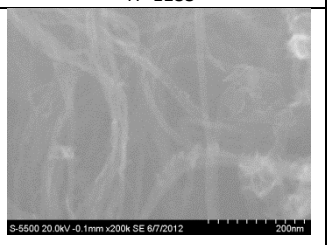 Figure 6.193: Ultra-High resolution cross section SEM image of SiAlFe-TP-E155
SiAlFe-PP-E151 (PP: 30 minutes)	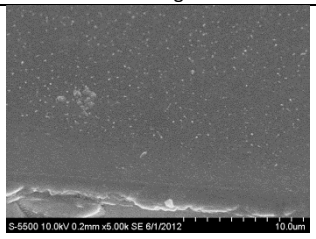 Figure 6.194: Low resolution SEM image of SiAlFe-PP-E151 with 30^0 tilting	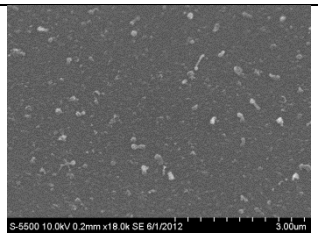 Figure 6.195: High resolution SEM image of SiAlFe-PP-E151 with 30^0 tilting	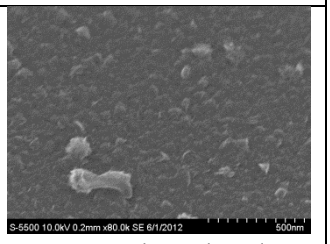 Figure 6.196: Ultra-High resolution SEM image of SiAlFe-PP-E151 with 30^0 tilting
SiAlFe-PP-E147 (PP: 15 minutes)	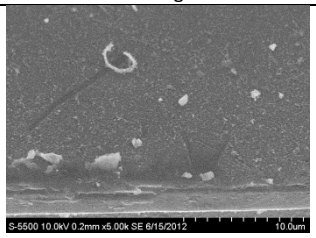 Figure 6.197: Low resolution SEM image of SiAlFe-PP-E147 with 30^0 tilting	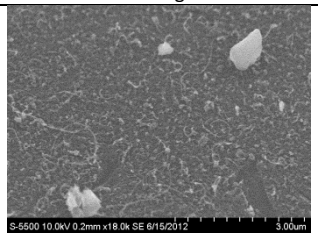 Figure 6.198: High resolution SEM image of SiAlFe-PP-E147 with 30^0 tilting	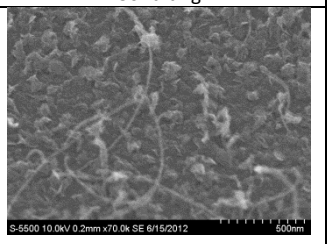 Figure 6.199: Ultra-High resolution SEM image of SiAlFe-PP-E147 with 30^0 tilting

SiAlFe-PP-E143 (PP: 5 minutes)	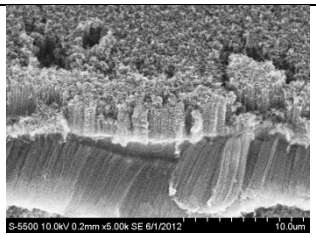 Figure 6.200: Low resolution SEM image of SiAlFe-PP-E143 with 30^0 tilting	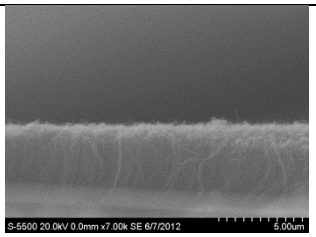 Figure 6.201: Low resolution cross section SEM image of SiAlFe-PP-E143	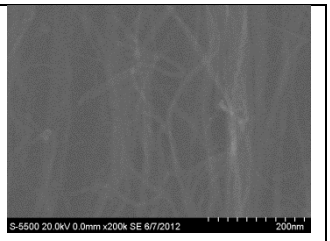 Figure 6.202: Ultra-High resolution cross section SEM image of SiAlFe-PP-E143

No growth were recorded for any of the batches with catalyst layers of 3, 6 and 10 nm, except for the batch that was treated with PP for 5 minutes which led to VACNTs growth on the 3 nm (E144) sample.

The tallest VACNTs were received with TP for 15 minutes. The growth that was provided by the PP samples was not very impressive, which this experiment disagrees with earlier suggestion of that PP is the best pretreatment among these two. But this could be caused as the optimal PP value has not been found yet. Long PP time can also cause particles to coalescence which would increase the diameter. A great example can be found by comparing sample E143 and E147, where an increased diameter occur for the E147 since it has longer TP time. Longer TP times should give better growth that is why it is strange that the tallest VACNTs are found in E183 and not in the E47. This could be because of coalescence/sintering of parties as 30 minutes is to long time, otherwise it could be since the E183 was made with the new preparation procedure which did not cause any damage to the CNTs (because the other was scribed and broken manually after CNT growth).

The average height, diameter and growth rate for this section can be found in Figure 6.203 - Figure 6.205.

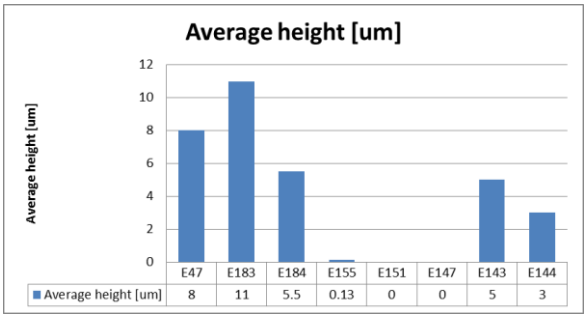

Figure 6.203: The average height of sample E47, E143, E147, E151, E155and E183

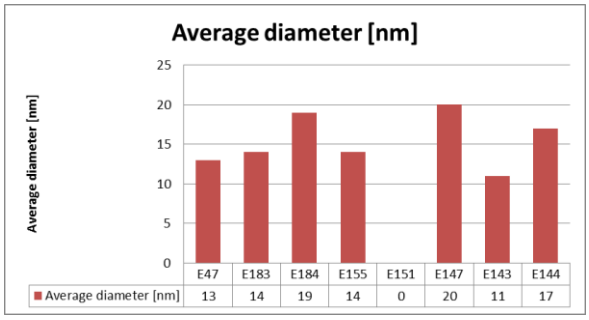

Figure 6.204: The average diameter of sample E47, E143, E147, E151, E155and E183

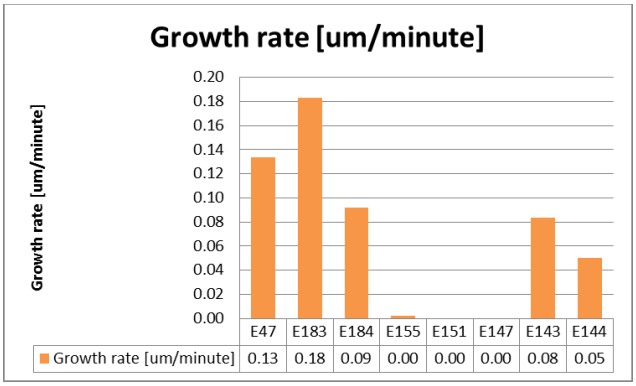

Figure 6.205: The growth rate of sample E47, E143, E147, E151, E155and E183

6.6.8 Replacing NH_3 with N_2O

For the samples (Figure 6.206 - Figure 6.220) in this section NH_3 was replaced with N_2O during the pretreatment stage only, to see the effect of how an oxidizing atmosphere would influence the growth.

SiAlFe-TP-E47 (TP: NH_3 50 sccm)	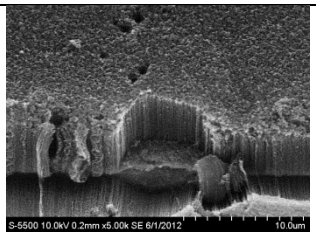 Figure 6.206: Low resolution SEM image of SiAlFe-TP-E47 with 30^0 tilting	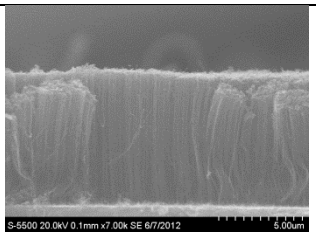 Figure 6.207: Low resolution cross section SEM image of SiAlFe-TP-E47	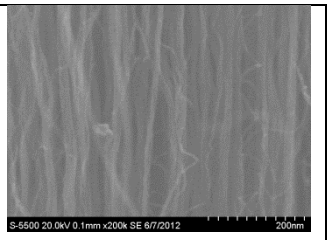 Figure 6.208: Ultra-High resolution cross section SEM image of SiAlFe-TP-E47
SiAlFe-TP-E115 (TP: N_2O 50 sccm, 1 nm catalyst layer thickness)	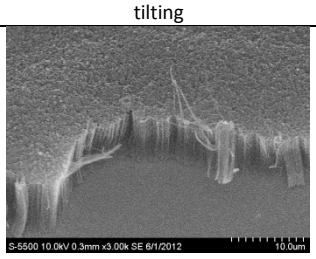 Figure 6.209: Low resolution SEM image of SiAlFe-TP-E115 with 30^0 tilting	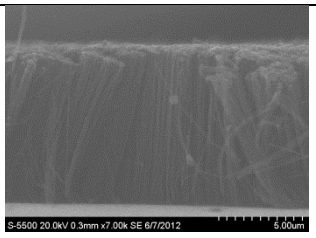 Figure 6.210: Low resolution cross section SEM image of SiAlFe-TP-E115	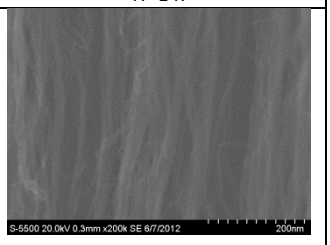 Figure 6.211: Ultra-High resolution cross section SEM image of SiAlFe-TP-E115
SiAlFe-TP-E116 (TP: N_2O 50 sccm, 3 nm catalyst layer thickness)	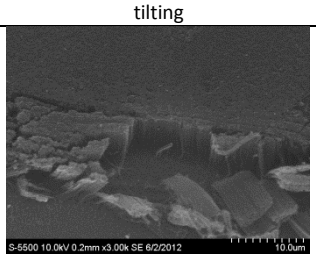 Figure 6.212: Low resolution SEM image of SiAlFe-TP-E116 with 30^0 tilting	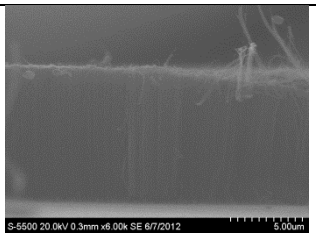 Figure 6.213: Low resolution cross section SEM image of SiAlFe-TP-E116	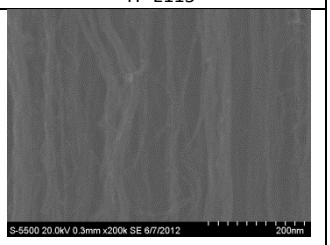 Figure 6.214: Ultra-High resolution cross section SEM image of SiAlFe-TP-E116
SiAlFe-TP-E117 (TP: N_2O 50 sccm, 6 nm catalyst layer thickness)	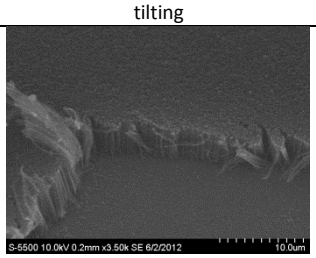 Figure 6.215: Low resolution SEM image of SiAlFe-TP-E117 with 30^0 tilting	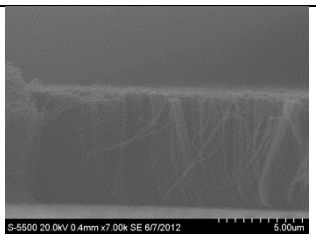 Figure 6.216: Low resolution cross section SEM image of SiAlFe-TP-E117	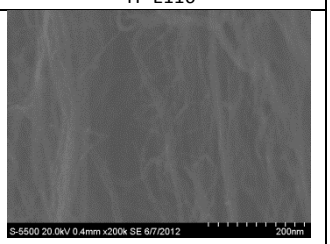 Figure 6.217: Ultra-High resolution cross section SEM image of SiAlFe-TP-E117
SiAlFe-TP-E118 (TP: N_2O 50 sccm, 10 nm catalyst layer thickness)	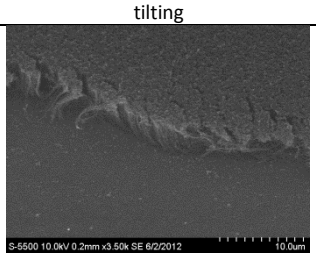 Figure 6.218: Low resolution SEM image of SiAlFe-TP-E118 with 30^0 tilting	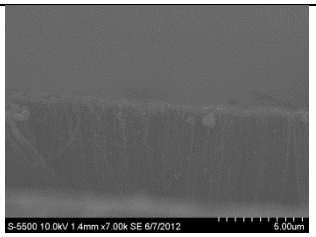 Figure 6.219: Low resolution cross section SEM image of SiAlFe-TP-E118	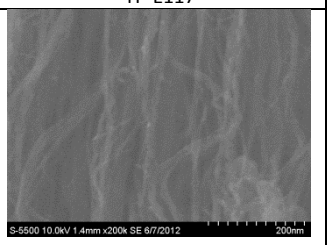 Figure 6.220: Ultra-High resolution cross section SEM image of SiAlFe-TP-E118

Pretreatment in an oxidized atmosphere seems to have a high potential, based on the SEM images for this section. This kind of treatment has shown to give the following:

- The highest VACNTs among the samples (E47 – E166).
- VACNTs with the smallest diameter (E47 – E166).
- VACNTs on all catalyst thicknesses within the batch (E47 – E166).

In addition, the oxidizing treatment could have enhanced the density, but this is difficult to verify it from these images. As it is widely believed that the catalytic activity occurs when it is in its metallic state only, the activation of them must have been triggered by the reducing atmosphere that are provided by the hydrocarbons.

As growth occurs for all the samples within the batch, it can clearly be observed that the size of the nanoparticles increase with increasing catalyst layer thicknesses. The growth for E115 and E116 exceeds height of the E47 by ≈ 1.5 um. This leads to a tiny increase in growth rate. The average height, diameter and growth rate of the samples within this section is found in Figure 6.221 - Figure 6.223.

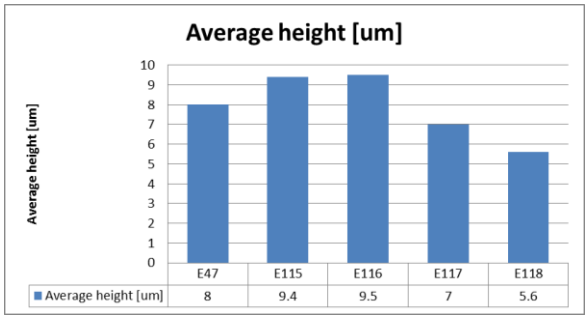

Figure 6.221: The average height of sample E47, E115, E116, E117 and E118

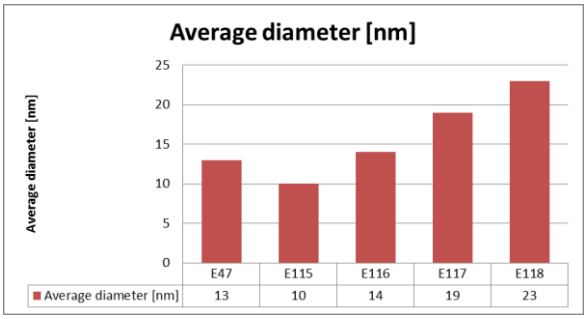

Figure 6.222: The average diameter of sample E47, E115, E116, E117 and E118

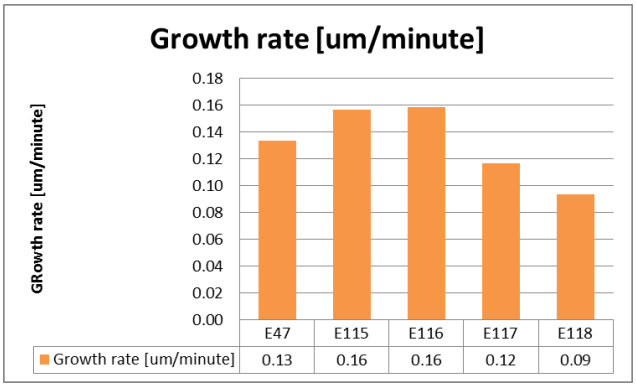

Figure 6.223: The growth rate of sample E47, E115, E116, E117 and E118

6.6.9 Starting directly at 650^{0}C

The purpose with the samples in this section was to figure out if the slow heating and cooling cycle had any purpose at all, since these cycles occupied about 50% of the time that was needed for executing one run with the "CNTRecipe".

SiAlFe-TP-E47 (Slow heating and cooling cycle used)	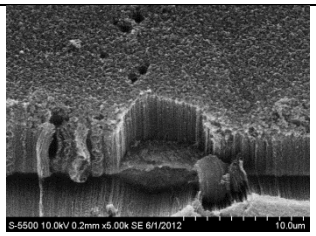 Figure 6.224: Low resolution SEM image of SiAlFe-TP-E47 with 30^0 tilting	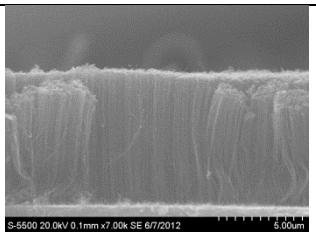 Figure 6.225: Low resolution cross section SEM image of SiAlFe-TP-E47	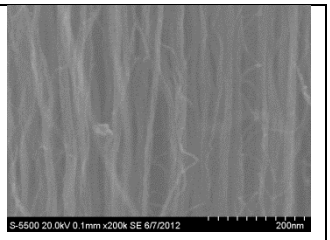 Figure 6.226 Ultra-High resolution cross section SEM image of SiAlFe-TP-E47
SiAlFe-TP-167 (TP)	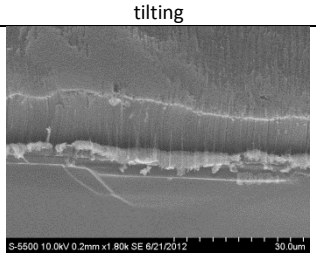 Figure 6.227: Low resolution SEM image of SiAlFe-TP-E167 with 30^0 tilting	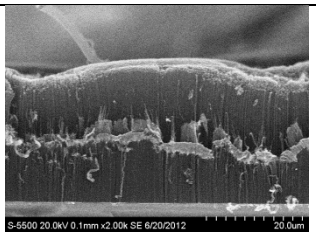 Figure 6.228: Low resolution cross section SEM image of SiAlFe-TP-E167	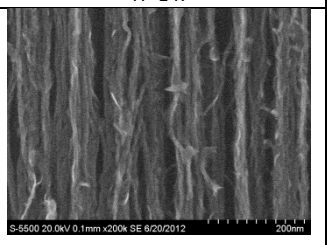 Figure 6.229: Ultra-High resolution cross section SEM image of SiAlFe-TP-E167
SiAlFe-PP-E171 (PP)	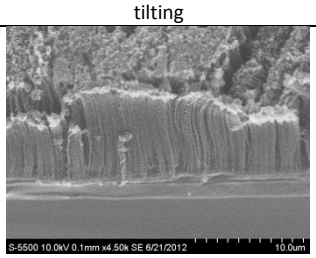 Figure 6.230: Low resolution SEM image of SiAlFe-PP-E171 with 30^0 tilting	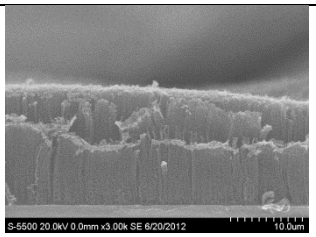 Figure 6.231: Low resolution cross section SEM image of SiAlFe-PP-E171	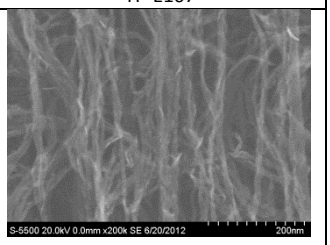 Figure 6.232: Ultra-High resolution cross section SEM image of SiAlFe-PP-E171
SiAlFe-TP-E219 (TP, growth time: 10 minutes)	Figure 6.233: Low resolution SEM image of SiAlFe-TP-E219 with 30^0 tilting	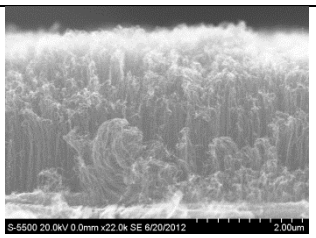 Figure 6.234: Low resolution cross section SEM image of SiAlFe-TP-E219	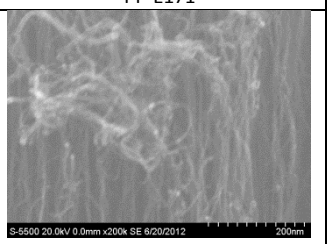 Figure 6.235: Ultra-High resolution cross section SEM image of SiAlFe-TP-E219

For all the samples within the three batches successful growth of VACNT was observed. This was also the situation for the samples that was processed for 10 minutes (E219).

The E167 sample has the tallest and densest VACNTs of the entire experiment. The sample that was grown confirms that the time for initiation among the samples in this section does not need over 30 minutes to be initiated. When comparing the height of sample E219 and E167, it is confirmed that the growth rate is not constant through the entire growth process, as this should have led 3*6 = 18 um tall VACNTs for E167. It is not possible to decide which one of the E47 or E167 sample that has the highest density. The average height, diameter and growth rate of the samples within this section is found in Figure 6.221 - Figure 6.223.

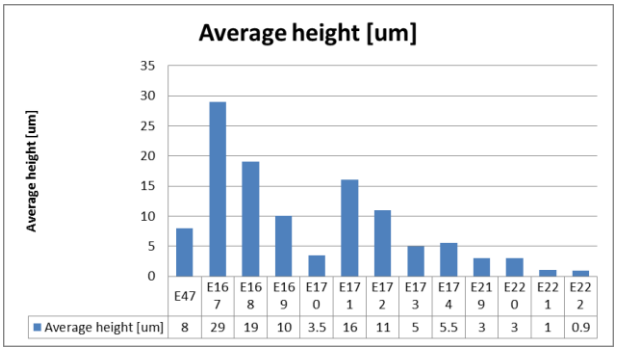

Figure 6.236: The average height of sample E167, E168, E169, E170, E171, E172, E173, E174, E219, E220, E221 and E22

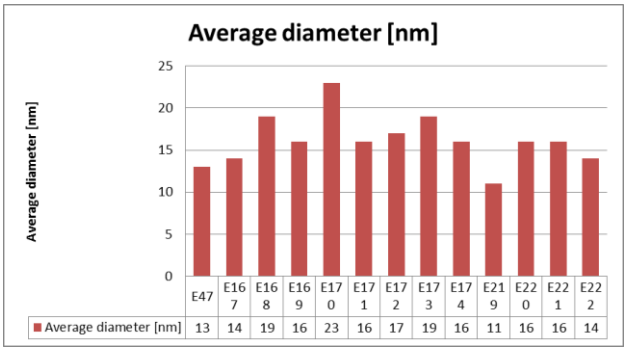

Figure 6.237: The average diameter of sample E167, E168, E169, E170, E171, E172, E173, E174, E219, E220, E221 and E22

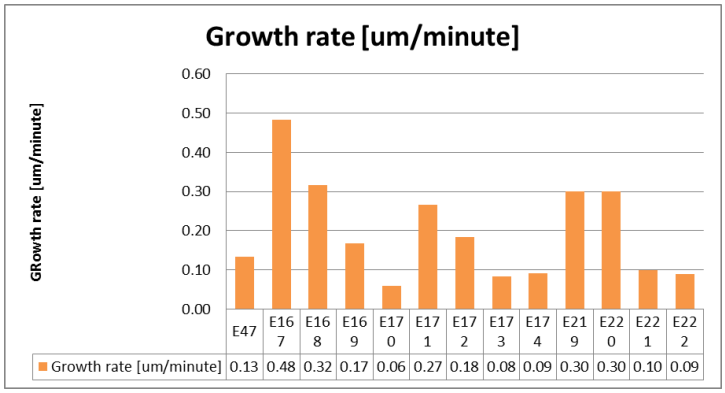

Figure 6.238: The growth rate of sample E167, E168, E169, E170, E171, E172, E173, E174, E219, E220, E221 and E22

6.6.10 TEM analysis

The images from the TEM session are presented below. Commercial holy grids can be seen to give much better quality in the high resolution images, since they contain voids. When comparing the E115 and E115 on CHG at 300k, it can be seen that the amorphous polymer film in E115 makes it challenging to differentiate between the polymer film and the walls, as the image gets blurry. The polymer films have been applied to all the holy grids except the E115 CHG.

E47	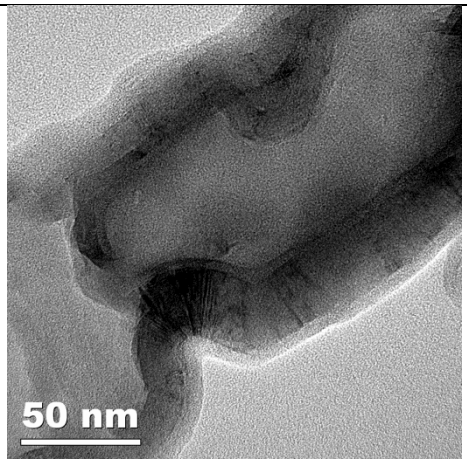 Figure 6.239: TEM images of E47 at 100k magnification	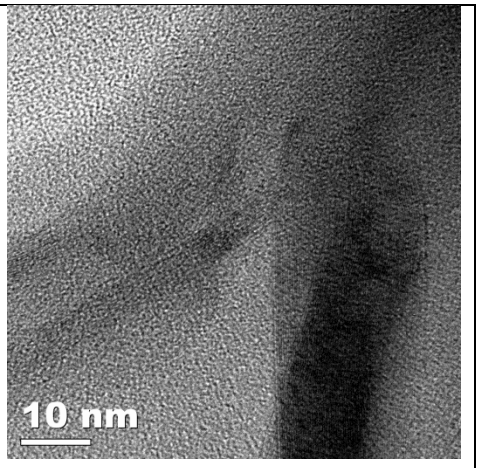 Figure 6.240: TEM images of E47 at 300k magnification

E91	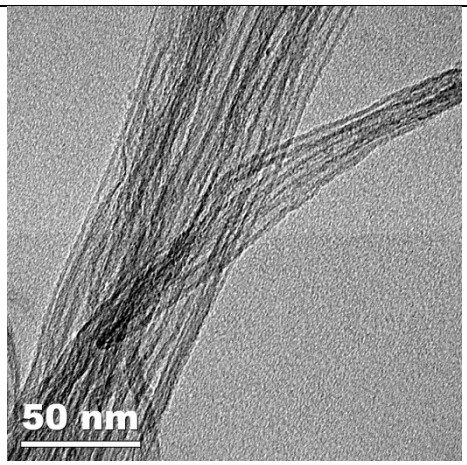 Figure 6.241: TEM images of E91 at 100k magnification	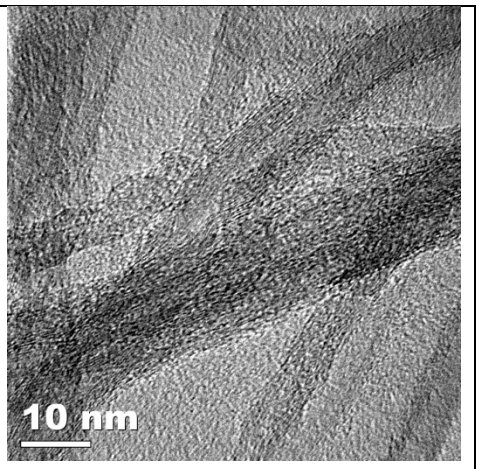 Figure 6.242: TEM images of E91 at 300k magnification
E115	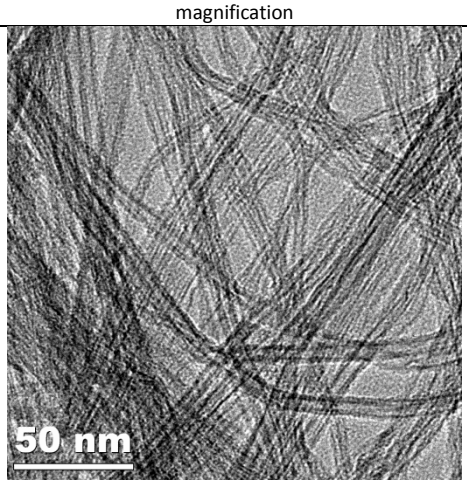 Figure 6.243: TEM images of E115 at 100k magnification	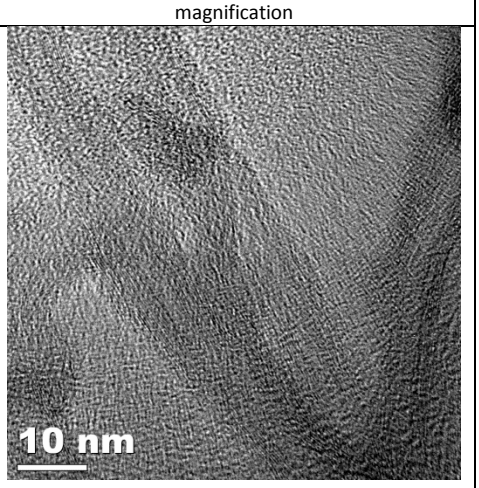 Figure 6.244: TEM images of E115 at 300k magnification
E115 on CHG (commercial holy grid)	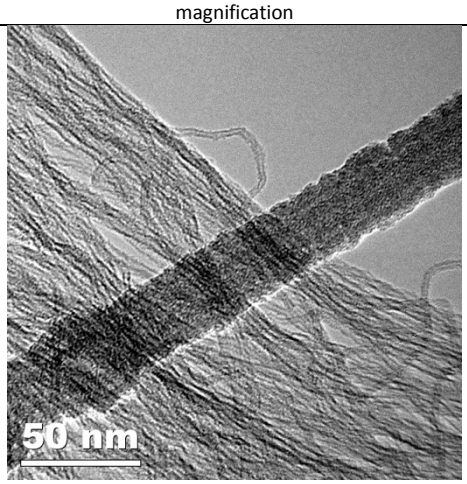 Figure 6.245: TEM images of E115 on CHG at 100k magnification	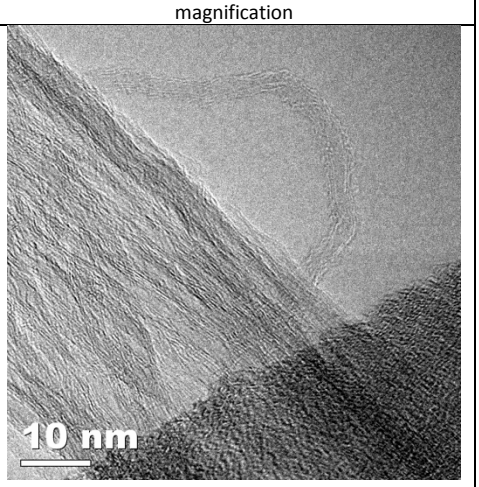 Figure 6.246: TEM images of 115 on CHG at 300k magnification

E115 (no barrier layer)	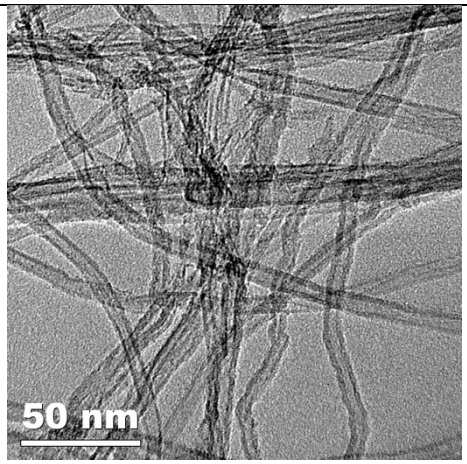 Figure 6.247: TEM images of E115 (no barrier layer) at 100k magnification	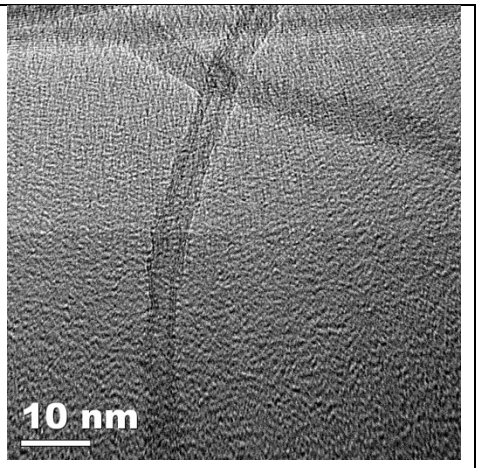 Figure 6.248: TEM images of E115 (no barrier layer) at 300k magnification
E119	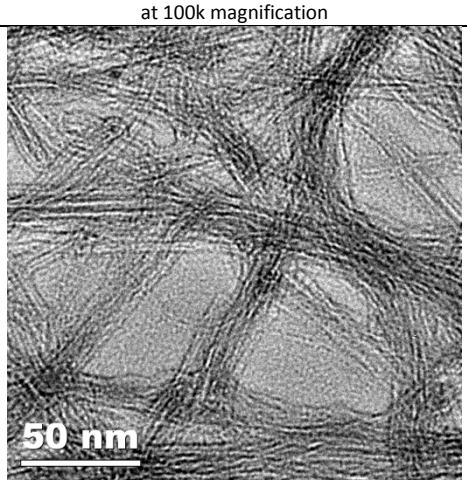 Figure 6.249: TEM images of E119 at 100k magnification	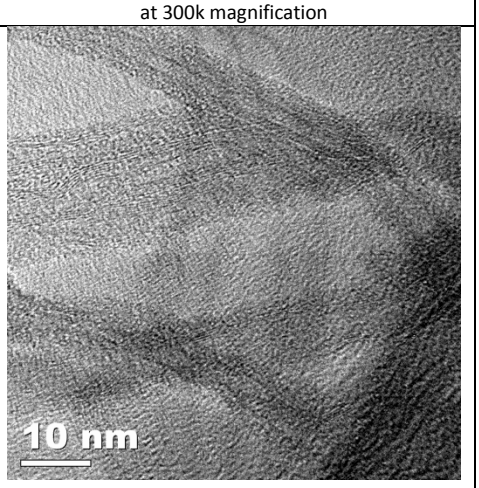 Figure 6.250: TEM images of E119 at 300k magnification
E143	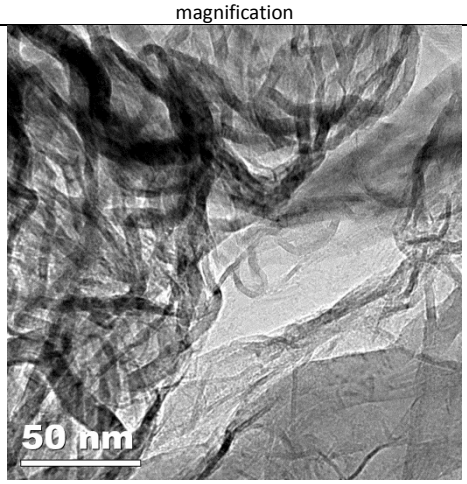 Figure 6.251: TEM images of E143 at 100k magnification	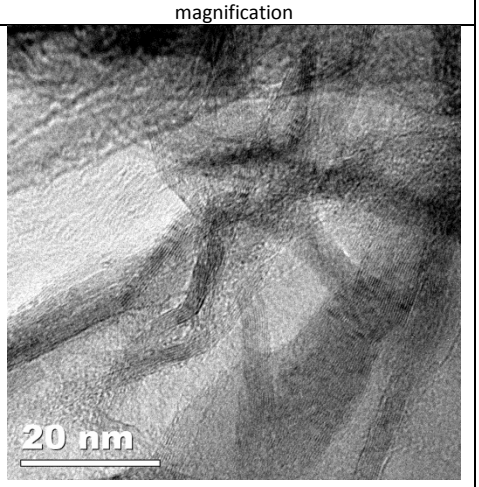 Figure 6.252: TEM images of E143 at 300k magnification

E159	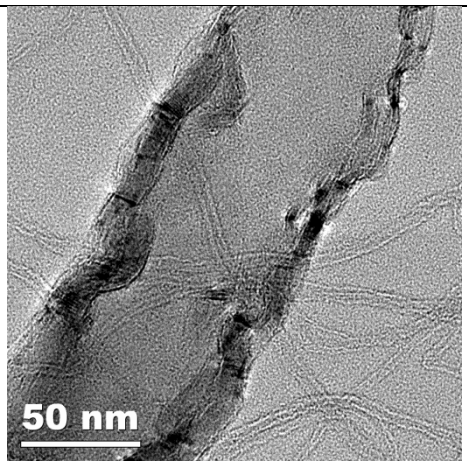 Figure 6.253: TEM images of E159 at 100k magnification	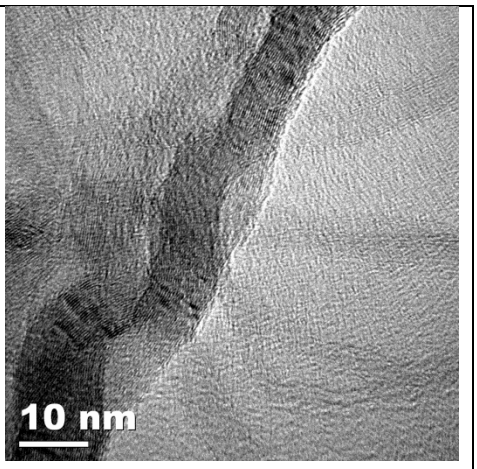 Figure 6.254: TEM images of E159 at 300k magnification

Even if it is difficult to see the individual tubes and their number of walls on the amorphous polymer film, it is possible to see that the walls/shells, which are sheets of graphene, are parallel in the tube's direction. This verifies that the filaments in the samples are CNTs. As the tubes are bright they have a crystalline structure, which was expected as they are verified to be CNTs.
All the tubes that are found in the samples are MWCNTs of various sizes. Different MWCNTs are also found within each sample, which is most likely because:

- The size of the nanoparticles that are formed during the pretreatment could different. Even if these are small, they will affect the size of the MWCNT.
- As CNT growth occurs on the edges as well (mentioned in chapter 6.2), these MWCNTs will be different than those which are grown on the surface, as they have particles of different sizes.

Some of the sample has been mentioned to have been scraped with a scalpel since they did not disperse into the ethanol during the ultrasonic bath. The CNTs that was scraped off the surface was more knotted and not as dispersed on the holy grids as the non-scraped sample were. That was why tracking individual tubes in the TEM part was difficult. It is uncertain whether any mechanical damage occurred for these samples or not. Scraping was done for the E47, E143 and E159 sample. Image of the bottles with dispersed CNTs in ethanol can be seen in Figure 6.255.

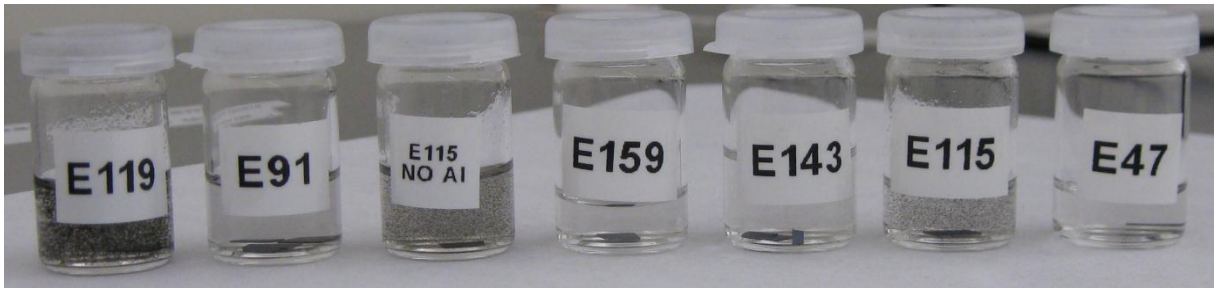

Figure 6.255: Image of the TEM samples. Particles for the samples where CNTs were dispersed in ethanol by ultrasonic methods are visible, while particles for the scraped samples are not.

The number of shells in the MWCNTs is provided in Table 6.13, and has its basis from the 300k images. It should be mention that this number is not accurate, as the amorphous polymer film in the background makes it difficult to count the number of shells. The diameter of E143 is not provided, since it was impossible to track any individual tubes. It can be seen that the diameter that were provided with the SEM images always seems to be larger than those from the TEM images. This is, as

mentioned earlier, because it is difficult to distinguish between individual or bundled CNTs in the SEM images.

Sample	Number of shells/walls in the MWCNT	Diameter [nm]
E47	10 - 15	15
E91	8 - 13	6
E115	2 - 10	7
E115 (no barrier layer)	2 - 9	5
E119	4 - 8	7
E143	6 - 12	N/A
E159	5 - 12	6

Table 6.13: The number of shells and diameter of the MWCNTs in the samples that were analyzed with the TEM

The distance between the shells of the MWCNTs can be figured out by the E155 CHG sample, since there is no amorphous polymer film in the background (Figure 6.256). The distances at both points were found to be 0.39 nm (point 1 and 2) when assuming that the distance between each shell is equal. This deviates from the expected value of 0.34 nm [135]. However, due to uncertain range from the TEM and the subsequent enlargement to the final format between the TEM and the computer, an error of plus-minus 0.05 nm is reasonable to assume.

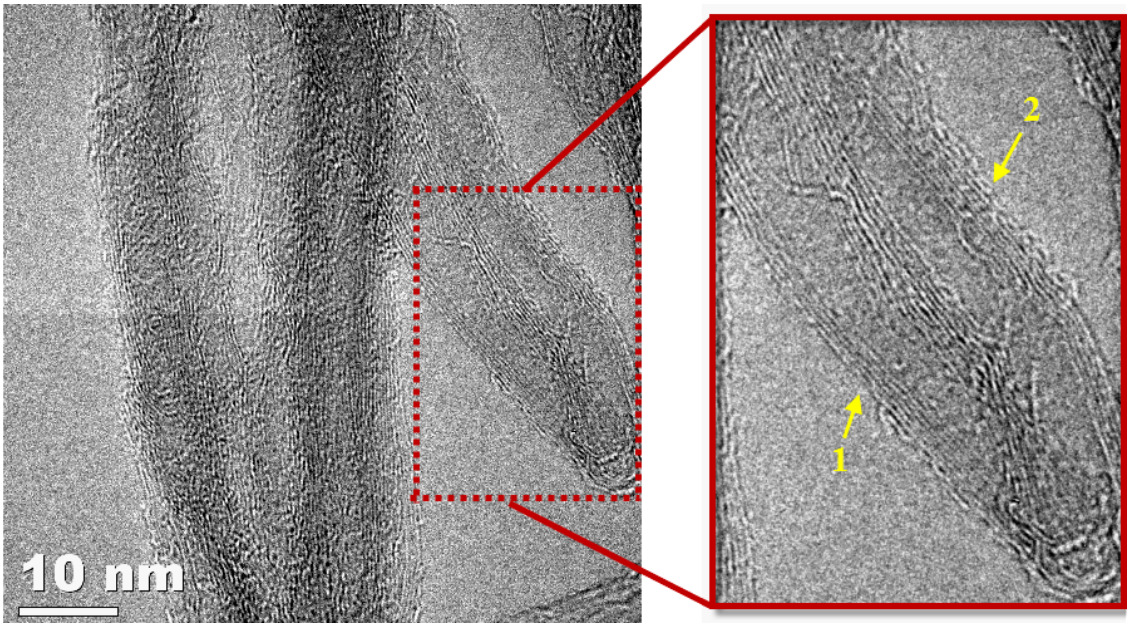

Figure 6.256: The distance between the graphene planes can be found this TEM image. The distance was measured with a ruler and the scale bar

7 Discussion

Let us first sum up the samples that did not yield any VACNT or sparse amounts of CNTs:

- Samples with CH4 flow less than 50 sccm.
- Samples where CH4 was mixed with NH3.
- Samples with growth time lower than 60 minutes.
- Samples with no power.
- Samples that were processed with temperatures lower than 600^0C.
- Samples with PP treatment time more than 5 minutes.

7.1 Decomposition of hydrocarbons

CH_4 is the most inert among the hydrocarbons and its direct conversion to higher hydrocarbons is well known to be a difficult process. In our experiment a RF plasma reactor was used to decompose CH_4 into other products, which in an earlier experiments, observed to be a mixture of C_2H_2, ethylene (C_2H_4) and ethane (C_2H_6) [136]. In addition, it is probable that not all the fed CH_4 gets converted. The composition of this mixture will vary with the following factors:

- Feeding rate (flow) of CH_4 into the plasma.
- Chamber pressure.
- Plasma power.

During the "CNTRecipe" an operational pressure of 1 Torr was used (1000 mTorr). That is why Figure 7.1 - Figure 7.2 does not provides accurate description of the content in the plasma for our case, but could give an indication of what would be happening when variation in pressure, feeding rate and plasma power is performed. It is impossible to provide an accurate value for the amount of C_2H_2, C_2H_4 and C_2H_6 in the CH_4 plasma, as the pressure in these figures is at least 20 times higher than to what was used in our experiment.

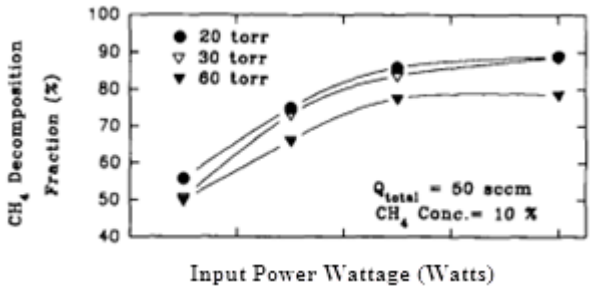

Figure 7.1: How much of the fed CH4 that is converted [136]

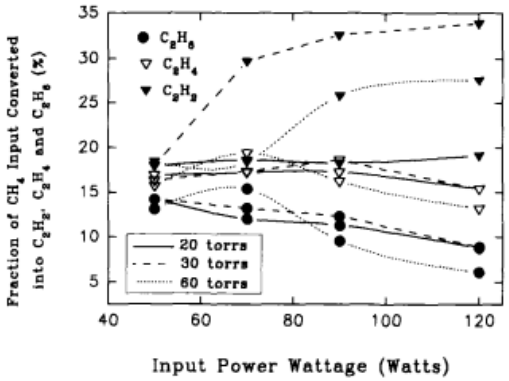

Figure 7.2: Fraction of C2H2, C2H4 and C2H6 of CH4 input for various plasma power and operating pressures [136]

In Figure 7.1 it can be seen that the amount of decomposed CH_4 increases with higher plasma power for all pressures, but after reaching a power of ≈ 120 W if becomes constant and an additional amount of power will not increase the decomposition rate of CH_4. A power between 90 – 120 W seems to give the highest amount of decomposed CH4. Based on these powers it can be noticed in Figure 7.2 that the mixture of the decomposed CH_4 develops by the following:

- Fraction of C_2H_2 increases with increasing power at all pressures.
- Fraction of C_2H_4 decreases with increasing power at all pressures.
- Fraction of C_2H_6 decreases with increasing power at all pressure.

These could indicate that C_2H_2 was the primary hydrocarbons gas that was decomposed on the catalysts and confirm the fact that the content of carbon species increases with higher power, which is suggested in earlier experiments. If the catalyst particle is able to decompose these increasing amounts of hydrocarbons, the growth rates would most likely increase. Otherwise it could lead to an overgrowth of a:C and a graphitic layer that could cover the catalyst's surface which could lead to termination of growth, as no hydrocarbons are able to reach through. It is important to be aware that increased power will lead to increasing etching rates as well. The ratio of the growth rate and etch rate need to be kept above 1 for achieving growth, but should be kept as high as possible to insure as high growth rate as possible.
For our experiments it can be seen that the VACNTs in the sample that was processed with 100 W yielded the tallest tubes among the samples were variation of the power parameter occurred. The increasing growth due to increased power is confirmed in our samples, when considering that:

- Reducing power resulted in no or shorter VACNTs.
- Increased power resulted in shorter VACNTs, when exceeding 100 W.

This is because the reducing power will cause lower amounts of decomposed hydrocarbons which decrease the growth. For the samples with reducing growth a more efficient decomposition will most likely exists, but as the etch rates becomes more intensified they becomes shortened. As sample E195 was processed with 0 W of power, it was really processed by CVD instead of PECVD. This particular sample illustrates the efficient decomposition of the plasma rather than by thermal, and that lower temperatures are possible when decomposition with an RF plasma reactor is used.

When considering the samples where CH_4 flow was varied, higher flows did not involve any higher growth. The sample that was processed with 50 and 100 sccm seemed like a duplicate of each other, as the height of the VACNTs was exactly the same. One explanation is that since their diameter was equal, the amount of hydrocarbons that was possible to decompose on the catalytic particle was equal as well, as it is known that small particles are able to decompose hydrocarbons more quickly as they have high surface energy and mobility which would lower the melting point, which would increase their activity.

Another reason is the that increased flow of CH_4 actually increased the growth rate for a short while, but since the catalyst was not able to handle this amount of flow more and more a:C was deposited which coated the catalyst particle. This led to that growth was terminated, while etching occurred for the remaining time of the growth step. Of course, this explanation seems less likely, but since it is impossible to observe the VACNTs during growth it is difficult to conclude which one that is truly right.

The chemical reactions for the decomposition of the hydrocarbons on the catalysts will most likely be affected by temperature, pressure, type of hydrocarbon, type of hydrocarbon etc. That is why is unknown exactly what these were. The only reaction that is certain, which is illustrated in Figure 7.4, is that CH_4 is fed into the PECVD reactor and result in CNT growth.

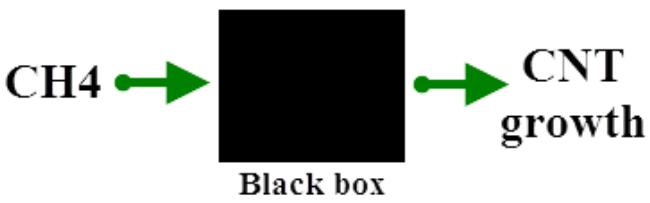

Figure 7.3: Basic reaction of how CH_4 result in CNT growth

7.2 Temperature during growth

The samples in the batches that was processed at different temperatures showed no growth below 600^0C, but while growth at 700^0C resulted in growth of VACNT in the samples with 1 and 3 nm thick catalyst layer. One of the main advantages with the PECVD is that growth should be possible to be done at lower temperatures, which would keep the catalyst in its solid phase. However, since it is not entirely figured out how the plasma assists in the decomposition process of the catalyst particles, it is difficult to explain why no growth has occurred at these samples.

The behavior among the samples at higher temperatures is caused by the increased carbon diffusion rate which increases with temperature, since a certain temperature are requires to phase transform the catalyst to a liquid. Lower temperatures keep the catalyst in its solid phase which decreases the diffusion rate. Since the catalytic activity of the catalyst increases at higher temperatures, the amount of a:C is also suggested to decrease.

In our results, the final height of the VACNTs as 650^0C was taller than those processed at 700^0C. This does not necessarily mean that highest temperature did not promote growth rate, but higher temperature could also lead to earlier exhaustion of the catalyst due to evaporation of Fe atoms, which could cause that growth ends sooner than for the 650^0C sample. Even though the growth stops, etching goes on for the remaining time of the growth step and shortens the VACNTs.

The importance of having a barrier layer can be seen when comparing those who have and have not. The barrier layer is a thermal protection layer towards diffusion of Fe into the Si substrate which would have promoted silicides that are known for giving lower growth and density. This can easily be observed from our samples that were grown with and without such a layer. In addition, a barrier layer is also believed to promote VACNT growth, which is verified by our samples as well.

7.3 Long initiation time before growth

The samples that were processed with mixing CH4 with NH_3 during the growth step did not cause any CNT growth. During variation of growth time, analysis of the SEM images indicated that growth initiated after being exposed for CH_4 plasma between 30 – 60 minutes. The common factors with these samples, is that they are all slowly heated from 300 - 650^0C in a flow of NH3. The results from those that were not heated with NH_3 flow show superior growth (E167, E168 and E219) compared to other samples, when considering the height only. This result was very strange as earlier experiments have reported successful when using NH_3 during the pretreatment and growth step.

To investigate whether the E167 sample suffered from long initiation time before growth, as sample with similar parameters (E219) but with growth time of 10 minutes only was processed. As it gained 3 um of growth after its growth time, this confirms that the pretreatment in NH_3 is not the main reason for the long initiation time.

The only factor that was left and had to be responsible for the slow imitation of growth was the slow heating in NH_3. If dividing the whole reaction of CNT growth into smaller reactions, it could be looking similar to this:

1. Decomposition of CH_4 into C_2H_2, C_2H_4 or/and C_2H_6 (higher hydrocarbons).
2. Transportation/diffusion of higher hydrocarbons down to the sample's surface.
3. Adsorption of them on the catalyst particles
4. Decomposition of them on the catalyst particles, where carbon are used for CNT growth while H remains.
5. Creation of H_2 from H.
6. Transportation/diffusion of H_2 away from the catalyst.

It does not seem likely that NH_3 can influence any other of these steps except number 3. So the slow initiation time could be explained to be because of slow adsorption of hydrocarbons. This could be because of the massive amounts of NH_3 that are left behind in the chamber which suppresses the decomposition of the hydrocarbons, because of the chemical bonds that are found to be weaker in the NH_3 molecule. This will in the start lead to an extreme slow decomposition of the hydrocarbon, but will increase with time. Remember that plasma etching does still occurs, so the decomposition need to reach a limit, where it need to exceeds etching to allow any CNTs to be grown. Somewhere after 30 minutes this was the case, and CNT growth was initiated.

7.4 PP versus TP

In general, one consider TP as being more time demanding pretreatment as it usually needs longer time for transforming the catalyst layer into nanoparticles when comparing with PP. From our samples it can be seen that is the actually the case, since 15 minutes of TP was required for achieving VACNTs. Shorter TP times led to CNTs only. Quite the opposite is seen for PP which yielded VACNTs when processing for 5 minutes, while longer treatment time leaves CNTs. This is believed to be the case since PP is more intense and are believed to give more stable nanoparticles, compared to the TP. This makes it more efficient in forming thicker catalyst layers into nanoparticles. An example is from our experiment shows that this is the case. In the batch when PP was run for 5 minutes, VACNT growth occurred to the 1 and 3 nm sample, which was not the case for any of the samples with TP.

However, long PP time destabilize the nanoparticles, similar to TP, which means that the particles are entitled to diffuse into the barrier layer and could involve termination of their catalytic activity. Anyway, long runs with PP or TP could most likely cause particles to coalescence which would increase their diameter. An excellent example is the increased diameter of E147 (15 minutes) to the E143 (5 minutes), as it has longer PP time. From our experiment TP yielded the tallest and densest VACNTs, which could be because that the optimal PP parameters were not found during our experiment.

Since the TP showed the highest potential, it was used for pretreatments with an oxidizing atmosphere. This was done by replacing the NH_3 flow with N_2O. The results are quite interesting, since the oxidizing PP gave VACNTs growth on all the samples within the batch. In addition, it resulted in VACNTs that was 50% taller. It is difficult to conclude whether the densities have increased or not.

There would be interesting to see if the oxidizing TP would promote taller VACNTs for the E167 sample, which was the best sample among those that were treated with a reducing atmosphere. Treating the E47 with an oxidizing TP instead of a reducing one yielded 17% taller VACNTs. That is why that there is reasonable to think that the same thing occurs with the E167 sample.

7.5 Reproducibility among the samples

7.5.1 In the Cressington 308R sputter and evaporator

When starting the Thesis, growing of CNTs/VACNTs was suspected to be an easy task that could be achieved by mixing parameters from earlier successful experiments which would yield CNTs at once. This was however not the case and was why trial and error methods was done, something which required a lot of samples. In addition, a total of 148 samples were processed with basis in the "CNTRecipe". This is, together with that there are limitations of how many samples that can be put into the sputter at once, the reason why there can be instability in the results as the samples was

processed under the exact same conditions. In Figure 7.4, 2 samples are present with 30 nm of sputtered-Al, but they were run in different rounds.

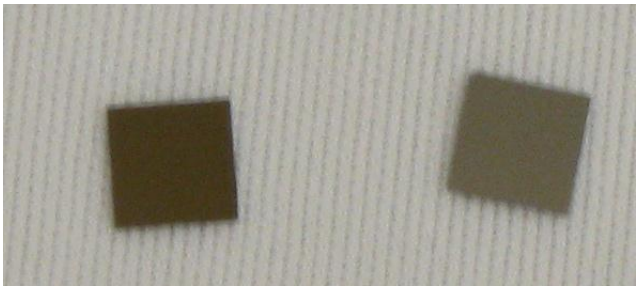

Figure 7.4: Shows two samples from different batches that has the equal Al thicknesses of 30 nm, but have completely different colors

The samples have different color, which is something that indicates that they have different thicknesses, even though the thickness measurement of the sputter unit is equal. The reason for this color difference could due to that:

- Different surface roughness for each sample. A rougher surface would adsorb more light and appear darker.
- The deposition rates varied from time to time, even though equal parameters were used. One reason could be the condition of the target, as a wavy surface on it was observed. Another can be the oxidized Al, as is mentioned next.
- Oxidizing of the Al layer during depositing would be present due to different oxygen and humidity content on the chamber walls (as the vacuum in the chamber is not that high and could have small deviates between each round). This would cause continuously oxidizing during the deposition process and could be an explanation of different deposition rates.
- Since other users were deposition other material, such as Au, Si, Cu etc., there were different particles between each round that was ran for our samples.

7.5.2 In the PECVD

A cleaning procedure was ran for the PECVD every once a week. The samples that were ran straightly after cleaning of the PECVD would experience cleaner chamber with less particles compared to the subsequent samplers that was processed afterwards. Observation of the Si carrier and the requires cleaning procedure for it, indicate that a:C was deposited. That is why batches that would be ran after being processing 6 earlier batches without any chamber cleaning, would experience to have a lot more particles flowing around in the chamber. These can lead to:

- Instability in the plasma.
- Making it more difficult to achieve higher pressures that are close to the limitation of the PECVD. When testing was run for finding the max chamber pressure, the highest pressure in the PECVD was 1200 – 1300 mTorr.
- Disturb the path between the decomposed species in the plasma to the substrate.

8 Conclusion

As copying parameters from earlier successful experiments did not yield any CNTs, there was necessary to start from scratch. Since none of 8 parameters that could be varied was known, a study of the resulting nanoparticles after pretreatment was executed. Pretreatment is one of the crucial steps in CNT growth as it transforms the continuous layer of catalyst material into nanoparticles, which is the basis of the CNTs in CVD processes since only one tube are grown from each particle.

The samples that were used in this experiment consisted of the following (where 3 is the bottom and 1 is the top):

1. Catalyst layer of Fe.
2. Barrier layer of Al.
3. Si substrates that were made from 2" Si wafers.

Due to the valuable information from the pretreatment study, successfully VACNTs was yielded with a RF-PECVD in our experiment. The best ones had very high density and height of 29 um. All the samples that were analyzed in TEM revealed MWCNT growth and where one of them only had 2 shells. All the samples were based on the first recipe that yielded CNTs, but where one and one parameter was changed at a time, so that their effect on the CNT growth could be observed. The following thing was verified from this session:

- Diameter increased with higher catalyst layer thicknesses.
- Temperature did not result in increased average diameter.
- Oxidizing pretreatments resulted in higher growth.
- TP was more efficient as pretreatment method compared to PP, as it yielded taller VACNTs in all our samples.
- Barrier layer is highly necessary to achieve high densities and long tubes.
- Higher power could be beneficial as the etching rate and amount of carbon species present increases

During our session a problem of having NH3 gas in the chamber influenced the growth significantly, as it caused very slow initiation of growth. This was probably because of the weaker chemical bonds of the NH3 molecule which suppressed composition of hydrocarbon at the catalyst particle.

Some further works has been proposed in in Appendix D. It would of huge interest to some applications of the CNTs know that they successfully have been grown. In additional, it would be interesting for the future if SWCNT was able to be grown, as this can show the true potential of one single tube.

9 Index of figures

Figure 1.1: Picture of the CNT space elevator, where the cable is believed to be made of CNTs [19]... 3
Figure 1.2: CNTs have a wide area of applications. In the future they could lead to development of anti-icing films for airplanes [20]... 3
Figure 1.3: Shows a graphene which is the basis for the formation of fullerenes. Defect-free hexagonal arrangement will remain flat, while defects (such as the pentagonal or heptagonal rings will curl the sheet [21]... 4
Figure 1.4: Buckministerfullerene, C60 [21]... 4
Figure 1.5: Carbon bonding in diamond and graphite [21]... 4
Figure 1.6: First reported electron microscope image of CNTs by Sumio Iijima [23]... 5
Figure 1.7: Structure of a SWCNT... 5
Figure 1.8: Structure of a MWCNT... 5
Figure 1.9: Illustration for finding the chirality [25]... 6
Figure 1.10: Armchair nanotube [26]... 6
Figure 1.11: Zigzag nanotube [26]... 6
Figure 1.12: Chiral nanotube [26]... 6
Figure 1.13: Structural form of a stacked CNF [27]... 7
Figure 1.14: Image of a stacked CNF [27]... 7
Figure 1.15: Structural form of an herringbone CNF [27]... 7
Figure 1.16: Image of a herringbone CNF [27]... 7
Figure 1.17: Structural form of a CNT [27]... 7
Figure 1.18: Image of a CNT [27]... 7
Figure 2.1: Overview of the synthesis methods for CNTs [30]. A figure of higher quality can be seen in Appendix A... 8
Figure 2.2: CNT formation and transport in the sheath of the arc discharge [31]... 9
Figure 2.3: The arc discharge technique [31]... 9
Figure 2.4: The electric arc discharge method [31]... 9
Figure 2.5: The laser ablation technique [35]... 9
Figure 2.6: Close up of the chamber in the laser ablation technique [32]... 9
Figure 2.7: Catalyst particle at the root during CNT growth (base growth) [35]... 10
Figure 2.8: Catalyst particle at the top during CNT growth (tip growth) [35]... 10
Figure 2.9: Illustration of the tip-growth model. Carbon diffuses around the catalyst particle to form the tubular structure [28]... 10
Figure 2.10: Typical schematic of PECVD set-up [39]... 11
Figure 2.11: Illustration of the PECVD [32]... 11
Figure 2.12: Illustration of the Radio frequency (RF) plasma. The RF signal is used to setup a time varying electric field between the plasma and the electrode. The electric field accelerates electrons in and out of the plasma. The electrons gain energy and ionize the local gas [40]... 11
Figure 2.13: Face of President Obama synthesized by growing vertically aligned CNTs on a patterned catalyst. Each face consists of about 150 million parallel CNTs. By patterning the catalyst, CNT can be grown out of selected regions on the substrate [32]... 11
Figure 2.14: Schematic representation of the PECVD process during catalyst pretreatment which leads to the formation of catalyst nanoparticles [38]... 13
Figure 2.15: Illustration and details regarding the PECVD [40]... 13
Figure 2.16: Measured and simulated cathode temperatures as a function of plasma power. The gas mixture simulated was 54:200 sccm C2H2/NH3 at 12 mbar [53]... 14

Figure 2.17: Cathode-to-anode temperatures profiles for the cases of pure plasma heating versus plasma plus external heating [53] 14
Figure 2.18: Simulated power flows through the cathode under the same conditions (as figure above). The dashed line denotes mechanisms in which energy is gained in the cathode (i.e. heating), while the solid line denotes energy loss mechanisms (i.e. cooling) [53] 14
Figure 2.19: Simulated neutral species in the gas phase as a function of plasma power. The six most dominant species with atomic hydrogen are shown here [53] 14
Figure 2.20: SEM images close to a dust particle and where the inset shows the area under it. No growth occurred directly under the dust particle [49] 15
Figure 2.21: a) Smaller particles are too active and dissolve too much carbon at the beginning. The excess carbon will form a thin layer of graphite that cover the surface of the catalyst particle and will cut the carbon supply to the particle, hence no SWCNT can grow 16
Figure 2.22: Carbon nanotubes grown at different gas ratios, while keeping the other parameters unchanged, a) shows well aligned CNTs, b) shows obelisk-like CNTs, c) shows significant amount of a:C [61] 17
Figure 3.1: Calculated melting points of Fe as a function of particle size (larger particle size to the left) [29] 18
Figure 3.2: Stages in the growth of filaments by the bulk diffusion mechanism [67] 19
Figure 3.3: Stages in the growth of filaments by the diffusion over surface mechanism [68] 20
Figure 3.4: Schematic illustration of the VLS growth mechanism where metallic particle is marked in black and the resulting CNT filament during growth is marked in grey 21
Figure 3.5: MWCNT growth scenario from large particles (typically >> 5 nm) [70] 22
Figure 3.6: SWCNT growth scenario from small particles (typically < 5 nm) [70] 22
Figure 4.1: SEM images after annealing treatment for Al_2O_3/Si wafer [82] 24
Figure 4.2: SEM images after annealing treatment for SiO_2/Si wafer [82] 24
Figure 4.3: SEM images of CNTs grown on Al_2O_3/Si [82] 25
Figure 4.4: SEM images of CNTs grown on SiO_2/Si [82] 25
Figure 4.5: AFM tophology images of as-evaporated and subsequently annealed Fe (≈1.1 nm) films on (a, b) SiO_2/Si and (c, d) Al_2O_3/Si. The catalyst films are annealed at 750^0C at atmospheric pressure in 200:500 sscm of Ar/H_2 for 3 min [85] 25
Figure 4.6: Catalyst evolution: AFM topography images of as-deposited catalyst and catalyst nanoparticles formed on different Al_2O_3 supports after exposure to growth conditions in the absence of C_2H_2 for 1.5 and 5 min. All scale bars are 100 nm [87] 26
Figure 4.7: SEM image showing the effect of Ar [92] 27
Figure 4.8: SEM image showing the effect of NH3 on pure catalyst surfaces. NH3 treatment enhances the formation of catalyzed nanoparticles [92] 27
Figure 4.9: H_2 signal for varying gas ratio [61] 27
Figure 4.10: AFM topography and line profiles of Fe thin films, 0.5 and 2 nm thick, as deposit and annealed at 500^0C in different atmospheres [97] 28
Figure 4.11: I_D/I_G in Raman spectra at different substrate temperatures [98] 29
Figure 4.12: Influence of the variation in temperature on individual CNTs. Increasing growth temperature increases the growth rate [99] 29
Figure 4.13: CNT growth at 550^0C [98] 29
Figure 4.14: CNT growth at 600^0C [98] 29
Figure 4.15: CNT growth at 650^0C [98] 29
Figure 4.16: CNT growth at 700^0C [98] 29
Figure 4.17: CNT growth at 750^0C [98] 29

Figure 4.18: Influence of the variation in time on individual CNTs. CNT height increases approximately linearly with growth time as long as catalyst material is available at the CNT tip [99] 30
Figure 4.19: Cross section SEM images of pretreated samples for 0 min (t_0), 1 min (t_1) and 3 min (t_3) [54] 30
Figure 4.20: Cross section SEM images of Pt-CNT growth on SiO_2 support using CH_4/NH_3 ratios of 3. T_0, t_1 and t_2 are equal to those in Figure 4.19 [54] 30
Figure 4.21: Variation of gas decomposition with plasma power [61] 31
Figure 4.22: Effect of varying the plasma power while keeping the other parameters constant. Power is 200W on the left and 66W on the right [61] 31
Figure 4.23: Influence of the variation in plasma power on individual CNTs. Increasing power increases etching of the CNT in the NH3 plasma [99] 31
Figure 4.24: Effect of microwave power on nanostructuration under hydrogen plasma at 200W (when pressure is 25 mbar and time is set to 2 min) [101] 31
Figure 4.25: Effect of microwave power on nanostructuration under hydrogen plasma at 250W (when pressure is 25 mbar and time is set to 2 min) [101] 31
Figure 4.26: Effect of microwave power on nanostructuration under hydrogen plasma at 300W (when pressure is 25 mbar and time is set to 2 min) [101] 31
Figure 4.27: Effect of microwave power on nanostructuration under hydrogen plasma at 350W (when pressure is 25 mbar and time is set to 2 min) [101] 31
Figure 4.28: Effect of microwave power on nanostructuration under hydrogen plasma at 400W (when pressure is 25 mbar and time is set to 2 min) [101] 31
Figure 4.29: Effect of microwave power on nanostructuration under hydrogen plasma at 450W (when pressure is 25 mbar and time is set to 2 min) [101] 31
Figure 4.30: TEM image of Ni catalyst nanoparticle at H2 plasma treatment flow of 200 sccm [102] 32
Figure 4.31: TEM image of Ni catalyst nanoparticle at H2 plasma treatment flow of 300 sccm [102] 32
Figure 4.32: TEM image of Ni catalyst nanoparticle at H2 plasma treatment flow of 400 sccm [102] 32
Figure 4.33: Influence of the variation in pressure on individual CNTs. With increasing pressure, etching of the CNT increases, leading to smaller CNTs [99] 32
Figure 4.34: Effect of pressure on nanostructuration at 25 mbar with 2 min by hydrogen plasma [101] 33
Figure 4.35: Effect of pressure on nanostructuration at 30 mbar with 2 min by hydrogen plasma [101] 33
Figure 4.36: Effect of pressure on nanostructuration at 35 mbar with 2 min by hydrogen plasma [101] 33
Figure 4.37: AFM topography and line profiles of Fe thin films 0.5 nm annealed in 500^0C [97] 33
Figure 4.38: The result of Fe nanoparticles size as a function of a 10 nm catalyst film [101] 34
Figure 4.39: The result of Fe nanoparticles size as a function of a 5 nm catalyst film [101] 34
Figure 4.40: The result of Fe nanoparticles size as a function of a 2 nm catalyst film [101] 34
Figure 4.41: Dependency of the average diameter of catalyst nanoparticles on the thickness of Co particles [89] 34
Figure 4.42: SEM image of CNT grown using Fe catalyst with thickness 7 nm (low magnification) [42] 34
Figure 4.43: SEM image of CNT grown using Fe catalyst with thickness 7 nm (high magnification) [42] 34
Figure 4.44: SEM image of CNT grown using Fe catalyst with thickness 3 nm (low magnification) [42] 34

Figure 4.45: SEM image of CNT grown using Fe catalyst with thickness 3 nm (high magnification) [42] 34
Figure 4.46: SEM image of CNT grown using Fe catalyst with thickness 1 nm (low magnification) [42] 34
Figure 4.47: SEM images of 1 nm Ni, Co, Fe deposited onto TiN auppoer and pretreated for 5 min at 500^0C in 100 mbar of H_2 under TP (a-c) and PP (d-f) under 50W plasma power [77] 35
Figure 4.48: Growth model for PP nanoparticles. Schematic diagram of PP sequence (of Fe coated TiN) as function of time or temperature. At PP critical time nanoparticles start diffusing into the underlying support, which is similar to TP growth [94] 36
Figure 4.49: SEM images of 1 nm Ni film deposited onto SiO_2 and pretreated for 5 min at 650^0C in atmospheric pressure, under a) reducing b) oxidizing environments [79] 37
Figure 4.50: High and low magnification top-view SEM images of CNTs grown for 10 min at 650^0C in atmospheric pressure on a 1 nm thin Ni film subjected to a) and b) in RP and d) and e) in OP [79] ... 37
Figure 4.51: Schematic representation of SiO_2 supported Ni restructuring into nanoparticles under RP or OP, and their influence on post-treatment/CNT growth [79] 37
Figure 5.1: The Dynatex DXIII scriber unit [105] 38
Figure 5.2: Shows a Si wafer after being scribed into several smaller samples by the Dynatex machine 38
Figure 5.3: The Pfeiffer Vacuum Classic 500 e-beam evaporator [106] 39
Figure 5.4: Cressington 308R Sputter and Evaporator [107] 39
Figure 5.5: The JetFirst 200 RTP unit [108] 39
Figure 5.6: The PlasmaLab System 100 PECVD (Oxford Instruments) [109] 41
Figure 5.7: The Femto plasma cleaner (Diener Electronics) [110] 41
Figure 5.8: The Hitachi S-5500 Scanning Transmission Electron Microscopy – S(T)EM [112] 42
Figure 5.9: The FEI Helios DualBeam Focused Ion Beam microscopy – FIB [113] 42
Figure 5.10: The JEOL JEM-2010 TEM [115] 43
Figure 5.11: The Vecco Dektak 150 profilometer [116] 43
Figure 6.1: A 5x5 mm sample (in black). The red line is the scribing line 46
Figure 6.2: After scribing away 1.5 mm on one of the edges, the final size becomes 3.5x5 mm. 46
Figure 6.3: The sample (in black) with a line of tape (in blue) across the sample 47
Figure 6.4: The next step is to remove the tape. The tape creates a valley into the deposited layer on the sample 47
Figure 6.5: Measurements with the profilometer on a 30 nm thick Al film, where the green bar is placed on the left side of the valley 47
Figure 6.6: Measurements with the profilometer on a 30 nm thick Fe film, where the green bar is placed on the left side of the valley 47
Figure 6.7: Measurements with the profilometer on a 30 nm thick Al film, where the green bar is placed on the right side of the valley 48
Figure 6.8: Measurements with the profilometer on a 30 nm thick Fe film, where the green bar is placed on the right side of the valley 48
Figure 6.9: Illustration of deposited layers for most samples. Some have been grown without the Al and Al_2O_3 layer 49
Figure 6.10: Illustration of the Cu substrate with the grid pattern. The polymer film is deposited to decrease the grid inner-distance. It is also sticky so that is it easy for particles to adhere to the grid 52
Figure 6.11: It is important to fill up water to the top of the container so that water are able to escape when depositing droplets of polymer 52

Figure 6.12: Image of self-made holy grids which consist of Cu substrates that are coated with a polymer and carbon film 52
Figure 6.13: Image of the load-dock of the PECVD and 6 samples which are supported on a Si wafer during processing. The black layer on the Si wafer is a:C and/or other carbonaceous particles which needs to be removed since they make the wafer slippery 52
Figure 6.14: SiAlFe-PP1 at 35k magnification 54
Figure 6.15: SiAlFe-PP1 at 80k magnification 54
Figure 6.16: SiAlFe-PP2 at 35k magnification 55
Figure 6.17: SiAlFe-PP2 at 80k magnification 55
Figure 6.18: SiAlFe-PP3 at 35k magnification 55
Figure 6.19: SiAlFe-PP3 at 80k magnification 55
Figure 6.20: SiAlFe-PP4 at 35k magnification 55
Figure 6.21: SiAlFe-PP4 at 80k magnification 55
Figure 6.22: SiAlFe-PP5 at 35k magnification 56
Figure 6.23: SiAlFe-PP5 at 80k magnification 56
Figure 6.24: SiAlFe-PP2 at 35k magnification 56
Figure 6.25: SiAlFe-PP2 at 80k magnification 56
Figure 6.26: SiAlFe-PP6 at 35k magnification 57
Figure 6.27: SiAlFe-PP6 at 80k magnification 57
Figure 6.28: SiAlFe-PP7 at 35k magnification 57
Figure 6.29: SiAlFe-PP7 at 80k magnification 57
Figure 6.30: SiAlFe-PP8 at 35k magnification 57
Figure 6.31: SiAlFe-PP8 at 80k magnification 57
Figure 6.32: SiAlFe-PP2 at 35k magnification 58
Figure 6.33: SiAlFe-PP2 at 80k magnification 58
Figure 6.34: SiAlFe-PP9 at 35k magnification 58
Figure 6.35: SiAlFe-PP9 at 80k magnification 58
Figure 6.36: SiAlFe-PP10 at 35k magnification 59
Figure 6.37: SiAlFe-PP10 at 80k magnification 59
Figure 6.38: SiAlFe-PP11 at 35k magnification 59
Figure 6.39: SiAlFe-PP11 at 80k magnification 59
Figure 6.40: SiAlFe-PP12 at 35k magnification 59
Figure 6.41: SiAlFe-PP12 at 80k magnification 59
Figure 6.42: SiAlFe-PP13 at 35k magnification 60
Figure 6.43: SiAlFe-PP13 at 80k magnification 60
Figure 6.44: SiAlFe-PP14 at 35k magnification 60
Figure 6.45: SiAlFe-PP14 at 80k magnification 60
Figure 6.46: SiAlFe-PP2 at 35k magnification 61
Figure 6.47: SiAlFe-PP2 at 80k magnification 61
Figure 6.48: SiAlFe-PP15 at 35k magnification 61
Figure 6.49: SiAlFe-PP15 at 80k magnification 61
Figure 6.50: SiAlFe-PP16 at 35k magnification 61
Figure 6.51: SiAlFe-PP16 at 80k magnification 61
Figure 6.52: SiAlFe-PP17 at 35k magnification 62
Figure 6.53: SiAlFe-PP17 at 80k magnification 62
Figure 6.54: SiAlFe-PP2 at 35k magnification 62
Figure 6.55: SiAlFe-PP2 at 80k magnification 62

Figure 6.56: SiAlFe-PP18 at 35k magnification 63
Figure 6.57: SiAlFe-PP18 at 80k magnification 63
Figure 6.58: SiAlFe-PP19 at 35k magnification 63
Figure 6.59: SiAlFe-PP19 at 80k magnification 63
Figure 6.60: SiAlFe-PP20 at 35k magnification 63
Figure 6.61: SiAlFe-PP20 at 80k magnification 63
Figure 6.62: SiAlFe-PP21 at 35k magnification 64
Figure 6.63: SiAlFe-PP21 at 80k magnification 64
Figure 6.64: SiAlFe-PP22 at 35k magnification 64
Figure 6.65: SiAlFe-PP22 at 80k magnification 64
Figure 6.66: SiAlFe-PP23 at 35k magnification 65
Figure 6.67: SiAlFe-PP23 at 80k magnification 65
Figure 6.68: SiAlFe-PP24 at 35k magnification 65
Figure 6.69: SiAlFe-PP24 at 80k magnification 65
Figure 6.70: SiAlFe-PP2 at 35k magnification 65
Figure 6.71: SiAlFe-PP2 at 80k magnification 65
Figure 6.72: SiAlFe-TP1 at 35k magnification 66
Figure 6.73: SiAlFe-TP1 at 80k magnification 66
Figure 6.74: SiAlFe-TP2 at 35k magnification 66
Figure 6.75: SiAlFe-TP2 at 80k magnification 66
Figure 6.76: SiAlFe-TP3 at 35k magnification 67
Figure 6.77: SiAlFe-TP3 at 80k magnification 67
Figure 6.78: SiAlFe-TP4 at 35k magnification 67
Figure 6.79: SiAlFe-TP4 at 80k magnification 67
Figure 6.80: Low resolution SEM image of SiAlFe-TP-E55 with 30^0 tilting 69
Figure 6.81: Low resolution cross section SEM image of SiAlFe-TP-E55 69
Figure 6.82: Ultra-High resolution cross section SEM image of SiAlFe-TP-E55 69
Figure 6.83: Low resolution SEM image of SiAlFe-TP-E47 with 30^0 tilting 69
Figure 6.84: Low resolution cross section SEM image of SiAlFe-TP-E47 69
Figure 6.85: Ultra-High resolution cross section SEM image of SiAlFe-TP-E47 69
Figure 6.86: Low resolution SEM image of SiAlFe-TP-E51 with 30^0 tilting 69
Figure 6.87: High resolution SEM image of SiAlFe-TP-E51 with 30^0 tilting 69
Figure 6.88: Ultra-High resolution SEM image of SiAlFe-TP-E51 with 30^0 tilting 69
Figure 6.89: The average height of sample E55, E47 and E51 70
Figure 6.90: The average diameter of sample E55, E47 and E51 70
Figure 6.91: The growth rate of sample E55, E47 and E51 70
Figure 6.92: Low resolution SEM image of SiAlFe-TP-E47 with 30^0 tilting 70
Figure 6.93: Low resolution cross section SEM image of SiAlFe-TP-E47 70
Figure 6.94: Ultra-High resolution cross section SEM image of SiAlFe-TP-E47 70
Figure 6.95: Low resolution SEM image of SiAlFe-TP-E79 with 30^0 tilting 71
Figure 6.96: High resolution SEM image of SiAlFe-TP-E79 with 30^0 tilting 71
Figure 6.97: Ultra-High resolution SEM image of SiAlFe-TP-E79 with 30^0 tilting 71
Figure 6.98: Low resolution SEM image of SiAlFe-TP-E75 with 30^0 tilting 71
Figure 6.99: High resolution SEM image of SiAlFe-TP-E75 with 30^0 tilting 71
Figure 6.100: Ultra-High resolution SEM image of SiAlFe-TP-E75 with 30^0 tilting 71
Figure 6.101: Low resolution SEM image of SiAlFe-TP-E71 with 30^0 tilting 71
Figure 6.102: High resolution SEM image of SiAlFe-TP-E71 with 30^0 tilting 71

Figure 6.103: Ultra-High resolution SEM image of SiAlFe-TP-E71 with 30^0 tilting 71
Figure 6.104: Low resolution SEM image of SiAlFe-TP-E103 with 30^0 tilting 71
Figure 6.105: High resolution SEM image of SiAlFe-TP-E103 with 30^0 tilting 71
Figure 6.106: Ultra-High resolution SEM image of SiAlFe-TP-E67 with 30^0 tilting 71
Figure 6.107: Low resolution SEM image of SiAlFe-TP-E59 with 30^0 tilting 71
Figure 6.108: High resolution SEM image of SiAlFe-TP-E59 with 30^0 tilting 71
Figure 6.109: Ultra-High resolution SEM image of SiAlFe-TP-E59 with 30^0 tilting 71
Figure 6.110: Low resolution SEM image of SiAlFe-TP-E63 with 30^0 tilting 72
Figure 6.111: High resolution SEM image of SiAlFe-TP-E63 with 30^0 tilting 72
Figure 6.112: Ultra-High resolution SEM image of SiAlFe-TP-E63 with 30^0 tilting 72
Figure 6.113: Low resolution SEM image of SiAlFe-TP-E67 with 30^0 tilting 72
Figure 6.114: High resolution SEM image of SiAlFe-TP-E67 with 30^0 tilting 72
Figure 6.115: Ultra-High resolution SEM image of SiAlFe-TP-E67 with 30^0 tilting 72
Figure 6.116: Low resolution SEM image of SiAlFe-TP-E99 with 30^0 tilting 72
Figure 6.117: High resolution SEM image of SiAlFe-TP-E99 with 30^0 tilting 72
Figure 6.118: Ultra-High resolution SEM image of SiAlFe-TP-E99 with 30^0 tilting 72
Figure 6.119: Low resolution SEM image of SiAlFe-TP-E91 with 30^0 tilting 72
Figure 6.120: Low resolution cross section SEM image of SiAlFe-TP-E91 72
Figure 6.121: Ultra-High resolution cross section SEM image of SiAlFe-TP-E91 72
Figure 6.122: Low resolution SEM image of SiAlFe-TP-E87 with 30^0 tilting 73
Figure 6.123: Low resolution cross section SEM image of SiAlFe-TP-E87 73
Figure 6.124: Ultra-High resolution cross section SEM image of SiAlFe-TP-E87 73
Figure 6.125: Low resolution SEM image of SiAlFe-TP-E47 with 30^0 tilting 73
Figure 6.126: Low resolution cross section SEM image of SiAlFe-TP-E47 73
Figure 6.127: Ultra-High resolution cross section SEM image of SiAlFe-TP-E47 73
Figure 6.128: Low resolution SEM image of SiAlFe-TP-E95 with 30^0 tilting 73
Figure 6.129: Low resolution cross section SEM image of SiAlFe-TP-E95 73
Figure 6.130: Ultra-High resolution cross section SEM image of SiAlFe-TP-E95 73
Figure 6.131: Low resolution SEM image of SiAlFe-TP-E195 with 30^0 tilting 73
Figure 6.132: High resolution SEM image of SiAlFe-TP-E195 with 30^0 tilting 73
Figure 6.133: Ultra-High resolution SEM image of SiAlFe-TP-E195 with 30^0 tilting 73
Figure 6.134: The average height of sample E47, E87, E91, E95 and E195 74
Figure 6.135: The average diameter of sample E47, E87, E91, E95 and E195 74
Figure 6.136: The growth rate of sample E47, E87, E91, E95 and E195 74
Figure 6.137: Low resolution SEM image of SiAlFe-TP-E95 with 30^0 tilting 74
Figure 6.138: Low resolution cross section SEM image of SiAlFe-TP-E139 74
Figure 6.139: Ultra-High resolution cross section SEM image of SiAlFe-TP-E139 74
Figure 6.140: Low resolution SEM image of SiAlFe-TP-E47 with 30^0 tilting 74
Figure 6.141: Low resolution cross section SEM image of SiAlFe-TP-E47 74
Figure 6.142: Ultra-High resolution cross section SEM image of SiAlFe-TP-E47 74
Figure 6.143: Low resolution SEM image of SiAlFe-TP-E107 with 30^0 tilting 75
Figure 6.144: High resolution SEM image of SiAlFe-TP-E107 with 30^0 tilting 75
Figure 6.145: Ultra-High resolution SEM image of SiAlFe-TP-E107 with 30^0 tilting 75
Figure 6.146: Low resolution SEM image of SiAlFe-TP-E111 with 30^0 tilting 75
Figure 6.147: High resolution SEM image of SiAlFe-TP-E111 with 30^0 tilting 75
Figure 6.148: Ultra-High resolution SEM image of SiAlFe-TP-E111 with 30^0 tilting 75
Figure 6.149: The average height of sample E47, E107, E111, E139 and E179 76

Figure 6.150: The average diameter of sample E47, E107, E111, E139 and E179 76
Figure 6.151: The growth rate of sample E47, E107, E111, E139 and E179 76
Figure 6.152: Low resolution SEM image of SiAlFe-TP-E119 with 30^0 tilting 76
Figure 6.153: Low resolution cross section SEM image of SiAlFe-TP-E119 76
Figure 6.154: Ultra-High resolution cross section SEM image of SiAlFe-TP-E119 76
Figure 6.155: Low resolution SEM image of SiAlFe-TP-E47 with 30^0 tilting 76
Figure 6.156: Low resolution cross section SEM image of SiAlFe-TP-E47 76
Figure 6.157: Ultra-High resolution cross section SEM image of SiAlFe-TP-E47 76
Figure 6.158: Low resolution SEM image of SiAlFe-TP-E123 with 30^0 tilting 77
Figure 6.159: High resolution SEM image of SiAlFe-TP-E123 with 30^0 tilting 77
Figure 6.160: Ultra-High resolution SEM image of SiAlFe-TP-E123 with 30^0 tilting 77
Figure 6.161: Low resolution SEM image of SiAlFe-TP-E127 with 30^0 tilting 77
Figure 6.162: High resolution SEM image of SiAlFe-TP-E127 with 30^0 tilting 77
Figure 6.163: Ultra-High resolution SEM image of SiAlFe-TP-E127 with 30^0 tilting 77
Figure 6.164: Low resolution SEM image of SiAlFe-TP-E131 with 30^0 tilting 77
Figure 6.165: High resolution SEM image of SiAlFe-TP-E131 with 30^0 tilting 77
Figure 6.166: Ultra-High resolution SEM image of SiAlFe-TP-E131 with 30^0 tilting 77
Figure 6.167: Low resolution SEM image of SiAlFe-TP-E135 with 30^0 tilting 77
Figure 6.168: High resolution SEM image of SiAlFe-TP-E135 with 30^0 tilting 77
Figure 6.169: Ultra-High resolution SEM image of SiAlFe-TP-E135 with 30^0 tilting 77
Figure 6.170: The average height of sample E47, E119, E123, E127, E131 and E135 78
Figure 6.171: The average diameter of sample E47, E119, E123, E127, E131 and E135 78
Figure 6.172: The growth rate of sample E47, E119, E123, E127, E131 and E135 78
Figure 6.173: Low resolution SEM image of SiAlFe-TP-E47 with 30^0 tilting 78
Figure 6.174: Low resolution cross section SEM image of SiAlFe-TP-E47 78
Figure 6.175: Ultra-High resolution cross section SEM image of SiAlFe-TP-E47 78
Figure 6.176: Low resolution SEM image of SiAlFe-TP-E159 with 30^0 tilting 78
Figure 6.177: Low resolution cross section SEM image of SiAlFe-TP-E159 78
Figure 6.178: Ultra-High resolution cross section SEM image of SiAlFe-TP-E159 78
Figure 6.179: Low resolution SEM image of SiAlFe-TP-E163 with 30^0 tilting 79
Figure 6.180: Low resolution cross section SEM image of SiAlFe-TP-E163 79
Figure 6.181: Ultra-High resolution cross section SEM image of SiAlFe-TP-E163 79
Figure 6.182: The average height of sample E47, E159 and E163 79
Figure 6.183: The average diameter of sample E47, E159 and E163 79
Figure 6.184: The growth rate of sample E47, E159 and E163 79
Figure 6.185: Low resolution SEM image of SiAlFe-TP-E47 with 30^0 tilting 80
Figure 6.186: Low resolution cross section SEM image of SiAlFe-TP-E47 80
Figure 6.187: Ultra-High resolution cross section SEM image of SiAlFe-TP-E47 80
Figure 6.188: Low resolution SEM image of SiAlFe-TP-E183 with 30^0 tilting 80
Figure 6.189: Low resolution cross section SEM image of SiAlFe-TP-E183 80
Figure 6.190: Ultra-High resolution cross section SEM image of SiAlFe-TP-E183 80
Figure 6.191: Low resolution SEM image of SiAlFe-TP-E155 with 30^0 tilting 80
Figure 6.192: Low resolution cross section SEM image of SiAlFe-TP-E155 80
Figure 6.193: Ultra-High resolution cross section SEM image of SiAlFe-TP-E155 80
Figure 6.194: Low resolution SEM image of SiAlFe-PP-E151 with 30^0 tilting 80
Figure 6.195: High resolution SEM image of SiAlFe-PP-E151 with 30^0 tilting 80
Figure 6.196: Ultra-High resolution SEM image of SiAlFe-PP-E151 with 30^0 tilting 80

Figure 6.197: Low resolution SEM image of SiAlFe-PP-E147 with 30^0 tilting 80
Figure 6.198: High resolution SEM image of SiAlFe-PP-E147 with 30^0 tilting 80
Figure 6.199: Ultra-High resolution SEM image of SiAlFe-PP-E147 with 30^0 tilting 80
Figure 6.200: Low resolution SEM image of SiAlFe-PP-E143 with 30^0 tilting 81
Figure 6.201: Low resolution cross section SEM image of SiAlFe-PP-E143 81
Figure 6.202: Ultra-High resolution cross section SEM image of SiAlFe-PP-E143 81
Figure 6.203: The average height of sample E47, E143, E147, E151, E155and E183 81
Figure 6.204: The average diameter of sample E47, E143, E147, E151, E155and E183 81
Figure 6.205: The growth rate of sample E47, E143, E147, E151, E155and E183 81
Figure 6.206: Low resolution SEM image of SiAlFe-TP-E47 with 30^0 tilting 82
Figure 6.207: Low resolution cross section SEM image of SiAlFe-TP-E47 82
Figure 6.208: Ultra-High resolution cross section SEM image of SiAlFe-TP-E47 82
Figure 6.209: Low resolution SEM image of SiAlFe-TP-E115 with 30^0 tilting 82
Figure 6.210: Low resolution cross section SEM image of SiAlFe-TP-E115 82
Figure 6.211: Ultra-High resolution cross section SEM image of SiAlFe-TP-E115 82
Figure 6.212: Low resolution SEM image of SiAlFe-TP-E116 with 30^0 tilting 82
Figure 6.213: Low resolution cross section SEM image of SiAlFe-TP-E116 82
Figure 6.214: Ultra-High resolution cross section SEM image of SiAlFe-TP-E116 82
Figure 6.215: Low resolution SEM image of SiAlFe-TP-E117 with 30^0 tilting 82
Figure 6.216: Low resolution cross section SEM image of SiAlFe-TP-E117 82
Figure 6.217: Ultra-High resolution cross section SEM image of SiAlFe-TP-E117 82
Figure 6.218: Low resolution SEM image of SiAlFe-TP-E118 with 30^0 tilting 82
Figure 6.219: Low resolution cross section SEM image of SiAlFe-TP-E118 82
Figure 6.220: Ultra-High resolution cross section SEM image of SiAlFe-TP-E118 82
Figure 6.221: The average height of sample E47, E115, E116, E117 and E118 83
Figure 6.222: The average diameter of sample E47, E115, E116, E117 and E118 83
Figure 6.223: The growth rate of sample E47, E115, E116, E117 and E118 83
Figure 6.224: Low resolution SEM image of SiAlFe-TP-E47 with 30^0 tilting 84
Figure 6.225: Low resolution cross section SEM image of SiAlFe-TP-E47 84
Figure 6.226 Ultra-High resolution cross section SEM image of SiAlFe-TP-E47 84
Figure 6.227: Low resolution SEM image of SiAlFe-TP-E167 with 30^0 tilting 84
Figure 6.228: Low resolution cross section SEM image of SiAlFe-TP-E167 84
Figure 6.229: Ultra-High resolution cross section SEM image of SiAlFe-TP-E167 84
Figure 6.230: Low resolution SEM image of SiAlFe-PP-E171 with 30^0 tilting 84
Figure 6.231: Low resolution cross section SEM image of SiAlFe-PP-E171 84
Figure 6.232: Ultra-High resolution cross section SEM image of SiAlFe-PP-E171 84
Figure 6.233: Low resolution SEM image of SiAlFe-TP-E219 with 30^0 tilting 84
Figure 6.234: Low resolution cross section SEM image of SiAlFe-TP-E219 84
Figure 6.235: Ultra-High resolution cross section SEM image of SiAlFe-TP-E219 84
Figure 6.236: The average height of sample E167, E168, E169, E170, E171, E172, E173, E174, E219, E220, E221 and E22 85
Figure 6.237: The average diameter of sample E167, E168, E169, E170, E171, E172, E173, E174, E219, E220, E221 and E22 85
Figure 6.238: The growth rate of sample E167, E168, E169, E170, E171, E172, E173, E174, E219, E220, E221 and E22 85
Figure 6.239: TEM images of E47 at 100k magnification 85
Figure 6.240: TEM images of E47 at 300k magnification 85

Figure 6.241: TEM images of E91 at 100k magnification 86
Figure 6.242: TEM images of E91 at 300k magnification 86
Figure 6.243: TEM images of E115 at 100k magnification 86
Figure 6.244: TEM images of E115 at 300k magnification 86
Figure 6.245: TEM images of E115 on CHG at 100k magnification 86
Figure 6.246: TEM images of 115 on CHG at 300k magnification 86
Figure 6.247: TEM images of E115 (no barrier layer) at 100k magnification 87
Figure 6.248: TEM images of E115 (no barrier layer) at 300k magnification 87
Figure 6.249: TEM images of E119 at 100k magnification 87
Figure 6.250: TEM images of E119 at 300k magnification 87
Figure 6.251: TEM images of E143 at 100k magnification 87
Figure 6.252: TEM images of E143 at 300k magnification 87
Figure 6.253: TEM images of E159 at 100k magnification 88
Figure 6.254: TEM images of E159 at 300k magnification 88
Figure 6.255: Image of the TEM samples. Particles for the samples where CNTs were dispersed in ethanol by ultrasonic methods are visible, while particles for the scraped samples are not. 88
Figure 6.256: The distance between the graphene planes can be found this TEM image. The distance was measured with a ruler and the scale bar 89
Figure 7.1: How much of the fed CH4 that is converted [136] 90
Figure 7.2: Fraction of C2H2, C2H4 and C2H6 of CH4 input for various plasma power and operating pressures [136] 90
Figure 7.3: Basic reaction of how CH_4 result in CNT growth 91
Figure 7.4: Shows two samples from different batches that has the equal Al thicknesses of 30 nm, but have completely different colors 94

10 Index of tables

Table 5.1: Technical information of the The Dynatex DXIII scriber unit [105] 38
Table 5.2: Technical information of the Pfeiffer Vacuum Classic 500 e-beam evaporator [106] 40
Table 5.3: Technical information of the Cressington 308R Sputter and Evaporator [107] 40
Table 5.4: Technical information of the JetFirst 200 RTP unit [108] 40
Table 5.5: Technical information of the PlasmaLab System 100 PECVD [109] 41
Table 5.6: Technical information of the PlasmaLab System 100 PECVD [110] 42
Table 5.7: Technical information of the Hitachi S-5500 S(T)EM [112] 43
Table 5.8: Technical information of the FEI Helios NanoLab DualBeam FIB [113] 44
Table 5.9: Technical information of the JEOL JEM-2010 TEM [115] 44
Table 5.10: Technical information of the Vecco Dektak 150 profilometer [116] 44
Table 6.1: The cleaning procedure that was used for all the samples in this experiment 45
Table 6.2: The scribe and break parameters for the Dynatex DXlll 46
Table 6.3: The scan parameters for the Deltak 150 profilometer 47
Table 6.4: Measured thicknesses for calibration of the TF 48
Table 6.5: Parameters used for deposition of Al and Fe during sputtering 48
Table 6.6: Settings used for the RTP process 49
Table 6.7: Settings used for imaging of the samples with the FIB and the S(T)EM 49
Table 6.8: Recipe that was used for making the holy grids for TEM analysis 51
Table 6.9: Settings used for cleaning Si wafers in the plasma cleaner 52
Table 6.10: Parameters of the pretreated samples. Higher quality can be found in Appendix B 54
Table 6.11: The parameters that showed the highest potential for CNT growth during the study of the pretreatment 68
Table 6.12: The "CNTRecipe" was the base recipe for all the processed samples in this experiment and required 4- 5 hours to finish 68
Table 6.13: The number of shells and diameter of the MWCNTs in the samples that were analyzed with the TEM 89

11 References

[1] C. H. Z. J. J. L. a. Y. L. Naiqin Zhao, "Fabrication and growth mechanism of carbon nanotubes by catalytic chemical vapor deposition," *Material Letters,* vol. 60, pp. 159-163, 2006.

[2] W. C. D. X. B. S. S. Y. Z. F. S. L. L. C. P. Z. J. C. X. a. N. A. K. Libin Wang, "Simple, Rapid, Sensitive, and Versatile SWNT – Paper Sensor for Environmental Toxin Detection Competitive with ELISA," *Nano Letters,* vol. 9, no. 12, pp. 4147-4152, 2009.

[3] Y.-K. K. E. L. C. W. A. a. Y. J. J. Myung Gwan Hahm, "Diameter Selective Growth of Vertically Aligned Single Walled Carbon Nanotubes and Study of their Growth Mechanism," *Journal of Physical Chemistry,* vol. 112, pp. 17143-17147, 2008.

[4] Q. X. J. W. a. J. M. Ziping Wu, "Preperation of Large Area Double-walled Carbon Nanotube Macro-films with self cleaning Properties," *Journal of Material Science Technology,* vol. 26(1), pp. 20-26, 2009.

[5] B. H. V. B. J. A. T. T. K. a. J. A. Lidiya Mishchenko, "Design of Ice-free Nanostructured Surfaces Based on Repulsion of Impacting Water Droplets," *American Chemical Society,* vol. 4, no. 12, 2010.

[6] X.-Q. S. a. X.-F. M. Hao-Jie Song, "Superhydrophobic Surfaces Produced by Carbon Nanotube Modified Polystyrene Composite Coating," *Journal of Dispersion Science and Technology,* vol. 31, pp. 1465-1468, 2010.

[7] S. P. K. a. K. S. M. S. Senthil Saravanan, "Mechanical Properties and Corrosion Behavior of Carbon Nanotubes Reinforced AA 4032 Nanocomposites," *Society for Experimental Mechanics,* 2011.

[8] K. G. L. H. P. L. a. C. T. Thor Christian Hobæk, "Surface Nanoengineering Inspired by Evolution," *BioNanoScience,* vol. 1, pp. 63-77, 2011.

[9] A. K. J. V. K. S. J. W. a. D. G. Liangliang Cao, "Anti-Icing Superhydrophobic Coatings," *Langmuir,* vol. 25(1), pp. 12444-12448, 2009.

[10] M. A. S. a. S. K. Sinha, "Mechanical, thermal and tribological characterization of a UHMWPE film reinforced with carbon nanotubes coated on steel," *Tribology International,* vol. 44, pp. 1932-1941, 2011.

[11] X. Q. W. M. W. F. F. W. a. H. L. G. Z. H. Li, "Preparation and tribological properties of the carbon nanotubes-Ni-P composite coating," vol. 39, pp. 953-957, 2006.

[12] X. L. J. H. Y. F. a. F.-z. C. Xiaoming Li, "Biomedical investigation of CNT based coatings," *Surface & Coating Technology,* vol. 206, pp. 759-766, 2011.

[13] M. K. H. S. a. H. I. Tsunehisa Suzuki, "Improved Adherence Strength between Diamond Grains and Electrolytic Nickel Bonds by Carbon Nanotube Coatings," *Journal of Solid Mechanics and Materials Engineering,* vol. 5, no. 8, 2011.

[14] S. S. L. C. P. M. A. a. A. D. Liehui Ge, "Carbon nanotube-based synthetic gecko tapes," *PNAS,* vol. 104, no. 26, 2006.

[15] A. B. C. D. R. K. B. M. P. D. J. I. a. A. J. C. Michael D. Bartlett, "Looking beyond fibrillar features to scale gecko-likle adhesion," *Advanced Materials,* vol. 24, pp. 1078-1083, 2012.

[16] P. S. E. F. M. R. C. L. A. P. W. B. a. J.-M. B. Marc Monthioux, "Introduction to Carbon Nanotubes".

[17] "Carbon Nanotubes Could Create World's First Space Elevator," [Online]. Available:

http://inhabitat.com/carbon-nanotubes-could-create-worlds-first-space-elevator/. [Accessed 15 04 2012].

[18] P. Org, "Long, Stretchy Carbon Nanotubes Could Make Space Elevators Possible," [Online]. Available: http://phys.org/news151938445.html. [Accessed 15 04 2012].

[19] "SciencePhotoLibrary," [Online]. Available: http://www.sciencephoto.com/media/338860/enlarge. [Accessed 31 03 2012].

[20] [Online]. Available: http://www.airtransparency.com/airtransparency/?currentPage=8. [Accessed 31 03 2012].

[21] C. Binns, Introduction to Nanoscience and Nanotechnology, New Jersey: John Wiley & Sons, 2010, pp. 53-58.

[22] Wikipedia, "Carbon Nanotubes," [Online]. Available: http://en.wikipedia.org/wiki/Carbon_nanotube. [Accessed 30 04 2012].

[23] C. Binns, Introduction to Nanoscience and Nanotechnology, New Jersey: John Wilsey & Sons, 2010, pp. 77-80.

[24] K. T. a. M. T.Natsuki, "Effects of carbon nanotube structures on mechanical properties," *Applied Physics A79,* pp. 117-124, 2004.

[25] W.-S. Jhang, "The Synthesis and Characterization of CdSe/ZnS/CNT," *Thesis for Master of Science, Department of Materials Engineering, Tatung University,* 2006.

[26] "Carbon Nanotubes & Buckyballs," NanoQuest, [Online]. Available: http://mrsec.wisc.edu/Edetc/nanoquest/carbon/index.html. [Accessed 30 04 2012].

[27] C. S. ,. M. C. a. W. I. M. Kenneth B.K. Teo, "Catalytic Synthesis of Carbon Nanotubes and Nanofibers," *American Scientific Publishers,* 2003.

[28] T. H. Y. A. K. a. H. M. Morinobu Endo, "Development and Application of Carbon Nanotubes," *Japanese Journal of Applied Physics,* vol. 45, no. 6A, pp. 4883-4892, 2006.

[29] S. a. J. R. C.T. Wirth, "State of catalyst during carbon nanotube growth," *Diamond & Related Materials,* vol. 18, pp. 940-945, 2009.

[30] J. D. C. H. J. A. a. R. K. Jan Prasek, "Methods for carbon nanotubes synthesis—review," *Journal of Materials Chemistry,* vol. 21, p. 15872–15884, 2011.

[31] M. P. a. T. Goswami, "Carbon nanotubes – Production and industrial applications," *Materials & Design,* vol. 28, pp. 1477-1489, 2007.

[32] C. Binns, Introduction to Nanoscience and Nanotechnology, New Jersey: John Wiley & Sons, 2010, pp. 121-127.

[33] R. J. a. C. R. Bertozzi, "Progress and challenges for the bottom-up synthesis of carbon nanotubes with discrete chirality," *Chemical Physics Letters,* vol. 494, pp. 1-7, 2010.

[34] H. D. J. L. K. H. a. A. H. W. Ernesto Joselevich, "Carbon Nanotube Synthesis and Organization," *Applied Physics,* vol. 111, 2008.

[35] [Online]. Available: http://mrsec.wisc.edu/Edetc/SlideShow/slides/contents/nanotubes.html. [Accessed 30 04 2012].

[36] H. W. a. J. J. Moore, "Low temperature growth mechanisms of vertically aligned carbon nanofibers and nanotubes by radio frequency-plasma enhanced chemical vapor deposition," *Carbon,* vol. 50, pp. 1235-1242, 2012.

[37] K. B. a. A. R. Feng Ding, "Nucleation and growth of singlewalled carbon nanotubes: A

molecular dynamics study," *Journal of Physical Chemistry B,* vol. 108, pp. 17369-17377, 2004.

[38] V. M. T. M. M. G. a. K. K. A.V. Melechko, "Vertically aligned carbon nanofibers and related structures: Controlled synthesis and directed assembly," *Journal of Applied Physics,* vol. 97, 2005.

[39] [Online]. Available: http://www.photonics.ethz.ch/research/core_competences/technology/processing/other. [Accessed 30 04 2012].

[40] M. J. Goeckner, "Aspect of Plasma Processing: A brief overview of plasma science in industry," UTD, [Online]. Available: http://www.utdallas.edu/~goeckner/plasma_sci_class/Plasma%20Process%203%20Types.pdf. [Accessed 30 04 2012].

[41] S.-Y. K. a. H.-W. L. Sang-Gook Kim, "Effect of ammonia gas etching on growth of vertically carbon nanotubes/nanofibers," *Transactions of Nonferrous Metals Society of China,* vol. 21, pp. 130-134, 2011.

[42] Y. Z. R. L. a. X. S. Mihnea Ioan Ionescu, "Selective growth, characterization, and field emission performance of single-walled and few-walled carbon nanotubes by plasma enhanced chemical vapor deposition," *Applied Surface Science,* vol. 258, pp. 1366-1372, 2011.

[43] T. N. a. K. Okazaki, "Carbon nanotube synthesis in atmospheric pressure glow discharge: A review," *Plasma Processes and Polymers,* vol. 5, pp. 300-321, 2008.

[44] R. L. Spencer, "A brief Introduction to Plasma Physics," [Online]. Available: http://maxwell.byu.edu/~spencerr/phys442/plasma.pdf.

[45] S. Li, "Plasma Assisted Nanofabrication Processes," [Online]. Available: http://www.eng.auburn.edu/~tzengy/ELEC7730/ELEC%207730%20Fall%202003/Fall%202003%20Presentation%202/Li-Plasma%20Assisted%20Nanofabrication%20Processes.ppt. [Accessed 30 04 2012].

[46] h. W. a. J. J. Moore, "Different growth mechanisms of vertical carbon nanotubes by rf- or dc-plasma enhanced chemical vapor deposition at low temperature," *American Vacuum Society,* 2010.

[47] C. D. a. J. R. S. Hofmann, "Low-temperature growth of carbon nanotubes by plasma-enhanced chemical vapor deposition," *Applied Physics Letters,* vol. 83, no. 1, 2003.

[48] T. K. S. Y. a. K. O. Tomohiro Nozaki, "Parametric study for selective growth of single-walled carbon nanotubes in plasma enhanced chemical vapor deposition," *Japanese Journal of Applied Physics,* vol. 50, 2011.

[49] J. D. a. T. G. d. M. Hélène Le poche, "Radio-frequency plasma system to selectively grow vertical field-aligned carbon nanofibers from a solid carbon source," *Carbon,* vol. 45, pp. 2904-2916, 2007.

[50] Z. L. Z. S. a. J. L. San Hua Lim, "Plasma-assisted synthesis of carbon nanotubes," *Nanoscale Res Lett,* vol. 5, pp. 1377-1386, 2010.

[51] E. B. a. E. J. Burak Caglar, "Production of carbon nanotubes by PECVD and their applications to supercapacitors".

[52] S.-P. C. a. A. R. M. Choon-Ming Seah, "Synthesis of aligned carbon nanotubes," *Carbon,* vol. 49, pp. 4613-4635, 2011.

[53] D. B. H. R. G. L. N. l. R. M. S. B. S. H. D. D. B. T. G. B. A. C. M. C. G. A. A. M. M. a. W. I. M.

Kenneth B.K. Teo, "The significance of plasma heating in carbon nanotube and nanofiber growth," *Nano letters,* vol. 4, no. 5, pp. 921-926, 2004.

[54] C. B. P. B. R. S. a. J. T. G. Billyde Brown, "Growth of vertically aligned bamboo-like carbon nanotubes from ammonia/methane precursors using a platinum catalyst," *Carbon,* vol. 49, pp. 266-274, 2011.

[55] R. C. L. D. Y. L. W. Z. Y. Z. Z. J. F. P. a. J. L. Yan Li, "How Catalysts Affect the Growth of Single-Walled Carbon Nanotubes on Substrates," *Advanced Materials,* vol. 22, pp. 1508-1515, 2010.

[56] T. K. T. K. a. R. H. Zohreh Ghorannevis, "Growth of Single-Walled Carbon Nanotubes from Nonmagnetic Catalysts by Plasma Chemical Vapor Deposition," *Japanese Journal of Applied Physics,* vol. 49, 2010.

[57] T. K. T. K. a. R. H. Zohreh Ghorannevis, "Narrow-Chirality Distributed Single-Walled Carbon Nanotube Growth from Nonmagnetic Catalyst," *Journal of American Chemical Society,* vol. 132, pp. 9570-9572, 2010.

[58] H. N. D. N. F. S. Y. T. Y. A. M. Y. M. E. N. M. Y. a. K. H. Shunsuke Sakurai, "Role of subsurface diffusion and ostwald ripening in catalyst formation for single-walled carbon nanotube forest growth," *Journal of American Chemical Society,* vol. 134, pp. 2148-2153, 2011.

[59] E. M. T. T. K. B. a. A. R. Avetik R. Harutyunyan, "Hidden features of the catalyst nanoparticles favorable for single-walled carbon nanotube growth," *Applied Physics Letter,* vol. 90, 2007.

[60] C. P. D. a. K. Vecchio, "Prediction of carbon nanotube growth success by the analysis of carbon-catalyst binary phase diagrams," *Carbon,* vol. 44, pp. 267-275, 2006.

[61] K. B. T. R. G. L. W. M. D. B. h. a. M. M. Martin S. Bell, "Carbon nanotubes by plasma-enhanced chemical vapor deposition," *Pure and Applied Chemistry,* vol. 78, no. 6, pp. 1117-1125, 2006.

[62] P.-A. Buffat, "Size-effect modifications of the Debye-Waller factor in small gold particles," *Solid State Communications,* vol. 23, pp. 547-550, 1977.

[63] A. K. S. Z. J. F. W. a. A. G. Haoqing Hou, "Large-scale synthesis of aligned carbon nanotubes using FeCl3 as floating catalyst precursor," *American Chemical Society,* vol. 15, pp. 580-585, 2003.

[64] O. J. W. P. a. A. G. A. Gorbunov, "Solid-liquid-solid growth mechanism of single-wall carbon nanotubes," *Carbon,* vol. 40, pp. 113-118, 2002.

[65] S. L. a. N. S. E.F. Kukovitsky, "VLS-growth of carbon nanotubes from the vapor," *Chemical Physics Letters,* vol. 317, pp. 65-70, 2000.

[66] V. V. a. V. K. S.K. Srivastava, "Effect of hydrogen plasma treatment on the growth and microstructures of multiwalled carbon nanotubes," *Nano-micro letters,* vol. 2, no. 1, pp. 42-48, 2010.

[67] M. B. P. H. F. F. a. R. W. R.T.K. Baker, "Nucleation and growth of carbon deposits from the nickel catalyzed decomposition of acetylene," *Journal of Catalysis,* vol. 26, pp. 51-62, 1972.

[68] M. E. a. T. K. A. Oberlin, "Filamentous growth of carbon through benzene decomposition," *Journal of Crystal Growth,* vol. 32, pp. 335-349, 1976.

[69] I. L. C. L. a. M. H. J.H. Yen, "Effect of catalyst pretreatment on the growth of carbon nanotubes," *Diamond and Related Materials,* vol. 13, pp. 1237-1241, 2004.

[70] C. E. T. M. a. M. D. A. Gohier, "Carbon nanotube growth mechanism switches from tip- to base-growth with decreasing catalyst particle size," *Carbon,* vol. 46, pp. 1331-1338, 2008.

[71] R. R. M. S. E. P. L. C. R. P. T. D. a. R. G. A. Rizzo, "Effect of Fe catalyst thickness and C2H2/H2 flow rate ratio on the vertical alignment of carbon nanotubes grown by chemical vapour deposition," *Diamond and Related Materials,* vol. 17, pp. 1502-1505, 2008.

[72] J. F. a. B. G. T. Baird, "Carbon formation on iron and nickel foils by hydrocarbon pyrolysis-reactions at 700 degrees," *Carbon,* vol. 12, pp. 591-602, 1974.

[73] K. T. C. D. N. R. G. J. A. A. F. D. R. J. R. a. W. W. M. Chhowalla, "Growth process conditions of vertically aligned carbon nanotubes using plasma enhanced chemical vapor deposition," *Journal of Applied Physics,* vol. 90, no. 10, 2001.

[74] R. W. a. W. Ellis, "Vaporliquidsolid mechanism of single crystal growth," *Applied Physics Letter,* vol. 4, no. 5, 1964.

[75] P. S. A. F. T. G. d. M. H. O. E. Q. V. M. E. D. V. N. B. A. B. a. N. B. J.Dijon, "How to switch from a tip to base growth mechanism in carbon nanotube growth by catalytic chemical vapour deposition," *Carbon,* vol. 48, pp. 3953-3963, 2010.

[76] W. J. Y. Y. S. C. G. S. C. a. D. K. In Kwang Song, "The determining factors for the growth mode of carbon nanotubes in the chemical vapour deposition process," *Nanotechnology,* vol. 15, pp. 590-595, 2004.

[77] B. C. B. M. F. C. W. a. C. D. S. Esconjauregui, "Growth of high-density vertically aligned arrays of carbon nanotubes by plasma-assisted catalyst pretreatment," *Applied Physics Letters,* vol. 95, 2009.

[78] W. M. W. J. M. W. A. G. J. P. E. J. V. M. a. P. S. D. David P. Burt, "Effects of metal underlayer grain size on carbon nanotube growth," *Journal of Physical Chemistry C,* vol. 113, pp. 15133-15139, 2009.

[79] M. F. B. B. a. J. R. Santiago Esconjauregui, "Carbon nanotube growth: From entanglement to vertical alignment," *Physical Status Solidi B,* vol. 247, pp. 2656-2659, 2010.

[80] M. Meyyappan, "A review of plasma enhanced chemical vapor deposition of carbon nanotubes," *Journal of Physics D: Applied Physics,* vol. 42, 2009.

[81] K. L. R. W. P. W. T. S. J. G. a. C. Y. Y. Xuhui Sun, "The effect of catalysts and underlayer metals on the properties of PECVD-grown carbon nanostructures," *Nanotechnology ,* vol. 21, 2010.

[82] A. P. C. M. D. M. M. C. F. R. F. S. a. N. P. Ricardo M. Silva, "Ultra simple catalyst layer preparation for the growth of vertically aligned CNTs and CNT-based nanostructures," *CrystEngComm,* vol. 14, no. 48, pp. 48-52, 2012.

[83] C. N. -. G. Mechanisms. [Online]. Available: http://pages.unibas.ch/phys-esca/cnt.html. [Accessed 08 04 2012].

[84] Z. W. a. P. O. T. de los Arcos, "Is aluminum a suitable buffer layer for carbon nanotube growth?," *Chemical Physics Letters,* vol. 380, pp. 419-423, 2003.

[85] C. T. W. S. H. R. B. M. C. C. D. C. C. A. K.-G. S. M. C. C.-C. S. D. A. G. R. S. a. J. R. Cecilia Mattevi, "In-situ X-ray photoelectron spectroscopy study of catalyst-support interactions and growth of carbon nanotube forests," *Journal of Physical Chemistry C,* vol. 112, pp. 12207-12213, 2008.

[86] R. B. C. T. W. M. C. R. S. C. D. M. H. S. Z. P. S. A. O. D. T. M. A. A. K.-G. R. S. a. J. R. Stephan Hofmann, "State of transition metal catalysts during carbon nanotube growth," *Journal of Physical Chemistry C,* vol. 113, pp. 1648-1656, 2009.

[87] C. L. P. S. M. K. L. M. K. G. E. E. A. S. R. H. H. a. B. M. Placidus B. Amama, "Influence of

alumina type on the evolution and activity of alumina supported Fe catalysts in single-walled carbon nanotube carpet growth," *ACS Nano,* vol. 4, no. 2, pp. 895-904, 2010.

[88] Z. H. J. X. J. W. P. B. M. S. a. P. P. Z.F. Ren, "Synthesis of large arrays of well-aligned carbon nanotubes on glass".

[89] J.-H. A. Y.-H. L. a. B.-K. J. Yoon-Taek Jang, "Effect of NH3 and thickness of catalyst on growth of carbon nanotubes using thermal chemical vapor deposition," *Chemical Physics Letters,* vol. 372, pp. 745-749, 2003.

[90] S. H. C. T. Y. L. J.-B. Y. C.-Y. P. T. J. S. Y. W. Y. I. T. H. a. J. M. K. Jae-Hee Han, "Growth characteristics of carbon nanotubes using platinum catalyst by plasma enhanced chemical vapor deposition," *Diamond and Related Materials,* vol. 12, pp. 878-883, 2003.

[91] Y.-P. C. a. L.-Y. L. Shih-Fong Lee, "Effects of annealing Ni catalyst in nitrogen-containing gases on the surface morphology and field-emission properties of thermal chemical vapor deposited carbon nanotubes," *New Carbon Materials,* vol. 23, no. 4, pp. 302-308, 2008.

[92] B. M. A. a. T. W. Florian Nitze, "Ammonia assisted growth of multiwalled carbon nanotubes," *Physica Status Solidi B,* vol. 246, pp. 2440-2443, 2009.

[93] E. A. G. K. A. M. a. E. S. A. Michael J. Behre, "Effect of hydrogen on catalyst nanoparticles in carbon nanotube growth," *Journal of Applied Physics,* vol. 108, 2010.

[94] B. B. M. F. C. W. a. F. Y. S. Esconjauregui, "Use of plasma treatment to grow carbon nanotube forests on TiN substrate," *Journal of Applied Physics,* vol. 109, 2011.

[95] S. Y. T. K. a. K. O. Tomohiro Nozaki, "Atmospheric-pressure plasma synthesis of carbon nanotubes," *Journal of Physics D: Applied Physics,* vol. 44, 2011.

[96] R. L. K. T. N. R. G. J. A. a. W. W. M.S. Bell, "Plasma composition during plasma-enhanced chemical vapor deposition of carbon nanotubes," *Applied Physics Letters,* vol. 85, no. 7, 2004.

[97] M. C. A. P. S. H. A. F. a. J. R. S. Pisana, "The role of the precursor gases on the surface restructuring of catalyst films during carbon nanotube growth," *Physica E,* vol. 37, pp. 1-5, 2007.

[98] L. X.-Y. X. W. M. Y.-P. H. K. a. Z. Y. Zhang Kai-Liang, "Effect of substrate temperature on aligned high-density carbon nanotubes deposited by RF-PECVD," *Optoelectronics Letters,* vol. 7, no. 2, 2011.

[99] M. H. G. V. H. W. X. W. D. Z. M. F. A. M. J. F. a. D. K. R. Loffler, "Optimization of plasma-enhanced chemical vapor deposition parameters for the growth of individual vertical carbon nanotubes as field emitters," *Carbon,* vol. 49, pp. 4197-4203, 2011.

[100] S. H. S. P. C. D. A. P. A. F. a. J. R. M. Cantoro, "Effects of pre-treatment and plasma enhancement on chemical vapor deposition of carbon nanotubes from ultra-thin catalyst films," *Diamond and Related Materials,* vol. 15, pp. 1029-1035, 2006.

[101] B. M. A. L. D. P. P. A. a. J. B. Sandra Rizk, "Controlled nanostructuration of catalyst particles for carbon nanotubes growth," *Journal of Physical Chemistry C,* vol. 113, pp. 8718-8723, 2009.

[102] H.-C. W. S.-R. J. j.-Y. J. Y.-S. L. C.-H. T. W.-F. W. K.-T. C. a. C.-P. C. Wen-Pin Wang, "The effects of hydrogen plasma pretreatment on the formation of vertically aligned carbon nanotubes," *Applied Surface Science,* vol. 253, pp. 9248-9253, 2007.

[103] M. C. B. K. C. C. A. P. a. J. R. S.Hofmann, "Effects of catalyst film thickness on plasma-

enhanced carbon nanotube growth," *Journal of Applied Physics,* vol. 98, 2005.

[104] M. F. B. B. S. E. a. S. K. S. Esconjauregui, "Manipulation of the catalyst-support interactions for inducing nanotube forest growth," *Journal of Applied Physics,* vol. 109, 2011.

[105] N. -. N. M.-. a. N. Facility. [Online]. Available: http://www.norfab.no/technologies/other-lab-specific-technologies/ntnu-nanolab/scriber/. [Accessed 31 03 2012].

[106] N. -. N. M.-. a. N. Facility. [Online]. Available: http://www.norfab.no/technologies/deposition/ntnu-nanolab/e-beam-evaporator/. [Accessed 31 03 2012].

[107] N. -. N. M.-. a. N. Facility. [Online]. Available: http://www.norfab.no/technologies/deposition/ntnu-nanolab/sputter-coater-and-thermal-evaporator/. [Accessed 31 03 2012].

[108] N. -. N. M.-. a. N. Facility. [Online]. Available: http://www.norfab.no/technologies/high-temp-processes/ntnu-nanolab/rapid-thermal-processing-rtp-oven/. [Accessed 31 03 2012].

[109] N. -. N. M.-. a. N. Facility. [Online]. Available: http://www.norfab.no/technologies/deposition/ntnu-nanolab/pecvd/. [Accessed 31 03 2012].

[110] N. -. N. M.-. a. N. Facility. [Online]. Available: http://www.norfab.no/technologies/etching-dry-and-wet/ntnu-nanolab/plasma-cleaner/. [Accessed 31 03 2012].

[111] [Online]. Available: http://en.wikipedia.org/wiki/Scanning_electron_microscope. [Accessed 30 04 2012].

[112] N. -. N. M.-. a. N. Facility. [Online]. Available: http://www.norfab.no/technologies/characterization/ntnu-nanolab/stem/. [Accessed 31 03 2012].

[113] N. -. N. M.-. a. N. Facility. [Online]. Available: http://www.norfab.no/technologies/characterization/ntnu-nanolab/fib/. [Accessed 31 03 2012].

[114] [Online]. Available: http://en.wikipedia.org/wiki/Transmission_electron_microscopy. [Accessed 31 03 2012].

[115] [Online]. Available: http://www-em.materials.ox.ac.uk/?instrument=JEOL+JEM-2010. [Accessed 31 03 2012].

[116] N. -. N. M.-. a. N. Facility. [Online]. Available: http://www.norfab.no/technologies/characterization/ntnu-nanolab/profilometer-2/. [Accessed 31 03 2012].

[117] E. G. o. Lebow, "VEM Thin Film Evaporation Guide," [Online]. Available: http://www.vacengmat.com/downloads/VEM_Thin_Film_Evaporation_Guide.pdf. [Accessed 31 03 2012].

[118] W. Z. J. L. Y. M. S. C. W. a. J. W. Q. Wang, "Al/Al2O3 film growth and laser-induced transformation," *Applied Surface Science,* vol. 183, pp. 182-190, 2001.

[119] G. E. T. a. D. S. MacKenzie, Handbook of Aluminum, vol. 2, New York: Marcel Dekker Inc., 2003, pp. 119-123.

[120] H. W. a. Z. Ren, "The evolution of carbon nanotubes during their growth by plasma enhanced chemical vapor deposition," *Nanotechnology,* vol. 22, 2011.

[121] Y. M. S. Y. H. L. B. S. L. G.-S. P. W. B. C. N. S. L. a. J. M. K. Young Chul Choi, "Controlling the

diameter, growth rate, and denisty of vertically aligned carbon nanotubes synthesized by microwave plasma-enhanced chemical vapor deposition," *Applied Physics letter,* vol. 76, no. 17, 2000.

[122] G.-H. J. T. H. R. H. K. T. a. K. M. Toshiaki Kato, "Single-walled carbon nanotubes produced by plasma-enhanced chemical vapor deposition," *Chemical Physics Letters,* vol. 381, pp. 422-426, 2003.

[123] K.-H. L. a. J.-M. T. Fei-Lung Lu, "Growth of carbon nanotubes on metallic substrates using a substrate-shielded microwave plasma-enhanced chemical vapor deposition," *Journal of The Electrochemical Society,* vol. 159, pp. 50-54, 2012.

[124] R. V. M. M. a. O. J. Jan Pekárek, "Preperation of freestanding carbon nanotubes using plasma enhanced chemical vapor deposition," *Ins. Spring Seminar on Electronics Technology,* 2011.

[125] T. k. K. O. a. k. O. Tomohiro Nozaki, "A pressure-dependent selective growth of single-walled and multi-walled carbon nanotubes using plasma enhanced chemical vapor deposition," *Carbon,* vol. 48, pp. 232-238, 2010.

[126] S. L. M. C. V. V. T. B. O. G. M. C. A. L. G. P. P. L. D. p. D. H. H. A. G. A. a. W. M. K.B.K Teo, "Plasma enhanced chemical vapour deposition carbon nanotubes/nanofibres-how uniform do they grow?," *Nanotechnology,* vol. 14, pp. 204-211, 2003.

[127] S.-P. C. G.-W. H. C.-C. L. W.-C. L. S.-J. T. a. C.-H. T. Ching-Hsiang Tsai, "Selective carbon nanotube growth on silicon tips with the soft electrostatic force bonding and catalyst transfer concepts," *Nanotechnology,* vol. 16, pp. 296-299, 2005.

[128] C. X. T. B. M. C. F. I. P. V. a. S. E. H. Griffiths, "Plasma assisted growth of carbon nanotube and nanowires," *Surface & Coatings Technology,* vol. 201, pp. 9215-9220, 2007.

[129] T. K. a. R. Hatakeyama, "Direct growth of short single-walled carbon nanotubes with narrow-chirality distribution by time-programmet plasma chemical vapor deposition," *ACS Nano,* vol. 4, no. 12, pp. 7395-7400, 2010.

[130] T. M. M. D. J. J. a. A. G. A. Gohier, "Growth kinetics of low temperature single-walled and few walled carbon nanotubes by plasma enhanced chemical vapor deposition," *Physica,* vol. 37, pp. 34-39, 2007.

[131] Z. L. a. Z. Z. Y.H. Man, "Influence of plasma condition on carbon nanotube growth by rf-pecvd," *Nano-Micro Letters,* vol. 2, no. 1, pp. 37-41, 2010.

[132] Y.-S. M. D. k. J.-H. K. a. W. P. Eun Ju Bae, "Low-temperature growth og single-walled carbon nanotubes by plasma enhanced chemical vapor deposition," *American Chemical Society,* vol. 17, pp. 5141-5145, 2005.

[133] K. O. K. O. a. U. K. Tomohiro Nozaki, "Fabrication of vertically aligned single-walled carbon nanotubes in atmospheric pressure non-thermal plasma CVD," *Carbon,* vol. 45, pp. 364-374, 2007.

[134] T. F. X. C. L. D. G. C. B. J. X. W. X. L. a. S. Z. Jun Jiang, "Synthesis and growth mechanism of Fe-catalyzed carbon nanotubes by plasma-enhanced chemical vapor deposition," *Nuclear Instruments and Methods in Physics Research B,* vol. 244, pp. 327-332, 2006.

[135] S. Iijima, "Helical microtubulus of graphite carbon," *Letters to nature,* vol. 354, pp. 56-58, 1991.

[136] W.-J. L. C.-Y. C. M.-B. C. a. H. C. C. Lien-Te Hsieh, "Converting Methane by Using an RF Plasma Reactor," *Plasma chemistry and plasma processing,* vol. 18, no. 2, 1997.

[137] R. H. a. K. T. Toshiaki Kato, "Diffusion plasma chemical vapour deposition yielding freestanding individual single-walled carbon nanotube on a silicon-based flat substrate," *Nanotechnology,* vol. 17, pp. 2223-2226, 2006.

Appendix A

Arc discharge
Electrolysis
CNTs synthesis methods
Laser ablation
Chemical vapour deposition
Sono-chemical or hydro-thermal
Hot filament
Water assisted
Oxygen assisted
Micro-wave plasma
Radio-frequency
Thermal
Plasma enhanced

Appendix B

Pre-treatment of samples

t	=	Thickness	Max limit NH3	50	sccm
PP	=	Plasma pre-treatment	Max limit CH4	100	sccm
TP	=	Thermal pre-treatment	Max limit Ar	2000	sccm

ID	tOxide[nm]	tCatalyst[nm]	Treatment	Table temp[^{0}C]	Chill temp[^{0}C]	Time[s]	Power[W]	Pressure[mTorr]	CH4[sccm]	NH3[sccm]	Ar[sccm]	N2[sccm]	Comments
SiAlFe-PP1	50	5	PP	700	20	60	50	500		50			Variation of time
SiAlFe-PP2	50	5	PP	700	20	180	50	500		50			
SiAlFe-PP3	50	5	PP	700	20	300	50	500		50			
SiAlFe-PP4	50	5	PP	700	20	600	50	500		50			
SiAlFe-PP5	50	5	PP	700	20	180	20	500		50			Variation of power
SiAlFe-PP6	50	5	PP	700	20	180	100	500		50			
SiAlFe-PP7	50	5	PP	700	20	180	200	500		50			
SiAlFe-PP8	50	5	PP	700	20	180	300	500		50			
SiAlFe-PP9	50	5	PP	700	20	180	50	500		40			Variation of gas flow
SiAlFe-PP10	50	5	PP	700	20	180	50	500		30			
SiAlFe-PP11	50	5	PP	700	20	180	50	500		20			
SiAlFe-PP12	50	5	PP	700	20	180	50	500		10			
SiAlFe-PP13	50	5	PP	700	20	180	50	50		50			Variation of pressure
SiAlFe-PP14	50	5	PP	700	20	180	50	200		50			PP13&PP14; Strike pressure: 0.4Torr, Ramp rate: 10
SiAlFe-PP15	50	5	PP	700	20	180	50	1000		50			
SiAlFe-PP16	50	5	PP	700	20	180	50	1500		50			
SiAlFe-PP17	50	2	PP	700	20	180	50	500		50			Variation of tCatalyst
SiAlFe-PP18	50	8	PP	700	20	180	50	500		50			
SiAlFe-PP19	50	15	PP	700	20	180	50	500		50			
SiAlFe-PP20	50	30	PP	700	20	180	50	500		50			
SiAlFe-PP21	50	5	PP	100	20	180	50	500		50			Variation of temperature
SiAlFe-PP22	50	5	PP	300	20	180	50	500		50			
SiAlFe-PP23	50	5	PP	450	20	180	50	500		50			
SiAlFe-PP24	50	5	PP	600	20	180	50	500		50			
SiAlFe-TP1	50	5	TP	500	20	600	0	500		50			TP, not PP
SiAlFe-TP2	50	5	TP	700	20	600	0	500		50			
SiAlFe-TP3	50	5	TP	500	20	900	0	500		50			
SiAlFe-TP4	50	5	TP	700	20	900	0	500		50			

Appendix C

The batches in black was executed, while the ones in blue were not.

CNT Growth schedule

t	=	Thickness	Max limit NH3	50	sccm
PP	=	Plasma pre-treatment	Max limit CH4	100	sccm
TP	=	Thermal pre-treatment	Max limit Ar	2000	sccm

The parameters below is only valid for the growth step. Pretreatment is given on the right side.

Tooling factor (TF) = 6 (used for all samples)

Alle samples have been run in the RTP unit after Al sputtering to enhance the thickness of the oxide layer [500°C, O2 flow=500sccm, time=30 minutes]

All samples have been heated from 300°C, and up to the TP temperature of 650°C in a NH3(50) flow, 0mTorr and 30 minutes.

Samples by TP(if other parameters are not mentioned):
[NH3(50), 30 minutes, 1000mTorr, 0W]

Samples by PP (if other parameters are not mentioned):
[NH3(50), 1000mTorr, 100W, 5 minutes]

The growth step is done directly after the TP/PP stage.

During cooling down to 300°C, the samples are exposed in an Ar(1200) flow, 0mTorr and 120 minutes.

ID	tBarrier[nm]	tCatalyst[nm]	Treatment	Table temp[°C]	Chill temp[°C]	Time[m]	Power[W]	Pressure[mTorr]	CH4[sccm]	NH3[sccm]	N2O[sccm]	VACNTs?	Comments
SiAlFe-TP-E47	30	1	TP	650	20	60	100	1000	50			VACNT	"CNTRecipe"
SiAlFe-TP-E48	30	3	TP	650	20	60	100	1000	50			X	
SiAlFe-TP-E49	30	6	TP	650	20	60	100	1000	50			X	
SiAlFe-TP-E50	30	10	TP	650	20	60	100	1000	50			X	
SiAlFe-TP-E51	30	1	TP	650	20	60	100	1000	35			X	Variantion of CH4 flow
SiAlFe-TP-E52	30	3	TP	650	20	60	100	1000	35			X	
SiAlFe-TP-E53	30	6	TP	650	20	60	100	1000	35			X	
SiAlFe-TP-E54	30	10	TP	650	20	60	100	1000	35			X	
SiAlFe-TP-E55	30	1	TP	650	20	60	100	1000	100			VACNT	Variantion of CH4 flow
SiAlFe-TP-E56	30	3	TP	650	20	60	100	1000	100			X	
SiAlFe-TP-E57	30	6	TP	650	20	60	100	1000	100			X	
SiAlFe-TP-E58	30	10	TP	650	20	60	100	1000	100			X	

SiAlFe-TP-E59	30	1	TP	650	20	60	100	1000	50	5		X	Adding NH3 flow[10:1 ratio]
SiAlFe-TP-E60	30	3	TP	650	20	60	100	1000	50	5		X	
SiAlFe-TP-E61	30	6	TP	650	20	60	100	1000	50	5		X	
SiAlFe-TP-E62	30	10	TP	650	20	60	100	1000	50	5		X	
SiAlFe-TP-E63	30	1	TP	650	20	60	100	1000	50	15		X	Adding more NH3 flow [3:1 ratio]
SiAlFe-TP-E64	30	3	TP	650	20	60	100	1000	50	15		X	
SiAlFe-TP-E65	30	6	TP	650	20	60	100	1000	50	15		X	
SiAlFe-TP-E66	30	10	TP	650	20	60	100	1000	50	15		X	
SiAlFe-TP-E67	30	1	TP	650	20	60	100	1000	50	25		X	Adding more NH3 flow [2:1 ratio]
SiAlFe-TP-E68	30	3	TP	650	20	60	100	1000	50	25		X	
SiAlFe-TP-E69	30	6	TP	650	20	60	100	1000	50	25		X	
SiAlFe-TP-E70	30	10	TP	650	20	60	100	1000	50	25		X	
SiAlFe-TP-E71	30	1	TP	650	20	60	100	1000	100	5		X	Adding NH3 flow[20:1 ratio]
SiAlFe-TP-E72	30	3	TP	650	20	60	100	1000	100	5		X	
SiAlFe-TP-E73	30	6	TP	650	20	60	100	1000	100	5		X	
SiAlFe-TP-E74	30	10	TP	650	20	60	100	1000	100	5		X	
SiAlFe-TP-E75	30	1	TP	650	20	60	100	1000	100	15		X	Adding more NH3 flow [6:1 ratio]
SiAlFe-TP-E76	30	3	TP	650	20	60	100	1000	100	15		X	
SiAlFe-TP-E77	30	6	TP	650	20	60	100	1000	100	15		X	
SiAlFe-TP-E78	30	10	TP	650	20	60	100	1000	100	15		X	
SiAlFe-TP-E79	30	1	TP	650	20	60	100	1000	100	25		X	Adding more NH3 flow [4:1 ratio]
SiAlFe-TP-E80	30	3	TP	650	20	60	100	1000	100	25		X	
SiAlFe-TP-E81	30	6	TP	650	20	60	100	1000	100	25		X	
SiAlFe-TP-E82	30	10	TP	650	20	60	100	1000	100	25		X	
SiAlFe-TP-E83	30	1	TP									X	TP only, so that analysis of the size
SiAlFe-TP-E84	30	3	TP									X	of the particles can be performed!
SiAlFe-TP-E85	30	6	TP									X	The CNT growth step is excluded!
SiAlFe-TP-E86	30	10	TP									X	
SiAlFe-TP-E87	30	1	TP	650	20	60	200	1000	50			VACNT	Variation of power
SiAlFe-TP-E88	30	3	TP	650	20	60	200	1000	50			X	
SiAlFe-TP-E89	30	6	TP	650	20	60	200	1000	50			X	
SiAlFe-TP-E90	30	10	TP	650	20	60	200	1000	50			X	

SiAlFe-TP-E91	30	1	TP	650	20	60	300	1000	50			VACNT	Variation of power
SiAlFe-TP-E92	30	3	TP	650	20	60	300	1000	50			VACNT	
SiAlFe-TP-E93	30	6	TP	650	20	60	300	1000	50			X	
SiAlFe-TP-E94	30	10	TP	650	20	60	300	1000	50			X	
SiAlFe-TP-E95	30	1	TP	650	20	60	20	1000	50			VACNT	Variation of power
SiAlFe-TP-E96	30	3	TP	650	20	60	20	1000	50			X	
SiAlFe-TP-E97	30	6	TP	650	20	60	20	1000	50			X	
SiAlFe-TP-E98	30	10	TP	650	20	60	20	1000	50			X	
SiAlFe-TP-E99	30	1	TP	650	20	60	100	1000	50	1		X	Adding NH3 flow [50:1 ratio]
SiAlFe-TP-E100	30	3	TP	650	20	60	100	1000	50	1		X	
SiAlFe-TP-E101	30	6	TP	650	20	60	100	1000	50	1		X	
SiAlFe-TP-E102	30	10	TP	650	20	60	100	1000	50	1		X	
SiAlFe-TP-E103	30	1	TP	650	20	60	100	1000	100	1		X	Adding NH3 flow [100:1 ratio]
SiAlFe-TP-E104	30	3	TP	650	20	60	100	1000	100	1		X	
SiAlFe-TP-E105	30	6	TP	650	20	60	100	1000	100	1		X	
SiAlFe-TP-E106	30	10	TP	650	20	60	100	1000	100	1		X	
SiAlFe-TP-E107	30	1	TP	650	20	30	100	1000	50			X	Variation of growth time
SiAlFe-TP-E108	30	3	TP	650	20	30	100	1000	50			X	
SiAlFe-TP-E109	30	6	TP	650	20	30	100	1000	50			X	
SiAlFe-TP-E110	30	10	TP	650	20	30	100	1000	50			X	
SiAlFe-TP-E111	30	1	TP	650	20	10	100	1000	50			X	Variation of growth time
SiAlFe-TP-E112	30	3	TP	650	20	10	100	1000	50			X	
SiAlFe-TP-E113	30	6	TP	650	20	10	100	1000	50			X	
SiAlFe-TP-E114	30	10	TP	650	20	10	100	1000	50			X	
SiAlFe-TP-E115	30	1	TP	650	20	60	100	1000	50			VACNT	NH3 during TP has been changed
SiAlFe-TP-E116	30	3	TP	650	20	60	100	1000	50			VACNT	with N2O(50sccm), but otherwise
SiAlFe-TP-E117	30	6	TP	650	20	60	100	1000	50			VACNT	with equal parameters.
SiAlFe-TP-E118	30	10	TP	650	20	60	100	1000	50			VACNT	
SiAlFe-TP-E119	30	1	TP	700	20	60	100	1000	50			VACNT	Variation in temperature
SiAlFe-TP-E120	30	3	TP	700	20	60	100	1000	50			VACNT	
SiAlFe-TP-E121	30	6	TP	700	20	60	100	1000	50			X	
SiAlFe-TP-E122	30	10	TP	700	20	60	100	1000	50			X	

SiAlFe-TP-E123	30	1	TP	600	20	60	100	1000	50			X	Variation in temperature
SiAlFe-TP-E124	30	3	TP	600	20	60	100	1000	50			X	
SiAlFe-TP-E125	30	6	TP	600	20	60	100	1000	50			X	
SiAlFe-TP-E126	30	10	TP	600	20	60	100	1000	50			X	
SiAlFe-TP-E127	30	1	TP	500	20	60	100	1000	50			X	Variation in temperature
SiAlFe-TP-E128	30	3	TP	500	20	60	100	1000	50			X	
SiAlFe-TP-E129	30	6	TP	500	20	60	100	1000	50			X	
SiAlFe-TP-E130	30	10	TP	500	20	60	100	1000	50			X	
SiAlFe-TP-E131	30	1	TP	400	20	60	100	1000	50			X	Variation in temperature
SiAlFe-TP-E132	30	3	TP	400	20	60	100	1000	50			X	
SiAlFe-TP-E133	30	6	TP	400	20	60	100	1000	50			X	
SiAlFe-TP-E134	30	10	TP	400	20	60	100	1000	50			X	
SiAlFe-TP-E135	30	1	TP	300	20	60	100	1000	50			X	Variation in temperature
SiAlFe-TP-E136	30	3	TP	300	20	60	100	1000	50			X	
SiAlFe-TP-E137	30	6	TP	300	20	60	100	1000	50			X	
SiAlFe-TP-E138	30	10	TP	300	20	60	100	1000	50			X	
SiAlFe-TP-E139	30	1	TP	650	20	120	100	1000	50			VACNT	Variation in growth time
SiAlFe-TP-E140	30	3	TP	650	20	120	100	1000	50			VACNT	
SiAlFe-TP-E141	30	6	TP	650	20	120	100	1000	50			X	
SiAlFe-TP-E142	30	10	TP	650	20	120	100	1000	50			X	
SiAlFe-PP-E143	30	1	PP	650	20	60	100	1000	50			VACNT	PP instead of TP
SiAlFe-PP-E144	30	3	PP	650	20	60	100	1000	50			VACNT	PP for 5 minutes
SiAlFe-PP-E145	30	6	PP	650	20	60	100	1000	50			X	
SiAlFe-PP-E146	30	10	PP	650	20	60	100	1000	50			X	
SiAlFe-PP-E147	30	1	PP	650	20	60	100	1000	50			X	PP instead of TP
SiAlFe-PP-E148	30	3	PP	650	20	60	100	1000	50			X	PP for 15 minutes
SiAlFe-PP-E149	30	6	PP	650	20	60	100	1000	50			X	
SiAlFe-PP-E150	30	10	PP	650	20	60	100	1000	50			X	
SiAlFe-PP-E151	30	1	PP	650	20	60	100	1000	50			X	PP instead of TP
SiAlFe-PP-E152	30	3	PP	650	20	60	100	1000	50			X	PP for 30 minutes
SiAlFe-PP-E153	30	6	PP	650	20	60	100	1000	50			X	
SiAlFe-PP-E154	30	10	PP	650	20	60	100	1000	50			X	

SiAlFe-TP-E155	30	1	TP	650	20	60	100	1000	50			VACNT	TP is set to 5 minutes, instead of
SiAlFe-TP-E156	30	3	TP	650	20	60	100	1000	50			X	30 minutes
SiAlFe-TP-E157	30	6	TP	650	20	60	100	1000	50			X	
SiAlFe-TP-E158	30	10	TP	650	20	60	100	1000	50			X	
SiAlFe-TP-E159		1	TP	650	20	60	100	1000	50			VACNT	NO Al barrier layer
SiAlFe-TP-E160		3	TP	650	20	60	100	1000	50			X	
SiAlFe-TP-E161		6	TP	650	20	60	100	1000	50			X	
SiAlFe-TP-E162		10	TP	650	20	60	100	1000	50			X	
SiAlFe-PP-E163		1	PP	650	20	60	100	1000	50			VACNT	NO Al barrier layer
SiAlFe-PP-E164		3	PP	650	20	60	100	1000	50			X	
SiAlFe-PP-E165		6	PP	650	20	60	100	1000	50			X	
SiAlFe-PP-E166		10	PP	650	20	60	100	1000	50			X	
SiAlFe-TP-E167	30	1	TP	650	20	60	100	1000	50			VACNT	NO heating and cooling
SiAlFe-TP-E168	30	3	TP	650	20	60	100	1000	50			VACNT	cycle. The TP and CNT growth starts
SiAlFe-TP-E169	30	6	TP	650	20	60	100	1000	50			VACNT	directly at 650 degrees.
SiAlFe-TP-E170	30	10	TP	650	20	60	100	1000	50			VACNT	
SiAlFe-PP-E171	30	1	PP	650	20	60	100	1000	50			VACNT	NO heating and cooling
SiAlFe-PP-E172	30	3	PP	650	20	60	100	1000	50			VACNT	cycle. The PP and CNT growth starts
SiAlFe-PP-E173	30	6	PP	650	20	60	100	1000	50			VACNT	directly at 650 degrees.
SiAlFe-PP-E174	30	10	PP	650	20	60	100	1000	50			VACNT	
SiAlFe-PP-E175	30	1	PP										PP only, so that analysis of the size
SiAlFe-PP-E176	30	3	PP										of the particles can be performed!
SiAlFe-PP-E177	30	6	PP										The CNT growth step is excluded!
SiAlFe-PP-E178	30	10	PP										
SiAlFe-TP-E179	30	1	TP	650	20	240	100	1000	50				Variation in growth time
SiAlFe-TP-E180	30	3	TP	650	20	240	100	1000	50				
SiAlFe-TP-E181	30	6	TP	650	20	240	100	1000	50				
SiAlFe-TP-E182	30	10	TP	650	20	240	100	1000	50				
SiAlFe-TP-E183	30	1	TP	650	20	60	100	1000	50			VACNT	TP is set to 15 minutes, instead of
SiAlFe-TP-E184	30	3	TP	650	20	60	100	1000	50			VACNT	30 minutes
SiAlFe-TP-E185	30	6	TP	650	20	60	100	1000	50			X	
SiAlFe-TP-E186	30	10	TP	650	20	60	100	1000	50			X	

SiAlFe-TP-E187	30	1	TP	650	20	60	100	1000	50		10		NH3 during TP has been changed
SiAlFe-TP-E188	30	3	TP	650	20	60	100	1000	50		10		with N2O(50sccm), but otherwise
SiAlFe-TP-E189	30	6	TP	650	20	60	100	1000	50		10		with equal parameters.
SiAlFe-TP-E190	30	10	TP	650	20	60	100	1000	50		10		
SiAlFe-PP-E191	30	1	PP	650	20	60	100	1000	50		10		NH3 during PP has been changed
SiAlFe-PP-E192	30	3	PP	650	20	60	100	1000	50		10		with N2O(50sccm), but otherwise
SiAlFe-PP-E193	30	6	PP	650	20	60	100	1000	50		10		with equal paramters.
SiAlFe-PP-E194	30	10	PP	650	20	60	100	1000	50		10		
SiAlFe-TP-E195	30	1	TP	650	20	60	0	1000	50			X	Variation of power
SiAlFe-TP-E196	30	3	TP	650	20	60	0	1000	50			X	(CVD since P=0W)
SiAlFe-TP-E197	30	6	TP	650	20	60	0	1000	50			X	
SiAlFe-TP-E198	30	10	TP	650	20	60	0	1000	50			X	
SiAlFe-TP-E199	30	1	TP	650	20	60	100	1000	50				TP is increased to 60 minutes
SiAlFe-TP-E200	30	3	TP	650	20	60	100	1000	50				
SiAlFe-TP-E201	30	6	TP	650	20	60	100	1000	50				
SiAlFe-TP-E202	30	10	TP	650	20	60	100	1000	50				
SiAlFe-TP-E203	30	1	TP	650	20	60	100	1500	50				Variation of pressure
SiAlFe-TP-E204	30	3	TP	650	20	60	100	1500	50				
SiAlFe-TP-E205	30	6	TP	650	20	60	100	1500	50				
SiAlFe-TP-E206	30	10	TP	650	20	60	100	1500	50				
SiAlFe-TP-E207	30	1	TP	650	20	60	100	500	50				Variation of pressure
SiAlFe-TP-E208	30	3	TP	650	20	60	100	500	50				
SiAlFe-TP-E209	30	6	TP	650	20	60	100	500	50				
SiAlFe-TP-E210	30	10	TP	650	20	60	100	500	50				
SiAlFe-PP-E211	30	1	PP	650	20	60	100	1000	50			VACNT	Pretreat is done with PP for
SiAlFe-PP-E212	30	3	PP	650	20	60	100	1000	50			VACNT	5 minutes, and at 300^{0}
SiAlFe-PP-E213	30	6	PP	650	20	60	100	1000	50			VACNT	(instead of 650^{0})
SiAlFe-PP-E214	30	10	PP	650	20	60	100	1000	50			VACNT	
SiAlFe-PP-E215	30	1	PP	650	20	60	100	1000	50				PP is done for 5 minutes at 100^{0}C
SiAlFe-PP-E216	30	3	PP	650	20	60	100	1000	50				(instead of 650^{0}C)
SiAlFe-PP-E217	30	6	PP	650	20	60	100	1000	50				
SiAlFe-PP-E218	30	10	PP	650	20	60	100	1000	50				

SiAlFe-TP-E219	30	1	TP	650	20	10	100	1000	50			VACNT	NO heating and cooling
SiAlFe-TP-E220	30	3	TP	650	20	10	100	1000	50			VACNT	cycle. Variation of growth time.
SiAlFe-TP-E221	30	6	TP	650	20	10	100	1000	50			VACNT	
SiAlFe-TP-E222	30	10	TP	650	20	10	100	1000	50			VACNT	
SiAlFe-TP-E223	30	1	TP	650	20	60	100	1000	50				Without any slow heating
SiAlFe-TP-E224	30	3	TP	650	20	60	100	1000	50				TP tme for 60 minutes
SiAlFe-TP-E225	30	6	TP	650	20	60	100	1000	50				(instead of 30)
SiAlFe-TP-E226	30	10	TP	650	20	60	100	1000	50				
SiAlFe-TP-E227	30	1	TP	650	20	10	100	1000	50			VACNT	NO heating and cooling
SiAlFe-TP-E228	30	3	TP	650	20	10	100	1000	50			VACNT	cycle. TP for 60 minutes
SiAlFe-TP-E229	30	6	TP	650	20	10	100	1000	50			CNT	(instead of 30)
SiAlFe-TP-E230	30	10	TP	650	20	10	100	1000	50			X	Variation in growth time too
SiAlFe-TP-E231	30	1	TP	650	20	60	100	1000	50				NO heating and cooling
SiAlFe-TP-E232	30	3	TP	650	20	60	100	1000	50				cycle. TP with N2O
SiAlFe-TP-E233	30	6	TP	650	20	60	100	1000	50				(instead of NH3)
SiAlFe-TP-E234	30	10	TP	650	20	60	100	1000	50				

Appendix D

For any future continuation of this project, there would be certain things that would be interesting to investigate, especially since VACNTs have successfully been yielded. Some suggestions are proposed below.

Growth of SWCNT

Growth of SWCNT has very strict requirements, but is of huge interest since it could reveal the true potential of CNTs. Testing of MWCNTs have been conducted, but since they consist of several concentric SWCNTs it is very difficult to predict the mechanical strength of a single tube.

Mechanical testing

Conducting tests on the mechanical strength of VACNTs and how it is affected by different diameters, such as:

- Tensile and comprehensive strength
- Modulus of elasticity (both axial and bending)
- Shear modulus

In earlier experiments, people have been welding the edge of CNTs with AFM tips by a carbonaceous material. Maybe there exists smart ways of doing the test or maybe it only demands more fitted equipment. To the autumn of 2012, the IVT faculty will receive a new nano-electro-mechanical testing system (NEMS). Maybe this could be used for such testing?

Testing of other catalyst materials

Other material than the traditional ones (Co, Ni and Fe) have been suggested to improve the quality of the grown tubes and demands lower growth temperatures. This is a huge task, since it would most probably not work to use equal parameters during PECVD growth for different materials.

Various other tasks

- Successful yield of VACNTs on stainless steel substrates.
- Investigate the bonding strength between VACNTs and different substrates (such as those for this experiment, stainless steel or other substrates) by wear tests.
- Check the superhydrophobic character of VACNT coated surfaces and compare the corrosion resistance between stainless steel VACNTs grown substrates to those which are uncoated.
- Compare the ice formation on coated, uncoated steel and Al substrates (this task is of special interest for making anti-icing systems for airplanes and applications in the Arctic regions).
- Mechanical testing of grown CNTs in the voids of the diatoms in Sindre Hove Bjørnøy's work (patterning of catalysts). Then run mechanical tests to see if any mechanical properties have been enhanced.
- Analysis of the plasma decomposition for different parameters, such as varying power, pressure, temperature etc, to figure out which species that exists during CNT growth.
- Optimize the results for higher growth, since the growth rates in this experiments was not as impressive.
- Achieve SWCNT growth (need very small particles)